Universiteit Gent
Faculteit van de Toegepaste Wetenschappen
Vakgroep Informatietechnologie

Afstembare laserdiodes voor WDM communicatie – *Methodes voor controle en karakterisering*

Tunable laser diodes for WDM communication – *Methods for control and characterisation*

Gert Sarlet

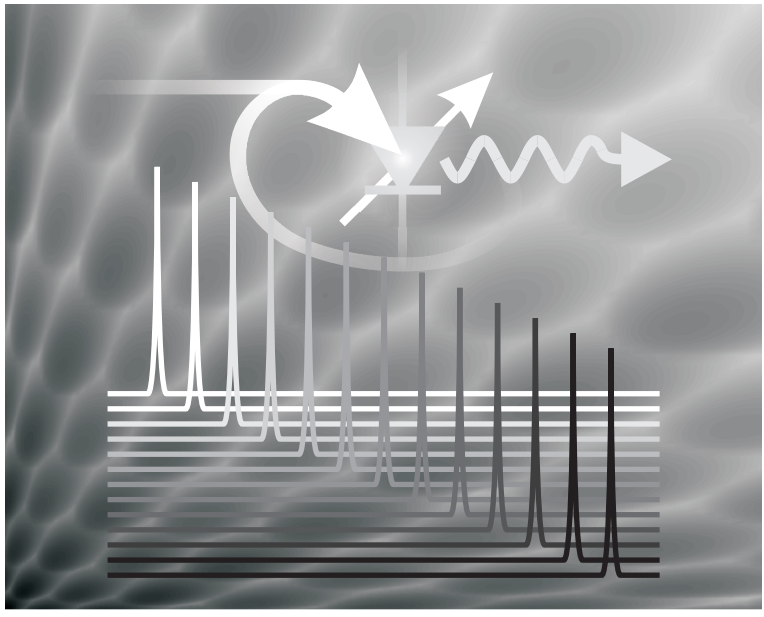

Proefschrift tot het bekomen van de graad van
Doctor in de Toegepaste Wetenschappen:
Elektrotechniek
Academiejaar 2000-2001

Promotors: Prof. Roel Baets
Prof. Geert Morthier

Universiteit Gent
Faculteit van de Toegepaste Wetenschappen

Vakgroep Informatietechnologie
Sint-Pietersnieuwstraat 41
B-9000 Gent, België

Tel: +32 9 2643316
Fax: +32 9 2643593

Dit werk kwam tot stand in het kader van een mandaat van Aspirant bij het Fonds voor Wetenschappelijk Onderzoek – Vlaanderen (België).

This work was carried out in the framework of a position as Research Assistant with the Fund for Scientific Research – Flanders (Belgium).

Preface

In the four years that it took to complete the research reported in this thesis, the image of the tunable laser diode has changed dramatically. In 1996, many research groups around the world were developing tunable laser diodes, but there was very little interest in them from the engineers that were developing fiber-optic communication systems. When in 1997 a company named Altitun was founded in Sweden to commercialise tunable laser technology, many considered this a reckless venture. Only three years later, manufacturers of tunable lasers can barely keep up with the demand. Nevertheless, market research firms expect this demand to continue to grow explosively for a number of years.

Before I let you discover the exciting universe of the tunable laser diode, I want to express a few words of gratitude to all the people that have – consciously or unconsciously – contributed to the realisation of this thesis.

First of all I would like to acknowledge Prof. Paul Lagasse for his continuous work behind the scenes to create and maintain a stimulating working environment at the Department of Information Technology (INTEC), allowing all the researchers at INTEC to fully exploit their talents. Many thanks of course also go out to my supervisors, Prof. Roel Baets and Prof. Geert Morthier, who helped me to set out the goals for my research and gave constructive feedback along the road. Their combined experience in optoelectronics always formed a reliable touchstone for new ideas.

Much of the work reported in this thesis was carried out in the context of two international research projects, BLISS and ACTUAL. I would therefore like to thank all the partners in those projects for the many fruitful discussions. More in particular, Jens Buus is acknowledged for the efficient management of these projects. Special thanks go to Dave Robbins and Doug Reid at Marconi – Caswell Technology in the UK for the collaboration on the design of multi-frequency reflectors, and Björn Broberg, Pierre-Jean Rigole and Jan-Olof Wesström at Altitun in Sweden for the help in figuring out the behaviour of the GCSR laser. Finally, I would like to express my gratitude to Hiroyuki Ishii, Yuzo Yoshikuni and Hiroshi Yasaka at NTT Optoelectronics in Japan for the many discussions on feedback control, for the help with the modulation experiments, and for their hard work to confirm my experimental results for numerous SSG-DBR lasers.

The following people are acknowledged for all the supportive work they performed throughout these four years: Eddy Hebbelinck, Marc Declercq and Luc Haentjens for the help in building the mechanics and electronics of the laser measurement set-up; Geert Diet for the many hours of LabVIEW programming; Guy Janssens,

Dimitri De Winne and Joachim Goeminne for their support in the ongoing struggle against chaos in the measurement lab.

Of course, this thesis would not have been realised if there had been no pleasant distractions once in a while. Therefore a warm thank you is addressed to all the colleagues – both the old ones at INTEC and the new ones at Altitun – who provided those distractions with a joke, a chat, a game of cards, or a discussion over some totally irrelevant subject, …

Last but not least, I would like to thank all the friends, relatives and future relatives who have supported and encouraged me throughout these four years. Special gratitude of course goes out to my parents, who have always stimulated me to expand my knowledge and explore new horizons. Finally, I send a big kiss to my girlfriend and wife-to-be Sylvie, to thank her for all the patience she has had throughout those four years, and especially these last two months, when I was far away in Stockholm, working at Altitun during daytime and finishing of this thesis at night and on weekends.

In short: thank you all so very much!

Gert

September 2000

Table of Contents

Samenvatting

S.1 Inleiding

S.1.1 Achtergrond – golflengtemultiplexering in de optische communicatie

Fabrikanten van telecommunicatiesystemen wereldwijd zijn voortdurend op zoek naar nieuwe, inventieve oplossingen die toelaten de netwerkcapaciteit snel en flexibel uit te breiden. De katalysator voor deze evolutie is uiteraard de explosieve groei van het Internet. Volgens een recente schatting (juli 2000) bedraagt het gemiddelde dataverkeer meer dan 1 Tbit/s, en heeft het aldus het klassieke telefoonverkeer voorbijgestoken [1]. Nog steeds verwacht men dat het dataverkeer ongeveer elke 9 maanden zal verdubbelen.

Een van de belangrijkste technologieën die deze evolutie mogelijk maakt is natuurlijk de optische communicatie. Via de golflengtemultiplexeringstechniek kunnen nooit eerder gekende datadebieten over één enkele glasvezel getransporteerd worden. Bij golflengtemultiplexering (wavelength division multiplexing, WDM) worden verschillende datasignalen (met een typische bitsnelheid van 2.5 Gbit/s of 10 Gbit/s) gemoduleerd op optische draaggolven met een verschillende frequentie. De optische signalen worden vervolgens gemultiplexeerd en over één enkele optische vezel verzonden. Conceptueel is golflengtemultiplexering identiek aan de frequentiemultiplexering die gebruikt wordt in klassieke radiotransmissie.

WDM kende een belangrijke doorbraak na de uitvinding van de glasvezelversterker (Erbium doped fiber amplifier, EDFA). Voordien moest het WDM-signaal ongeveer elke 100 km gedemultiplexeerd worden om detectie, elektronische regeneratie en hertransmissie van de individuele kanalen mogelijk te maken. De EDFA maakt het daarentegen mogelijk om meerdere kanalen tegelijk te versterken, zodat veel langere afstanden overbrugd kunnen worden zonder elektronische regeneratie. Standaard glasvezelversterkers kunnen signalen versterken in de frequentieband van 192 THz tot 196 THz (conventionele of C-band). Meer recent werden EDFA's ontwikkeld die versterken in de zogenaamde L-band (lange golflengteband), d.w.z. van 187 THz tot 191 THz.

Vandaag bestaat een typische transmissie-eenheid in een WDM-systeem uit een laser met gedistribueerde terugkoppeling (distributed feedback, DFB) met een geïntegreerde of externe modulator, die de optische draaggolf gegenereerd door de

laser aan een hoog tempo aan- en uitschakelt om de digitale data op de draaggolf te coderen. De eerste commerciële WDM systemen (daterend van 1996) gebruikten 4 tot 8 frequentiekanalen, elk gemoduleerd aan een snelheid van 2.5 Gbit/s. De kanaalafstand bedroeg 400 of 200 GHz. Naarmate de vraag naar capaciteit toenam werd het aantal kanalen vergroot en de kanaalafstand verkleind. De frequenties voor gebruik in WDM systemen werden recent gestandaardiseerd door de Internationale Telecommunicatie Unie. Een regelmatig raster werd vastgelegd, met een ankerfrequentie van 193.1 THz en met een kanaalspatiëring gelijk aan een geheel veelvoud van 50 GHz of 100 GHz [2]. Vandaag zijn systemen beschikbaar met 80 kanalen bij 50 GHz spatiëring voor 2.5 Gbit/s datasignalen of 40 kanalen bij 100 GHz spatiëring voor 10 Gbit/s datasignalen [3]-[4]. Om te kunnen voldoen aan de vraag naar capaciteit zal het aantal kanalen allicht verder moeten toenemen, zowel door de kanaalafstand te verkleinen als door de frequentieband uit te breiden (door bijvoorbeeld de L-band te gebruiken).

S.1.2 Toepassingen van afstembare lasers in WDM systemen

Zoals vermeld zijn de lichtbronnen in de huidige WDM transmissiesystemen DFB lasers, die licht emitteren met een vaste frequentie. In vele toepassingen zou het voordelig zijn om over een afstembare laser te beschikken, dat wil zeggen een laser waarvan de emissiefrequentie op verschillende kanalen van het ITU raster kan ingesteld worden. In wat volgt geven we een overzicht van de meest geciteerde voordelen van afstembare lasers.

Back-up lasers

In een communicatiesysteem is het uiterst belangrijk dat het verkeer niet onderbroken wordt. Daarom wordt meestal een back-up systeem voorzien, dat overneemt in geval een laser uitvalt. Indien enkel lasers met een vaste frequentie gebruikt worden, moet in ieder knooppunt een back-up laser voorzien worden voor elk afzonderlijk kanaal. Worden daarentegen afstembare lasers gebruikt, dan kan elke laser als back-up dienen voor een groot aantal kanalen. Vandaag zijn er afstembare lasers beschikbaar die meer dan 80 kanalen met 50 GHz spatiëring kunnen bestrijken.

Inventarisbeheer

Wanneer een laser uitvalt moet de defecte transmissie-eenheid zo snel mogelijk vervangen worden, zelfs wanneer een back-up systeem voorzien is. Bijgevolg moet een netwerkoperator een stock van transmissie-eenheden bijhouden. Indien DFB lasers gebruikt worden, moet een reservevoorraad van lasers onderhouden worden voor elk kanaal. Het beheer van een dergelijk inventaris wordt snel omslachtig en duur naarmate het aantal kanalen toeneemt. Met afstembare lasers moet ofwel slechts één type laser gestockeerd worden, ofwel een sterk gereduceerd aantal verschillende lasers (waarbij elk type laser een deel van de kanalen bestrijkt).

Frequentie-omzetting

Heel wat geavanceerde netwerkconcepten vereisen een component die een signaal kan overzetten van de ene optische draagfrequentie naar de andere. Indien deze laatste afstembaar moet zijn, vereist dit uiteraard een afstembare laser. De omzetting

kan ofwel via een elektronische tussenstap (O/E/O-omzetting) of rechtstreeks optisch gebeuren (met behulp van een niet-lineaire optische component).

Heterodyne detectie

Naarmate de kanaalspatiëring in WDM systemen verkleint, wordt het alsmaar moeilijker om naburige kanalen te scheiden met behulp van optische filters. Door middel van heterodyne detectie wordt dit probleem verlegd naar het elektrische domein, waar in het algemeen veel betere filters beschikbaar zijn. Een essentieel onderdeel van een heterodyne ontvanger is een afstembare laser, die dient als lokale oscillator [5]. Het licht van de lokale oscillator (frequentie ν_{LO}) wordt gecombineerd met het gemoduleerde licht (frequentie ν_{data}) door middel van een 3 dB-koppelaar en gedetecteerd met een paar fotodiodes. Aldus wordt een radiofrequent signaal gegenereerd bij de verschilfrequentie $\nu_{RF} = \nu_{data} - \nu_{LO}$. Om het signaal bij een bepaalde frequentie ν_{data} te detecteren moet de LO laser afgestemd worden tot binnen een paar GHz van de draagfrequentie van het geselecteerde kanaal en vervolgens werken als een spanningsgecontroleerde oscillator die de kanaalfrequentie volgt om ν_{RF} constant te houden. De naburige kanalen worden onderdrukt met behulp van een elektrisch banddoorlaatfilter gecentreerd rond ν_{RF}.

Dynamische capaciteitsallocatie in golflengterouterende netwerken

Netwerkoperatoren behoeven steeds meer flexibiliteit in hun netwerk om capaciteit te kunnen voorzien waar en wanneer nodig. Een mogelijke oplossing bestaat erin golflengterouterende componenten te plaatsen in de netwerkknooppunten, en gebruik te maken van afstembare lasers om dynamisch verbindingen op te zetten doorheen het netwerk. Een dergelijk netwerkconcept werd bijvoorbeeld bestudeerd in het ACTUAL project [6]-[8].

Optisch schakelen van datapakketten

Hoewel het telecommunicatieverkeer snel volledig gedomineerd zal worden door dataverkeer, houden de huidige (optische) netwerkarchitecturen geen rekening met het typische karakter van dit dataverkeer. Data wordt normaal verzonden in relatief korte pakketten, die doorheen het netwerk gerouteerd worden zonder een specifieke punt-tot-punt verbinding op te zetten. Door gebruik te maken van snel afstembare lasers kan men een netwerk opbouwen waarin optische pakketten gerouteerd worden op basis van de frequentie van de draaggolf [6], [8]-[10]. In deze toepassing is het uiteraard van belang dat de laser kan afgestemd worden in een tijdsspanne die veel korter is dan de typische lengte van een datapakket.

S.2 Afstembare laserdiodes – stand van de technologie

In de volgende paragrafen geven we een overzicht van de geïntegreerde afstembare laserdiodes die momenteel (herfst 2000) in aanmerking komen voor toepassingen in WDM optische communicatie. Al deze lasers bestaan uit een longitudinale integratie van secties met een verschillende functie. Typisch vindt men een actieve sectie, die voor de optische versterking zorgt, een of meerdere filtersecties met een afstembare frequentieselectieve transmissie of reflectie, en een fasesectie die zorgt voor de fijnafstemming van de caviteitsresonanties [11].

S.2.1 Elektronische frequentiecontrole

Om in een laser lichtemissie te genereren bij een bepaalde frequentie ν moeten twee voorwaarden voldaan zijn. De kringwinst G moet gelijk zijn aan 1 bij die frequentie, en er moet voldaan zijn aan de fasevoorwaarde $\phi(\nu) = 2\pi k$ (met k een geheel getal):

$$\begin{aligned} G(\nu) &= \frac{A}{H(\nu)} = 1 \\ \phi(\nu) &= \frac{2\pi\nu}{c} 2\sum_l n_l L_l = 2\pi k \end{aligned} \tag{S.1}$$

Hierbij zijn de n_l en L_l de effectieve indices en lengtes van de verschillende secties. In de eerste uitdrukking werd de kringwinst geschreven als de verhouding van een frequentie-onafhankelijke winstfactor A en een frequentie-afhankelijke verliesfactor $H(\nu)$. De laser zal oscilleren bij de frequentie ν_n die aan de fasevoorwaarde voldoet en een minimale waarde voor $H(\nu_n)$ oplevert.

Om een laser af te stemmen zijn er bijgevolg principieel twee mogelijkheden: men kan de filterkarakteristiek $H(\nu)$ afstemmen, of men kan de caviteitsresonanties (of caviteitsmodes) afstemmen. In het eerste geval zal de frequentie initieel constant blijven bij de originele waarde ν_n. Pas wanneer een van de naburige modes (ν_{n-1} of ν_{n+1}) een lagere waarde voor $H(\nu)$ geeft, zal de laserfrequentie naar deze mode springen. In de praktijk gebeurt het afstemmen van $H(\nu)$ door het verschuiven van de piekfrequentie van een optisch filter geïntegreerd in de lasercaviteit. Het filter wordt afgestemd door een brekingsindex in de filterstructuur aan te passen. Wijzigt men de fasevoorwaarde, bijvoorbeeld door een van de brekingsindices n_l te veranderen, dan variëren de modefrequenties continu. De emissiefrequentie vertoont een cyclisch gedrag, aangezien de laser steeds oscilleert in de caviteitsmode ν_n die een minimaal verlies $H(\nu_n)$ ervaart.

In de laserdiodes wordt het licht geleid door een golfgeleiderstructuur die bestaat uit een InGaAsP kern met hoge brekingsindex (en lage bandafstand) omringd door InP materiaal met een lagere brekingsindex (en hogere bandafstand). In de filter- en fasesecties zorgt men ervoor dat het InGaAsP materiaal een bandafstand heeft die groter is dan de fotonenergie $h\nu$ van het licht gegenereerd in de actieve sectie, zodat het materiaal transparant is voor dit licht. Beide afstemmingsmethodes vereisen dat de effectieve brekingsindex van een dergelijke structuur gewijzigd wordt. Hiervoor zijn drie mechanismes beschikbaar: injectie van ladingsdragers in de InGaAsP kernlaag, aanleggen van een elektrisch veld, of wijzigen van de temperatuur. Deze mechanismes worden vergeleken in Tabel S.1 [11].

De eerste lijn in de tabel geeft de typische variaties van de materiaalbrekingsindex Δn'. Bij de eerste twee mechanismes wordt enkel de brekingsindex van de InGaAsP kernlaag gewijzigd. Om de verandering van de effectieve brekingsindex Δn_{eff} te bekomen moet men Δn' vermenigvuldigen met de opsluitingsfactor Γ, die de verhouding geeft van het deel van het optisch vermogen van de golfgeleidermode in de kern van de golfgeleider tot het totale vermogen van de mode. Jammer genoeg zullen in parallel met de toename/afname van de brekingsindex de absorptieverliezen per eenheidslengte α toenemen. De koppeling tussen beide wordt vaak beschreven aan de hand van de alfafactor:

Tabel S.1 Vergelijking van de fysische mechanismes die kunnen gebruikt worden om de brekingsindex te wijzigen [11].

Parameter	*Ladingsdragers*	*Elektrisch veld*	*Temperatuur*
$\Delta n'$	-0.05	-0.01	0.01
Γ	0.5	0.2	1
Δn_{eff}	-0.025	-0.002	0.01
α_H	-20	-10	groot
3-dB bandbreedte	100 MHz	> 10 GHz	< 1 MHz
vermogenconsumptie	groot	verwaarloosbaar	zeer groot

$$\alpha_H = 2\frac{2\pi\nu}{c}\frac{\Delta n'}{\Delta\alpha} \tag{S.2}$$

Uiteraard is een zo hoog mogelijke waarde voor $|\alpha_H|$ gewenst. Verder worden in de tabel nog de typische 3 dB-bandbreedte en de vermogenconsumptie van de afstemmingsmechanismes vergeleken.

Indexverandering door injectie van ladingsdragers

Door stroominjectie kunnen hoge ladingsdragerconcentraties opgebouwd worden in de InGaAsP kern, aangezien het omringende InP materiaal een hogere bandafstand heeft en de ladingsdragers dus opgesloten worden in een potentiaalput. De hoge concentratie aan elektronen en gaten wijzigt de absorptiecoëfficiënt $\alpha(\nu)$ (materiaalabsorptie per eenheidslengte) van het InGaAsP materiaal [12]-[13]. Aangezien de absorptiecoëfficiënt evenredig is met het imaginair deel van de brekingsindex n" en veranderingen in imaginair en reëel deel van de brekingsindex gekoppeld zijn door de Kramers-Kronig vergelijkingen zullen deze effecten ook het reëel deel van de brekingsindex beïnvloeden, zelfs bij fotonenergieën lager dan de bandafstand. Voor typische ladingsdragerconcentraties ($\sim 10^{18}$ cm^{-3}) en voor fotonenergieën die minstens 0.1 eV beneden de bandafstand liggen vermindert (het reëel deel van) de brekingsindex lineair met de ladingsdragerconcentratie N.

Indexverandering door een statisch elektrisch veld

In bulk III/V halfgeleiders zijn de elektro-optische effecten te zwak voor toepassingen in afstembare lasers: de maximale indexveranderingen zijn slechts van de orde 10^{-4} [14]-[15]. In quantumput structuren kunnen grotere brekingsindex-variaties geïnduceerd worden door een elektrisch veld, orde 10^{-3} tot 10^{-2} [16]-[17]. De opsluitingsfactor Γ is in dit geval echter veel kleiner, zelfs indien meerdere quantumputten naast elkaar geplaatst worden. Een voordeel is dan weer de grotere snelheid: aangezien geen ladingsdragerconcentraties moeten opgebouwd worden gebeurt de afstemming nagenoeg ogenblikkelijk.

Indexverandering door temperatuurvariatie

De temperatuurscoëfficiënt van de brekingsindex van InGaAsP/InP is ongeveer $2\cdot10^{-4}$ K^{-1}. Het voordeel van thermisch afstemmen is dat de temperatuur nagenoeg geen invloed heeft op de absorptieverliezen. Een groot nadeel is echter de trage respons, met tijdsconstanten die kunnen variëren van enkele μs tot meerdere ms.

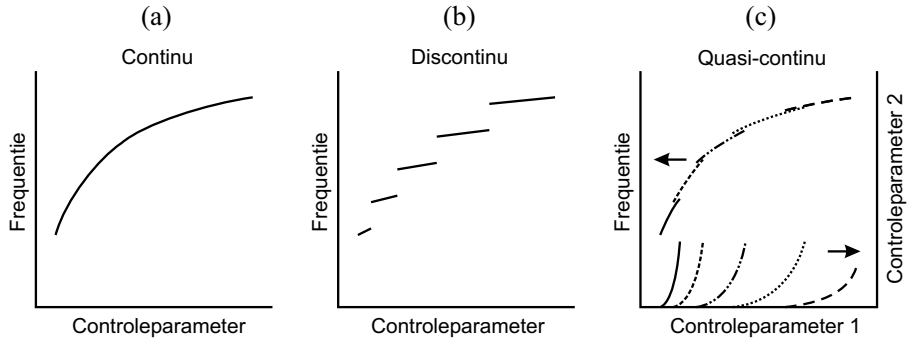

Figuur S.1 Emissiefrequentie als functie van de controleparameter(s) voor continue (a), discontinue (b) en quasi-continue afstemming (c).

Warmte wordt ook gegenereerd wanneer de laser afgestemd wordt door stroominjectie, ten gevolge van de serieweerstand van de diode en niet-stralende recombinatieprocessen. Hierbij dient opgemerkt te worden dat de geïnjecteerde ladingsdragers de index verlagen, terwijl thermische processen de index verhogen. Dit zal uiteindelijk het afstembereik beperken. Bij lage stroomdichtheid is de indexverandering door de ladingsdragers dominant en daalt de brekingsindex. Aangezien de ladingsdragerdichtheid sub-lineair toeneemt met de stroom, terwijl de temperatuur super-lineair stijgt met de stroom, zal op een gegeven ogenblik de thermische afstemming groter worden en zal de brekingsindex terug stijgen.

Uiteindelijk wordt meestal de afstemming door stroominjectie verkozen, omdat deze het beste compromis geeft tussen afstembereik, snelheid en vermogenconsumptie.

S.2.2 Specificaties voor afstembare lasers

Afstembereik – afstemmingsnauwkeurigheid

Het afstembereik is natuurlijk het eerste criterium waarop een afstembare laser beoordeeld wordt. Bij het vergelijken van afstembereiken van verschillende lasers moet men er echter op letten dat de vergelijking op de zelfde basis gebeurt. Normaal worden drie soorten afstemming onderscheiden: continu, discontinu en quasi-continu. Het onderscheid is geïllustreerd in Figuur S.1. Continue afstemming is uiteraard het moeilijkst, en geeft dus het kleinste afstembereik. De grootste afstembereiken werden bekomen met discontinue afstemming, tot meer dan 10 THz [18]-[19]. Voor WDM toepassingen is echter meestal quasi-continue afstemming vereist. Typisch eist men volledige dekking van de C- of L-band (i.e. een bereik van 4 THz). Het aantal kanalen dat men kan gebruiken in deze frequentiebanden is hoofdzakelijk beperkt door de nauwkeurigheid waarmee men de laser kan afstemmen. In ITU aanbeveling G.692 [2] eist men een minimale nauwkeurigheid van ±10% van de kanaalafstand. Wenst men de kanaalafstand te reduceren met een factor N, dan moet de nauwkeurigheid met dezelfde factor verbeterd worden.

Zoals verder zal blijken, is de controle van de meeste afstembare lasers met quasi-continue afstemming nogal complex. Meestal wordt een dergelijke laser dan ook geleverd samen met de nodige controle-elektronica die de externe eisen (frequentie, uitgangsvermogen) vertaalt naar de correcte waarden van de stuurstromen. Dit gebeurt aan de hand van een opzoektabel die opgeslagen wordt in een semi-permanent geheugen. Een van de problemen die in dit proefschrift aangepakt wordt is de bepaling van een dergelijke tabel. Om de produktiekosten laag te houden is het uiteraard belangrijk dat dit volledig geautomatiseerd, snel en nauwkeurig gebeurt.

Om de frequentie op lange termijn stabiel te houden kan men een terugkoppelingssysteem voorzien dat eventuele afwijkingen in de frequentie of het uitgangsvermogen corrigeert. Het ontwikkelen van een dergelijk systeem was een tweede hoofddoel van ons onderzoekswerk.

Zijmode-onderdrukking

Voor communicatietoepassingen is het ook belangrijk dat de laser slechts licht emitteert in één enkele spectrale lijn. De spectrale zuiverheid wordt meestal gekwantificeerd aan de hand van de zijmode-onderdrukking (side-mode suppression ratio, SMSR), i.e. de verhouding van het vermogen in de dominante mode tot het vermogen in de sterkste zijmode. De SMSR wordt meestal uitgedrukt in dB. Typisch wordt vereist dat de laser kan afgestemd worden op elke frequentie binnen het afstembereik met een SMSR van minstens 30 dB, liefst zelfs 40 dB.

Uitgangsvermogen

Voor communicatietoepassingen is meestal een vermogen van enkele mW vereist. Zoals eerder vermeld, nemen de absorptieverliezen in de passieve secties toe bij afstemming. Het gevolg is dat bij constante versterkerstroom het vermogen zal variëren over het afstembereik. Vaak is het belangrijk dat deze variaties zo klein mogelijk gehouden worden.

Lijnbreedte

De lijnbreedte is een belangrijke parameter in coherente communicatiesystemen met heterodyne detectie. Een typische eis is dat de lijnbreedte niet meer bedraagt dan enkele GHz. Bij het gebruik van stroomsturing voor afstemming treedt vaak een zeer grote lijnverbreding op ten gevolge van hagelruis [20]. Willekeurige fluctuaties in de ladingsdragerconcentratie veroorzaken immers brekingsindexvariaties, die op hun beurt resulteren in snelle schommelingen van de emissiefrequentie. Een mogelijke oplossing bestaat erin spanningssturing te gebruiken i.p.v. stroomsturing [21].

S.2.3 Gedistribueerde Bragg-reflector laser

Het gebruik van een gedistribueerde Bragg-reflector (DBR) laser als afstembare laser werd voor het eerst voorgesteld in 1977 [22]. Figuur S.2 toont een longitudinale doorsnede van een 3-sectie DBR laser. De reflectorsectie bevat een diffractierooster, dat licht reflecteert in een smalle frequentieband. Het rooster kan beschreven worden als een (kleine) periodieke modulatie van de effectieve brekingsindex, met periode Λ. Volgens de gekoppelde-mode theorie [23] zal elke ruimtelijke frequentiecomponent f van de indexmodulatie een piek veroorzaken in het reflectiespectrum bij een frequentie bepaald door de Bragg-voorwaarde:

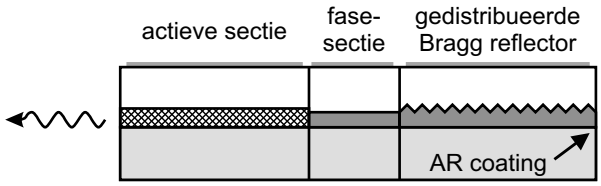

Figuur S.2 Longitudinale doorsnede van een 3-sectie gedistribueerde Bragg-reflector laser.

$$\nu_B = \frac{c}{2n(\nu_B)} f \tag{S.3}$$

Hier is n de gemiddelde effectieve brekingsindex van de golfgeleider in de Bragg-sectie. De uitdrukking (S.3) houdt rekening met een eventuele frequentie-afhankelijkheid van de effectieve index. Meestal wordt de eerste-orde diffractie van het rooster gebruikt, zodat $f = 1/\Lambda$.

Wordt er stroom geïnjecteerd in de Bragg-sectie, dan verandert de (gemiddelde) effectieve brekingsindex n en wordt de frequentie van het verliesminimum (i.e. de Bragg-frequentie ν_B) verschoven, zodat de laser op discontinue wijze afgestemd wordt. Om quasi-continue afstemming mogelijk te maken is een fasesectie nodig (Figuur S.2). Deze sectie heeft dezelfde structuur als de DBR, maar dan zonder het diffractierooster. De fasevoorwaarde luidt in dit geval:

$$\frac{2\pi\nu_k}{c}\left(2n_aL_a + 2n_pL_p\right) + \phi_d(\nu_k) = 2\pi k \tag{S.4}$$

Waarbij n_x en L_x de effectieve index en lengte van de actieve sectie, respectievelijk fasesectie voorstellen. $\phi_d = -\arg(r)$ is de fase van de amplitudereflectie r van de DBR. Wanneer de laser boven de drempel aangestuurd wordt, is de ladingsdragerconcentratie in de actieve sectie vergrendeld. Variaties in de stroom door de actieve sectie hebben bijgevolg geen invloed op de brekingsindex (indien thermische effecten verwaarloosd worden). De index van de fasesectie kan daarentegen wel veranderd worden door stroominjectie. Op die manier kan steeds een caviteitsmode uitgelijnd worden met de Bragg-frequentie ν_B. Door de fasesectie en de Bragg-sectie synchroon af te stemmen kan de laser continu afgestemd worden over een bereik van typisch enkele 100 GHz. In het quasi-continue regime kunnen grotere afstembereiken bekomen worden, tot ongeveer 2 THz [24]-[25]. Het afstembereik wordt in dat geval beperkt door de maximale indexverandering die kan bereikt worden in de DBR sectie (zie §S.2.1):

$$\frac{\Delta\nu_{B,max}}{\nu_B} = -\frac{\Delta n_{d,max}}{n_{d,g}(\nu_B)} \tag{S.5}$$

waar

$$n_{d,g}(\nu) = n_d(\nu) + \nu\frac{\partial n_d}{\partial \nu} \tag{S.6}$$

de groepsindex voorstelt, die de dispersie van de effectieve index rond ν_B in rekening brengt.

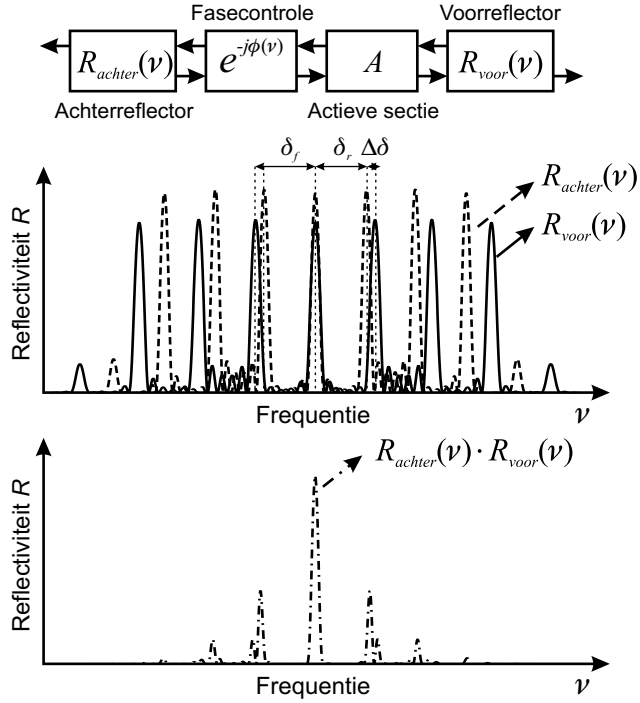

Figuur S.3 Vernier-effect toegepast op een afstembare laser, waarvan beide spiegels een kamvormig reflectiespectrum hebben. Laserwerking kan enkel optreden in de frequentieband waar twee pieken samenvallen.

S.2.4 Verbreden van het afstembereik van DBR lasers

Het maximale afstembereik van een conventionele DBR laser (2 THz) is heel wat kleiner dan de bandbreedte van de winst in de actieve sectie (typisch meer dan 10 THz) en de bandbreedte van de EDFA (4 THz). Bijgevolg is men op zoek gegaan naar laserstructuren die afstemming voorbij de $\Delta\nu/\nu = -\Delta n/n_g$ limiet toelaten. Het basisprincipe van alle breed afstembare lasers is dat een brekingsindex*verschil* gewijzigd wordt. Op die manier wordt de relatieve frequentieverandering gelijk aan een relatieve verandering van dit indexverschil, en kan dus veel groter worden dan bovenstaande limiet.

Gebruik van een Vernier-effect tussen twee kamreflectoren

De Vernier-schaal (of nonius) op een schuifmaat is een gekend middel om een kleine verplaatsing om te zetten in een grotere. Dit gebeurt door twee schalen met een klein verschil in periode langs elkaar te schuiven. Verschuift men een van beide schalen over een afstand gelijk aan het verschil in periode, dan verspringt het punt waar onderverdelingen op de twee schalen samenvallen met één periode.

Hetzelfde principe kan toegepast worden in een afstembare laser, als de laser twee spiegels heeft met een kamvormig reflectiespectrum (Figuur S.3) [26]. De spiegels zijn zo ontworpen dat de piekafstand van de voorreflector (δ_f) en van de

achterreflector (δ_r) een weinig verschillen (δ_f - $\delta_r = \Delta\delta$). Laserwerking kan dan enkel optreden in het frequentiebereik waar twee pieken samenvallen. De fasesectie kan opnieuw gebruikt worden om een caviteitsmode uit te lijnen met het verliesminimum.

Wordt een van de spiegels afgestemd over $\pm\Delta\delta$, dan zullen twee naburige reflectiepieken samenvallen. Indien de fasesectie gelijktijdig afgestemd wordt zodat opnieuw een caviteitsmode uitgelijnd is met de samenvallende pieken, dan zal de frequentie met δ_f ($-\delta_r$) veranderen wanneer de voorreflector (achterreflector) afgestemd wordt over $\Delta\delta$. Het samenvallen van twee bepaalde pieken wordt conventioneel betiteld als een "super-mode" en de frequentiesprongen die optreden wanneer het Vernier-mechanisme toegepast wordt, noemt men bijgevolg super-modesprongen. Praktische implementaties van het Vernier-principe zijn gebaseerd op de DBR laser uit de vorige paragraaf, alleen bevindt er zich nu een Bragg-reflector aan beide zijden van de actieve sectie. De diffractieroosters in de Bragg-secties worden aangepast om meerdere reflectiepieken te bekomen. Dit gebeurt door de roosterfunctie periodiek te moduleren. De ideale reflector heeft een beperkt aantal uniforme pieken, zodat telkens slechts één paar pieken kan samenvallen.

Zoals geweten is uit de signaaltheorie, zal de modulatie van een draaggolf zijbanden veroorzaken in het Fourier-spectrum. Een periodieke modulatie zal aanleiding geven tot een kamvormig spectrum, gecentreerd op de frequentie van de draaggolf en met piekafstand gelijk aan de frequentie van de modulatie. Dit principe kan ook toegepast worden op een Bragg-rooster, aangezien de gekoppelde-mode theorie zegt dat elke ruimtelijke frequentiecomponent van de indexmodulatie een piek zal veroorzaken in het reflectiespectrum bij een frequentie bepaald door de Bragg-voorwaarde (S.3). Een modulatie met periode Λ_s van het originele rooster (de draaggolf met periode Λ) zal dus aanleiding geven tot reflectiepieken bij de frequenties ν_k (waarbij k een geheel getal is):

$$\nu_k = \frac{c}{2n(\nu_k)}\left(\frac{1}{\Lambda} + \frac{k}{\Lambda_s}\right) \tag{S.7}$$

Twee types modulatie worden in de praktijk gebruikt: een periodieke bemonstering (sampled grating, SG [27]) en een periodieke frequentie- of fasemodulatie (super-structure grating, SSG [28]). Het bemonsterd rooster heeft het voordeel dat het even eenvoudig te fabriceren is als een gewoon Bragg-rooster. Het reflectiespectrum is echter niet ideaal, aangezien de sterkte van de reflectiepieken geleidelijk afneemt met toenemende waarden voor $|k|$. In een super-structuur rooster kan de vorm van de fasemodulatie geoptimaliseerd worden, zodanig dat enkel sterke reflectiepieken optreden in een beperkte frequentieband en deze pieken bovendien allemaal even sterk zijn [28]. Het nadeel is dat een dergelijk gecompliceerd rooster enkel door middel van elektronenstraallithografie kan gedefinieerd worden.

Afstemmen van een SG-DBR of SSG-DBR laser gebeurt in drie stappen. Eerst wordt de voor- of achterreflector afgestemd om het geschikte paar reflectiepieken te doen samenvallen. Vervolgens worden beide reflectoren gelijktijdig afgestemd om de samenvallende pieken naar de juiste frequentie te brengen. Tenslotte wordt de fasesectie afgestemd zodanig dat een caviteitsmode uitgelijnd wordt met de samenvallende reflectiepieken.

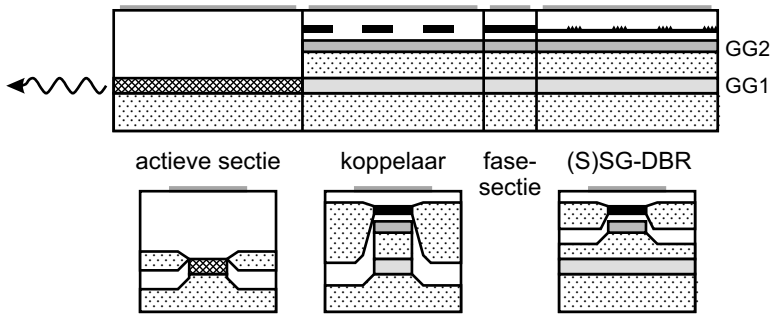

Figuur S.4 Longitudinale en laterale doorsneden van een GCSR laser.

Combinatie van een co-directionele roosterkoppelaar met een kamreflector

Om een breed afstembare laser te ontwikkelen kan men ook op zoek gaan naar filters met een groter afstembereik dan een DBR. Een voorbeeld van een dergelijk filter is de co-directionele roosterkoppelaar [30]. Dit filter bestaat uit twee parallelle, asymmetrische golfgeleiders (Figuur S.4). Deze structuur geleidt twee modes, *R* en *S*, waarbij mode *R* voornamelijk beperkt is tot de ene golfgeleider, en mode *S* tot de andere golfgeleider. Normaal gezien is de koppeling tussen beide modes relatief zwak, en wordt er bijgevolg weinig vermogen overgedragen van de ene golfgeleider naar de andere. Met behulp van een roosterstructuur (met periode Λ) kan echter een efficiënte vermogenstransfer bekomen worden in een beperkte frequentieband. De koppelingsfrequentie ν_c is:

$$\nu_c = \frac{c}{\Lambda\left[n_R(\nu_c) - n_S(\nu_c)\right]} \tag{S.8}$$

waarbij n_R en n_S de effectieve indices van de modes *R* en *S* voorstellen. Zorgt men ervoor dat licht dat niet overgekoppeld wordt, verloren gaat door diffractie of absorptie, dan kan men een dergelijke koppelaar gebruiken als filter in een lasercaviteit. Aangezien de koppelingsfrequentie afhangt van een *verschil* in brekingsindex zal een kleine verandering in n_R of n_S aanleiding geven tot een grote frequentieverandering:

$$\frac{\Delta\nu_{c,max}}{\nu_c} = -\frac{\Delta\left(n_R - n_S\right)_{max}}{n_{R,g} - n_{S,g}} \tag{S.9}$$

Het grotere afstembereik wordt echter bekomen ten koste van een lagere selectiviteit. Daarom is het niet mogelijk om met enkel een roosterkoppelaar een laser te maken die breed afstembaar is en toch een voldoende grote zijmode-onderdrukking heeft. Combineert men de koppelaar met een SG of SSG reflector, dan kan men gebruik maken van het brede afstembereik van de koppelaar zonder dit te moeten afwegen tegen selectiviteit [30]-[31]. In dat geval kan men immers de koppelaar gebruiken om een bepaalde reflectiepiek te selecteren, waarbij deze piek vervolgens zorgt voor voldoende selectiviteit. De resulterende laserstructuur is geschetst in Figuur S.4. (GCSR: grating-assisted coupler with rear sampled reflector).

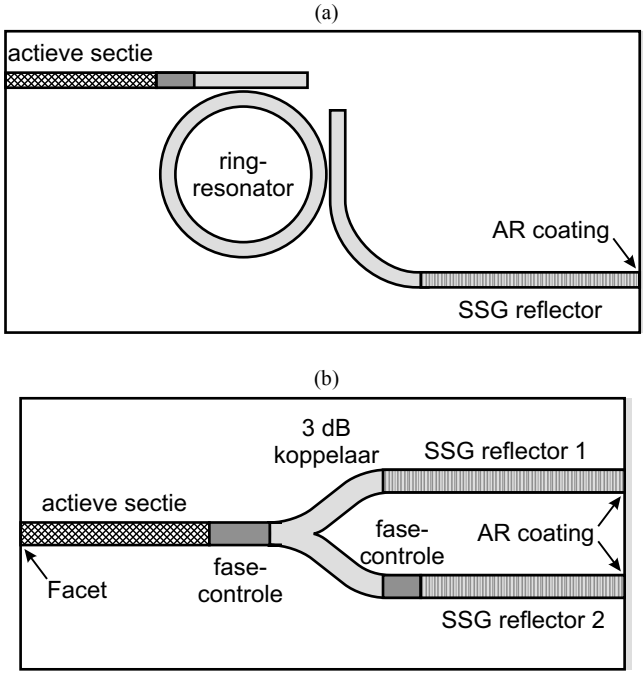

Figuur S.5 Alternatieve ontwerpen voor breed afstembare lasers, die gebruik maken van het Vernier-effect, maar alle filters aan één kant van de actieve sectie hebben.

Het grootste voordeel van de GCSR laser t.o.v. de SG- en SSG-DBR lasers is de kleinere variatie van het uitgangsvermogen over het afstembereik. In de laatste moet het gegenereerde licht namelijk doorheen de voorreflector, waarin de absorptieverliezen toenemen naarmate de reflector meer afgestemd wordt. Aan de andere kant zorgen de beide kamreflectoren in de SG- en SSG-DBR lasers voor een betere selectiviteit, temeer daar de effectieve caviteitslengte van deze lasers typisch korter is dan die van de GCSR laser en de caviteitsmodes dus verder van elkaar liggen. Verder is de GCSR laser ook moeilijker te fabriceren.

Alternatieve ontwerpen voor breed afstembare lasers

In een octrooiaanvraag die we recent indienden samen met J. Buus beschrijven we een aantal alternatieven die de sterke punten van de (S)SG-DBR en GCSR lasers proberen te combineren [88]. Twee alternatieven zijn voorgesteld in Figuur S.5. Het eerste ontwerp combineert een ring resonator, die een kamvormig transmissiespectrum heeft, met een SSG reflector. Het tweede gebruikt een 3 dB-koppelaar om de reflectie van twee SSG reflectoren te combineren. Er dient opgemerkt te worden dat de reflecties van beide SSG structuren hier opgeteld worden en niet vermenigvuldigd zoals in de gewone SSG-DBR laser. Daarom moet er ook een tweede fasesectie voorzien worden in een van beide armen, zodat men ervoor kan zorgen dat beide reflecties in fase zijn.

Tabel S.2 Vergelijking van de prestaties van diverse afstembare lasers. Quasi-continu afstembereik, zijmode-onderdrukking (SMSR), maximaal uitgangsvermogen (ex-facet), en vermogenuniformiteit worden vergeleken voor 3S-DBR, SG-DBR, SSG-DBR, en GCSR lasers. De gekleurde kolommen tonen waarden voor commercieel beschikbare lasers.

	3S-DBR		*SG-DBR*			*SSG-DBR*			*GCSR*		
	[25], [33]	[34]	[35]	[36]	[37]	[38]	[39]	[40]	[41]	[42]	[43]
QC afstembereik (THz)	2.1	1.6	5.5	7.4	>5.0	5.0	7.8	4.2	8.3	5.0	>5.0
SMSR (dB)	>35	>35	>30	>30	>35	>30	>25	>35	>25	>30	>30
Max. vermogen (dBm)	20	15	10	5	14	3	10	10	6	10	6
Uniformiteit (dB)	1.7	2	5	5	5	9	10	8	13	5	2

S.2.5 Vergelijking van de verschillende afstembare lasers

Tabel S.2 vergelijkt de prestaties van de diverse lasertypes die hierboven besproken werden. SG-DBR, SSG-DBR en GCSR lasers hebben typisch een quasi-continu afstembereik van meer dan 4 THz. De GCSR laser heeft zoals reeds vermeld een betere vermogenuniformiteit over het afstembereik, maar daarentegen gemiddeld gezien een iets lagere zijmode-onderdrukking.

S.3 Modelleren van geïntegreerde afstembare lasers met passieve filtersecties

Het ontwikkelen van controle- en karakteriseringsmethodes voor afstembare lasers vergt uiteraard een diepgaand inzicht in het gedrag van dergelijk lasers. Als hulpmiddel om een dergelijk inzicht te verwerven is een simulatiemodel onontbeerlijk. In de volgende paragrafen geven we een korte beschrijving van het model dat we ontwikkelden.

S.3.1 Caviteitsmodel

Aangezien we vooral geïnteresseerd zijn in het afstemgedrag van de laser, werd het model beperkt tot de statische werking. De afstembare laser kan beschreven worden als een Fabry-Perot caviteit met frequentie-afhankelijke spiegelreflecties $r_L(\omega)$ en $r_R(\omega)$, waarbij $\omega = 2\pi\nu$ de hoekfrequentie voorstelt (Figuur S.6) [44]. De actieve sectie bestaat uit een golfgeleider met kerndimensies L (lengte), w (breedte), en d (dikte), die een enkele transversale mode met een opsluitingsfactor Γ geleidt. Het kernmateriaal heeft een brekingsindex n' en een winst g, die afhangen van de ladingsdragerdichtheid N en de frequentie ω.

Drempelvoorwaarde

Zoals vermeld in §S.2.1 valt de drempelvoorwaarde uiteen in een voorwaarde voor de winst:

$$\Gamma g(\omega, N) = \alpha_{int} - \frac{1}{L}\ln\left|r_L(\omega)r_R(\omega)\right| = \alpha_{int} + \alpha_m(\omega) = \alpha_{tot}(\omega) \qquad \text{(S.10)}$$

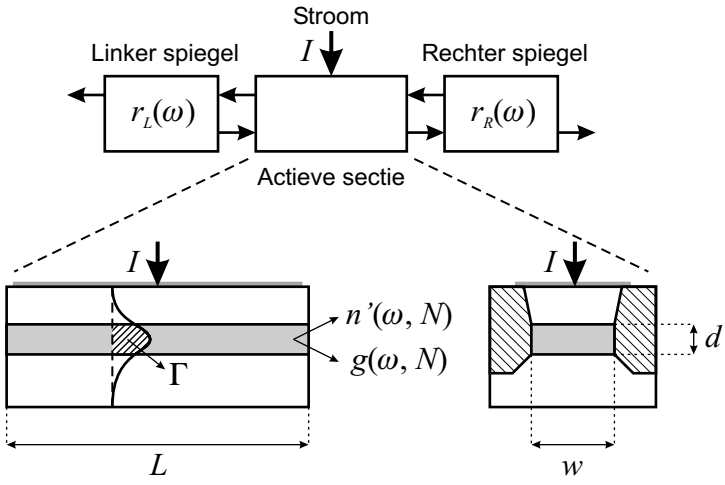

Figuur S.6 Fabry-Perot caviteitsmodel voor longitudinaal geïntegreerde afstembare lasers met passieve filtersecties. De afstembare filters worden voorgesteld door de spiegels met frequentie-afhankelijke reflecties $r_L(\omega)$ en $r_R(\omega)$. De actieve sectie bestaat uit een golfgeleider met kerndimensies L, w, en d. Het kernmateriaal heeft een brekingsindex n' en een winst g, die veranderen als functie van de stroom I.

en een voorwaarde voor de fase:

$$2L\frac{\omega}{c}n(\omega, N) - \arg\left[r_L(\omega)r_R(\omega)\right] = 2\pi i\,, \qquad i \text{ geheel} \tag{S.11}$$

Uit de eerste vergelijking kan men de ladingsdragerdichtheid N afleiden als functie van de frequentie ω. Door $N(\omega)$ te substitueren in de fasevoorwaarde (S.11) bekomt men een vergelijking voor de frequentie op zich.

$$h(\omega) = 2L\frac{\omega}{c}n(\omega, N(\omega)) - \arg\left[r_L(\omega)r_R(\omega)\right] = 2\pi m \tag{S.12}$$

Oplossen van deze vergelijking levert een set van mogelijk lasermodes ω_m. De eigenlijke laserfrequentie ω_{out} wordt dan gevonden als de frequentie ω_m die een minimale ladingsdragerconcentratie $N(\omega_m)$ vereist. Dit bepaalt de drempelconcentratie N_{th}.

$$N_{th} = \min\left\{N(\omega_m) \;\middle|\; h(\omega_m) = 2\pi m\right\} \tag{S.13}$$

Om de andere caviteitsmodes ω_i te vinden moet (S.11) opgelost worden met $N = N_{th}$.

Balansvergelijkingen

Om voor elke mode i het aantal per tijdseenheid gegenereerde fotonen te berekenen, lossen we de klassieke balansvergelijkingen voor de laser op [45]-[46]. De ladingsdragervergelijking luidt:

$$0 = \frac{dN}{dt} = \frac{I}{qV_a} - \left(AN + BN^2 + CN^3\right) - \frac{v_g}{V_a}\sum_i \Gamma g(\omega_i, N)S_i \tag{S.14}$$

Deze drukt uit dat het aantal ladingsdragers toeneemt door stroominjectie ($V_a = Lwd$ is het volume van de kernlaag) en afneemt door niet-stralende recombinatie (AN),

spontane emissie (BN^2), Auger-recombinatie (CN^3) en gestimuleerde emissie. De vergelijking voor het aantal fotonen S_i in mode i luidt:

$$0 = \frac{dS_i}{dt} = \left(v_g \Gamma g(\omega_i, N) - \frac{1}{\tau(\omega_i)} \right) S_i + \beta_{sp} B N^2 V_a \tag{S.15}$$

Hier stelt $\tau(\omega)$ de fotonlevensduur voor, gedefinieerd als:

$$\frac{1}{\tau(\omega)} = v_g \left[\alpha_{int} - \frac{1}{L} \ln \left| r_L(\omega) r_R(\omega) \right| \right] = v_g \alpha_{tot}(\omega) \tag{S.16}$$

De laatste term in (S.15) beschrijft de koppeling van een kleine fractie β_{sp} van de spontane emissie naar mode i. Voor de lasermode heeft dit tot gevolg dat de netto winst Γg - α_{tot} niet exact gelijk is aan nul boven de drempel. Het verschil is echter miniem, zodat men toch N gelijk aan N_{th} kan veronderstellen in de berekening van de modefrequenties ω_i. Nadat de balansvergelijkingen opgelost zijn naar N en S_i, kan op basis van deze waarden eenvoudig extern meetbare grootheden bepalen, zoals het uitgangsvermogen (links en/of rechts), de zijmode-onderdrukking, en de spanning over de actieve sectie.

S.3.2 Transfermatrixbeschrijving van de passieve secties

Het caviteitsmodel dat zonet beschreven werd veronderstelt de kennis van de complexe veldreflectiecoëfficiënt van beide spiegels. De spiegels kunnen diverse vormen aannemen: een eenvoudig facet, een Bragg-reflector, maar ook meer ingewikkelde structuren zoals de aaneenschakeling van een fasesectie en een reflector met bemonsterd rooster, ... Gemeenschappelijk aan al deze structuren is het feit dat het elektrisch veld kan beschreven worden als de superpositie van een rechts-propagerende golf $E^R(z)$ en een links-propagerende golf $E^S(z)$:

$$E(z) = E^R(z) + E^S(z) \tag{S.17}$$

De transfermatrix (of ABCD-matrix) is een vaak gebruikt hulpmiddel om de koppeling te beschrijven tussen de links- en rechts-propagerende golven aan één kant van een structuur en de links- en rechts-propagerende golven aan de andere kant [47]-[49]. Gebruiken we de conventie:

$$E_m^X = E^X(z_m), \quad \text{met} \quad X = R \text{ of } X = S \tag{S.18}$$

dan worden de velden bij $z = z_m$ gerelateerd aan de velden bij $z = z_{m-1}$ door de transfermatrix $\mathbf{F}_m$:

$$\begin{bmatrix} E_m^R \\ E_m^S \end{bmatrix} = \mathbf{F}_m \begin{bmatrix} E_{m-1}^R \\ E_{m-1}^S \end{bmatrix} = \begin{bmatrix} F_{11}^m & F_{12}^m \\ F_{21}^m & F_{22}^m \end{bmatrix} \begin{bmatrix} E_{m-1}^R \\ E_{m-1}^S \end{bmatrix} \tag{S.19}$$

De eerste voor de hand liggende eigenschap van de transfermatrices is dat de transfermatrix van een aaneenschakeling van secties eenvoudigweg gegeven wordt door het produkt van de matrices van de individuele secties:

$$\begin{bmatrix} E_N^R \\ E_N^S \end{bmatrix} = \mathbf{F}_N \cdot \mathbf{F}_{N-1} \cdot \ldots \cdot \mathbf{F}_2 \cdot \mathbf{F}_1 \begin{bmatrix} E_0^R \\ E_0^S \end{bmatrix} = \mathbf{F}_{tot} \begin{bmatrix} E_0^R \\ E_0^S \end{bmatrix} \tag{S.20}$$

De complexe veldreflectie r en transmissie t worden eenvoudig berekend door de links-propagerende golf aan de rechterkant gelijk aan nul te stellen:

$$E_N^S = 0 \qquad \Rightarrow \qquad \begin{cases} r = \dfrac{E_0^S}{E_0^R} = -\dfrac{F_{21}^{tot}}{F_{22}^{tot}} \\ t = \dfrac{E_N^R}{E_0^R} = F_{11}^{tot} - \dfrac{F_{12}^{tot} F_{21}^{tot}}{F_{22}^{tot}} \end{cases} \tag{S.21}$$

Als de aaneengeschakelde structuur periodiek is, i.e. de N secties zijn identiek, dan wordt de totale transfermatrix $\mathbf{F}_{tot}$ gelijk aan de N-de macht van de transfermatrix $\mathbf{F}$ van een sectie.

$$\mathbf{F}_{tot} = (\mathbf{F})^N \tag{S.22}$$

In dit geval kan de totale transfermatrix efficiënt berekend worden door de eigenwaardevergelijking voor $\mathbf{F}$ op te lossen:

$$\det\begin{bmatrix} F_{11} - \lambda & F_{12} \\ F_{21} & F_{22} - \lambda \end{bmatrix} = 0 \tag{S.23}$$

De oplossingen zijn uiteraard:

$$\lambda_{\pm} = \frac{1}{2}\left[F_{11} + F_{22} \pm \left((F_{11} + F_{22})^2 - 4(F_{12}F_{21} - F_{11}F_{22}) \right)^{1/2} \right] \tag{S.24}$$

In het algemeen is de N-de macht van $\mathbf{F}$ dan gegeven door:

$$\mathbf{F}_{tot} = (\mathbf{F})^N = \frac{\lambda_+^N - \lambda_-^N}{\lambda_+ - \lambda_-}\mathbf{F} - \frac{\lambda_-\lambda_+^N - \lambda_+\lambda_-^N}{\lambda_+ - \lambda_-}\mathbf{1} \tag{S.25}$$

waar $\mathbf{1}$ de eenheidsmatrix is.

De transfermatrices voor een discrete reflectie, een gewone golfgeleider en een DBR worden eenvoudig afgeleid. Door deze te combineren en gebruik te maken van (S.25) kan men ook de matrices voor SG- en SSG-DBR structuren bepalen. De effectieve brekingsindex n van deze structuren is opnieuw een functie van de frequentie ω en de ladingsdragerconcentratie N. Deze laatste wordt voor de passieve secties enkel bepaald door de geïnjecteerde stroom I volgens:

$$\frac{I}{qLwd} = AN + BN^2 + CN^3 \tag{S.26}$$

S.3.3 Berekening van afstemkarakteristieken

Om de afstemkarakteristiek van een laser te berekenen worden volgende stappen herhaald:

- De controlestromen van de verschillende passieve secties worden ingesteld op de gewenste waarden. Dit bepaalt de ladingsdragerconcentratie in elke sectie via (S.26), en dus ook de effectieve index. Deze bepaalt op zijn beurt de transfermatrix van de sectie.
- Alle oplossingen ω_m van (S.12) worden berekend in een vooraf bepaald bereik $[\omega_{min}\ \omega_{max}]$, dat uiteraard groter moet zijn dan het verwachte afstembereik van

de laser. De spiegelreflecties in (S.12) worden berekend aan de hand van de transfermatrices van de passieve secties.

- De drempelwaarde van de ladingsdragerconcentratie N_{th} en de laserfrequentie ω_{out} volgen dan uit (S.13).
- De fasevoorwaarde (S.11) wordt opgelost met $N = N_{th}$ om alle caviteitsmodes te lokaliseren in het bereik $[\omega_{min}\ \omega_{max}]$.
- Vervolgens worden de balansvergelijkingen (S.14) en (S.15) opgelost. Enkel de modes ω_i met de laagste waardes voor $N(\omega_i)$ (uit (S.10)) worden in rekening gebracht.
- Met N en S_i worden het uitgangsvermogen, de zijmode-onderdrukking, de spanning, enz. berekend.

S.3.4 Alternatieve ontwerpen voor kamreflectoren

In S.2.4 werd reeds vermeld dat de ideale kamreflector een beperkt aantal, even sterke reflectiepieken vertoont. Een dergelijk reflectiespectrum kan bekomen worden met een super-structuur rooster door optimalisatie van de fasemodulatie. Het grote nadeel van een dergelijk structuur is echter dat elektronenstraallithografie met een hoge resolutie vereist is om het rooster te fabriceren. In samenwerking met onderzoekers bij Marconi – Caswell Technology in het Verenigd Koninkrijk werden twee alternatieven bestudeerd.

Meervoudige holografische belichting

Het rooster voor een gewone Bragg-reflector wordt meestal gedefinieerd door een fotoresistlaag te belichten met het interferentiepatroon van twee ultraviolette laserbundels, die onder een tegengestelde hoek invallen op het substraat. De roosterperiode wordt bepaald door de golflengte van het licht en de invalshoek. Een – op het eerste zicht voor de hand liggende – manier om een kamreflector te genereren, zou erin bestaan de resistlaag meerdere keren te belichten onder verschillende invalshoeken. De praktijk is echter niet zo eenvoudig, aangezien zowel de belichting van het fotoresist als het daaropvolgende etsproces sterk niet-lineaire processen zijn. De globale transferfunctie van de belichting naar de uiteindelijke roosterstructuur is vrijwel gelijk aan een stapfunctie. Dit maakt dat het reflectiespectrum van een rooster dat op deze wijze gefabriceerd wordt moeilijk te voorspellen is.

Onze berekeningen wezen uit dat in het algemene geval het reflectiespectrum er vrij grillig uitziet, met sterk variërende piekwaarden. In specifieke gevallen kan echter een vrij uniforme kam van reflectiepieken bekomen worden. Dit vereist in de eerste plaats dat het gemiddelde belichtingsniveau van de gesuperponeerde interferentiepatronen gelijk is aan het drempelniveau van de eerder vermelde stapfunctie. In de tweede plaats moeten de fases (op een bepaald referentiepunt) van de verschillende (sinusoidale) interferentiepatronen anti-symmetrisch gekozen worden. Het resulterende rooster blijkt dan een grotendeels uniform rooster te zijn.

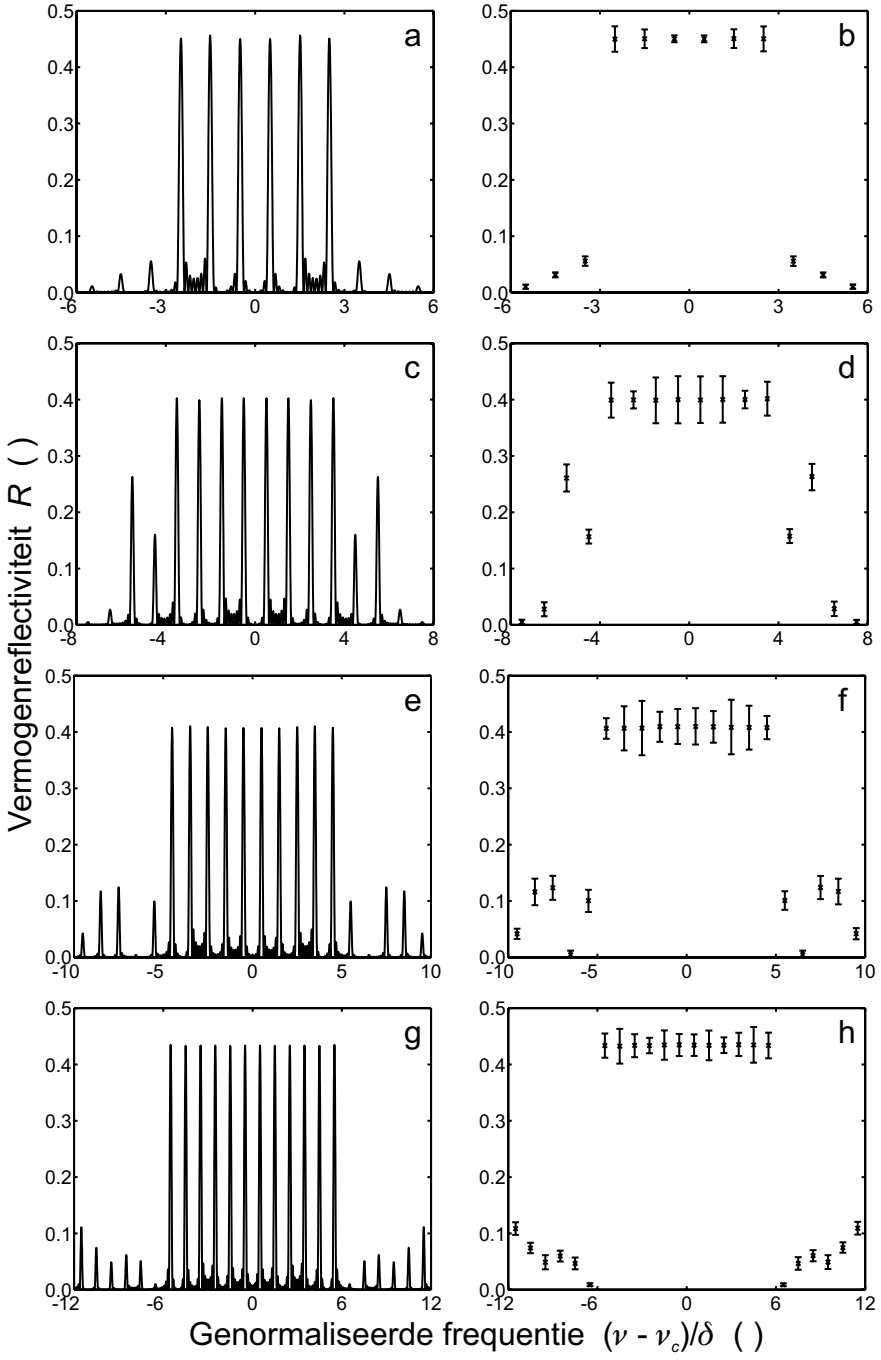

Figuur S.7 Geoptimaliseerde reflectiespectra voor 6 (a), 8 (c), 10 (e) en 12 (g) gesuperponeerde belichtingen. Foutvlaggen (intervallen met 95% waarschijnlijkheid) voor Gaussiaans verdeelde fouten op de fases $\phi_{\pm i}$ met een standaardafwijking $\sigma = 4\pi \cdot 10^{-3}$ (b, d, f, h).

Op bepaalde plaatsen treden echter fasesprongen van 180° op, en deze herhalen zich periodiek (i.e. het rooster heeft een super-periode). Door de anti-symmetrische fases verder numeriek te optimaliseren kan uiteindelijk een kamreflector met uniforme reflectiepieken in een beperkte band bekomen worden.

Figuur S.7 toont het resultaat van een dergelijke optimalisatie, voor 6 (a), 8 (c), 10 (e) en 12 (g) gesuperponeerde belichtingen. De reflectiepieken in de gewenste frequentieband zijn duidelijk alle even sterk, al zijn de reflectiepieken buiten deze band niet volledig onderdrukt. Het resultaat is echter zeer gevoelig aan afwijkingen op de fases van de gesuperponeerde interferentiepatronen, zoals blijkt uit de grafieken in de rechter kolom van Figuur S.7. Deze tonen de foutvlaggen op de piekreflecties uit de linker kolom, wanneer normaal verdeelde fouten met een standaardafwijking $\sigma = 4\pi \cdot 10^{-3}$ bij de geoptimaliseerde fases worden opgeteld. Om deze fases met een dergelijke nauwkeurigheid te definiëren, zou men de positie van het substraat tussen twee belichtingen met nanometer-resolutie moeten kunnen aanpassen. Het is bijgevolg uiterst twijfelachtig of dit in de praktijk haalbaar zal zijn.

Super-structuur rooster met 180° fasesprongen

De hierboven beschreven procedure lijkt een zeer omslachtige manier om uiteindelijk een vrij eenvoudig rooster te bekomen: een super-structuur rooster met fasemodulatie, waarbij enkel fasesprongen van 180° optreden. In een octrooi-aanvraag die we recent indienden, wordt een methode beschreven om een dergelijk rooster met één holografische belichting te definiëren [87]. Dit gebeurt door gebruik te maken van een fasemasker dat een fasedraaiing van 180° introduceert in een van beide interfererende bundels op vooraf gedefinieerde plaatsen.

De plaatsing van de 180° fasesprongen binnen de super-periode kan in principe afgeleid worden uit de hierboven beschreven optimalisatie. De kans is echter groot dat nog betere resultaten kunnen bekomen worden door de plaatsing rechtstreeks te optimaliseren. Dit werd gedaan als volgt. De super-periode werd verdeeld in Q delen met fractionele lengtes x_l, die uiteraard moeten voldoen aan:

$$\sum_{l=1}^{Q} x_l = 1 \tag{S.27}$$

Om symmetrieredenen moet Q oneven zijn voor een even aantal reflectiepieken K en vice-versa. Inderdaad, voor even K moeten reflecties van opeenvolgende super-periodes destructief interfereren bij de Bragg frequentie. Met oneven Q hebben opeenvolgende super-periodes een faseverschil van 180°. Initieel kiezen we daarom $Q = K + 1$. Na een eerste optimalisatie van de lengtes x_l, convergeren er verschillende x_l naar een zeer kleine waarde. In een tweede stap worden dan alle secties met een lengte korter dan de roosterperiode Λ weggenomen, en wordt de lengte van de overige secties opnieuw geoptimaliseerd. De resultaten voor $K = 6$, 8, 10, en 12 worden weergegeven in Figuur S.8. De foutvlaggen werden in dit geval bepaald door normaal verdeelde fouten met een standaardafwijking $\sigma = 2.5 \cdot 10^{-3}$ bij de geoptimaliseerde fractionele lengtes te tellen. Dit stemt typisch overeen met een halve roosterperiode. Een dergelijk rooster kan daarom ook gefabriceerd worden met elektronenstraallithografie met een resolutie gelijk aan de halve roosterperiode ($\Lambda/2$), wat veel sneller en goedkoper zou moeten zijn dan de lithografie met hoge resolutie ($\Lambda/20$) die nodig is voor klassieke super-structuur roosters.

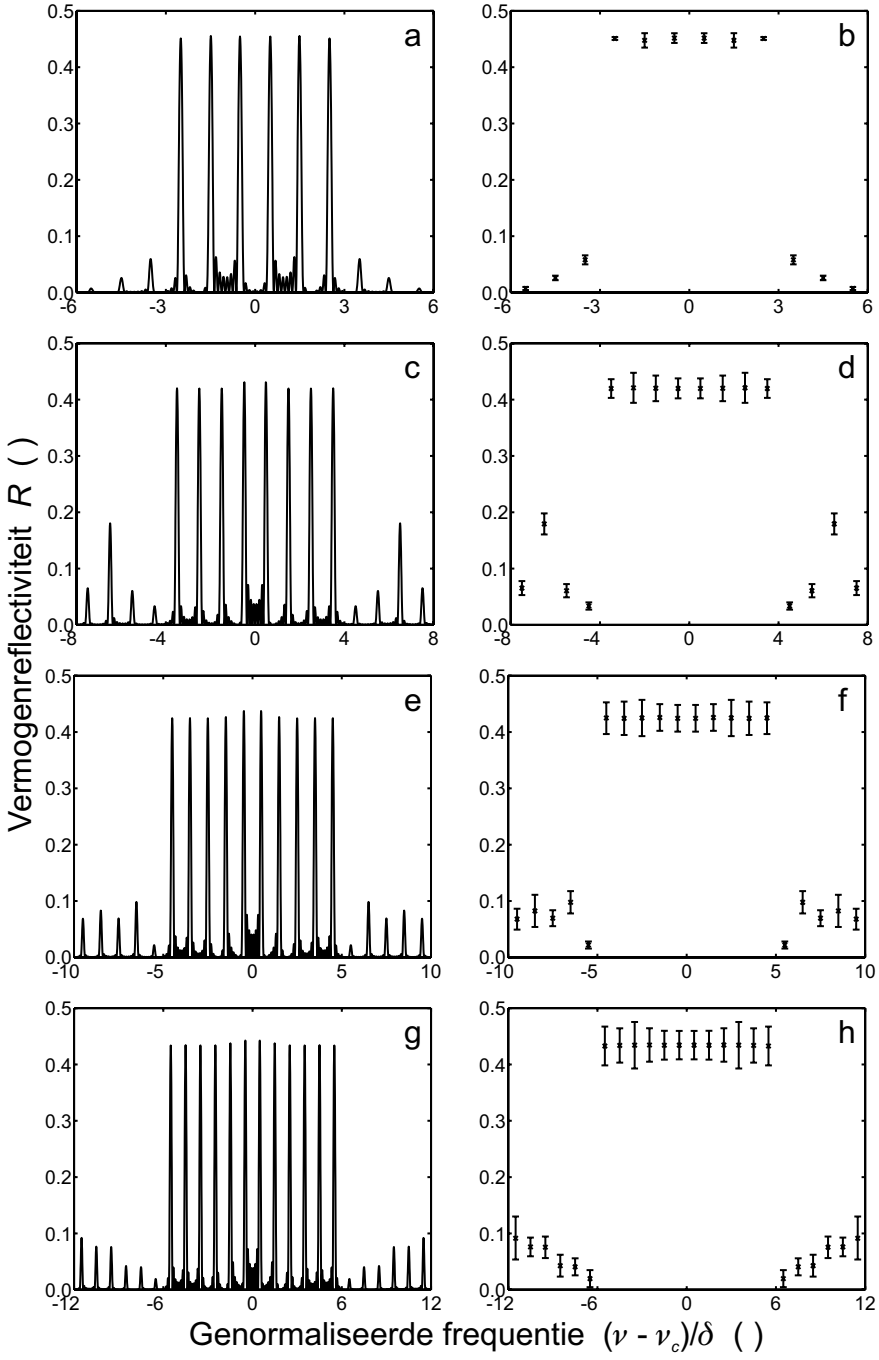

Figuur S.8 Geoptimaliseerde reflectiespectra van MPS-SSG reflectoren met 180° fasesprongen voor 6 (a), 8 (c), 10 (e) en 12 (g) pieken. Foutvlaggen (intervallen met 95% waarschijnlijkheid) voor Gaussiaans verdeelde fouten op de fractionele lengtes x_l met een standaardafwijking $\sigma = 2.5 \cdot 10^{-3}$ (b, d, f, h).

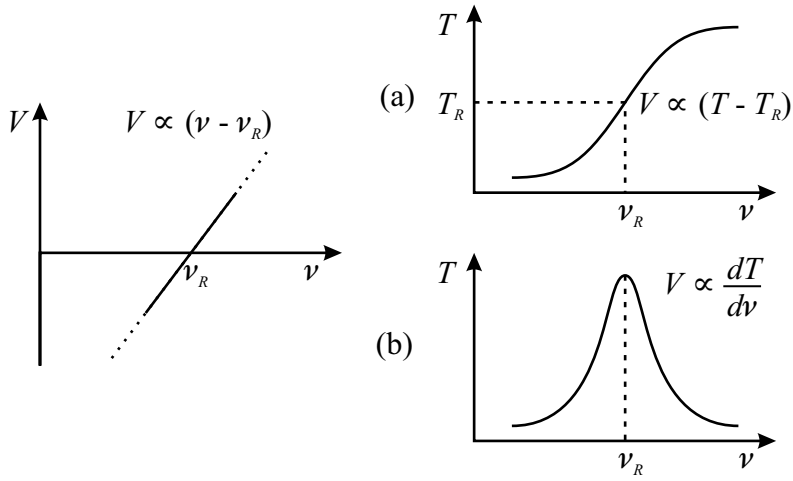

Figuur S.9 Foutsignaal V voor frequentiestabilisatie, gegenereerd door gebruik te maken van de flank van een optisch filter (wat een vermogenreferentie vereist) (a), of van de piek van een filter (wat een kleine frequentiemodulatie vereist) (b).

S.4 Feedback-controle voor frequentie- en mode-stabilisatie

Tijdens het gebruik zullen de karakteristieken van elke elektronische component degraderen. In het geval van een afstembare laser zal dit ervoor zorgen dat de emissiefrequentie – weliswaar zeer langzaam – van de oorspronkelijke waarde zal wegdrijven. Met behulp van een feedback-systeem kan men trachten deze langzame degradatie te corrigeren.

S.4.1 Frequentiestabilisatie

Elke vorm van feedback-controle vereist in de eerste plaats dat een geschikt foutsignaal gegenereerd wordt. Voor frequentiestabilisatie kan men gebruik maken van een optisch filter, dat frequentievariaties omzet in vermogenvariaties die eenvoudig kunnen gemeten worden. Principieel zijn er twee mogelijkheden, geïllustreerd in Figuur S.9. In het eerste geval maakt men gebruik van de flank van een optisch filter. Het foutsignaal wordt gegeven door het verschil tussen de gemeten transmissie T en de transmissie T_R bij de referentiefrequentie ν_R. Dit vereist uiteraard een meting van het ingangsvermogen. In het tweede geval wordt de laserfrequentie gestabiliseerd bij de piekfrequentie van het filter. Hier wordt het foutsignaal gegenereerd door de laserfrequentie licht te moduleren, zodat men de frequentie-afgeleide van de filtertransmissie kan meten.

Voorbeelden van filters die in de literatuur gebruikt werden voor frequentiestabilisatie zijn: Bragg roosters ingebed in een optische vezel, phased-array demultiplexers, en Fabry-Perot etalons. De laatste zijn bijzonder attractief voor de stabilisatie van een afstembare laser, omwille van hun inherente periodiciteit.

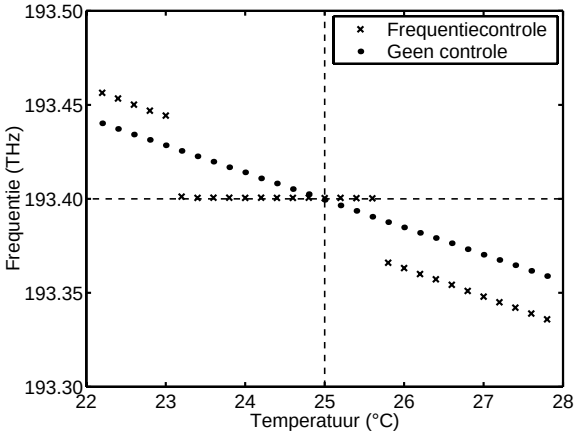

Figuur S.10 Evolutie van de emissiefrequentie van een SSG-DBR laser als functie van de temperatuur, met en zonder frequentiestabilisatie. Initieel werd de laser afgestemd op een frequentie van 193.4 THz bij een temperatuur van 25 °C.

In onze experimenten maakten we gebruik van een commercieel beschikbare frequentiereferentie die gebaseerd is op een etalon (E-Tek FPWL, [50]). Deze component levert een referentiepunt op bij gehele veelvouden van 100 GHz in het frequentiebereik rond de ITU ankerfrequentie van 193.1 THz [2].

Het foutsignaal V moet uiteraard gebruikt worden om de laserfrequentie te corrigeren. Principieel zijn er twee mogelijkheden voor fijnregeling van de laserfrequentie (cfr. §S.2). Ofwel kan men de temperatuur van de laser veranderen, ofwel kan men de stroom door de fasesectie aanpassen. Wij opteerden voor de laatste mogelijkheid, omdat deze principieel een snellere regeling toelaat en omdat variaties van de temperatuur dan kunnen gebruikt worden om een frequentie-afwijking te induceren.

Figuur S.10 toont de evolutie van de emissiefrequentie van een SSG-DBR laser als functie van de temperatuur, met en zonder frequentiestabilisatie. Initieel werd de laser afgestemd op een frequentie van 193.4 THz bij een temperatuur van 25 °C. Zonder stabilisatie varieert de frequentie met een helling van circa -14.5 GHz/°C. Wordt het foutsignaal van de FPWL gebruikt om de fasestroom te corrigeren, dan blijft de frequentie constant in het temperatuurbereik van 23.2 tot 25.6 °C. Aan de rand van dit temperatuurbereik vermindert de zijmode-onderdrukking echter. Wordt de temperatuur buiten dit bereik gebracht dan treedt een modesprong op. De fasestroom verzadigt dan zeer snel, wat betekent dat de frequentie niet langer gecontroleerd wordt. Uiteraard zal de frequentie van dan af opnieuw lineair variëren met de temperatuur.

Dit experiment maakt duidelijk dat voor een afstembare laser niet alleen de frequentie moet gestabiliseerd worden, maar dat ook de zijmode-onderdrukking hoog moet gehouden worden door één of andere vorm van modestabilisatie

S.4.2 Modestabilisatie

Een afstembare laser zal slechts in een enkele spectrale lijn emitteren indien het afstembare intra-caviteitsfilter min of meer uitgelijnd is met een caviteitsmode. Om de laser te kunnen stabiliseren zodanig dat de emissie monomodaal blijft, moet men uiteraard eerst een geschikt controlesignaal vinden. In de literatuur werden verscheidene experimenten beschreven waarin variaties van het uitgangsvermogen gebruikt werden om af te leiden of het intra-caviteitsfilter al dan niet uitgelijnd is met een caviteitsmode [51]-[56]. In de geïntegreerde afstembare lasers die hier beschouwd worden wordt dergelijke (kleine) variaties in het uitgangsvermogen vaak gemaskeerd door de globale afname van het vermogen met toenemende afstemming, ten gevolge van de toename van de absorptieverliezen in de filtersecties. Zoals we in de volgende paragraaf zullen aantonen vertoont de spanning over de actieve sectie in het verliesloze geval gelijkaardige variaties. Aangezien het spanningssignaal – zoals verder zal blijken – vaak minder beïnvloed wordt door de toename van de absorptieverliezen, ontwikkelden wij een feedback-systeem dat dit signaal gebruikt om de laser te stabiliseren [81]-[84].

Geïdealiseerde afstembare laser

Allereerst beschouwen we een geïdealiseerde afstembare laser, die bestaat uit een Fabry-Perot caviteit met een frequentie-onafhankelijke spiegel r_L en een afstembare frequentie-afhankelijke spiegel $r_R(\omega)$. Het totale caviteitsverlies $\alpha_{tot}(\omega)$ wordt benaderd door een parabool, en we veronderstellen dat het verliesminimum initieel uitgelijnd is met een caviteitsmode. We normaliseren alle frequenties ten opzichte van de frequentie van deze mode ν_0:

$$\delta\nu = (\nu - \nu_0)/\Delta\nu \,, \tag{S.28}$$

waarbij $\Delta\nu$ de modespatiëring voorstelt. Winst en verlies worden genormaliseerd ten opzichte van de caviteitslengte L:

$$A = L\alpha_{tot} \quad \text{en} \quad G = L\Gamma g \tag{S.29}$$

Indien de interne verliezen verwaarloosd worden ($\alpha_{int} = 0$), dan is de spiegelreflectie $r_R(\delta\nu)$ gerelateerd aan het genormaliseerde caviteitsverlies $A(\delta\nu)$ als volgt:

$$r_R(\delta\nu) = \frac{1}{r_L} e^{-A(\delta\nu)} \tag{S.30}$$

Figuur S.11 illustreert het afstemmen van het verliesminimum van de ene caviteitsmode (mode 0) naar de volgende (mode 1) en de overeenkomstige variaties van de (genormaliseerde) winst en de emissiefrequentie. Voor de lasermode zijn winst en verlies uiteraard gelijk (cfr. (S.10)). De laserfrequentie springt van mode 0 naar mode 1 wanneer het verliesminimum met een halve modeafstand opgeschoven is ($\delta\nu_B = 0.5$), aangezien van dan af mode 1 een lager verlies ervaart dan mode 0.

Het uitgangsvermogen van de laser is evenredig met het verschil tussen de stuurstroom I en de drempelstroom I_{th}, waarbij de helling bepaald wordt door de differentiële efficiëntie η_d. Voor het uitgangsvermogen aan de linker kant vindt men:

$$P_L = \eta_{d,L} \frac{\hbar\omega}{q} (I - I_{th}) \tag{S.31}$$

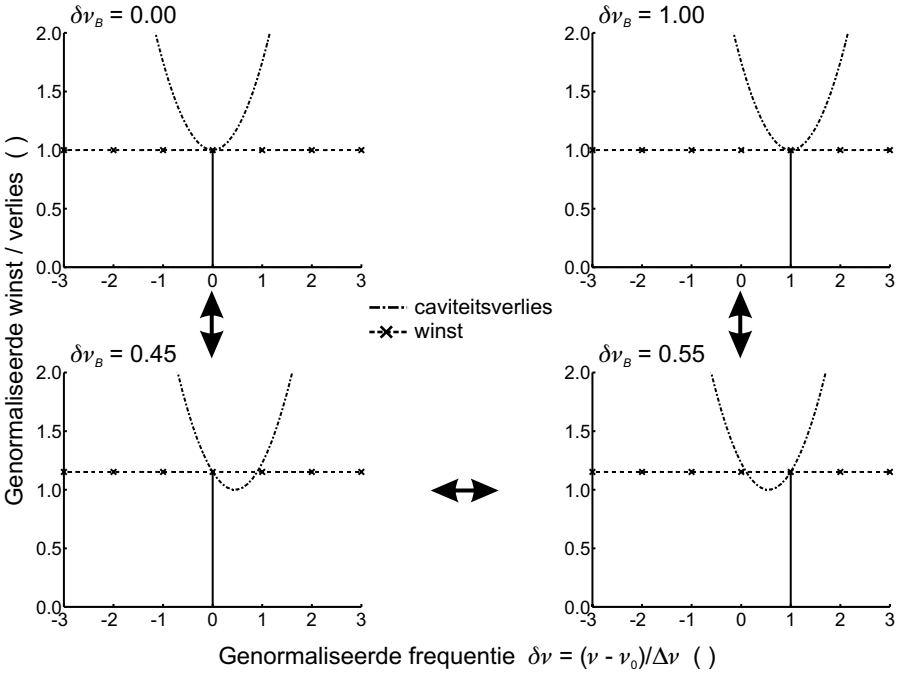

Figuur S.11 Evolutie van genormaliseerde winst en verlies in een geïdealiseerde afstembare laser wanneer de frequentie van minimaal verlies $\delta\nu_B$ afgestemd wordt van caviteitsmode 0 naar caviteitsmode 1. Voor de lasermode, aangeduid door de verticale lijn, is de winst uiteraard gelijk aan het verlies.

met
$$\eta_{d,L} = \frac{\left(1 - r_L^2\right) r_R}{\left(1 - r_L r_R\right)\left(r_L + r_R\right)} \tag{S.32}$$

De differentiële efficiëntie aan de rechter kant $\eta_{d,R}$ wordt uiteraard gevonden door de indices L en R te verwisselen. Aangezien interne verliezen verwaarloosd werden, geldt:

$$\eta_{d,L} + \eta_{d,R} = 1 \tag{S.33}$$

Figuur S.12 toont de variatie van de differentiële efficiënties en de drempelwinst als functie van de afstemming van het verliesminimum. Wanneer het minimum uitgelijnd is met een caviteitsmode, of met andere woorden wanneer de lasermode een maximale reflectie r_R ziet, is de drempelwinst minimaal, de linker efficiëntie maximaal en de rechter efficiëntie minimaal.

Wordt de laser bij voldoende hoge stroom aangestuurd ($I >> I_{th}$), dan zal het uitgangsvermogen voornamelijk bepaald worden door de differentiële efficiëntie. Om de reflectiepiek van de rechterspiegel uit te lijnen met een caviteitsmode moet men bijgevolg het uitgangsvermogen aan de linker (rechter) kant maximaliseren (minimaliseren). De variaties in de drempelwinst zorgen er anderzijds voor dat de ladingsdragerconcentratie in de actieve sectie varieert, wat zich extern manifesteert in variaties van de spanning over de actieve sectie. Minimalisatie van de spanning zal er dus ook voor zorgen dat de reflectiepiek uitgelijnd wordt met een mode.

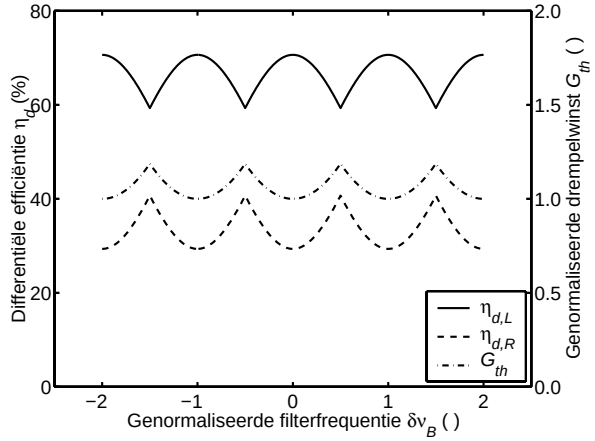

Figuur S.12 Variatie van de differentiële efficiëntie η_d en de genormaliseerde drempelwinst G_{th} met afstemming voor een geïdealiseerde afstembare laser.

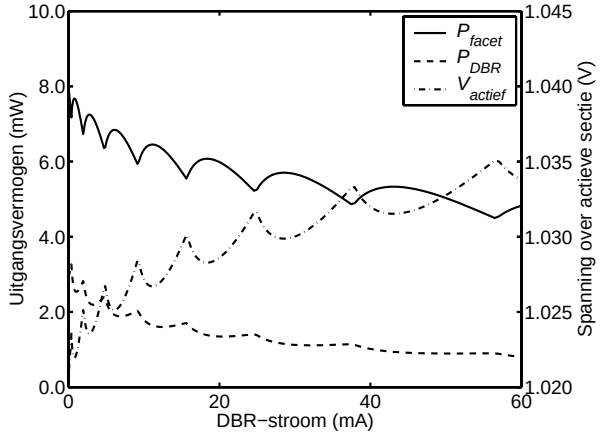

Figuur S.13 Berekende variaties van het uitgangsvermogen en de spanning over de actieve sectie als functie van de DBR stroom voor een typische DBR laser.

DBR laser

Figuur S.13 geeft het resultaat van een simulatie voor een typische DBR laser weer. De grafiek toont de variaties als functie van de DBR-stroom van het uitgangsvermogen, zowel aan de kant van het gekliefde facet (P_{facet}) als aan de kant van de DBR (P_{DBR}), en van de spanning over de actieve sectie (V_{actief}). In de spanning en het uitgangsvermogen aan het facet treden duidelijke extrema op ongeveer halverwege tussen twee modesprongen. Naarmate de DBR-stroom toeneemt, zullen de absorptieverliezen in de DBR-sectie groeien. Dit verklaart de globale toename van de spanning en afname van het vermogen, en zorgt ervoor dat de extrema enigszins naar lagere stroomwaarden verschoven worden. Stabilisatie

van de laser op deze extrema zal echter nog steeds een goede zijmode-onderdrukking opleveren. Het uitgangsvermogen aan de DBR-kant wordt natuurlijk veel meer beïnvloed door de toename van de verliezen. De minima in dit vermogen worden significant naar hogere stroomwaarden verschoven, en verdwijnen zelfs bij hoge DBR-stromen. Dit signaal is bijgevolg veel minder geschikt voor modestabilisatie.

Een belangrijke voorwaarde opdat de spanning en het uitgangsvermogen aan het gekliefde facet bruikbare signalen zouden opleveren is dat de reflector voldoende selectief is. Dit bleek uit metingen op een DBR laser met een zeer brede reflectiepiek. Een breedbandige Bragg-reflector zal als hij afgestemd wordt slechts kleine variaties induceren in het uitgangsvermogen en de spanning, zodat deze vaak zullen gemaskeerd worden door de invloed andere effecten zoals de toename van de absorptieverliezen. Een bijkomend gevolg van de relatief lage selectiviteit is dat niet-lineaire effecten kunnen optreden, wat zich o.a. manifesteert in een vrij aanzienlijke hysteresis in de afstemkarakteristieken van de laser bij hoge uitgangsvermogens [57]-[58]. Deze effecten beïnvloeden ook de variaties in spanning en uitgangsvermogen. Dit alles maakt het zeer moeilijk om een dergelijke laser te stabiliseren aan de hand van variaties in spanning of uitgangsvermogen.

SSG-DBR laser

Een SSG-DBR laser zal licht emitteren in één enkele mode indien een reflectiepiek van de voorreflector, een reflectiepiek van de achterreflector en een caviteitsmode uitgelijnd worden. In een correct ontworpen laser kan slechts één paar reflectiepieken tegelijkertijd samenvallen. Voor kleine afwijkingen ten opzichte van de optimale situatie zal de SSG-DBR laser zich gedragen als een tweezijdige DBR laser.

Wordt de reflectiepiek van de voorreflector weggeschoven van de caviteitsmode, dan zal de differentiële efficiëntie aan de voorzijde toenemen (cfr. de $\eta_{d,R}$-curve in Figuur S.12). Wordt daarentegen de reflectiepiek van de achterreflector verschoven, dan zal de differentiële efficiëntie aan de voorzijde afnemen (cfr. de $\eta_{d,L}$-curve in Figuur S.12). Wordt het uitgangsvermogen aan de voorzijde opgemeten als functie van de reflectorstromen, dan verwachten we bijgevolg een zadelpunt in het vermogen bij het optimale werkingspunt (minimaal vermogen als functie van de voorreflectorstroom, maximaal vermogen als functie van de achterreflectorstroom). Het controlesysteem beschreven in [56] stabiliseerde de laser door hem vast te pinnen op een dergelijk zadelpunt in het uitgangsvermogen. In de spanning verwachten we anderzijds een minimum bij het optimale werkingspunt [81]-[84].

Figuur S.14 en Figuur S.15 tonen de opgemeten variaties van het uitgangsvermogen en de spanning als functie van de reflectorstromen. Bij lage stromen vindt men de verwachte zadelpunten in het vermogen. De zadelpunten liggen wel niet centraal tussen de modegrenzen[1], maar zijn verschoven naar lagere achterreflectorstromen en hogere voorreflectorstromen. Bij hoge stroomwaarden verdwijnen de zadelpunten. Dit is uiteraard te wijten aan de stijging van de absorptieverliezen in beide reflectorsecties met toenemende stroom (cfr. Figuur S.13). In de spanning treden daarentegen minima op voor elk modegebied.

[1] Dit zijn de lijnen die het gebied begrenzen waarin een bepaalde caviteitsmode de lasermode is.

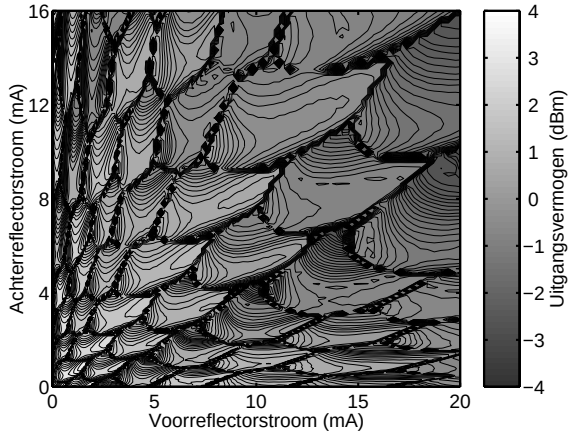

Figuur S.14 Gemeten variaties van het uitgangsvermogen van een SSG-DBR laser als functie van de reflectorstromen.

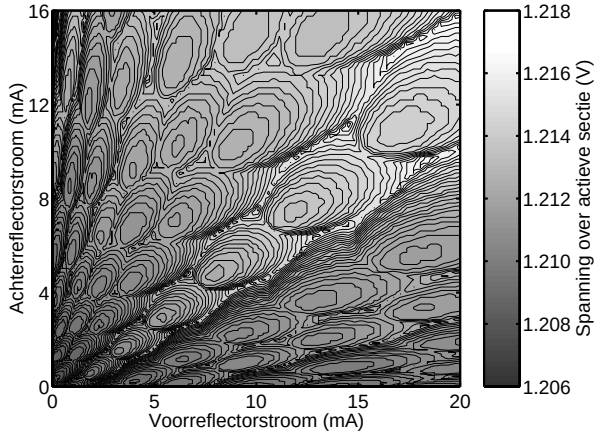

Figuur S.15 Gemeten variaties van de spanning over de actieve sectie van een SSG-DBR laser als functie van de reflectorstromen.

De spanning levert bijgevolg een veel betrouwbaarder controlesignaal voor modestabilisatie van een SSG-DBR laser.

GCSR laser

Bij een vaste waarde voor de koppelaarstroom, gedraagt een GCSR laser zich min of meer als een gewone DBR laser met een zeer lange fasesectie. Wanneer de reflector afgestemd wordt verwachten we dan ook een maximum in het uitgangsvermogen en een minimum in de spanning wanneer de reflectiepiek geselecteerd door de koppelaar uitgelijnd is met een caviteitsmode. Wordt daarentegen de koppelaar afgestemd, dan verwacht op analoge wijze een maximaal uitgangsvermogen en een

minimale spanning wanneer de transmissiepiek van de koppelaar uitgelijnd is met een reflectiepiek van de kamreflector.

Bij metingen op GCSR lasers die ons ter beschikking werden gesteld, bleek noch de spanning, noch het vermogen een geschikt controlesignaal op te leveren. Bij het afstemmen van de reflector trad net als bij de eerder vermelde DBR laser hysteresis op. In de GCSR laser zijn de reflectiepieken weliswaar relatief smalbandig, maar door de lange caviteit is de modespatiëring klein, wat netto hetzelfde resultaat voor de modeselectiviteit oplevert. De niet-lineaire effecten die aan de oorsprong liggen van de hysteresis zorgen er ook voor dat de verwachte extrema in spanning en uitgangsvermogen niet optreden. De filterkarakteristiek van de koppelaar bleek anderzijds ook niet voldoende selectief om significante variaties in het uitgangsvermogen en de spanning te veroorzaken wanneer het filter afgestemd wordt.

S.4.3 Feedback-controle van SSG-DBR lasers

Controlecircuit

Voor SSG-DBR lasers werd een volledig feedback-controlesysteem ontworpen, schematisch weergegeven in Figuur S.16. Drie verschillende controlelussen kunnen onderscheiden worden.

Voor de modestabilisatie worden kleine sinusoidale modulatiesignalen (met een verschillende frequentie) toegevoegd aan de reflectorstromen. Met behulp van twee lock-in versterkers worden de overeenkomstige modulatiecomponenten V_f en V_r in de spanning over de actieve sectie V_a gemeten. Deze signalen zijn evenredig met de helling van het spanningsoppervlak (Figuur S.15) in de richting van respectievelijk de voor- en de achterreflectorstroom. Bij elke iteratie van de controlelus wordt een correctie evenredig met V_f (V_r) afgetrokken van de voorreflectorstroom (achterreflectorstroom), aangezien de stroom moet verhoogd worden bij een negatieve helling en verlaagd bij een positieve helling. Op die manier wordt de spanning steeds geminimaliseerd als functie van de reflectorstromen.

Voor de frequentiestabilisatie wordt gebruik gemaakt van de etalon-gebaseerde frequentiereferentie beschreven in §S.4.1 [50]. Het foutsignaal is gegeven door $V = 10\cdot\log(\eta P_2/P_1)$, waarbij η een kalibreringsfactor is. Een positieve waarde van V stemt overeen met een te hoge frequentie. Daarom wordt telkens een correctie evenredig met V van de fasestroom afgetrokken.

Om het uitgangsvermogen te stabiliseren wordt de stroom door de actieve sectie tenslotte gecorrigeerd met een bedrag evenredig met $(P_{ref} - P_1)$, waarbij P_{ref} een referentievermogen is.

Voor de praktische experimenten die verder beschreven worden, werd het controlesysteem opgebouwd uit afzonderlijke meetinstrumenten die gecontroleerd worden door een LabVIEW programma dat draait op een PC. Om het systeem te testen moet een zekere frequentie-afwijking geïnduceerd worden. Een geleidelijke degradatie van de laser werd gesimuleerd door de temperatuur in kleine stappen (0.2 °C) te verhogen. Na elke temperatuursverhoging lieten we het systeem gedurende 30 tot 60 seconden lopen, om vervolgens de frequentie, het vermogen en de zijmode-onderdrukking te meten.

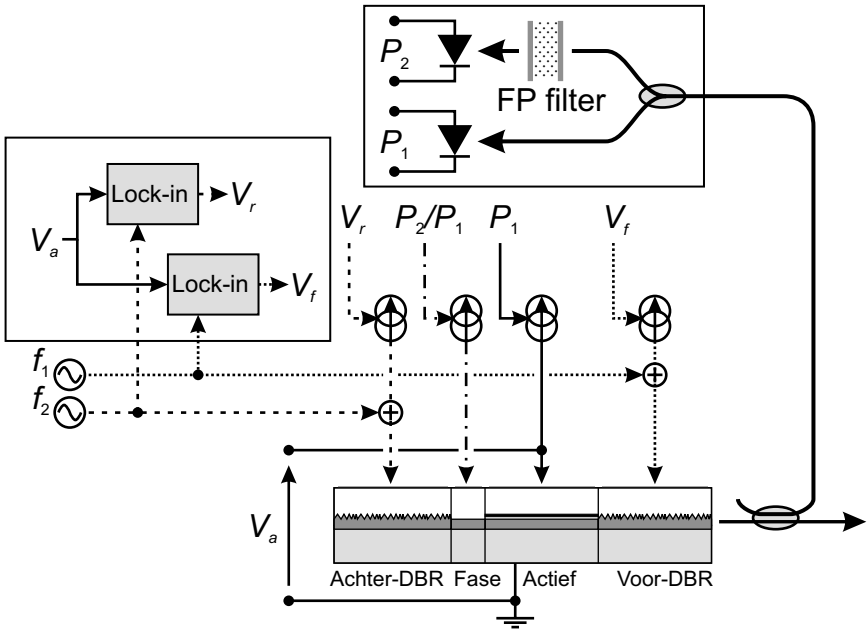

Figuur S.16 Schema van het controle systeem voor frequentie-, mode- en vermogenstabilisatie van een SSG-DBR laser.

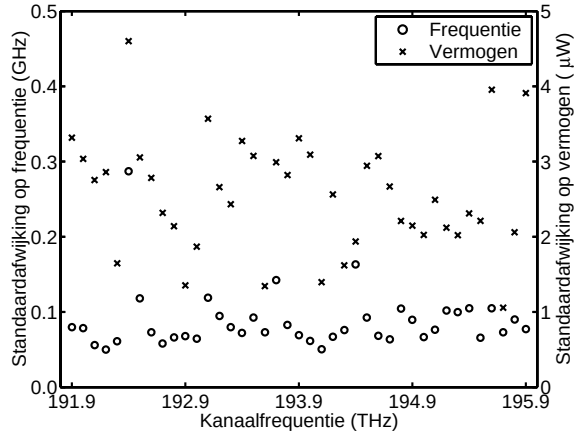

Figuur S.17 Standaardafwijking op de frequentie en het uitgangsvermogen voor 41 ITU kanalen over een temperatuursbereik van 20 tot 30 °C. Het vermogen werd gestabiliseerd op 0.5 mW.

Werking in statisch bedrijf

Het systeem werd uitvoerig getest op 3 SSG-DBR lasers [81]-[84]. De resultaten voor een van deze lasers worden hier samengevat. De laser werd achtereenvolgens afgestemd op 41 kanalen op het 100 GHz ITU-raster, van 191.9 tot 195.9 THz.

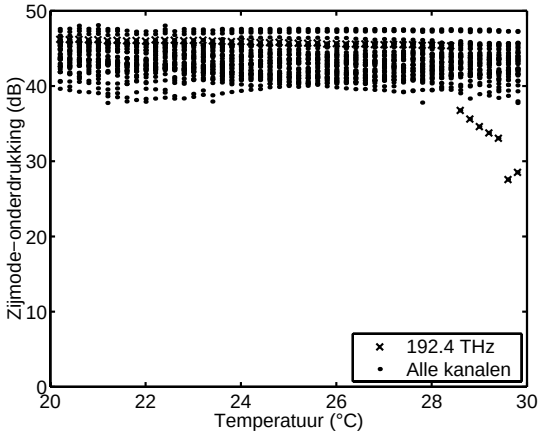

Figuur S.18 Variatie van de zijmode-onderdrukking voor 41 ITU kanalen over een temperatuursbereik van 20 tot 30 °C. Kruisjes markeren de resultaten voor het slechtste kanaal.

Frequentie-afwijkingen werden geïnduceerd door de temperatuur stelselmatig te verhogen van 20 tot 30 °C, in stappen van 0.2 °C. Zoals Figuur S.17 aantoont, was de standaardafwijking op de frequentie over dat temperatuursbereik kleiner dan 0.2 GHz voor alle kanalen, met uitzondering van het 192.4 THz kanaal. Ook de vermogenvariaties waren zeer klein ten opzichte van het ingestelde vermogenniveau van 0.5 mW. Voor alle kanalen behalve het 192.4 THz kanaal werd de zijmode-onderdrukking ook ruim boven 35 dB gehouden. Voor dit laatste kanaal daalde de zijmode-onderdrukking voor temperaturen boven 28 °C.

De hogere frequentie-afwijking en dalende zijmode-onderdrukking voor het 192.4 THz kanaal kunnen verklaard worden door thermische effecten. Dit kanaal vereist namelijk relatief hoge stromen door alle secties. Met stijgende omgevingstemperatuur moeten deze stomen verder versterkt worden om de frequentie stabiel te houden. Aangezien de afstemmingsefficiëntie bovendien daalt met toenemende stroom leidt dit tot zeer hoge stromen. Daardoor wordt de temperatuur in de laser heel wat hoger wordt dan de omgevingstemperatuur, zodat elke indexverandering door de toenemende ladingsdragerconcentratie op een gegeven ogenblik volledig tegengewerkt wordt door de thermische indexverandering. Wordt de omgevingstemperatuur dan nog verder opgedreven, dan zal de laser niet langer kunnen gestabiliseerd worden.

Werking bij directe modulatie van de laser

De frequentie- en modestabilisatie werd ook getest terwijl de laser direct gemoduleerd werd. Een pseudo-random digitaal modulatiesignaal met een amplitude van 60 mA werd aangelegd aan de actieve sectie. De bitsnelheid was 1.244 Gbit/s. De modulatie van de stroom door de actieve sectie verstoort de signalen V_f en V_r enigszins. Om de signaal-ruis verhouding van de controlesignalen V_f en V_r te verhogen werd de stroommodulatie van de reflectorsecties verhoogd van 5 µA tot 25 µA. Bovendien werd de tijdsconstante van de lock-in versterkers verhoogd.

Mits deze aanpassingen kan de laser ook gestabiliseerd worden terwijl hij direct gemoduleerd wordt. De gemeten frequentie-afwijkingen worden wel iets groter (±2.0 GHz), wat te wijten kan zijn aan de frequentiemodulatie die onvermijdelijk gepaard gaat met de intensiteitsmodulatie.

S.5 Karakteriseringsmethodes om een frequentie-opzoektabel te genereren

Het zou ondertussen duidelijk moeten zijn dat de controle van de geïntegreerde afstembare lasers voorgesteld in §S.2 eerder complex is. Om de laser af te stemmen op een bepaalde frequentie met een gegeven uitgangsvermogen moeten drie tot vier stromen ingesteld worden. Bovendien zal een verandering in één van de stromen zowel de frequentie als het vermogen wijzigen. Meestal wordt een dergelijke laser dan ook geleverd samen met de nodige controle-elektronica die de externe eisen (frequentie, uitgangsvermogen) vertaalt naar de correcte waarden van de stuurstromen. Dit gebeurt aan de hand van een opzoektabel die opgeslagen wordt in een semi-permanent geheugen. In §S.5.2 tot §S.5.4 presenteren we drie methodes die kunnen gebruikt worden om een dergelijke tabel te genereren, waarbij we ons focusseren op de SSG-DBR laser. Eerst overlopen we echter kort de typische vereisten voor de karakteriseringsmethodes.

S.5.1 Vereisten

De belangrijkste vereiste is uiteraard de nauwkeurigheid van de opzoektabel. Voor WDM-toepassingen wordt meestal een frequentiefout van minder dan ±10% van de kanaalafstand geëist. Dit betekent met ander woorden dat kleinere fouten een dichtere stapeling van frequentiekanalen toelaten. Voor alle werkingspunten in de tabel moet de zijmode-onderdrukking ten minste 30 dB zijn. Verder wenst men meestal ook een zo klein mogelijke variatie van het uitgangsvermogen over de kanalen in de tabel.

Voor een fabrikant van afstembare lasermodules is het uiteraard van belang dat de tabel snel en efficiënt gegenereerd wordt. Dit betekent ook dat een goede methode weinig of geen interventie van een operator vergt, en zo weinig mogelijk gebruik maakt van dure (en trage) meetinstrumenten zoals een golflengtemeter en een optische spectrumanalysator.

S.5.2 Curve-aanpassing aan opgemeten afstemkarakteristieken

Om een SSG-DBR laser af te stemmen op een bepaalde frequentie moet in de eerste plaats een reflectiepiek van elk van beide spiegels naar deze frequentie afgestemd worden. Vervolgens moet de fasesectie afgestemd worden zodanig dat een caviteitsmode uitgelijnd wordt met de samenvallende reflectiepieken. Deze stappen zijn ook terug te vinden in de hieronder beschreven methode.

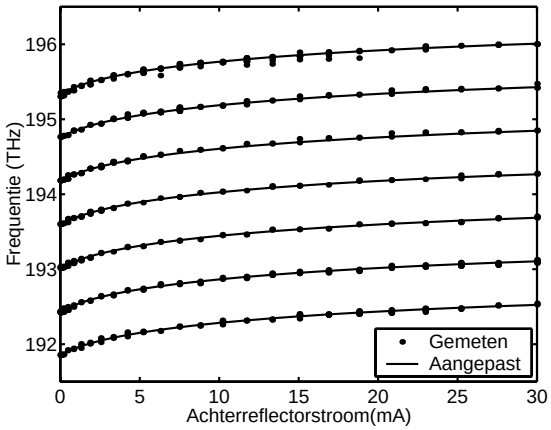

Figuur S.19 Frequentiewaarden gemeten als functie van I_{achter} en I_{voor} (25×25 matrix), uitgezet als functie van I_{achter} (puntjes). Aangepaste afstemcurves van de achterreflector (volle lijnen).

Afstemmen van de reflectoren

In een eerste stap wordt de emissiefrequentie gemeten als functie van de reflectorstromen, typisch op een raster van 25×25 meetpunten in het (I_{voor}, I_{achter})-vlak. De matrix van frequentiewaarden wordt vervolgens uitgezet als functie van één reflectorstroom, bijvoorbeeld de achterreflectorstroom (Figuur S.19). De meetpunten verzamelen zich langsheen parallelle curven die de afstemming van de verschillende reflectiepieken weergeven. Het verloop van deze curven kan in goede benadering beschreven worden door:

$$\nu_k(I) = \nu_0(0) - aI_0^{1/3} + a(I + I_0)^{1/3} - bI + k\delta \qquad \text{(S.34)}$$

Hier is $\nu_0(0)$ de frequentie van piek 0 zonder stroominjectie en δ de piekafstand. Als K het totaal aantal reflectiepieken voorstelt, dan worden de pieken genummerd als volgt:

$$k = -\left\lfloor \tfrac{1}{2}(K-1) \right\rfloor, \ \ldots\ , 0, \ \ldots\ , \left\lceil \tfrac{1}{2}(K-1) \right\rceil \qquad \text{(S.35)}$$

De parameters $\nu_0(0)$, a, b, I_0, en δ kunnen berekend worden door curve-aanpassing. Wordt de matrix van frequentiewaarden uitgezet als functie van de voorreflectorstroom, dan wordt uiteraard een gelijkaardige figuur bekomen, zodat ook voor deze reflector bovenstaande parameterset berekend kan worden door curve-aanpassing. Eens de parameters voor beide reflectoren bepaald zijn, kan men de frequentie versus stroom karakteristieken eenvoudig inverteren. Voor elke frequentie in het afstembereik van de laser kan men reflectorstromen berekenen die een piek van de respectievelijke reflector op die frequentie afstemmen. In bepaalde gevallen zullen er meerdere oplossingen zijn. Aangezien de absorptieverliezen in de caviteit toenemen met de stroom door de passieve secties, wordt meestal de oplossing verkozen die een minimale stroom vergt. De streeplijnen in Figuur S.20 stellen de (I_{voor}, I_{achter})-paren voor die op die manier berekend werden voor alle frequenties in het afstembereik.

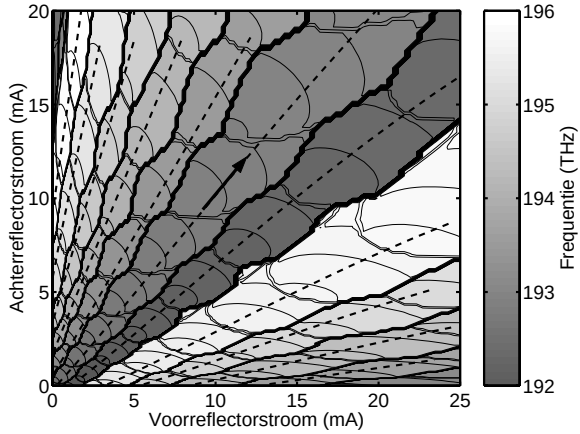

Figuur S.20 Contourgrafiek van de emissiefrequentie als functie van de reflectorstromen. De streeplijnen stellen de (I_{voor}, I_{achter})-trajecten voor die berekend werden met behulp van de berekende parametersets.

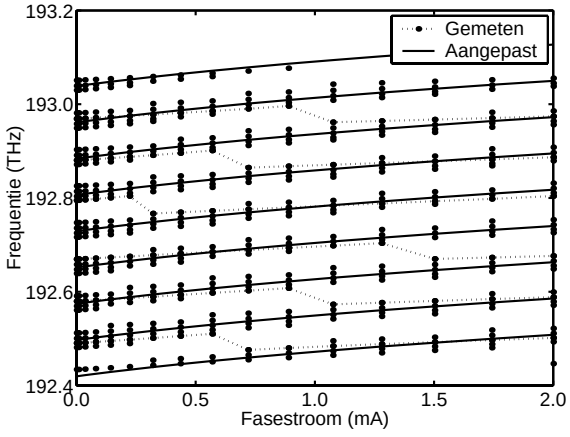

Figuur S.21 Frequentiewaarden gemeten als functie van I_{fase} en I_{achter}, uitgezet als functie van I_{fase} (puntjes). De reflectorstromen zijn uniek gerelateerd door de curve aangeduid door de pijl in Figuur S.20. Aangepaste afstemcurves van de caviteitsmodes (volle lijnen).

Afstemmen van de fasesectie

In de tweede fase wordt de fasestroom bepaald voor elke mogelijke frequentie. Dit vergt een tweede set metingen. (I_{voor}, I_{achter})-paren worden berekend voor een uniform frequentieraster dat het gewenste frequentiebereik dekt en een frequentiestap heeft die kleiner is dan de modespatiëring. Voor elk van deze punten wordt de frequentie gemeten als functie van de fasestroom. Vervolgens worden de meetwaarden voor elk (I_{voor}, I_{achter})-traject afzonderlijk beschouwd en uitgezet als functie van de fasestroom (Figuur S.20).

Opnieuw groeperen de meetpunten zich rond parallelle curven, die nu echter de afstemming van individuele caviteitsmodes weergeven. Deze kunnen weer beschreven worden met behulp van (S.34). Curve-aanpassing levert voor elk van de (I_{voor}, I_{achter})-trajecten in Figuur S.20 een parameterset op die kan gebruikt worden om voor elke frequentie de passende fasestroom te berekenen.

Experimentele resultaten

Bovenstaande procedure werd toegepast op verscheidene SSG-DBR en SG-DBR lasers. De nauwkeurigheid van de berekende opzoektabel werd vervolgens getest door voor alle punten in de tabel de frequentie en de zijmode-onderdrukking te meten. Voor lasers met een voldoende regelmatig afstemgedrag werd steeds een zijmode-onderdrukking van meer dan 40 dB gemeten [77]. De frequentie-afwijkingen zijn echter vaak relatief groot: maximale fouten tot ±9 GHz, met kwadratisch gemiddelde fout van ongeveer 3 GHz. Dit is amper voldoende voor systemen met een kanaalafstand van 100 GHz. Een verder nadeel is dat de stroom door de actieve sectie constant gehouden wordt, wat betekent dat het uitgangsvermogen met 7 tot 8 dB varieert over het afstembereik.

De meettijd werd wel teruggebracht van één of meerdere dagen tot 1 à 2 uur. Andere nadelen zijn dat de procedure de hele tijd een golflengtemeter vereist, en dat interventie van een operator is nodig om geschikte beginwaarden voor de curve-aanpassing te kiezen.

S.5.3 Combineren van curve-aanpassing en feedback-controle

In de hierboven beschreven methode werd het grootste deel van de meettijd gespendeerd aan de tweede meetcyclus, waar de fasestroom wordt bepaald voor alle frequenties. Indien de uiteindelijke lasermodule voorzien is van een controlesysteem zoals voorgesteld in §S.4.3, dan kan de fijn-afregeling van de laser overgelaten worden aan dit systeem.

De eerste meetsequentie is dezelfde als in bovenstaande procedure. Met behulp van de parametersets voor de reflectorsecties worden vervolgens de reflectorstromen berekend voor alle kanalen van de frequentiereferentie in het controlesysteem (in ons geval zijn dat de kanalen bij gehele veelvouden van 100 GHz). Voor elk (I_{voor}, I_{achter})-paar wordt de frequentie gemeten voor enkele fasestromen (typisch 5) en daaruit wordt een initiële schatting voor de fasestroom in het gewenste werkingspunt afgeleid. Op die manier kan een ruwe opzoektabel afgeleid worden in een tijdsspanne van enkele minuten.

Om de nauwkeurigheid van de tabel te verbeteren, wordt de laser dan achtereenvolgens op elk van de werkingspunten in de ruwe tabel afgestemd. Vervolgens wordt de feedback-controle ingeschakeld tot de stromen gestabiliseerd zijn. De uiteindelijke stroomwaarden worden opgeslagen in de finale opzoektabel. Een belangrijk voordeel is dat op die manier ook het uitgangsvermogen op een zekere gewenste waarde kan ingesteld worden.

In dit geval wordt de nauwkeurigheid van de tabel uitsluitend bepaald door de nauwkeurigheid van het controlesysteem. Het circuit van §S.4.3 geeft frequentiefouten kleiner dan ±1.0 GHz, en een zijmode-onderdrukking van 40 dB of meer.

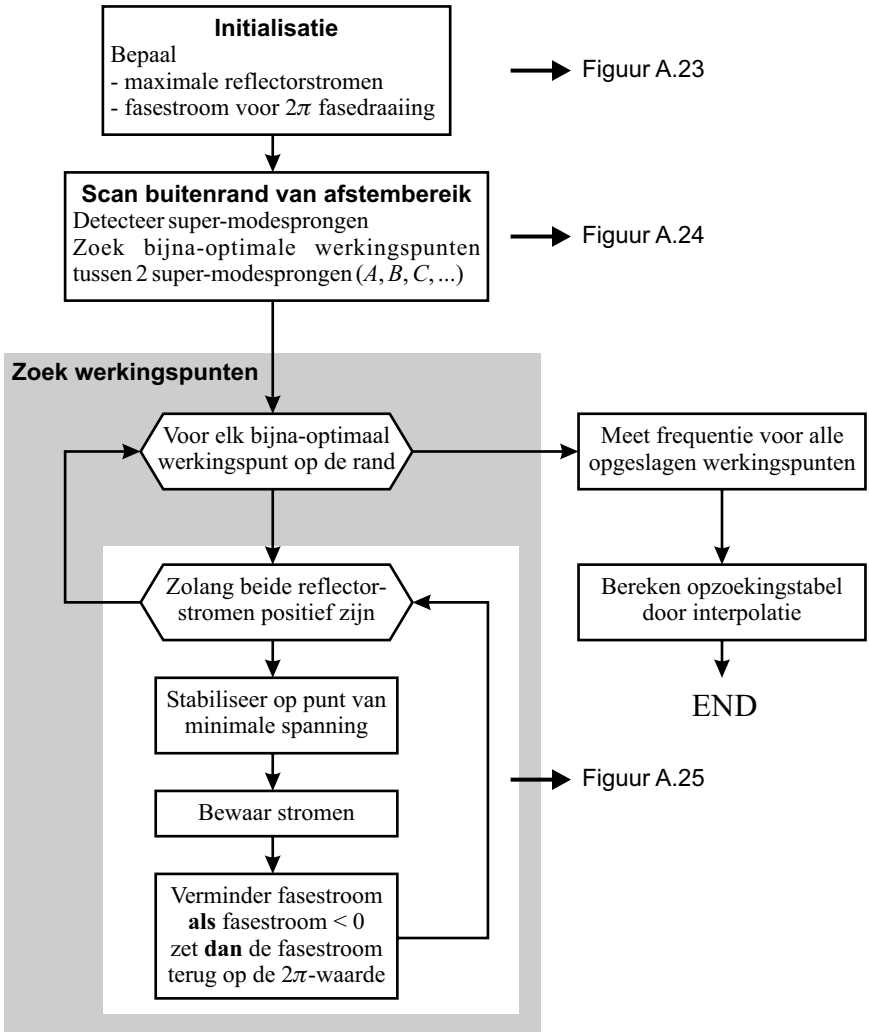

Figuur S.22 Overzicht van het algoritme dat een opzoektabel genereert door gebruik te maken van spanningsminimalisatie.

S.5.4 Lokaliseren van werkingspunten door het minimaliseren van de spanning over de actieve sectie

Volgens de resultaten van §S.4, volstaat het de spanning over de actieve sectie van een SSG-DBR laser te minimaliseren als functie van de reflectorstromen om monomodale emissie te bekomen. In het laatst algoritme wordt deze eigenschap gebruikt om geschikte werkingspunten te lokaliseren in de driedimensionale ruimte van voorreflector-, achterreflector-, en fasestroom. Frequentiemetingen worden enkel uitgevoerd voor deze geoptimaliseerde werkingspunten, die gegroepeerd worden per caviteitsmode. Tenslotte wordt de tabel berekend door interpolatie.

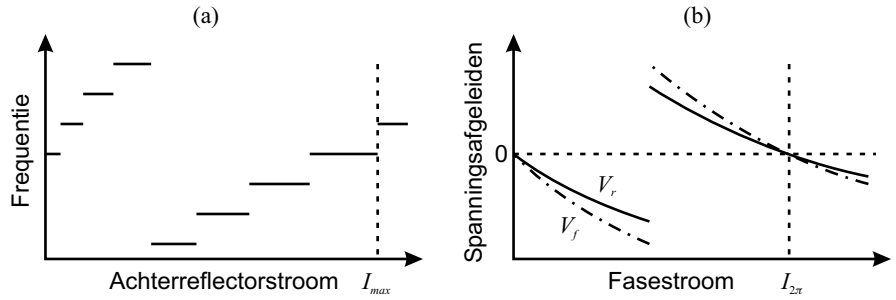

Figuur S.23 Initialisatie van de procedure: bepalen van de maximale reflectorstromen (a) en de fasestroom voor een fasedraaiing van 2π (b).

Figuur S.22 geeft een schematisch overzicht van de procedure.

Initialisatie

Het algoritme vergt allereerst een schatting voor de maximale stromen die moeten aangelegd worden aan de reflectorsecties om volledige dekking van het afstembereik te bekomen ($I_{voor,max}$ en $I_{achter,max}$). Verder moet ook de fasestroom bepaald worden die een fasedraaiing van 2π geeft ($I_{fase,2\pi}$). Deze stromen kunnen afgeleid worden uit relatief eenvoudige metingen (Figuur S.23).

Wordt een reflectorstroom verhoogd dan zal de frequentie met relatief grote sprongen veranderen. Dergelijke grote frequentiesprongen kunnen gemeten worden door gebruik te maken van een eenvoudig optisch filter [59]. Inherent aan de Vernier-afstemming is een zekere periodiciteit. De maximaal vereiste reflectorstroom wordt bereikt wanneer de frequentie de oorspronkelijke waarde opnieuw gekruist heeft (Figuur S.23(a)). Om de fasestroom voor een fasedraaiing van 2π te bepalen wordt de laser ingesteld op een willekeurig spanningsminimum bij fasestroom gelijk aan nul. De signalen V_f en V_r (cfr. Figuur S.16) zijn dan uiteraard nul. Wordt de fasestroom vervolgens verhoogd, dan zullen de spanningssignalen eerst dalen onder 0 ($|V_f|$ en $|V_r|$ nemen toe). Op een gegeven moment treedt echter een modesprong op, zodat de spanningssignalen plots van teken veranderen. Van dan af dalen $|V_f|$ en $|V_r|$ opnieuw. $I_{fase,2\pi}$ wordt bereikt wanneer deze signalen terug gelijk worden aan nul (Figuur S.23(b)).

Scannen van de buitenrand van het afstembereik

In de tweede fase wordt de buitenrand gescand om de super-modesprongen te lokaliseren (Figuur S.24). De achterreflectorstroom wordt ingesteld op zijn maximale waarde en de voorreflectorstroom wordt stapsgewijze verhoogd van 0 tot $I_{voor,max}$. Vervolgens wordt de voorreflectorstroom constant gehouden en de achterreflectorstroom stapsgewijze verlaagd van $I_{achter,max}$ tot 0. De super-modesprongen kunnen opnieuw gedetecteerd worden door gebruik te maken van een optisch filter.

Voor elke super-mode wordt dan een beginpunt gezocht waar een caviteitsmode en de twee reflectiepieken die overeenstemmen met die super-mode min of meer uitgelijnd zijn. In de punten op de rand tussen twee super-modesprongen worden de signalen V_f en V_r gemeten als functie van de fasestroom (van 0 tot $I_{fase,2\pi}$).

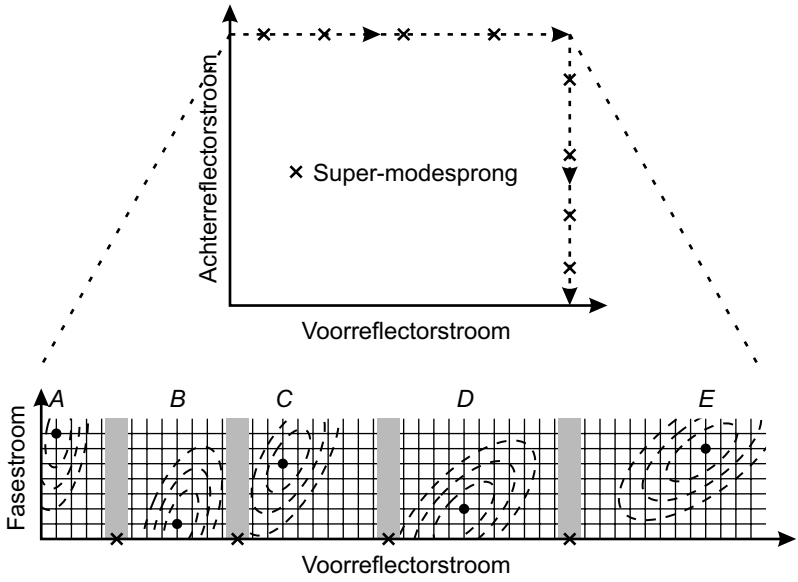

Figuur S.24 Scannen van de buitenrand van het afstembereik om goede beginpunten te vinden binnen elke super-mode.

Uit de (I_{voor}, I_{achter}, I_{fase})-combinaties die tot een bepaalde super-mode behoren wordt het punt weerhouden dat volgende testfunctie minimaliseert (cfr. Figuur S.24):

$$T\left(I_{front}, I_{rear}, I_{phase}\right) = I_{front} \cdot V_f^2 + I_{rear} \cdot V_r^2 \qquad \text{(S.36)}$$

Op die manier wordt een set van bijna-optimale werkingspunten *A*, *B*, *C*, ... bekomen op de buitenrand van het afstemmingsbereik.

Lokaliseren van werkingspunten

In de eigenlijke kern van algoritme (Figuur S.22) wordt een iteratieve procedure gestart voor elk van de bijna-optimale werkingspunten *A*, *B*, *C*, ... De afstemstromen worden ingesteld op de gekozen waarden en de modestabilisatie wordt ingeschakeld. Volgende stappen worden dan herhaald tot I_{voor} of I_{achter} de ondergrens van 0.1 mA bereiken:

- Wacht tot I_{voor} en I_{achter} gestabiliseerd zijn.
- Bewaar de waarden van de verschillende stromen.
- Verminder de fasestroom. Mocht de fasestroom negatief worden, stel dan de fasestroom terug in op $I_{fase,2\pi}$.

Op die manier wordt een caviteitsmode gevolgd in het (I_{voor}, I_{achter})-vlak naarmate de fasestroom vermindert wordt (Figuur S.25). Telkens de fasestroom nul bereikt, wordt deze teruggezet op de 2π-waarde, zodat de naburige caviteitsmode (met lagere frequentie) uitgelijnd wordt met de samenvallende reflectiepieken en de lasermode wordt.

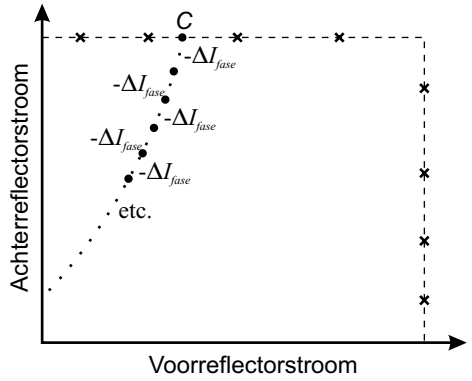

Figuur S.25 Traceren van caviteitsmodes in het (I_{voor}, I_{achter})-vlak met dalende fasestroom.

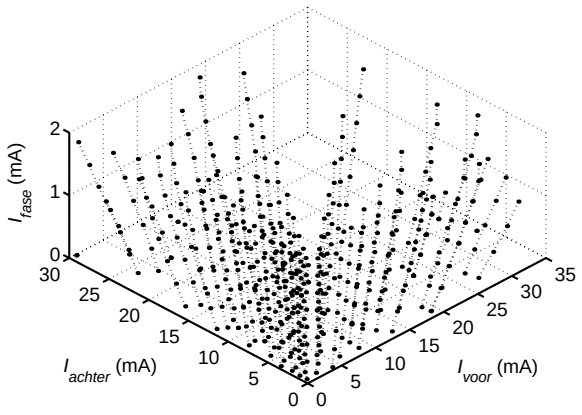

Figuur S.26 Optimale werkingspunten in de driedimensionale ruimte van voorreflector-, achterreflector-, en fasestroom. De stippellijnen verbinden punten die tot dezelfde caviteitsmode behoren.

Uiteindelijk wordt een tabel bekomen van geoptimaliseerde werkingspunten, die het volledige afstembereik dekken. Figuur S.26 toont deze punten in de driedimensionale ruimte van afstemstromen, gegroepeerd per caviteitsmode.

Bepalen van de opzoektabel

In de laatste fase wordt de frequentie gemeten voor alle punten in Figuur S.26. Aan de hand van de meetwaarden wordt dan de uiteindelijke opzoektabel berekend als volgt. Voor een gegeven frequentie worden eerst de caviteitsmodes gezocht die kunnen afgestemd worden op deze frequentie, door te controleren of de gewenste frequentie tussen de minimale en maximale meetwaarde voor een gegeven mode ligt. Als er meerdere oplossingen zijn, wordt deze met minimale stroom weerhouden. Vervolgens worden de eigenlijke waarden van de afstemstromen voor de gewenste frequentie bepaald door kubische interpolatie tussen de meetpunten van die caviteitsmode.

Zoals de procedure hierboven beschreven werd, veronderstelt ze een constante stroom door de actieve sectie. Aangezien het algoritme echter feedback-controle gebruikt om de werkingspunten te vinden kan men eenvoudig een vermogencontrolelus toevoegen, die de stroom door de actieve sectie gedurig aanpast om het vermogen constant te houden.

Experimentele resultaten

Met deze procedure werden de frequentie-afwijkingen teruggebracht tot onder ±0.5 GHz, met een kwadratisch gemiddelde fout van minder dan 0.15 GHz [84]. Dat betekent dat de kanaalafstand kan teruggebracht worden tot 25 GHz of zelfs 10 GHz. De gemeten frequentie-afwijkingen zijn hoofdzakelijk bepaald door de nauwkeurigheid van de golflengtemeter (absolute nauwkeurigheid ±0.6 GHz, relatieve nauwkeurigheid ±0.4 GHz [60]). De zijmode-onderdrukking was minstens 35 dB, meestal zelfs 40 dB. De vermogenvariaties werden teruggebracht van bijna 8 dB tot minder dan 0.8 dB.

De meettijd is momenteel ongeveer 100 minuten zonder vermogencontrole en 150 minuten met vermogencontrole. Het huidige controlesysteem is echter vrij traag, aangezien gebruik gemaakt wordt van discrete meetinstrumenten (cfr. §S.4.3). We verwachten daarom dat de meettijd gemakkelijk kan teruggebracht worden tot 20 à 30 minuten, mits een geïntegreerd elektronisch controlecircuit opgebouwd wordt.

S.6 Modulatie-eigenschappen van afstembare lasers

In de meeste hedendaagse optische communicatie systemen wordt digitale data getransporteerd door de optische draaggolf gegenereerd door een laserdiode aan en uit te schakelen. Dit kan gebeuren door rechtstreeks de stroom door de actieve sectie te moduleren of door gebruik te maken van een externe modulator.

Het grootste voordeel van de eerste aanpak is uiteraard de kostprijs. Jammer genoeg veroorzaakt de modulatie van de stroom niet enkel een intensiteitsvariatie, maar ook een frequentievariatie. Aangezien verschillende frequenties aan een verschillende snelheid propageren in een optische vezel, heeft dit tot gevolg dat de digitale pulsen zullen verbreden met toenemende afstand. Uiteindelijk zal de intensiteit van een digitale 1 overvloeien in een digitale 0, zodat een transmissiefout ontstaat. Daarom wordt directe modulatie enkel gebruikt voor relatief lage bitsnelheden (tot 2.5 Gbit/s) en korte afstanden (minder dan 100 km).

De bitsnelheden die kunnen behaald worden met directe modulatie worden uiteraard ook begrensd door de bandbreedte van de laserdiode. DFB lasers kunnen bandbreedtes hebben van meer dan 30 GHz [46], [61], wat in principe directe modulatie aan bitsnelheden van 10 Gbit/s en meer moet toelaten. Voor afstembare lasers worden lagere bandbreedtes verwacht omwille van de langere caviteit. Tot nu toe werd echter relatief weinig gepubliceerd over de modulatie-eigenschappen van afstembare lasers [62]-[69]. In de volgende paragrafen presenteren we zowel theoretische berekeningen als experimentele resultaten.

S.6.1 Theoretische analyse

Klein-signaalmodulatie

Voor een één-sectie laser, zoals een DFB of Fabry-Perot laser, wordt de (genormaliseerde) klein-signaalrespons beschreven door:

$$H(\Omega) = H(2\pi f) = \frac{\Omega_r^2}{-\Omega^2 + j\gamma\Omega + \Omega_r^2} \tag{S.37}$$

Dit is transferfunctie van een tweede-orde laagdoorlaatfilter met resonantiefrequentie $f_r = \Omega_r/(2\pi)$ en demping γ. De resonantiefrequentie is gegeven door:

$$\Omega_r^2 = G_N \frac{I - I_{th}}{qV_a} \tag{S.38}$$

met $$G = v_g \Gamma g = \frac{c}{n_g}\Gamma g \qquad \text{en} \qquad G_N = \frac{\partial G}{\partial N} \tag{S.39}$$

Hier is g de materiaalwinst in de actieve sectie, Γ de opsluitingsfactor, v_g de groepssnelheid en $V_a = Lwd$ het volume van de kernlaag (cfr. §S.3.1). Verder is I de DC instelstroom en I_{th} de drempelstroom. De demping is anderzijds:

$$\gamma = \frac{1}{\tau_d} + \left(\frac{1}{G}G_N + \varepsilon_S V_a\right)\frac{I - I_{th}}{qV_a} = \frac{1}{\tau_d} + \left(\frac{1}{G} + \frac{\varepsilon_S V_a}{G_N}\right)\Omega_r^2 \tag{S.40}$$

τ_d is de differentiële levensduur van de ladingsdragers (zie o.a. (S.14)):

$$\frac{1}{\tau_d} = A + 2BN + 3CN^2 \tag{S.41}$$

en ε_S de winstonderdrukkingsfactor die de daling van de winst bij hoge aantallen fotonen S in rekening brengt [45]-[46], [61]:

$$\varepsilon_S = -\frac{1}{G}\frac{\partial G}{\partial S} \tag{S.42}$$

Zowel het kwadraat van de resonantiefrequentie als de demping stijgen lineair met de stroom. Ver boven de drempel geldt bovendien:

$$\gamma \approx K f_r^2 \tag{S.43}$$

Het tweede-orde systeem (S.37) zal een maximale bandbreedte f_{max} bereiken wanneer [70]-[71]:

$$\gamma = 2\pi\sqrt{2} f_r \tag{S.44}$$

wat voor de maximale bandbreedte volgende uitdrukking geeft:

$$f_{max} = \frac{2\pi\sqrt{2}}{K} \tag{S.45}$$

Wordt de stroom I opgedreven voorbij het punt waar (S.44) geldt, dan daalt de bandbreedte opnieuw lichtjes en verzadigt deze uiteindelijk bij $2\pi/K$.

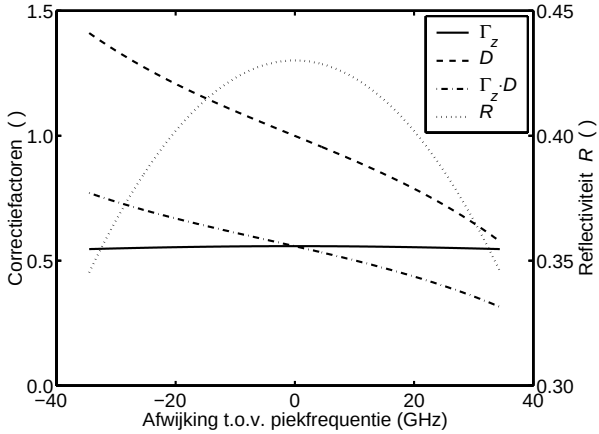

Figuur S.27 Invloed van een verschil in afstemming tussen de lasermode en de reflectiepiek van de DBR op de modulatie-eigenschappen van een DBR laser. Longitudinale opsluitingsfactor Γ_z en verstemmingsfactor D als functie van het frequentieverschil. Als referentie is ook de reflectiviteit R van de Bragg-reflector weergegeven.

Voor een DBR laser worden de uitdrukkingen voor de demping en de resonantiefrequentie:

$$\Omega_r^2 \approx \Gamma_z D \cdot G_N \frac{I_s - I_{th}}{qV_a} \qquad \gamma \approx \frac{1}{\tau_d} + \left(\frac{1}{\Gamma_z G_s} + \frac{\varepsilon_S V_a}{G_N} \right) \frac{\Omega_r^2}{D} \tag{S.46}$$

Ten opzichte van (S.38) en (S.40) zijn er twee correctiefactoren. De eerste is een soort longitudinale opsluitingsfactor:

$$\Gamma_z = \frac{n_{g,a} L_a}{n_{g,a} L_a + n_{g,p} L_p + n_{g,d} L_{eff,d}} \tag{S.47}$$

waarin $n_{g,x}$ de groepsindex en L_x de lengte van sectie x is (a = actief, p = fase, d = DBR). $L_{eff,d}$ is de effectieve lengte van de DBR sectie, gedefinieerd als:

$$L_{eff,d} = -\frac{c}{2n_{g,d}} \frac{\partial \arg(r_{DBR})}{\partial \omega} \tag{S.48}$$

De andere factor is de verstemmingsfactor:

$$D \approx 1 + \alpha_H x \qquad \text{met} \qquad x = \frac{c\Gamma_z}{2n_{g,a} L_a} \frac{\partial \ln(|r_{DBR}|)}{\partial \omega} \tag{S.49}$$

α_H is de alfafactor (S.2) (typisch 3 tot 6 voor actief materiaal) en x is een factor evenredig met de helling van de reflectiecoëfficiënt bij de laserfrequentie. Is de laserfrequentie lager dan de frequentie van de reflectiepiek dan is x positief en zal de factor D er bijgevolg voor zorgen dat de resonantiefrequentie toeneemt (Figuur S.27). De resonantiefrequentie blijft wel lager dan voor de één-sectie laser, aangezien $\Gamma_z \cdot D < 1$. De K-factor van de DBR laser kan echter lager worden dan die van de één-sectie laser, omwille van de factor D in de noemer. Dit betekent met

andere woorden dat de maximale bandbreedte f_{max} van een DBR laser groter kan worden dan die van een vergelijkbare DFB laser, mits de lasermode voldoende ver beneden de piekfrequentie van de DBR afgestemd wordt [72]-[73]. In het algemeen zal een afstembare laser echter aangestuurd worden in een werkingspunt waar de lasermode zo dicht mogelijk bij de reflectiepiek ligt om de zijmode-onderdrukking te maximaliseren (cfr. §S.4 en §S.5), zodat D ongeveer gelijk zal zijn aan 1. Deze resultaten kunnen vrij eenvoudig uitgebreid worden naar SG-DBR, SSG-DBR en GCSR lasers.

De eerder gegeven uitdrukkingen voor de klein-signaalrespons houden geen rekening met de eventuele parasitaire capaciteit van de diodestructuur, noch met de eventuele zelfinductie van de verbindingsdraad. Dergelijke parasitairen zorgen ervoor dat de eigenlijke klein-signaalrespons beter beschreven wordt door het produkt van (S.37) met de transferfunctie van een eerste-orde (RC) laagdoorlaatfilter:

$$H_{RC}(\Omega) = \frac{\Omega_{RC}}{j\Omega + \Omega_{RC}} \tag{S.50}$$

De maximale bandbreedte wordt dan:

$$f_{max} = \frac{\Omega_{RC}}{2\pi} < \frac{2\pi\sqrt{2}}{K} \tag{S.51}$$

Zelfs indien de parasitairen verwaarloosbaar zijn, kan de maximale bandbreedte (S.45) vaak niet bereikt worden omwille van thermische effecten [74]. De warmte gegenereerd door de stroom I kan ervoor zorgen dat de resonantiefrequentie verzadigt op een waarde $f_{r,therm}$, zodat de maximale bandbreedte gegeven wordt door:

$$f_{max} = \sqrt{1+\sqrt{2}}\, f_{r,therm} \tag{S.52}$$

Relatieve intensiteitsruis

De relatieve intensiteitsruis (relative intensity noise, RIN) is gedefinieerd als de verhouding van de spectrale dichtheid van de intensiteitsfluctuaties tot het kwadraat van de gemiddelde intensiteit. Men kan aantonen dat het RIN-spectrum van een laserdiode beschreven wordt door:

$$RIN(\Omega) = A\,\frac{\Omega^2 + \tilde{\gamma}^2}{\left(\Omega_r^2 - \Omega^2\right)^2 + \gamma^2\Omega^2} \tag{S.53}$$

waarbij Ω_r en γ dezelfde waarden aannemen als in de klein-signaalrespons. Het is vaak eenvoudiger om de resonantiefrequentie en de demping af te leiden uit metingen van het RIN-spectrum dan uit rechtstreekse metingen van de AM-respons [74]. Voor RIN-metingen moet immers enkel een DC stroom aangelegd worden. Bovendien hangen de RIN-spectra enkel af van de parameters van de intrinsieke laserdiode en worden ze niet beïnvloed door parasitairen.

Groot-signaal digitale modulatie

De klein-signaalbandbreedte geeft een eerste indicatie van de bitsnelheden die met een gegeven laserdiode kunnen behaald worden door directe modulatie. Het gedrag bij groot-signaalmodulatie wordt echter ook nog door andere parameters beïnvloed.

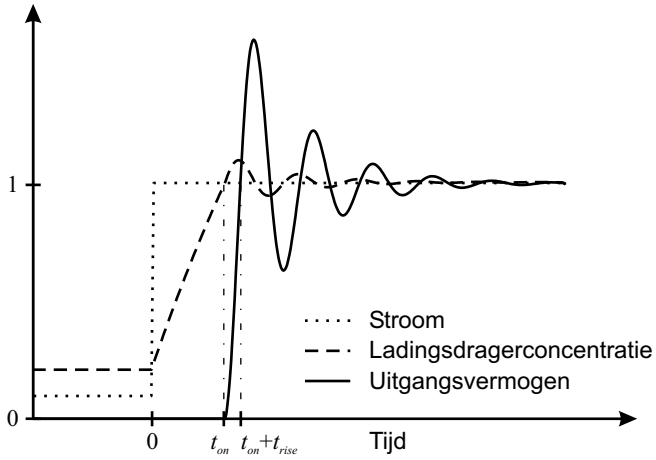

Figuur S.28 Groot-signaalmodulatie van een laserdiode. Evolutie van de stroom, de ladingsdragerconcentratie en het uitgangsvermogen wanneer de laser aangeschakeld wordt van onder de drempel (op $t = 0$). De diverse grootheden werden genormaliseerd t.o.v. hun uiteindelijke waarden.

In dit geval wordt de stroom door de actieve sectie geschakeld tussen twee niveaus, I_0 en I_1, waardoor het uitgangsvermogen varieert van P_0 tot P_1. Een goede instelling van de stroom I_0 is belangrijk. Idealiter zou het vermogen voor een 0-bit zo laag mogelijk zijn. Wordt een laserdiode echter aangeschakeld van stroom I_0 onder de drempel I_{th}, dan begint het uitgangsvermogen pas toe te nemen na een zekere vertraging t_{on} (typisch enkele nanoseconden) omdat eerst een voldoend hoge ladingsdragerconcentratie moet opgebouwd worden. Een dergelijke vertraging is onaanvaardbaar voor transmissie aan snelheden van enkele Gbit/s. Bovendien ontstaan zeer grote variaties in de ladingsdragerconcentratie, wat betekent dat de brekingsindex en dus ook de frequentie sterk zal fluctueren. Dit kan vaak zelfs een verlaagde zijmode-onderdrukking tot gevolg hebben. Grote frequentiefluctuaties hebben zoals reeds vermeld een nadelig effect op de bereikbare transmissieafstand omwille van de dispersie.

Anderzijds mag I_0 niet te groot gekozen worden aangezien een kleine extinctieverhouding P_1/P_0 een nadelige invloed heeft op het vermogenbudget van een glasvezelverbinding [75]. Uiteindelijk blijkt een extinctieverhouding van 10 dB een goed compromis op te leveren.

S.6.2 Resultaten voor SSG-DBR lasers

RIN-metingen

RIN-metingen werden uitgevoerd op een SSG-DBR laser voor 84 frequentiekanalen, van 191.90 tot 196.05 THz met 50 GHz kanaalafstand. Figuur S.29 toont de drempelstroom $I_{a,th}$ en de afstemstromen voor deze kanalen, die bekomen werden met behulp van het algoritme in §S.5.4. Voor elk kanaal werden RIN-spectra gemeten bij volgende stroomwaarden:

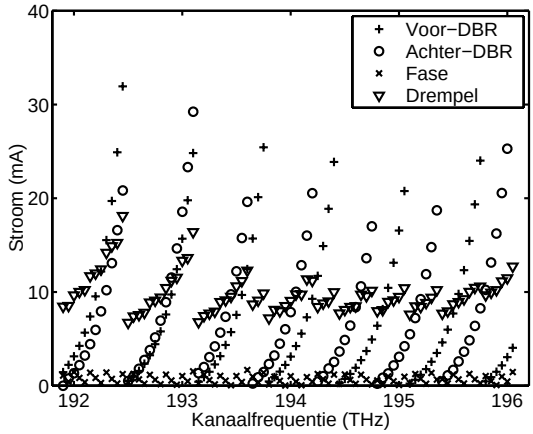

Figuur S.29 Stroominstellingen voor RIN-metingen voor 84 kanalen (50 GHz afstand) van een SSG-DBR laser.

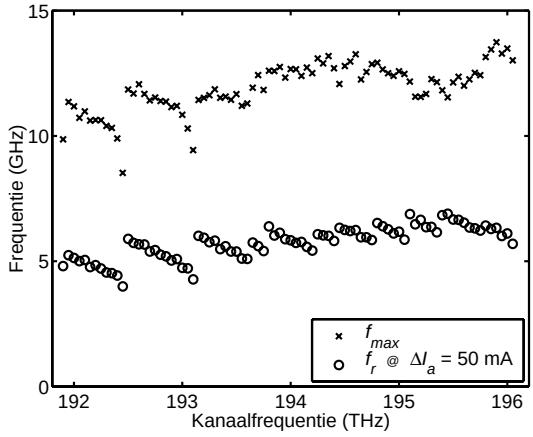

Figuur S.30 Maximale intrinsieke modulatiebandbreedte f_{max} en resonantiefrequentie f_r bij een instelstroom 50 mA boven de drempelstroom, voor alle 84 kanalen (50 GHz afstand).

$$I_a = I_{a,th} + \Delta I_a = I_{a,th} + \left(\frac{k}{10}\right)^2 \cdot 60\,\text{mA} \qquad k = 1, 2, \ldots, 10 \qquad \text{(S.54)}$$

Uit alle RIN-spectra werd de resonantiefrequentie en de demping bepaald door curve-aanpassing. Vervolgens werd voor ieder kanaal de demping uitgezet als functie van het kwadraat van de resonantiefrequentie, zodat de *K*-factor kon berekend worden door de best passende rechte door de meetpunten te bepalen. Figuur S.30 toont de geëxtraheerde waarden voor de maximale intrinsieke modulatiebandbreedte f_{max} en de resonantiefrequentie f_r bij een instelstroom 50 mA boven de drempelstroom.

Voor bijna alle kanalen ligt de maximale bandbreedte boven 10 GHz. De minimale waarde is ongeveer 8 GHz, voor het 192.45 THz kanaal. Dit zou erop kunnen wijzen dat directe modulatie aan 10 Gbit/s – in theorie althans – mogelijk moet zijn. Anderzijds is de resonantiefrequentie bij een instelstroom 50 mA boven de drempelstroom gemiddeld slechts 5.5 GHz, en varieert deze tussen 4.0 GHz en 6.9 GHz. Directe modulatie bij 2.488 Gbit/s zou zeker mogelijk moeten zijn, indien de parasitaire capaciteit en zelfinductie voldoende laag gehouden worden.

De variaties in de resonantiefrequentie kunnen verklaard worden door variaties in de differentiële winst G_N (cfr. (S.46)). Wanneer de ladingsdragerconcentratie in de actieve sectie verhoogd wordt, zal de globale winst toenemen, maar tegelijkertijd zal de winstpiek ook verschuiven naar hogere frequenties. Dit betekent dat bij een gegeven concentratie de differentiële winst toeneemt met de optische frequentie. Anderzijds zal de differentiële winst bij een gegeven optische frequentie dalen met toenemende ladingsdragerconcentratie. Vergelijkt men Figuur S.29 met Figuur S.30 dan valt onmiddellijk de sterke correlatie op tussen de drempelstroom en de resonantiefrequentie. Naarmate de drempel toeneemt, stijgt de ladingsdrager-concentratie in de actieve sectie en daalt de differentiële winst. Bijgevolg zal de resonantiefrequentie bij een gegeven stroomniveau ΔI_a boven de drempel afnemen. De globale stijgende trend van f_r is uiteraard te wijten aan de toename van de differentiële winst met de optische frequentie.

De correlatie tussen de maximale bandbreedte en de drempelstroom is niet zo duidelijk. Uit (S.45) en (S.46) kan men afleiden dat:

$$f_{max} = \frac{D\sqrt{2}}{2\pi}\left(\frac{1}{\Gamma_z G} + \frac{\varepsilon_S V_a}{G_N}\right)^{-1} \tag{S.55}$$

Wanneer de drempelstroom stijgt, neemt de winst G toe maar daalt de differentiële winst G_N. Het netto effect op f_{max} hangt bijgevolg af van de verhouding van de twee termen tussen de haken.

Groot-signaalmodulatie

Voor de groot-signaalmetingen werd volgende procedure gevolgd. De laser werd afgestemd op een bepaald kanaal met een relatief hoge instelstroom voor de actieve sectie. Vervolgens werd een datasignaal met een amplitude van 60 mA toegevoegd aan de instelstroom. Het datasignaal bestond uit een $2^{23} - 1$ pseudo-random bitsequentie (PRBS). Het gemoduleerde optische signaal werd geleid naar een optische ontvanger en het resulterende elektrische signaal werd afgebeeld op een oscilloscoop met hoge bandbreedte. Aan de hand van het oscilloscoopbeeld werd de instelstroom bijgeregeld tot een extinctieverhouding van 10 dB bekomen werd. Met een stroommodulatie van 60 mA betekent dit dat de instelstroom voor een gegeven frequentiekanaal ongeveer 30 mA boven de drempelstroom voor dat kanaal ligt.

Parasitairen beperkten de klein-signaalbandbreedte in onze opstelling tot ongeveer 750 MHz. Daarom werd de bitsnelheid beperkt tot 1.244 Gbit/s. Metingen werden uitgevoerd voor 20 kanalen met 200 GHz spatiëring, van 191.9 tot 195.7 THz. Een typisch oogdiagram dat op deze manier bekomen werd is afgebeeld in Figuur S.31. Merk op dat geen relaxatie-oscillaties zichtbaar zijn (cfr. Figuur S.28) omdat de optische ontvanger een vierde-orde Bessel-Thompson filter met een afsnijfrequentie van 1.88 GHz bevat.

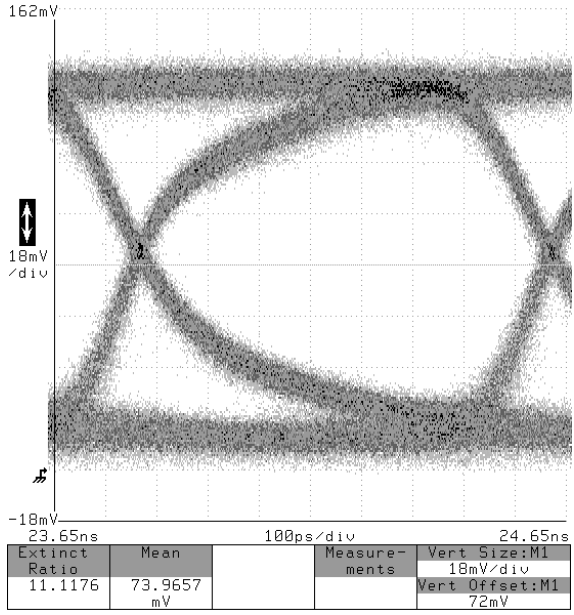

Figuur S.31 Oogdiagram gemeten voor een SSG-DBR laser gemoduleerd aan 1.244 Gbit/s. Parasitairen beperkten de klein-signaalbandbreedte tot ongeveer 0.75 GHz. De relaxatie-oscillaties werden onderdrukt door een vierde-orde Bessel-Thompson filter met een afsnijfrequentie van 1.88 GHz in de ontvanger.

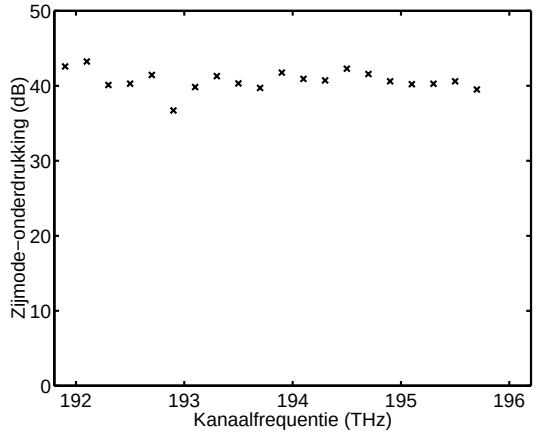

Figuur S.32 Zijmode-onderdrukking met directe modulatie bij 1.244 Gbit/s, voor 20 kanalen (200 GHz afstand) van een SSG-DBR laser.

De zijmode-onderdrukking met directe modulatie voor de 20 beschouwde kanalen is weergegeven in Figuur S.32. De minimale waarde is 35 dB, wat erop wijst dat deze SSG-DBR lasers in principe geschikt zijn voor transmissie gebruik makend van directe modulatie.

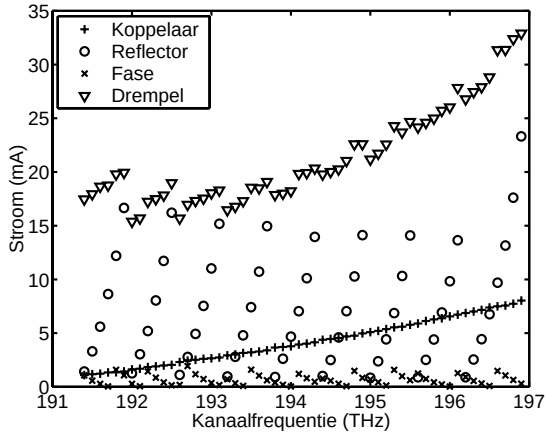

Figuur S.33 Stroominstellingen voor RIN-metingen voor 56 kanalen (100 GHz afstand) van een GCSR laser.

Meer uitvoerige transmissie-experimenten werden recent uitgevoerd door de fabrikant van deze lasers, NTT in Japan, waaruit bleek dat transmissie aan 2.5 Gbit/s mogelijk is tot afstanden van ongeveer 80 km.

S.6.3 Resultaten voor GCSR lasers

RIN-metingen

In dit geval werden RIN-metingen uitgevoerd voor 56 frequentiekanalen met 100 GHz spatiëring, van 191.5 tot 196.9 THz. De afstemstromen voor deze kanalen zijn weergegeven in Figuur S.33. Voor elk kanaal werden RIN-spectra gemeten als functie van de stroom door de actieve sectie. Vervolgens werden de resonantiefrequentie en de demping geëxtraheerd en werd de maximale intrinsieke bandbreedte f_{max} berekend. De resultaten zijn uitgezet in Figuur S.34. De afgeleide waarden voor f_{max} zijn over het algemeen iets lager dan voor de SSG-DBR laser, al liggen ze nog steeds alle boven 8 GHz. De lagere bandbreedte kan allicht verklaard worden door de grotere effectieve lengte van de passieve secties in de GCSR laser (cfr. (S.46)-(S.47)). Een gedetailleerde vergelijking is echter moeilijk aangezien de GCSR lasers en SSG-DBR lasers een verschillende samenstelling van de actieve sectie hebben, wat uiteraard zijn invloed heeft op de (differentiële) winst.

Bij een instelstroom die 50 mA boven de drempel ligt is de resonantiefrequentie f_r voor alle kanalen ongeveer gelijk aan 5 GHz. Dit kan waarschijnlijk verklaard worden door het feit dat de toename van de differentiële winst G_N met de optische frequentie grotendeels gecompenseerd wordt door de afname van G_N als gevolg van de stijgende drempelstroom.

De belangrijkste conclusie is echter dat ook voor deze laser directe modulatie aan 2.488 Gbit/s mogelijk moet zijn.

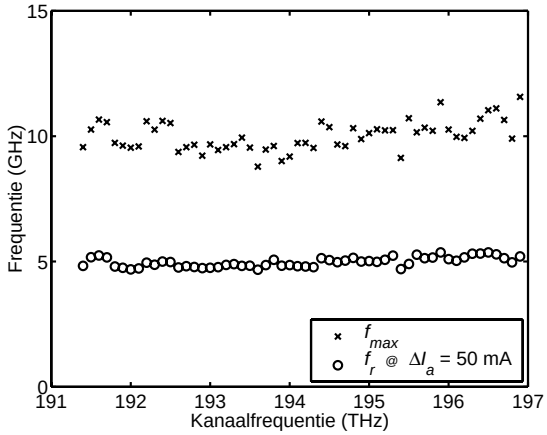

Figuur S.34 Maximale intrinsieke modulatiebandbreedte f_{max} en resonantiefrequentie f_r bij een instelstroom 50 mA boven de drempelstroom, voor alle 56 kanalen (100 GHz afstand).

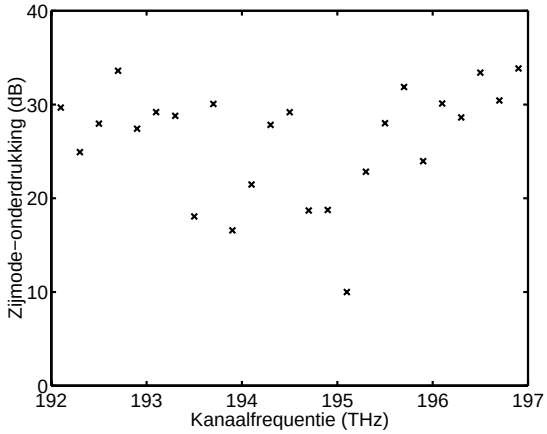

Figuur S.35 Zijmode-onderdrukking met directe modulatie bij 1.244 Gbit/s, voor 25 kanalen (200 GHz afstand) van een SSG-DBR laser. De afstemstromen werden manueel geoptimaliseerd om een zo hoog mogelijke zijmode-onderdrukking te bekomen bij een extinctieverhouding van 10 dB.

Groot-signaalmodulatie

Voor groot-signaalmetingen werd grotendeels dezelfde procedure gevolgd als voor de SSG-DBR laser. Ook in dit geval beperkten parasitairen de klein-signaalbandbreedte tot ongeveer 750 MHz, zodat de bitsnelheid opnieuw beperkt werd tot 1.244 Gbit/s. Metingen werden uitgevoerd voor 25 kanalen met 200 GHz afstand, van 192.1 tot 196.9 THz. Een belangrijk verschil was dat met een extinctieverhouding van 10 dB in een aantal kanalen een zeer lage zijmode-onderdrukking gemeten werd, zelfs nadat de afstemstromen manueel geoptimaliseerd werden (Figuur S.35). Dit is allicht te wijten aan de kleinere

modespatiëring in deze lasers. De variaties in de ladingsdragerconcentratie bij het aan- en uitschakelen van de laser (Figuur S.28) kunnen er dan voor zorgen dat gedurende deze transities een zijmode kortstondig de lasermode wordt.

S.7 Algemeen besluit

Het onderzoek op afstembare laserdiodes heeft reeds een vrij lange geschiedenis (meer dan 20 jaar, cfr. §S.2). Nochtans werden dergelijke lasers tot voor kort niet geschikt geacht voor toepassingen in de optische communicatie: ze waren te moeilijk te controleren en zouden nooit kunnen voldoen aan de strenge eisen die gesteld worden aan componenten voor telecommunicatiesystemen. Recente onderzoeksresultaten – waaronder deze gepresenteerd in dit werk – hebben echter het tegendeel bewezen. Vandaag worden dergelijke lasers als essentieel beschouwd voor de ontwikkeling van de volgende generatie van optische communicatiesystemen (§S.1).

De sleutel voor dit succes ligt in het feit dat de laser niet afzonderlijk geleverd wordt, maar daarentegen geïntegreerd is in een module samen met de nodige controle-elektronica. Deze vormt een interface tussen het externe systeem en de laser, en vertaalt de frequentie- en uitgangsvermogenvereisten naar de gepaste waarden van de stuurstromen. Daartoe wordt een opzoektabel met werkingspunten voor alle frequentiekanalen opgeslagen in een semi-permanent geheugen. In §S.5 beschreven we drie methodes die kunnen gebruikt worden om een dergelijke tabel snel en efficiënt te genereren. Met de beste methode (§S.5.4) kon een tabel gegenereerd worden met frequentie-afwijkingen van minder dan ±0.5 GHz.

Om stabiliteit en nauwkeurigheid op lange termijn te garanderen kan men een feedback-controlesysteem toevoegen, zoals besproken in §S.4. Als ondersteuning van het ontwikkelingswerk beschreven in §S.4 en §S.5 werd ook een simulatiemodel voor longitudinaal geïntegreerde afstembare lasers opgebouwd (§S.3). Berekeningsresultaten van dit model werden doorheen het proefschrift gebruikt om experimentele resultaten te verklaren en/of bevestigen. In §S.6 werden tenslotte de modulatie-eigenschappen van afstembare lasers geanalyseerd. Daaruit bleek dat transmissie aan 2.5 Gbit/s in principe mogelijk moet zijn met een direct gemoduleerde afstembare laserdiode.

Referenties

Algemene referenties

[1] "Internet traffic tops 350000 Tbytes per month," *Lightwave Magazine*, vol. 17, no. 8, July 2000. <http://lw.pennnet.com/>

[2] International Telecommunication Union – Telecommunication Standardization Sector (ITU-T), Recommendation G.692: "Optical interfaces for multichannel systems with optical amplifiers," *Series G: Transmission systems and media, digital systems and networks (Transmission media characteristics – Characteristics of optical components and sub-systems)*, October 1998.

[3] Lucent Technologies WaveStar OLS 400G. <http://www.lucent.com/>

[4] Nortel Networks OPTera LH. <http://www.nortelnetworks.com/>

[5] L. Kazowsky, S. Benedetto, and A.E. Willner, *Optical fiber communication systems*, Artech House, Norwood, MA, USA, 1996.

[6] R. Plastow, "Emerging tunable laser applications in optical networks," *Lightwave Magazine*, vol. 17, no. 3, March 2000. <http://lw.pennnet.com/>

[7] E. Zouganeli, "Tunable lasers route optical signals," *WDM Solutions – a supplement to Laser Focus World*, vol. 2, no. , pp. 26, June 2000.

[8] P. Rigby, "Network trials tune in to wavelength routing," *FibreSystems*, vol. 4, no. 6, pp. 35-40, July 2000.

[9] I.M. White, Y. Fukashiro, K. Shrikhande, D. Wonglumsom, M.S. Rogge, M. Avenarius, and L.G. Kazovsky, "Experimental demonstration of a media access protocol for HORNET: a WDM multiple acces metropolitan area ring network," *Proceedings Conference on Optical Fiber Communications 2000*, paper WD3, Baltimore, MD, USA, March 2000.

[10] R. Pease, "HORNET creates a new buzz in the use of tunable laser technology," *Lightwave Magazine*, vol. 17, no. 8, July 2000. <http://lw.pennnet.com/>

[11] M.-C. Amann, and J. Buus, *Tunable laser diodes*, Artech House, Norwood, MA, USA, 1998.

[12] B.R. Bennett, R.A. Soref, and J.A. Del Alamo, "Carrier-induced change in refractive index of InP, GaAs and InGaAsP," *IEEE J. Quantum Electron.*, vol. 26, no. 1, pp. 113-122, January 1990.

[13] J.-P. Weber, "Optimization of the carrier-induced effective index change in InGaAsP waveguides - Application to tunable Bragg filters," *IEEE J. Quantum Electron.*, vol. 30, no. 8, pp. 1801-1816, August 1994.

[14] A. Sneh, and C.R. Doerr, "Indium Phosphide-based photonic circuits and components," *Chapter 7 in Integrated optical circuits and components*, ed. E.J. Murphy, Marcel Dekker, New York, NY, USA, 1999.

[15] J.E. Zucker, "Linear and quadratic electro-optic coefficients in InGaAsP," *in Properties of lattice-matched and strained Indium Gallium Arsenide*, ed. P. Bhattacharya, INSPEC, the Institution of Electrical Engineers, London, UK, 1993.

[16] H. Yamamoto, M. Asada, and Y. Suematsu, "Electric-field-induced refractive index variation in quantum-well structure," *Electron. Lett.*, vol. 21, no. 13, pp. 579-580, June 1985.

[17] N. Susa, and T. Nakahara, "Enhancement of change in refractive index in asymmetric quantum well," *Appl. Phys. Lett.*, vol. 60, no. 20, pp. 2457-2459, May 1992.

[18] P.-J. Rigole, S. Nilsson, L. Bäckbom, T. Klinga, J. Wallin, B. Stålnacke, E. Berglind, and B. Stoltz, "Access to 20 evenly distributed wavelengths over 100 nm using a single current tuning in a four-electrode monolithic semiconductor laser," *IEEE Photon. Technol. Lett.*, vol. 7, no. 11, pp. 1249-1251, November 1995.

[19] H. Ishii, Y. Tohmori, Y. Yoshikuni, T. Tamamura, and Y. Kondo, "Multiple-phase-shift super structure grating DBR lasers for broad wavelength tuning," *IEEE Photon. Technol. Lett.*, vol. 5, no. 6, pp. 613-615, June 1993.

[20] M.-C. Amann, and R. Schimpe, "Excess linewidth broadening in wavelength-tunable laser diodes," *Electron. Lett.*, vol. 26, no. 5, pp. 279-280, March 1990.

[21] M.-C. Amann, S. Illek, and H. Lang, "Linewidth reduction in wavelength tunable laser diodes by voltage control," *Electron. Lett.*, vol. 27, no. 6, pp. 531-532, March 1991.

[22] M. Okuda, and K. Onaka, "Tunability of distributed Bragg-reflector laser by modulating refractive index in corrugated waveguide," *Jpn. J. Appl. Phys.*, vol. 16, pp. 1501-1502, 1977.

[23] H. Kogelnik, and C.V. Shank, "Coupled-wave theory of distributed feedback lasers," *J. Appl. Phys.*, vol. 43, no. 5, pp. 2327-2335, March 1972.

[24] F. Delorme, S. Slempkes, G. Alibert, B. Rose, and J. Brandon, "Butt-jointed DBR laser with 15 nm tunability grown in three MOVPE steps," *Electron. Lett.*, vol. 31, no. 15, pp. 1244-1245, July 1995.

[25] F. Delorme, S. Grosmaire, A. Gloukhian, and A. Ougazzaden, "High power operation of widely tunable 1.55 µm distributed Bragg-reflector lasers," *Electron. Lett.*, vol. 33, no. 3, pp. 210-211, January 1997.

[26] L.A. Coldren, "Multi-section tunable laser with differing multi-element mirrors," *US Patent*, no. 4,896,325, January 1990.

[27] V. Jayaraman, Z.-M. Chuang, and L.A. Coldren, "Theory, design and performance of extended tuning range semiconductor lasers with sampled gratings," *IEEE J. Quantum Electron.*, vol. 29, no. 6, pp. 1824-1834, June 1993.

[28] H. Ishii, F. Kano, Y. Tohmori, Y. Kondo, T. Tamamura, and Y. Yoshikuni, "Narrow spectral linewidth under wavelength tuning in thermally tunable super-structure-grating (SSG) DBR lasers," *IEEE J. Selected Topics Quantum Electron.*, vol. 1, no. 2, pp. 401-407, June 1995.

[29] J. Willems, *Modeling and design of integrated optical filters and lasers with a broad wavelength tuning range*, Ph.D. Thesis, University of Gent, January 1995.

[30] J. Willems, G. Morthier, and R. Baets, "Novel widely tunable integrated optical filter with high spectral selectivity," *Proc. ECOC '92*, pp. 413-416, paper WeB9.2, Berlin, Germany, September 1992.

[31] J. Willems, and R. Baets, "Integrated tunable optical filter," *European Patent*, no. EP 0613571 B1, filed September 17, 1993, published July 29, 1998.

[32] M. Öberg, S. Nilsson, K. Streubel, L. Bäckbom, and T. Klinga, "74 nm wavelength tuning range of an InGaAsP/InP vertical grating assisted codirectional coupler laser with rear sampled grating reflector," *IEEE Photon. Technol. Lett.*, vol. 5, no. 7, pp. 735-738, July 1993.

[33] F. Delorme, "Widely tunable 1.55 µm lasers for wavelength-division-multiplexed optical fiber communications," *IEEE J. Quantum Electron.*, vol. 34, no. 9, pp. 1706-1716, September 1998.

[34] Commercial DBR laser, Alcatel Optronics, Route de Villejust, 91625 Nozay Cedex, France. <http://www.alcatel.com/telecom/optronics/>

[35] F. Delorme, G. Alibert, C. Ougier, S. Slempkes, and H. Nakajima, "Sampled grating DBR lasers with 101 wavelengths over 44 nm and optimised power variation for WDM applications," *Electron. Lett.*, vol. 34, no. 3, pp. 279-281, February 1998.

[36] D.J. Robbins, N.D. Whitbread, P.J. Williams, and J.R. Rawsthorne, "Sampled grating DBR lasers for WDM systems," *Proc. 1998 IEE Colloquium on Multiwavelength Optical Networks: Devices, Systems and Network*, pp. 9/1-9/4, London, UK, June 1998.

[37] Commercial SG-DBR tunable laser, Marconi Caswell Ltd., Caswell, Towcester, Northants NN12 8EQ, UK. <http://www.caswelltechnology.com/>

[38] M. Öberg, P.-J. Rigole, S. Nilsson, T. Klinga, L. Bäckbom, K. Streubel, J. Wallin, and T. Kjellberg, "Complete single mode wavelength coverage over 40 nm with a super structure grating DBR laser," *J. Lightwave Technol.*, vol. 13, no. 10, pp. 1892-1897, October 1995.

[39] H. Ishii, H. Tanobe, F. Kano, Y. Tohmori, Y. Kondo, and Y. Yoshikuni, "Broad-range wavelength coverage (62.4 nm) with superstructure-grating DBR laser," *Electron. Lett.*, vol. 32, no. 5, pp. 454-455, February 1996.

[40] Commercial SSG-DBR laser, NTT Electronics Corporation, 3-1 Morinosato Wakamiya, Atsugi-shi 243-0198, Kanagawa, Japan. <http://www.nel.co.jp/>

[41] P.-J. Rigole, S. Nilsson, L. Bäckbom, B. Stålnacke, T. Klinga, E. Berglind, B. Stoltz, D.J. Blumenthal, and M. Shell, "Wavelength coverage over 67 nm with a GCSR laser. Tuning characteristics and switching speed.," *Proc. XV IEEE Int. Semiconductor Laser Conference*, pp. 125-126, paper W1.1, Haifa, Israel, October 1996.

[42] P.-J. Rigole, S. Nilsson, L. Bäckbom, B. Stålnacke, E. Berglind, J.-P. Weber, and B. Stoltz, "Quasi-continuous tuning range from 1560 to 1520 nm in a GCSR laser, with high power and low tuning currents," *Electron. Lett.*, vol. 32, no. 25, pp. 2352-2354, December 1996.

[43] Commercial GCSR laser, ADC / Altitun, P.O. Box 911, Bruttovägen 7, SE-175 29 Järfälla-Stockholm, Sweden. <http://www.altitun.com/>

[44] X. Pan, H. Olesen, and B. Tromborg, "A theoretical model of multielectrode DBR lasers," *IEEE J. Quantum Electron.*, vol. 24, no. 12, pp. 2423-2432, December 1988.

[45] G.P. Agrawal, and N.K. Dutta, *Long-wavelength semiconductor lasers*, Van Nostrand Reinhold, New York, NY, USA, 1986.

[46] K. Petermann, *Laser diode modulation and noise*, Kluwer Academic Publishers, Dordrecht, Holland, 1988.

[47] G. Björk, and O. Nilsson, “A new exact and efficient numerical matrix theory of complicated laser structures: properties of asymmetric phase-shifted DFB lasers,” *J. Lightwave Technol.*, vol. 5, no. 1, pp. 140-146, January 1987.
[48] M. Yamada, and K. Sakuda, “Analysis of almost-periodic distributed feedback slab waveguides via a fundamental matrix approach,” *Appl. Optics*, vol. 26, no. 16, pp. 3474-3478, August 1987.
[49] T. Makino, “Transfer-matrix formulation of spontaneous emission noise of DFB semiconductor lasers,” *J. Lightwave Technol.*, vol. 9, no. 1, pp. 84-91, January 1991.
[50] Fabry-Perot Wavelength Locker (FPWL), E-Tek Dynamics Inc., 1865 Lundy Avenue, San Jose, CA 95131, USA. <http://www.e-tek.com/>
[51] K.R. Preston, “Simple spectral control technique for external cavity laser transmitters,” *Electron. Lett.*, vol. 18, no. 25, pp. 1092-1094, December 1982.
[52] N.A. Olsson, W.T. Tsang, and R.A. Logan, “Active spectral stabilisation of cleaved-coupled-cavity (C3) lasers,” *J. Lightwave Technol.*, vol. 2, no. 1, pp. 49-51, February 1984.
[53] S.L. Woodward, I.M.I. Habbab, T.L. Koch, and U. Koren, “The side-mode-suppression ratio of a tunable DBR laser,” *IEEE Photon. Technol. Lett.*, vol. 2, no. 12, pp. 854-856, December 1990.
[54] S.L. Woodward, T.L. Koch, and U. Koren, “A control loop which ensures high side-mode-suppression ratio in a tunable DBR laser,” *IEEE Photon. Technol. Lett.*, vol. 4, no. 5, pp. 417-419, May 1992.
[55] H. Ishii, H. Yasaka, H. Tanobe, and Y. Yoshikuni, “Wavelength stabilisation of a three-electrode distributed Bragg-reflector laser with longitudinal mode control,” *Electron. Lett.*, vol. 33, no. 6, pp. 494-496, March 1997.
[56] H. Ishii, F. Kano, Y. Yoshikuni, and H. Yasaka, “Mode stabilisation method for superstructure-grating DBR lasers,” *J. Lightwave Technol.*, vol. 13, no. 3, pp. 433-442, March 1998.
[57] I. Maio, G.P. Bava, I. Montrosset, “Mode competition and switching in three section DBR tunable lasers,” *IEE Proc.-Optoelectron.*, vol. 138, no. 1, pp. 52-56, February 1991.
[58] P. Ottolenghi, S. Benedetto, and I. Montrosset, “Switching and optical modulation of three-section DBR lasers,” *IEEE J. Quantum Electron.*, vol. 60, no. 6, pp. 1381-1388, June 1994.
[59] T. Farrell, J. Dunne, and R. O'Dowd, “Complete wavelength control of GCSR lasers over EDFA band,” *Proc. LEOS '99*, pp. 329-330, paper TuY1, San Francisco, CA, USA, November 1999.
[60] HP86120B multi-wavelength meter, Agilent Technologies – Test & Measurement, 5301 Stevens Creek Blvd., Santa Clara, CA 95052, USA. < http://www.tm.agilent.com/>
[61] G. Morthier, and P. Vankwikelberge, *Handbook of distributed feedback laser diodes*, Artech House, Norwood, MA, 1997.
[62] F. Kano, M. Fukuda, K. Sato, and K. Oe, “High-speed intensity modulation of 1.5 µm DBR lasers with wavelength tuning,” *IEEE J. Quantum Electron.*, vol. 26, no. 8, pp. 1340-1346, August 1990.
[63] F. Delorme, S. Slempkes, D. Mathoorasing, and J.-C. Bouley, “High speed and high density wavelength multichannel butt-jointed DBR lasers,” *Electron. Lett.*, vol. 27, no. 21, pp. 1969-1971, October 1991.
[64] J.C. Cartledge, “Accessible tuning range of direct intensity modulated three-section DBR lasers in WDM applications,” *J. Lightwave Technol.*, vol. 14, no. 3, pp. 480-4853, March 1996.
[65] C. Ougier, A. Talneau, F. Delorme, Y. Raffle, J. Landreau, and D. Mathoorasing, “Sampled-grating DBR lasers with 80 addressable wavelengths over 33 nm for 2.5 Gbit/s WDM applications,” *Electron. Lett.*, vol. 32, no. 17, pp. 1592-1593, August 1996.
[66] S.-L. Lee, D.A. Tauber, V. Jayaraman, M.E. Heimbuch, L.A. Coldren, and J.E. Bowers, “Dynamic responses of widely tunable sampled grating DBR lasers,” *IEEE Photon. Technol. Lett.*, vol. 8, no. 12, pp. 1597-1599, December 1996.
[67] B. Mason, S.-L. Lee, M.E. Heimbuch, and L.A. Coldren, “Directly modulated sampled grating DBR lasers for long-haul WDM communication systems,” *IEEE Photon. Technol. Lett.*, vol. 9, no. 3, pp. 377-379, March 1997.
[68] F. Delorme, “Widely tunable 1.55-µm lasers for wavelength-division-multiplexed optical fiber communications,” *IEEE J. Quantum Electron.*, vol. 34, no. 9, pp. 1706-1716, September 1998.
[69] A.A. Saavedra, P.-J. Rigole, E. Goobar, R. Schatz, and S. Nilsson, “Amplitude and frequency modulation characteristics of widely tunable GCSR lasers,” *IEEE Photon. Technol. Lett.*, vol. 10, no. 10, pp. 1383-1385, October 1998.
[70] R. Olshansky, P. Hill, V. Lanzisera, and W. Powazinik, “Frequency response of 1.3 µm InGaAsP high speed semiconductor lasers,” *IEEE J. Quantum Electron.*, vol. 23, no. 9, pp. 1410-1418, September 1987.

[71] O. Kjebon, R. Schatz, S. Lourdudoss, S. Nilsson, and B. Stålnacke, "Modulation response measurements and evaluation of MQW InGaAsP lasers of various designs," *Proc. SPIE*, vol. 2684, pp. 138-152, San Jose, CA, USA, February 1996.
[72] K. Vahala, and A. Yariv, "Detuned loading in coupled cavity semiconductor lasers – effect on quantum noise and dynamics," *Appl. Phys. Lett.*, vol. 45, no. 5, pp. 501-503, March 1984.
[73] M. Öberg, O. Kjebon, S. Lourdudoss, S. Nilsson, L. Bäckbom, K. Streubel, and J. Wallin, "Increased modulation bandwidth up to 20 GHz of a detuned-loaded DBR laser," *IEEE Photon. Technol. Lett.*, vol. 6, no. 2, pp. 161-163, February 1994.
[74] R. Schatz, D. McDonald, and H. Hillmer, "Parameter extraction," *Chapter 9 in Photonic devices for telecommunications – How to model and measure*, ed. G. Guekos, Springer Verlag, Berlin Heidelberg, Germany, 1999.
[75] G.P. Agrawal, *Fiber-optic communication systems*, John Wiley & Sons, New York, NY, USA, 1997.

Publicaties in de context van dit werk

[76] G. Morthier, T. Gyselings, G. Sarlet, P. Verhoeve, D. Van Thourhout, R. Baets, T. Van Caenegem, I. Moerman, P. Van Daele, W. Van Parys, B. Van Caenegem, P. Demeester, "Wavelength dependent routing in WDM optical communications: implications on components, systems and networks," *Revue HF Tijdschrift Electronics / Communications*, no. 2, 1998.
[77] G. Sarlet, G. Morthier and R. Baets, "A characterisation-efficient procedure for setting the wavelength of widely tunable lasers," *Proceedings IEEE/Lasers & Electro-Optics Society Benelux Symposium '98*, pp. 21-24, Gent, Belgium, November 1998.
[78] G. Sarlet, G. Morthier, R. Baets, D.J. Robbins, and D.C.J. Reid, "Optimization of multiple exposure gratings for widely tunable lasers," *IEEE Photon. Technol. Lett.*, vol. 11, no. 1, pp. 21-23, January 1999.
[79] B. Vanderhaegen, D. Van Thourhout, J. De Merlier, G. Sarlet, L. Vanwassenhove, I. Moerman, P. Van Daele, R. Baets, X.J.M. Leijtens, J.W.M. van Uffelen, and M.K. Smit, "High Q InGaAsP ring resonator filters," *Proceedings European Conference on Integrated Optics '99*, paper ThI8, Torino, Italy, April 1999.
[80] G. Morthier, and G. Sarlet, "Widely tunable lasers and their control," *Proceedings European Conference on Optical Communications '99,* paper WeB3.1, Nice, France, September 1999.
[81] G. Sarlet, G. Morthier and R. Baets, "Novel mode stabilisation scheme for widely tunable lasers," *Proceedings European Conference on Optical Communications '99*, paper WeB3.5, Nice, France, September 1999.
[82] G. Sarlet, G. Morthier, and R. Baets, "Wavelength and mode stabilization of widely tunable SG-DBR and SSG-DBR lasers," *IEEE Photon. Technol. Lett.*, vol. 11, no. 11, November 1999.
[83] G. Sarlet, G. Morthier, and R. Baets, "Frequency, mode and power stabilization of a widely tunable SSG-DBR laser at 40 ITU channels," *Proceedings Conference on Optical Fiber Communications 2000*, paper WM21, Baltimore, MD, USA, March 2000.
[84] G. Sarlet, G. Morthier, and R. Baets, "Control of widely tunable SSG-DBR lasers for dense wavelength division multiplexing," *J. Lightwave Technol.*, vol. 18, no. 8, pp. 1128-1138, August 2000.
[85] G. Morthier, G. Sarlet, R. Baets, R. O'Dowd, H. Ishii, and Y. Yoshikuni, "The direct modulation bandwidth of widely tunable DBR laser diodes," *Proc. XVII International Semiconductor Laser Conference*, paper P12, Monterey, CA, USA, September 2000.
[86] D. Van Thourhout, G. Sarlet, G. Morthier, and R. Baets, "Comparison of multiwavelength and widely tunable laser diodes," submitted to *Optical and Quantum Electronics*.

Octrooi-aanvragen

[87] D.C.J. Reid, D.J. Robbins, and G. Sarlet, "Multi-wavelength optical reflector," *UK Patent Application*, no. GB 2337135 A, filed May 6, 1998, published November 10, 1999 – *European Patent Application*, no. EP 0955558 A2, filed May 6, 1999, published November 10, 1999.
[88] G. Sarlet, J. Buus, and R. Baets, "Multi-section widely wavelength tunable integrated semiconductor laser with different reflection or transmission sections," *European Patent Application*, filed in 1999.

Chapter 1

Introduction

1.1 Background

1.1.1 Wavelength division multiplexed fiber-optic communication

Telecom system manufacturers world-wide are continuously facing the enormous challenge to provide operators with network solutions that allow flexible and rapid scaling of network capacity. The major catalyst for this evolution is of course the explosive growth of the Internet. According to a recent estimation (July 2000), the average Internet traffic exceeds 1 Tbit/s, and has thus surpassed ordinary telephone traffic [1]. Even now, the traffic is still doubling approximately every 9 months. Not only is the number of Internet users still growing rapidly, the increased use of complex graphics, audio, and even video, is also boosting the average traffic volume per user. It is expected that in the future, when new access network technologies like DSL (digital subscriber line) and cable modems bring increased bandwidth to the end-user, new applications will emerge that will push bandwidth demand even higher.

One of the key enabling technologies for this (r)evolution has undoubtedly been fiber-optic transmission [2]. Silica fiber can carry an infrared signal for scores of kilometres with extremely low loss. At its frequency of minimum attenuation, 193 THz, the loss is as low as 0.2 dB/km. Moreover, silica fiber also has an unprecedented bandwidth around this loss minimum of about 25000 GHz (compare e.g. to the 25 GHz bandwidth available for radio communications).

Two techniques can principally be used to combine digital signals from different sources and transmit them across a single optical fiber: time division multiplexing (TDM) and wavelength division multiplexing (WDM).

In the TDM approach, the bits of the different tributary signals are compressed in time and combined into a single high bit-rate signal. Presently available electronics however only allow multiplexing up to speeds of 40 Gbit/s (10 Gbit/s in commercial systems). At higher bit-rates, the signals have to be multiplexed in the optical domain. Optical time division multiplexing (OTDM) is obviously much more challenging, which explains why OTDM systems have so far not been able to make the transition from the lab to real-life applications. The present lab record for the OTDM bit-rate stands at 320 Gbit/s [3], which is still only a small fraction of the available fiber bandwidth.

Using WDM, throughputs that are ten times higher have already been demonstrated (e.g. [4]). In WDM transmission, the tributary signals are time division multiplexed up to a certain level (2.5 Gbit/s or 10 Gbit/s in present commercial systems, 20 Gbit/s to 40 Gbit/s in laboratory experiments [4]). Subsequently, each TDM signal is modulated onto an optical carrier wave with a different frequency, after which the optical signals are coupled into a single fiber. Conceptually, WDM is the same as the frequency division multiplexing (FDM) used to place many radio channels on carrier waves of different frequencies.

Although the concept has obviously been known for a long time, WDM only experienced a real break-through after the invention of the erbium-doped fiber amplifier (EDFA) in the late 1980s. Prior to that, the WDM signal had to be demultiplexed every 100 km or so to allow detection, electronic regeneration and retransmission of the individual TDM signals. The EDFA can on the other hand amplify many optical channels on a fiber simultaneously, which means that much larger distances can be bridged without electronic regeneration.

Illuminating a fiber amplifier with a pump laser operating at a frequency of 306 THz or 203 THz excites the erbium ions in the fiber to a higher, metastable energy level. If an excited erbium ion is stimulated by a signal photon at any frequency from 192 THz to 196 THz, it will cascade back down to the ground state, emitting a photon with precisely the same direction, phase, and frequency as the incoming signal photon. All these coherent photons constitute gain. Standard EDFAs can thus amplify optical signals in the frequency band from 192 THz to 196 THz (often called the conventional or C-band). More recently, EDFAs have been developed which amplify in the so-called L-band (long wavelength band), i.e. from 187 THz to 191 THz.

Recent progress in the fabrication of very high-power pump lasers allows stretching the frequency range where signals can be amplified optically even further by employing the stimulated Raman scattering phenomenon [5]. Stimulated Raman scattering is a non-linear optical process in which intense pump light interacts with a signal of lower frequency, simultaneously amplifying the signal and producing an optical phonon. Raman scattering occurs in all optical fibers, with its strength depending only on the type of optical fiber and the frequency offset and power of the interacting waves. Raman scattering thus in principle allows amplification at any frequency in the 25 THz broad low-loss window of the optical fiber.

Wavelength division multiplexing was first applied in long haul point-to-point links. A typical configuration is sketched in Figure 1.1. The transmitters (Tx) typically consist of distributed feedback (DFB) lasers with an integrated or external modulator, which switches the laser light on and off at a high rate to encode the digital information on the optical carrier wave. Each of the DFB lasers emits at a predetermined frequency. The signals are subsequently combined using an optical multiplexer and coupled into a single-mode fiber. At regular distances along the fiber link (typically every 60 to 80 km), the signals are amplified using an EDFA to compensate for the losses experienced along the fiber. At the end of the link, the signals at the different frequencies are split up again using a demultiplexer and converted back to electrical signals by a receiver (Rx). The earliest commercial systems (1996) consisted of 4 to 8 frequency channels, each carrying a 2.5 Gbit/s data signal. The channels were spaced by 400 or 200 GHz.

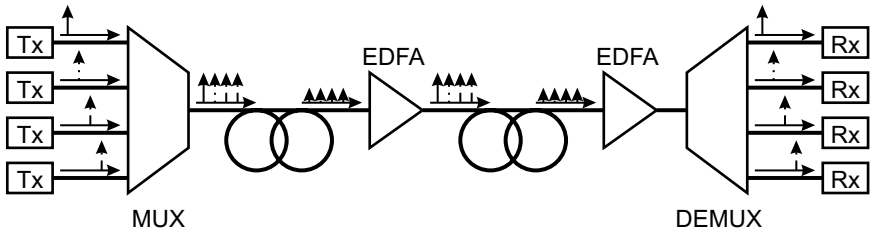

Figure 1.1 Typical configuration of a WDM point-to-point link.

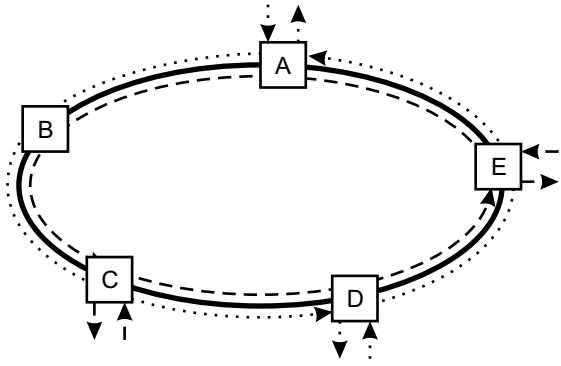

Figure 1.2 A WDM ring network with optical add/drop multiplexers (OADMs).

As the capacity demand grew, the number of channels was increased. Since the standard EDFA only has a limited bandwidth of about 4 THz, this meant that the channel spacing had to be reduced. The frequencies to be used in WDM systems have recently been standardised by the International Telecommunications Union. A regularly spaced frequency grid, anchored at 193.1 THz, with an inter-channel spacing at an integer multiple of 50 GHz or 100 GHz, was specified [6]. Present-day commercially available systems use the entire C-band, with up to 80 channels spaced at 50 GHz for 2.5 Gbit/s data signals or 40 channels spaced at 100 GHz for 10 Gbit/s data signals [7]-[8]. To keep up with capacity demands the number of channels will probably have to be increased even further, both by reducing the channel spacing and by extending the frequency band (e.g. by using the L-band).

The second area where WDM transmission experienced a break-through was in metropolitan area networks. A popular configuration for such networks is a dual ring topology, a so-called self-healing ring, which offers a back-up (protection) route when one of the links or one of the nodes in the network fails. Each of the nodes in the ring network consists of an optical add/drop multiplexer (OADM) (Figure 1.2). The OADM terminates one or more frequency channels destined for that node (drop) and adds new data on those frequency channels, while it simply passes on the other frequency channels. In that way, bi-directional communication can be set up between any two nodes along a single fiber ring, as illustrated in Figure 1.2.

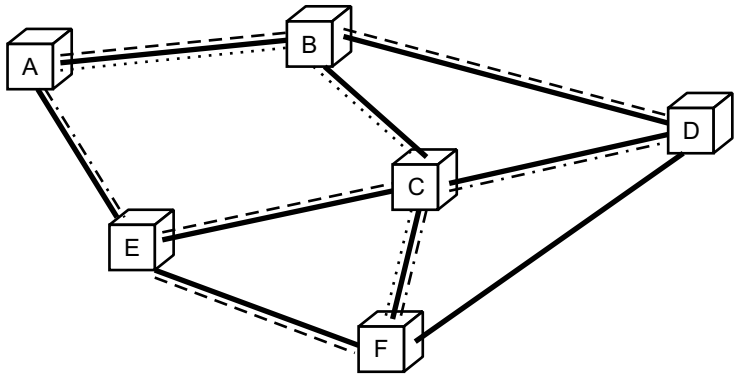

Figure 1.3 A WDM mesh network.

The secondary fiber ring in the self-healing ring configuration is used for back-up purposes. When e.g. a fiber cut occurs, traffic is looped back onto the secondary fiber in the nodes at either end of the fiber cut.

Future WDM networks will probably use a mesh topology, as shown in Figure 1.3. A major advantage of this topology is that the available frequency channels can be used much more efficiently, since channels can be reused for different connections. In Figure 1.3, the same frequency channel can for example be used along the connections ABD and CEF. In the nodes, the different signals are routed by an optical cross-connect (OXC). An OXC demultiplexes the light on the incoming fibers into the individual frequency channels, switches the different signals to the appropriate output port and remultiplexes the signals arriving at each of the output ports for transmission. Such a mesh network offers a lot more flexibility than the ring network of Figure 1.2, since connections between any two nodes can be set up or taken down by reconfiguring the switches in the optical cross-connects.

1.1.2 Applications of tunable lasers in WDM systems

As mentioned above, the light sources in today's WDM transmitters are DFB lasers, emitting at a fixed frequency. In many applications, it would be advantageous to have a tunable laser, i.e. a laser that can be made to emit at any of a large number of frequencies on the ITU grid. Below, we will give an overview of the most commonly cited benefits of tunable lasers.

Back-up lasers

In a communication system, it is of course of the utmost importance to keep all links up and running. Therefore, some kind of back-up system has to be provided, which takes over in event of a transmitter laser failure. One possibility is to use a new transmission channel that is specifically designated for back-up purposes. This works quite well in simple point-to-point systems. However, in systems that are more complex this requires an intervention from the central management system, since all nodes in the affected path will have to be reconfigured. Another solution is

to provide back-up lasers in each node. When only fixed-frequency lasers are used, a back-up laser would have to be provided for each individual channel. A tunable laser, conversely, can act as a back-up laser for a large number of frequency channels. Today, tunable lasers are available that can cover more than 80 channels with 50 GHz channel separation (as well as any frequency between those channels).

Inventory management

When a transmitter fails, the defective transmitter card has to be replaced as soon as possible, even when a back-up system is available. Consequently, a network operator has to keep a stock of spare transmitter cards. If DFB lasers are used, a supply of lasers has to be maintained for each frequency channel. It is clear that the management of such a spare laser inventory quickly becomes complicated and costly as the number of channels increases. Matters are simplified significantly when tunable lasers are stocked. In that case, either only one type of laser has to be stored, or the number of different types is at least drastically reduced (when each tunable laser covers only a subset of all required channels).

Frequency conversion

In the most general configuration of an optical cross-connect, frequency conversion will be necessary to avoid that two data signals are transmitted on the same frequency channel on an outgoing fiber. Some OXC architectures require that the frequency channel to which the signal is converted can be tuned. Tunable frequency conversion is also required in some new system concepts that have recently been proposed, e.g. the switchless network studied in the SONATA project [9]. The simplest way to realise tunable frequency conversion is to use a tunable laser as the transmitter in a transponder arrangement. In a transponder, the incoming optical signal is converted to an electrical signal by a photodiode, the electrical signal is amplified (as well as perhaps reshaped/retimed) and subsequently applied to an external modulator that modulates the output of the tunable laser. In the future, all-optical frequency conversion will probably be preferred. This however still requires a tunable laser to generate the new carrier wave on which the data signal from the original carrier has to be transferred.

Heterodyne detection

As the channel separation in WDM systems decreases it becomes harder to separate adjacent channels using optical filtering. With heterodyne detection, the problem of separating the densely packed frequency channels is moved to the electrical domain, where filters that are much more selective are generally available. One essential element in a heterodyne receiver is a tunable laser, which acts as a local oscillator (Figure 1.4). The light from the local oscillator (LO) laser (frequency ν_{LO}) is combined with the light carrying the data (frequency ν_{data}) using a 3 dB coupler and the composite signal is detected with a pair of photodiodes. Thus, a radio frequency signal is generated at the difference frequency $\nu_{RF} = \nu_{data} - \nu_{LO}$.

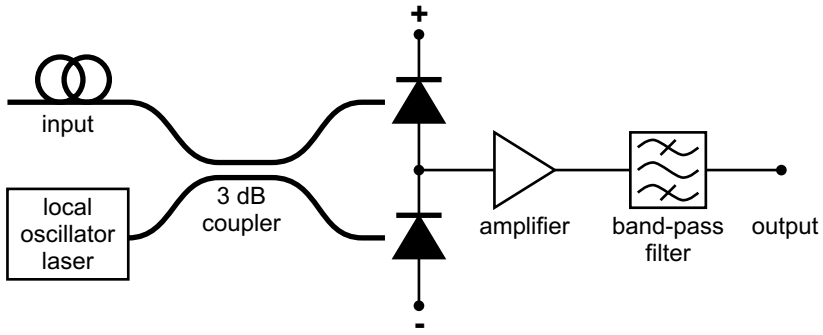

Figure 1.4 A heterodyne receiver, using a tunable laser as local oscillator.

To detect the signal at a particular frequency ν_{data}, the LO laser must tune to within a few GHz of the carrier frequency of the selected channel, and then work as a voltage-controlled oscillator (VCO), tracking the channel carrier frequency to keep ν_{RF} constant. The neighbouring channels are suppressed by passing the RF signal to a band-pass filter centred at ν_{RF}.

A principal advantage of heterodyne detection for optical systems is the fact that the local oscillator power may be set such that the receiver noise is dominated by the shot noise contribution from the local oscillator [10]. The RF signal power is proportional to the local oscillator power, which for large local oscillator powers yields a signal to noise ratio (SNR) that is independent of electronic amplifier noise. This allows a significant improvement in SNR at the receiver. The sensitivity of a heterodyne receiver is even 3 dB higher than that of a noiseless direct-detection receiver. In addition, heterodyne detection is insensitive to unwanted background light.

The cost of these advantages is an increase in the system's complexity since heterodyning requires a stable LO, an optical coupler in which the polarisations of the mixed fields are precisely aligned, and complex circuits for phase locking.

Dynamic capacity allocation in wavelength routing networks

Due to the spectacular growth of the Internet, with its rapidly shifting traffic patterns, network operators are looking for network solutions that allow rapid reconfiguration and dynamic capacity allocation. Large business customers would like to have capacity available on demand, instead of having to dimension the capacity of their permanent leased-line connection for peak traffic. Increased flexibility would also allow operators to allocate more capacity to business areas during working hours, and shift part of that capacity to residential areas at night and on weekends. Such flexibility could be provided by a WDM mesh network with optical cross-connects as described above. At present, however, no OXCs are available which can handle the large numbers of channels of current WDM networks [11]. An intermediate solution can be found by using fixed wavelength routers at the nodes, and use tunable transmitters to dynamically set-up paths across the network.

A simple example of a wavelength routing network was described in the previous section: a ring network with optical add/drop multiplexers. When fixed-frequency components are used, this type of network can provide full connectivity with low complexity, but at the expense of flexibility and reconfigurability. With tunable transmitters, some functionality is added [12], since the node where a particular signal is dropped can be changed by adjusting the emission frequency of the transmitter.

A more advanced wavelength routing network was studied in the ACTUAL research project, where a reconfigurable all-optical mesh network was realised [12]-[14].

Optical packet switching

Although telecommunications traffic will soon be entirely dominated by data traffic, the network architectures discussed up until now do not take into account the bursty nature of this data traffic. All of the above systems assume that connections are set up between points for hours, days or longer. Data traffic is however typically transmitted in relatively short packets, which are routed across the network without setting up long-term point-to-point connections. Using rapidly tunable lasers, one can develop an optical packet switching network, in which data packets are routed based on the frequency of their carrier wave. Such architecture is for example studied in the HORNET project [12], [14]-[16]. In this application, it is of course crucial that the tunable laser can change its frequency much faster than the typical duration of a packet.

1.2 Problems to be solved – Goals of this work

The above discussion should have made clear that the use of tunable laser diodes in WDM systems opens up many new opportunities, both to increase network capacity, as well as to improve network flexibility. At the start of the research work that is reported in this dissertation, several types of tunable laser diodes that could potentially be used in such applications had already been demonstrated. Yet, several issues remained to be resolved, before the potential of these tunable lasers could truly be unleashed.

As will be illustrated in Chapter 2, tunable laser diodes require simultaneous control of several (typically 3 to 4) analogue currents/voltages to emit light at a particular frequency with a given output power. Moreover, a change in any control current/voltage usually affects both the frequency and the output power. Controlling such a tunable laser is hence rather complex. For practical applications, it should be possible to set the laser to a certain frequency using simple, digital commands. These should then be translated into the appropriate values of the control currents/voltages by the laser's control circuitry. For this, a look-up table of operation points can be used, which is stored in an EPROM (erasable, programmable read-only memory). Operation points could for example be stored for all the frequencies on the ITU-grid to which the laser can be tuned. When the frequency has to be changed, a microprocessor interprets the digital commands,

reads the appropriate data from the look-up table, and adjusts the control currents/voltages accordingly.

Due to fabrication tolerances, no two lasers will be identical, which means that a separate look-up table has to be determined for each individual laser. The main challenge lies in finding a way to accurately characterise the laser without requiring long measurement cycles, in order to keep the cost of the tunable laser module as low as possible. For instance, a typical frequency measurement takes at least one second. For a laser with three controls, simply measuring the frequency on a 100×100×100 grid would take almost 12 days. Yet, only a small fraction of these measurement points will in the end turn out to be suitable operation points, hence most of this time is wasted. The first goal of our research was therefore to develop an intelligent characterisation strategy, which allows determining the look-up table both accurately and efficiently.

In a telecom system, the tunable laser module will have to maintain high frequency accuracy over many years. As any electronic device, tunable lasers will however slowly degrade over time. Additionally, environmental changes can cause the laser frequency to drift. To keep the laser at the correct frequency, some sort of feedback control can be applied. The frequency can for example be monitored by tapping of part of the emitted light and passing it through a stable optical filter, which serves as a frequency reference. It is not sufficient though to just keep the frequency constant. One also has to assure that the laser always emits in a single spectral line, in order to avoid cross-talk and other signal degradation (due to noise, dispersion, ...) in an optical communication system. To counteract device degradation and environmental changes, the control currents/voltages have to be adjusted such that the emission frequency and output power are kept constant and such that a high spectral purity is maintained. This is a complex task, since each of the controls affects all of the above parameters to some extent. Developing a feedback control system for tunable lasers hence constituted a second major objective of our study.

Developing characterisation and control algorithms for a tunable laser obviously requires a profound understanding of the operation of these devices. A simulation program that can calculate the tuning characteristics of a laser would be a very useful tool to gain such understanding. Yet, none of the commercially available laser simulators allows calculating such characteristics in a reasonable time. The problem is that these laser simulators mainly focus on the gain section of the laser, taking into account many complicated effects, but do not include models for the tunable filters that are typically incorporated in a tunable laser cavity. We therefore decided to develop our own simulation environment, which uses a fairly simple gain section model and rather focuses on the tuning behaviour of the laser.

As mentioned in §1.1.1, digital data is usually transmitted by simple on/off keying of an optical carrier wave in today's fiber-optic communication systems. For the highly demanding long-haul applications, the data is encoded on the carrier wave by using an external modulator. However, for shorter transmission distances, e.g. in a metropolitan network, it would often be more economical to use direct modulation of the laser's gain current. The bit-rates achievable in this case are of course limited by the modulation bandwidth of the laser diode. Since only little has been published on the dynamic characteristics of tunable lasers until now, the final goal of our research was to gain a better understanding of this modulation behaviour.

1.3 Overview of the thesis and main achievements

Chapter 2 presents a rundown of the monolithically integrated tunable laser diodes that are most commonly cited as suitable candidates for applications in WDM systems. Basically, these lasers are all variations of the "original" tunable laser diode, the distributed Bragg reflector (DBR) laser. They consist of a concatenation of an active section, providing the optical gain for the laser oscillator, and one or more passive filter sections, determining the emission frequency. In section 2.1, the relevant physical mechanisms enabling electronic control of the emission frequency of a semiconductor laser are presented. Subsequently, we summarise the requirements a tunable laser should fulfil for WDM applications (§2.2). Section 2.3 describes the DBR laser and section 2.4 discusses how the design of the DBR laser can be improved to yield a wider tuning range, ideally covering at least the entire C- or L-band. This section also introduces some novel designs for widely tunable lasers, which were inspired by the experience gained during our research. These designs are the subject of a patent application we recently submitted jointly with J. Buus [29]. Finally, in §2.5 the present state-of-the-art of the different laser types is compared.

Chapter 3 covers the simulation model for longitudinally integrated tunable laser diodes we developed and implemented. The model consists of two main parts, one describing the active section using the classic laser rate equations (§3.1), and one describing the passive sections using transfer matrices (§3.2). The advantage of a transfer matrix description for the passive sections is that the transfer matrix of a concatenation of sections is simply given by the product of the transfer matrices of the individual sections. The reflectivities of the passive structures left and right of the active section, which are needed as input to the rate equation model, are readily derived from the overall transfer matrices of these structures. Section 3.3 briefly discusses the implementation of the models in software.

The transfer matrix description of the passive sections has also been used in design studies of alternative types of distributed Bragg reflectors with a comb-shaped reflectivity spectrum for applications in tunable lasers (§3.4) [19]. One of these designs is the subject of another patent application, submitted jointly with researchers from Marconi – Caswell Technology in the UK [28].

The next two chapters deal with the control and characterisation of the tunable laser diodes introduced in Chapter 2. In Chapter 4, we focus on feedback control. §4.1 gives an overview of techniques that can be used to stabilise the laser frequency. Experimental results in this section clearly demonstrate the need for a control method that allows maintaining a high spectral purity. Two possible approaches are compared in §4.2. The first method, which was already described in literature several years ago, is based on monitoring changes in output power when tuning currents are adjusted. We propose an alternative method, based on monitoring the voltage across the laser's active section. We will show that, although in an ideal laser both should be equivalent, the latter approach is more suitable in practice, since the voltage signal is much less disturbed by the increase of absorption losses in the passive sections when the tuning currents are increased [22]-[25]. A practical

implementation of the control loops and test results are presented in §4.3. The control loops were tested by varying the environmental temperature by 10 °C, which would normally yield a frequency variation of more than 100 GHz. The control system however maintained the frequency to within ±1.0 GHz of the desired frequency, and this for all ITU channels within the tuning range of the laser [24]-[25]. Simultaneously, a stable output power and a high spectral purity were also maintained. The control system was demonstrated at the European Exhibition on Optical Communication in Nice, France in September 1999.

Chapter 5 tackles the complementary problem of the look-up table generation. Section 5.1 first establishes the requirements that a characterisation procedure should fulfil. The following sections present three methods that were developed during the course of our research. The first is based on curve fitting to a reduced set of frequency measurements (§5.2) [18]. Although this already yielded a significant reduction in characterisation time (from days to hours), the accuracy of the resulting operation points was not always sufficient for practical applications, since the frequency errors could amount to several GHz. Another disadvantage is that intervention of a human operator is required to select suitable starting values of the parameters used in the curve-fitting.

In the second method (§5.3), the first curve-fitting step of the previous method is used to generate a very coarse look-up table. This table is subsequently updated using the feedback control system from Chapter 4. This both yielded a much better frequency accuracy (±1.0 GHz) as well as an even further reduced characterisation time. Disadvantages of the procedure are that it still requires quite many frequency measurements, that it still needs operator intervention and that it can only yield operation points for a small number of frequencies determined by the frequency reference in the control loop.

The last method, described in §5.4, improves on that in the following manner. First a set of suitable operation points covering the entire tuning range of the laser is located using the voltage monitoring technique described in Chapter 4. The frequency then only has to be measured for these – already optimised – operation points, after which operation points for any frequency within the laser's tuning range can be calculated by straightforward interpolation. This procedure runs completely automatically and reduces the number of frequency measurements to a minimum. Moreover, it yields very low frequency errors (less than ±0.5 GHz), and even allows equalisation of the output power across the different operation points [25].

Finally, Chapter 6 covers the direct modulation characteristics of tunable laser diodes. First, we derive expressions describing the small-signal modulation response and the relative intensity noise (RIN) spectrum of a general tunable laser and compare the results with the well-known expressions for Fabry-Perot and DFB lasers (§6.1). The main conclusion is that the bandwidth of a tunable laser will be somewhat lower than the bandwidth of an equivalent DFB laser (i.e. with the same composition as the active section of the tunable laser). §6.2 and §6.3 summarise the experimental results that were obtained for two types of tunable laser, the SSG-DBR and the GCSR laser (cf. Chapter 2). The parameters describing the modulation response of the intrinsic laser diode (i.e. without parasitic capacitances and inductances) were derived from relative intensity noise measurements. Both laser types had an intrinsic modulation bandwidth of at least 8 GHz, with some variation

across the tuning range [26]. When a large-signal digital modulation was applied, only the SSG-DBR laser maintained a high spectral purity. This is attributed to the higher selectivity of the intra-cavity filters in the SSG-DBR laser compared to the GCSR laser. For completeness, we also summarise the results of fiber transmission experiments performed with a directly modulated SSG-DBR laser at NTT Optoelectronics in Atsugi, Japan. These illustrate that transmission at a bit-rate of 2.5 Gbit/s is possible with a directly modulated SSG-DBR laser. However, the maximum achievable transmission distance of 80 km is somewhat shorter than what is commonly achievable with a DFB laser (at least 100 km).

References

General references

[1] "Internet traffic tops 350000 Tbytes per month," *Lightwave Magazine*, vol. 17, no. 8, July 2000. <http://lw.pennnet.com/>

[2] A.E. Willner, "Mining the optical bandwidth for a terabit per second," *IEEE Spectrum*, vol. 34, no. 4, April 1997.

[3] G. Raybon, B. Mikkelsen, R.-J. Essiambre, A.J. Stentz, T.N. Nielsen, D.W. Peckham, L. Hsu, L. Grüner-Nielsen, K. Dreyer, and J.E. Johnson, "320 Gbit/s single-channel pseudo-linear transmission over 200 km of nonzero-dispersion fiber," *Proceedings Conference on Optical Fiber Communications 2000 – Post-deadline papers*, paper PD29, Baltimore, MD, USA, March 2000.

[4] T.N. Nielsen, A.J. Stentz, K. Rottwitt, D.S. Vengsarkar, Z.J. Chen, P.B. Hansen, J.H. Park, K.S. Feder, T.A. Strasser, S. Cabot, S. Stuylz, D.W. Peckham, L. Hsu, C.K. Kan, A.F. Judy, J. Sulhoff, S.Y. Park, L.E. Nelson, and L. Grüner-Nielsen, "3.28 Tb/s (82 × 40 Gb/s) transmission over 3 × 100 km nonzero-dispersion fiber using dual C- and L-band hybrid Raman/Erbium-doped inline amplifiers," *Proceedings Conference on Optical Fiber Communications 2000 – Post-deadline papers*, paper PD23, Baltimore, MD, USA, March 2000.

[5] R.H. Stolen, and E.P. Ippen, "Raman gain in glass optical waveguides," *Appl. Phys. Lett.*, vol. 22, no. , pp. 276-278, March 1973.

[6] International Telecommunication Union – Telecommunication Standardization Sector (ITU-T), Recommendation G.692: "Optical interfaces for multichannel systems with optical amplifiers," *Series G: Transmission systems and media, digital systems and networks (Transmission media characteristics – Characteristics of optical components and sub-systems)*, October 1998.

[7] Lucent Technologies WaveStar OLS 400G. <http://www.lucent.com/>

[8] Nortel Networks OPTera LH. <http://www.nortelnetworks.com/>

[9] S. Binetti, M. Listanti, A. Maga, and R. Sabella, "Analysis and dimensioning of switchless networks for single-layer optical architecture," *J. Lightwave Technol.*, vol. 18, no. 2, pp. 144-153, February 2000.

[10] L. Kazowsky, S. Benedetto, and A.E. Willner, *Optical fiber communication systems*, Artech House, Norwood, MA, USA, 1996.

[11] M. Koga, A. Watanabe, T. Kawai, K.-I. Sato, and Y. Ohmori, "Large capacity optical path cross-connect for WDM photonic transport network," *IEEE J. Sel. Areas in Communications*, vol. 16, no. 7, pp.1260-1269, September 1998.

[12] R. Plastow, "Emerging tunable laser applications in optical networks," *Lightwave Magazine*, vol. 17, no. 3, March 2000. <http://lw.pennnet.com/>

[13] E. Zouganeli, "Tunable lasers route optical signals," *WDM Solutions – a supplement to Laser Focus World*, vol. 2, no. , pp. 26, June 2000.

[14] P. Rigby, "Network trials tune in to wavelength routing," *FibreSystems*, vol. 4, no. 6, pp. 35-40, July 2000.

[15] I.M. White, Y. Fukashiro, K. Shrikhande, D. Wonglumsom, M.S. Rogge, M. Avenarius, and L.G. Kazovsky, "Experimental demonstration of a media access protocol for HORNET: a WDM multiple acces metropolitan area ring network," *Proceedings Conference on Optical Fiber Communications 2000*, paper WD3, Baltimore, MD, USA, March 2000.

[16] R. Pease, "HORNET creates a new buzz in the use of tunable laser technology," *Lightwave Magazine*, vol. 17, no. 8, July 2000. <http://lw.pennnet.com/>

Publications in the context of this work

[17] G. Morthier, T. Gyselings, G. Sarlet, P. Verhoeve, D. Van Thourhout, R. Baets, T. Van Caenegem, I. Moerman, P. Van Daele, W. Van Parys, B. Van Caenegem, P. Demeester, "Wavelength dependent routing in WDM optical communications: implications on components, systems and networks," *Revue HF Tijdschrift Electronics / Communications*, no. 2, 1998.

[18] G. Sarlet, G. Morthier and R. Baets, "A characterisation-efficient procedure for setting the wavelength of widely tunable lasers," *Proceedings IEEE/Lasers & Electro-Optics Society Benelux Symposium '98*, pp. 21-24, Gent, Belgium, November 1998.

[19] G. Sarlet, G. Morthier, R. Baets, D.J. Robbins, and D.C.J. Reid, "Optimization of multiple exposure gratings for widely tunable lasers," *IEEE Photon. Technol. Lett.*, vol. 11, no. 1, pp. 21-23, January 1999.

[20] B. Vanderhaegen, D. Van Thourhout, J. De Merlier, G. Sarlet, L. Vanwassenhove, I. Moerman, P. Van Daele, R. Baets, X.J.M. Leijtens, J.W.M. van Uffelen, and M.K. Smit, "High Q InGaAsP ring resonator filters," *Proceedings European Conference on Integrated Optics '99*, paper ThI8, Torino, Italy, April 1999.

[21] G. Morthier, and G. Sarlet, "Widely tunable lasers and their control," *Proceedings European Conference on Optical Communications '99*, paper WeB3.1, Nice, France, September 1999.

[22] G. Sarlet, G. Morthier and R. Baets, "Novel mode stabilisation scheme for widely tunable lasers," *Proceedings European Conference on Optical Communications '99*, paper WeB3.5, Nice, France, September 1999.

[23] G. Sarlet, G. Morthier, and R. Baets, "Wavelength and mode stabilization of widely tunable SG-DBR and SSG-DBR lasers," *IEEE Photon. Technol. Lett.*, vol. 11, no. 11, November 1999.

[24] G. Sarlet, G. Morthier, and R. Baets, "Frequency, mode and power stabilization of a widely tunable SSG-DBR laser at 40 ITU channels," *Proceedings Conference on Optical Fiber Communications 2000*, paper WM21, Baltimore, MD, USA, March 2000.

[25] G. Sarlet, G. Morthier, and R. Baets, "Control of widely tunable SSG-DBR lasers for dense wavelength division multiplexing," *J. Lightwave Technol.*, vol. 18, no. 8, pp. 1128-1138, August 2000.

[26] G. Morthier, G. Sarlet, R. Baets, R. O'Dowd, H. Ishii, and Y. Yoshikuni, "The direct modulation bandwidth of widely tunable DBR laser diodes," *Proceedings XVII International Semiconductor Laser Conference*, paper P12, Monterey, CA, USA, September 2000.

[27] D. Van Thourhout, G. Sarlet, G. Morthier, and R. Baets, "Comparison of multiwavelength and widely tunable laser diodes," submitted to *Optical and Quantum Electronics*.

Patent applications

[28] D.C.J. Reid, D.J. Robbins, and G. Sarlet, "Multi-wavelength optical reflector," *UK Patent Application*, no. GB 2337135 A, filed May 6, 1998, published November 10, 1999 – *European Patent Application*, no. EP 0955558 A2, filed May 6, 1999, published November 10, 1999.

[29] G. Sarlet, J. Buus, and R. Baets, "Multi-section widely wavelength tunable integrated semiconductor laser with different reflection or transmission sections," *European Patent Application*, filed in 1999.

Chapter 2

State-of-the-art tunable laser diodes

This chapter gives an overview of the monolithically integrated tunable laser diodes that are at present (autumn 2000) considered suitable for applications in wavelength division multiplexed (WDM) fiber-optic communications. For a more comprehensive review of integrated tunable laser diodes, the reader is referred to the excellent book by Amann and Buus [1]. All of these tunable lasers consist of a longitudinal integration of sections with different functionality. Typically, one has an active section providing the optical gain for the laser oscillator, one or more filter sections with a (tunable) frequency selective transmission or reflection characteristic, and a phase shifter section for fine-tuning of the cavity resonance frequencies.

Lasers in which the frequency selection and tuning functions are external to the semiconductor structure are not discussed here, since they are considered incompatible with the requirements for telecommunication applications. Typically, the frequency selectivity in an external cavity tunable laser is provided by an external diffraction grating, which reflects only a small fraction of the optical spectrum back into the semiconductor optical amplifier (SOA) supplying the gain (cf. Chapter 8 in [1]). The centre frequency of the light that is reflected back into the SOA can be tuned by rotating the diffraction grating. The main problem in such a configuration is the mechanical and thermal stability, since the different components in the system have to be kept aligned to within a fraction of a micron. Stabilisation systems have obviously been developed to take care of this, but they render the entire configuration quite bulky and do not guarantee reliable operation over the 10 to 20 years lifetime that is typically required in telecom applications. External cavity lasers are mainly used in laboratory instruments, where for example the advantage of the extremely narrow linewidth of the emitted light outweighs the disadvantages of the larger size and the lower reliability.

In the first section of the chapter, the relevant physical mechanisms enabling electronic control of the emission frequency of a monolithic semiconductor laser are presented. Next, we run through the main requirements posed on tunable lasers for WDM applications. In the subsequent sections the basic tunable laser – the distributed Bragg reflector (DBR) laser – and a number of more advanced laser structures are described. Finally, the present state-of-the-art of these lasers is compared.

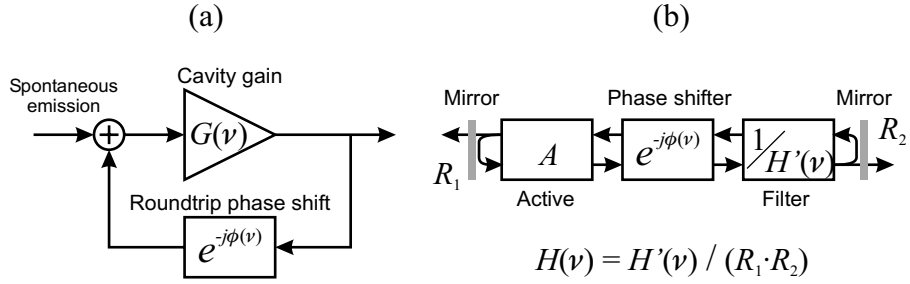

Figure 2.1 Simplified representations of a (tunable) laser oscillator: equivalent circuit (a) and block diagram showing the concatenation of active (gain), phase shifter, and filter sections (b).

2.1 Electronic frequency control

Figure 2.1(a) shows a simplified equivalent circuit of a laser oscillator. For laser operation at a frequency ν two requirements need to be fulfilled simultaneously: the roundtrip cavity gain $G(\nu)$ should be unity and the roundtrip phase $\phi(\nu)$ should be an integer multiple of 2π.

$$\begin{aligned} G(\nu) &= 1 \\ \phi(\nu) &= \frac{2\pi\nu}{c} 2\sum_l n_l L_l = 2\pi k \end{aligned} \tag{2.1}$$

Here c is the speed of light in vacuum. The summation over l represents the optical length of the laser cavity, i.e. the sum of the optical lengths of the different concatenated sections, where the optical length of a section l is defined as the product of the physical length L_l with the effective refractive index n_l.

We assume for simplicity that the roundtrip cavity gain G can be written as the division of a frequency-independent gain factor A by a frequency dependent loss factor $H(\nu)$ (Figure 2.1(b)).

$$G(\nu) = \frac{A}{H(\nu)} \tag{2.2}$$

The phase condition defines a set of discrete frequencies ν_k, the so-called cavity modes. The laser will oscillate at the frequency ν_n among this set of frequencies, which requires minimal pumping of the laser to fulfil the gain condition $G(\nu_n) = 1$, i.e. the cavity mode frequency ν_n for which the loss $H(\nu_n)$ is minimal. The emission frequency can be tuned either by changing the frequency of minimal cavity loss H or by shifting the set of frequencies ν_k, which requires altering the roundtrip phase condition. Both mechanisms are illustrated in Figure 2.2.

If the frequency of minimal loss is adjusted while maintaining a pre-set roundtrip phase, the lasing frequency at first remains fixed at ν_n (Figure 2.2(a)). The gain level A adapts automatically to compensate for the varying losses $H(\nu_n)$, such that the gain condition continues to be fulfilled.

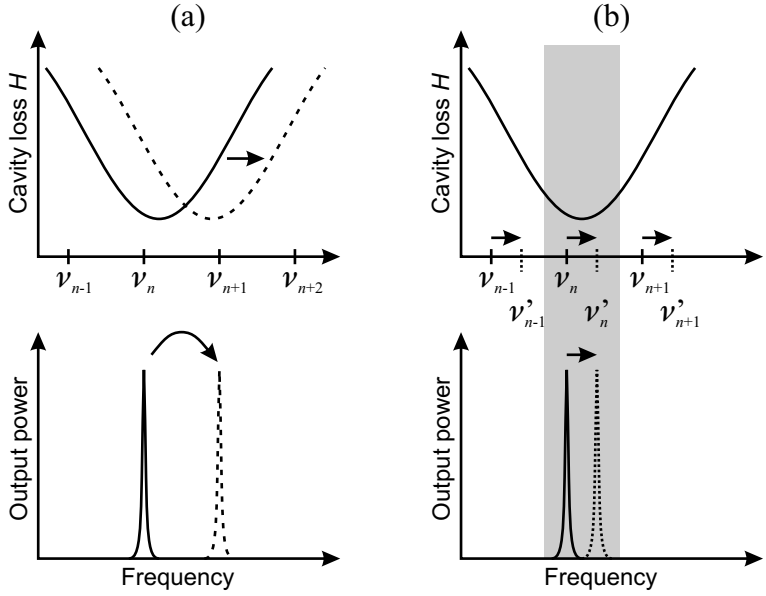

Figure 2.2 Two basic mechanisms to tune the emission frequency of a laser: changing the frequency of minimal cavity loss (a) and/or changing the roundtrip phase (b). In (a) the lasing mode hops from one cavity mode frequency ν_k to the next as the loss minimum is tuned. In (b) the cavity mode frequencies ν_k change continuously. The lasing mode is the longitudinal mode with lowest roundtrip loss, i.e. the cavity mode that falls within the shaded region.

At a certain point, though, an adjacent cavity mode (mode n+1) will experience a lower loss and the oscillation frequency will jump to that mode.

Alternatively, the optical length of the cavity can be adjusted, which shifts the position of the cavity modes in a continuous manner (Figure 2.2(b)). Accordingly, the oscillation frequency will also change continuously, albeit within a limited range. Because of the gain condition, the tuning range is limited to a range centred on the frequency of minimal loss with a width equal to the mode spacing $\Delta\nu = \nu_n - \nu_{n-1}$ (indicated by the shaded area in Figure 2.2(b)). When the emission frequency reaches the edge of this range, it jumps discontinuously to the cavity mode at the other edge.

As mentioned in the introduction, the present study is limited to the most common category of tunable semiconductor lasers, namely those lasers consisting of a longitudinal integration of sections with different functionality. The three principal functions are providing optical gain, tunable frequency selective filtering, and changing the optical length of the cavity to achieve phase resonance at the appropriate frequency. This is illustrated by the block diagram in Figure 2.1(b). Note that in practice the different functions can not always be entirely separated. Tuning the loss minimum will for example often also affect the roundtrip phase. In the following paragraphs, we briefly describe the physical mechanisms that can be used to electronically tune the filter transfer function or the phase resonance frequencies.

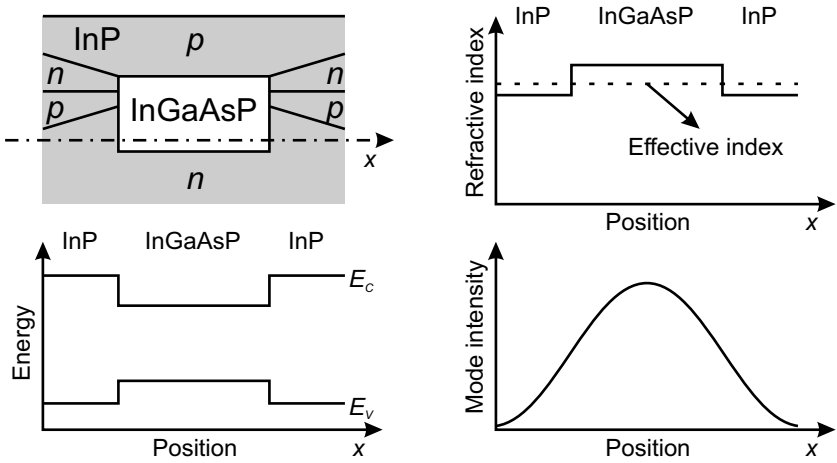

Figure 2.3 Typical InGaAsP/InP waveguide structure with energy band diagram, refractive index profile, and intensity distribution of the waveguide mode. The core InGaAsP layer has both a higher refractive index, yielding optical confinement, as well as a lower band-gap energy ($E_g = E_C - E_V$), yielding confinement of injected carriers.

In optical filters, two types of parameters govern the filter transfer function: the physical dimensions and the refractive indices of the different elements that make up the filter. The same applies to the roundtrip phase condition, as can be seen from (2.1). Since only monolithically integrated lasers are considered here, no change of any mechanical parameter can be used for tuning. This only leaves the effective refractive index of the optical waveguide as tuning parameter.

Figure 2.3 shows a cross-section of a typical InGaAsP/InP waveguide, as is used in various laser structures. For application in the tuning sections, the band-gap energy E_g (= $E_C - E_V$) of the quaternary InGaAsP material is chosen sufficiently larger than the energy $h\nu$ of the photons generated by the laser, such that the material is transparent for these photons. The effective refractive index can be seen as a weighed average of the refractive indices of the different layers that build the waveguide. The weight of a certain layer's refractive index is more or less equal to the fraction of the optical power of the waveguide mode that is confined within this layer. Thus, the effective index is a function of the refractive indices of the different layers that build the optical waveguide and their physical dimensions. Electronic variation of the refractive index of any of these layers, e.g. the InGaAsP core layer, yields a change of the effective refractive index of the waveguide. If this waveguide is part of an optical filter, the frequency of maximal transmission/reflection of the filter will vary accordingly. If, on the other hand, the waveguide is part of a phase shifter section, then the optical length of this section will change and the phase resonance frequencies will move.

In practice, three physical mechanisms can be used to change the refractive index of a semiconductor: injecting free carriers, applying an electrical field, and changing the temperature.

2.1.1 Carrier-induced index change

In the InGaAsP/InP double hetero-structure waveguide as depicted in Figure 2.3, the undoped InGaAsP core layer is sandwiched between a p-doped and an n-doped InP cladding layer. If the resulting p-i-n diode is forward-biased, majority carriers flow from the doped cladding layers to the undoped core layer (holes from the p-doped layer, electrons from the n-doped layer). Because of the higher band-gap of the InP cladding layers, the injected carriers are confined to the InGaAsP layer and thus high hole densities P and electron densities N can be attained ($N = P$ because of charge neutrality). The injected electron-hole plasma is the source of a number of effects influencing the refractive index [2]-[3].

Band-filling

The injected electrons occupy the lowest energy states in the conduction band, just as the injected holes fill the states in the valence band closest to the band edge (which is the same as saying that electrons are removed from the upper energy states in the valence band). Consequently, on average higher photon energies $h\nu$ are required to excite electrons from occupied energy states in the valence band to empty energy states in the conduction band. This causes a reduction of the absorption coefficient $\alpha(\nu)$ (i.e. the material absorption per unit length) for photon energies $h\nu$ slightly above the nominal band-gap energy.

Band-gap shrinkage

Electron-electron interactions at the densely populated states at the bottom of the conduction band reduce the energy of the conduction band edge E_C. A similar correlation effect for holes increases the energy of the valence band edge E_V. The sum of these effects causes a band-gap shrinkage, which lowers the minimum photon energy for which significant absorption occurs.

Free-carrier absorption (intra-band absorption)

A free carrier can absorb a photon and move to a higher energy state within a band. The excess energy is released in the form of lattice vibrations as the carrier relaxes towards its equilibrium state.

Inter-valence band absorption

For holes, another important absorption mechanism exists: inter-valence band absorption (IVBA). In this case, transitions occur between the heavy hole valence band and the spin-orbit split-off valence band [4]-[5].

Through the combination of these effects, the absorption as a function of the photon frequency $\alpha(\nu)$ changes significantly with carrier density. The absorption coefficient is proportional to the imaginary part of the refractive index n'':

$$\alpha(\nu) = -2\frac{2\pi\nu}{c} n''(\nu) \tag{2.3}$$

Since changes in the imaginary part ($\Delta n''$) and the real part ($\Delta n'$) of the refractive index are linked through the Kramers-Kronig relations:

$$\Delta n'(\nu) = \frac{2}{\pi} P\int_0^\infty \frac{\nu' \Delta n''(\nu')}{\nu'^2 - \nu^2} d\nu' = -\frac{c}{2\pi^2} P\int_0^\infty \frac{\Delta\alpha(\nu')}{\nu'^2 - \nu^2} d\nu' \tag{2.4}$$

these effects also yield a change in refractive index, even at photon energies below the band-gap. It appears that for typical carrier densities (~10^{18} cm^{-3}), and for photon energies sufficiently (~0.1 eV) below the band-gap energy, the refractive index decreases linearly with the carrier density N [3].

$$n'(N) = n'_0 + \frac{\partial n'}{\partial N} N \qquad \text{with} \qquad \frac{\partial n'}{\partial N} < 0 \tag{2.5}$$

Normal values for $\partial n'/\partial N$ at frequencies around 193 THz (wavelengths around 1.55 µm) are on the order of -10^{-20} cm^3. The effective refractive index n_{eff} of the waveguide obviously also decreases linearly with carrier density:

$$n_{eff}(N) = n_{eff,0} + \Gamma \frac{\partial n'}{\partial N} N \tag{2.6}$$

Here Γ is the optical confinement factor of the mode propagating along the waveguide, i.e. the ratio of the mode power in the core layer to the total mode power, see e.g. [1]. Through careful design of the core material composition, the core dimensions, and the cladding doping, effective index variations up to -0.04 can be achieved [3].

Unfortunately, at the same time the absorption losses in the core layer increase linearly with carrier density, mainly due to free-carrier and inter-valence band absorption (for the same photon energies of about 0.1 eV below the band-gap). The coupling between changes in the real and the imaginary part of the refractive index (at a particular photon frequency ν) is commonly described by means of the linewidth-enhancement factor (also called chirp parameter, alpha factor…):

$$\alpha_H = -\frac{\partial n'/\partial N}{\partial n''/\partial N} = 2\frac{2\pi\nu}{c}\frac{\Delta n'}{\Delta\alpha} \tag{2.7}$$

A typical value for InGaAsP material with a band-gap wavelength of 1.3 µm in the 193 THz frequency range is -20. Because the loss and (effective) index changes of the waveguide scale equally with the confinement factor, the alpha factor of the waveguide equals the alpha factor of the core material.

The carrier density N is determined by the current I through the forward biased hetero-junction, as described by the carrier rate equation:

$$\frac{dN}{dt} = \frac{I}{qLwd} - \left(AN + BN^2 + CN^3\right) \tag{2.8}$$

Here q is the electron charge and L, w, and d are the length, width, and thickness of the core respectively. The terms between brackets describe the non-radiative, radiative and Auger recombination processes respectively. Since the injected electron-hole pairs recombine, a sustained current must be applied to the tuning section in order to maintain a certain carrier density. The injection-recombination process has a relatively large time constant (several nanoseconds), which limits the tuning speed.

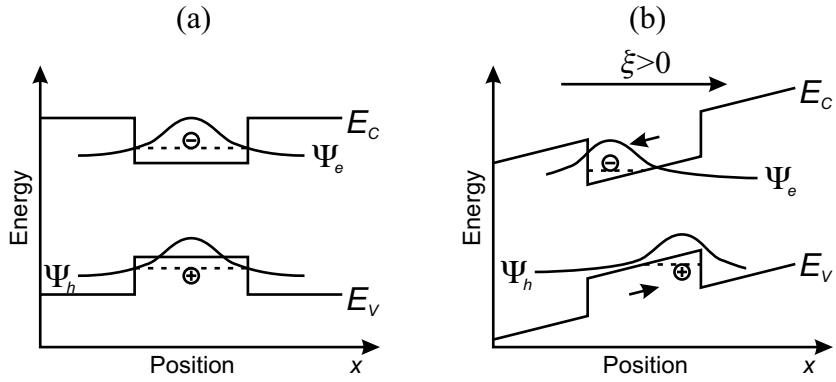

Figure 2.4 The quantum confined Stark effect. By applying an electric field ξ perpendicular to a quantum well structure (a), the band edges are tilted (b). Consequently, the electron and hole wavefunctions are shifted with respect to each other and their energy difference (i.e. the effective band-gap energy) is reduced [1], [8].

Another disadvantage is the parasitic heating of the waveguide due to the non-zero series resistance of the tuning diode (Joule heating) and the non-radiative recombination processes. The resultant thermal tuning partially counteracts the carrier-induced tuning (cf. §2.1.3). If very accurate tuning is required, the thermal effects will even further reduce the tuning speed. Indeed, because of the large time-constants of thermal processes (ranging from microseconds to milliseconds), it will take a long time before the refractive index has completely stabilised.

2.1.2 Electric-field-induced index change

In bulk III/V-semiconductors, the electric-field dependence of the absorption and the refractive index is rather weak. Two effects change the refractive index when an electric field is applied: the linear electro-optic (or Pockels) effect and the quadratic electro-optic (or Franz-Keldysh) effect [6]-[7]. Typical strengths for both effects in InGaAsP material, at photon energies below the band-gap are [7]:

$$\begin{aligned} \Delta n_{Pockels} &\approx -3 \cdot 10^{-11}\ \mathrm{m/V} \cdot \xi \\ \Delta n_{FK} &\approx +1 \cdot 10^{-18}\ \mathrm{m^2/V^2} \cdot \xi^2 \end{aligned} \tag{2.9}$$

Hence, both effects counteract each other and even with a strong applied field ($\xi \approx 10^7$ V/m) the refractive index change is only on the order of 10^{-4}.

However, in multi-quantum well (MQW) structures these changes are greatly enhanced by the quantum confined Stark (QCSE) effect [8]-[9]. In this case, the core of the tuning waveguide consists of a number of thin "well" layers (a few nanometers thick) with low band-gap, separated by thicker "barrier" layers with higher band-gap (Figure 2.4). In the narrow potential wells quantisation effects occur: the conduction and valence band are split up into a number of sub-bands. The effective band-gap energy, i.e. the energy difference between the first order sub-bands in conduction and valence band, is larger than the band-gap of the corresponding bulk material.

If an electric field is applied perpendicular to the quantum wells, the band edges are tilted. Consequently, the electron and hole wavefunctions are shifted with respect to each other and their energy difference (i.e. the effective band-gap energy) is reduced. This also shifts the absorption edge to lower frequencies and thus modifies the refractive index, even at frequencies below the absorption edge, as can be seen from the Kramers-Kronig relation (2.4). Of course, significant changes of the refractive index only occur for photon energies near the band-gap energy, where also significant absorption occurs. Hence, a careful adjustment of the laser frequency and quantum well structure is required. The refractive index changes are normally on the order of 10^{-3} to 10^{-2}, depending on how close the laser wavelength is to the band-gap wavelength of the quantum well. The chirp parameter α_H is usually only about 10 [10]. Using more complicated quantum well structures, consisting of two asymmetric coupled quantum wells, somewhat larger refractive index changes are achievable with a higher alpha factor and therefore lower losses [11]-[12].

What matters for applications in tunable lasers is the change in effective refractive index of the waveguide (2.6). Since quantum wells are very thin, the optical confinement Γ in a single quantum well is low (only a few percent). By stacking a number of quantum wells separated by barrier layers into a multi-quantum well (MQW) structure, the confinement factor is roughly multiplied by the number of wells. Nevertheless, even then the confinement is still much lower than in the bulk waveguide core that is used for the carrier-induced tuning (0.1-0.2 versus 0.4-0.7), because a significant part of the mode field is located within the barrier layers. Thus, the maximum effective index change that can be achieved with electro-optic effects is only about $2 \cdot 10^{-3}$.

On the other hand, electric-field-induced tuning also has some advantages. Just as the bulk waveguide core used for carrier-induced tuning, the (undoped) MQW structure is placed between a p-doped and an n-doped cladding layer. In order to apply a strong electric field to the MQW, the p-i-n diode is now reverse-biased, which means that almost no current flows and no extra heat is generated. Furthermore, no carrier concentrations have to be built up, so the tuning can be almost instantaneous. The tuning speed is only limited by parasitic capacitances and inductances and the rise time can be on the order of a few tens of picoseconds.

2.1.3 Thermally-induced index change

The refractive index of III/V-semiconductors also exhibits considerable temperature dependence. A well-known rule of thumb is that the emission wavelength of a single-mode InGaAsP/InP laser emitting in the 1550 nm (193 THz) region increases with temperature at a rate of approximately 0.1 nm/K [13]. Accordingly, the temperature coefficient of the refractive index $\partial n'/\partial T$ is about $2 \cdot 10^{-4}$ K^{-1}. Note that with thermal tuning the confinement factor is always 1, since both core and cladding of the waveguide are heated. Heating the entire laser however has the disadvantage that the threshold current increases and the differential efficiency (change in output power per unit change in drive current) decreases. Moreover, driving a laser at high temperatures for longer periods reduces the lifetime of the device. Hence, the temperature variation usually has to be limited to a few tens of degrees.

Table 2.1 Comparison of the physical mechanisms for electronic refractive index variation, quoting typical parameter values [1].

Parameter	*Carriers*	*Electric field*	*Temperature*
$\Delta n'$	-0.05	-0.01	0.01
Γ	0.5	0.2	1
Δn_{eff}	-0.025	-0.002	0.01
α_H	-20	-10	large
3-dB bandwidth	100 MHz	> 10 GHz	< 1 MHz
power consumption	large	negligible	very large

If the heating is only applied to the tuning section(s) of the laser, and the thermal isolation is sufficient to avoid excessive heating of the active section, higher temperatures can be accepted. Usually resistive heating is used. In practice this is done by reverse biasing the tuning diode described in §2.1.1 [14], by integrating a resistor in the top InP cladding layer [15], or by placing thin-film resistive heaters on top of the waveguide [16]. A big advantage of this method is that the heating only has a limited influence on the absorption losses in the tuning waveguide, yielding a high alpha parameter. Probably the largest drawback of thermal tuning is the slow response speed, which can range from microseconds to milliseconds.

Some heat is also generated when carrier-induced tuning is used, due to the non-zero resistance of the tuning diode and the non-radiative recombination processes (cf. §2.1.1). It should be noted that the carrier effects decrease the refractive index, whereas the thermal effect increases the refractive index. This ultimately limits the tuning range achievable using carrier injection. At low tuning currents, the carrier-induced refractive index change is dominant and the refractive index decreases. At some point, though, the thermal tuning efficiency becomes larger than the carrier-induced tuning efficiency, since carrier density increases sub-linearly with current (cf. (2.8)), whereas the temperature increases super-linearly with current. If the current is raised beyond that point, the refractive index starts to increase again.

2.1.4 Comparison of tuning mechanisms

The tuning mechanisms are compared in Table 2.1, which summarises the typical parameter values mentioned in the above paragraphs. The electric-field-induced tuning has the advantages of low power consumption and very high tuning speed, but on the other hand, only small effective index changes are achievable, with considerable absorption losses. Thermal tuning yields larger index changes and is easiest to implement, but requires a very high electrical input power and has a low response speed. At present, the preferred mechanism seems to be carrier-induced tuning, which has so far yielded the largest tuning ranges, at reasonable tuning speeds (if the parasitic thermal effects can be neglected), yet at the cost of considerable power consumption.

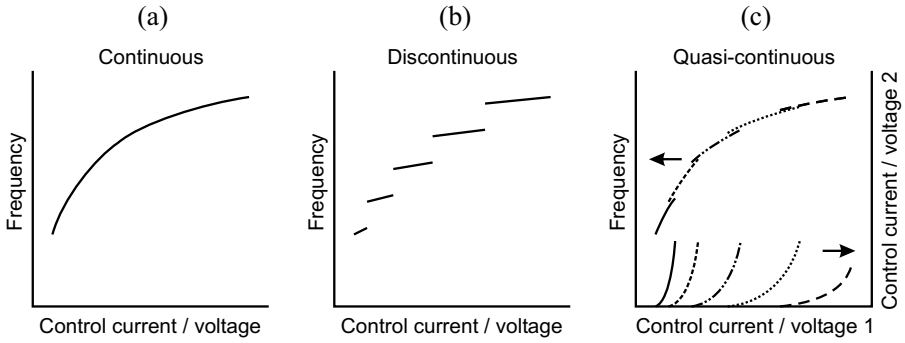

Figure 2.5 Emission frequency versus control current(s) or voltage(s) for continuous (a), discontinuous (b) or quasi-continuous tuning (c).

2.2 Characteristics of tunable lasers

2.2.1 Tuning range – tuning accuracy

The frequency tuning range is naturally the first property by which a tunable laser is evaluated. When tuning ranges of different lasers are compared, care has to be taken though that comparisons are made on the same basis. Normally three different types of tuning are distinguished: continuous, discontinuous, and quasi-continuous tuning. Figure 2.5 illustrates the basic frequency versus control current (or voltage) characteristics for these tuning schemes.

Continuous tuning

Continuous tuning is the ideal scheme from a practical point of view (Figure 2.5(a)). The laser frequency can be tuned smoothly, in arbitrarily small steps, by adjusting a single control parameter (or multiple control parameters, provided there is a 1-to-1 relation between any two of these parameters). Continuous tuning over a small range can for example be achieved by merely adjusting the optical length of the cavity, without changing the frequency of minimal roundtrip loss (Figure 2.2(b)). In that case, the continuous tuning range is limited to somewhat less than the cavity mode spacing $\Delta\nu$.

If the cavity modes and the frequency of minimal loss are tuned simultaneously, larger continuous tuning ranges are possible. In most tunable lasers, this however requires synchronised adjustment of at least two control parameters. Owing to the stringent requirement that the same cavity mode has to remain the lasing mode across the entire tuning range, the tuning range is smallest in the continuous tuning scheme. The present record value is about 13 nm or 1.6 THz for lasers emitting in the 193 THz frequency region [17]. On the other hand, for the longitudinally integrated tunable lasers that will be described further on, the continuous tuning range is usually limited to a few 100 GHz [18].

Discontinuous tuning

Larger tuning ranges can be achieved if sudden, discontinuous frequency changes are allowed for. An example was already given in Figure 2.2(a). When the frequency of minimal roundtrip loss is tuned without adjusting the roundtrip phase, the emission frequency initially remains constant. Only when a cavity mode adjacent to the lasing mode experiences a lower loss, does the laser frequency jump to this adjacent mode. In practice the tuning of the loss minimum is always accompanied by some tuning of the cavity modes, as is illustrated in Figure 2.5(b).

Here the tuning range is not limited by the tunability of a single longitudinal mode, but rather by the tunability of the roundtrip loss minimum. An upper limit is naturally also imposed by the bandwidth of the optical gain in the active section of the laser. Nonetheless, if the active section consists of a multi-quantum well (MQW) structure, this bandwidth can be more than 100 nm (12.5 THz around 193 THz). Discontinuous tuning ranges of more than 100 nm have indeed already been demonstrated [19]-[20].

Quasi-continuous tuning

Quasi-continuous tuning is achieved by joining overlapping continuous tuning ranges in order to get full frequency coverage over a wider range. Quasi-continuous tuning thus requires the adjustment of at least two control parameters. The principle is illustrated in Figure 2.5(c) for two controls. By setting an appropriate combination of the two parameter values, the laser can be tuned to any frequency within a wide range. Still, there is no 1-to-1 relation between the two controls across the entire range, so there is no possibility to tune smoothly from one frequency to any other frequency. Continuous tuning is only achievable over the ranges corresponding to individual control 2 versus control 1 curves. Referring to Figure 2.2, quasi-continuous tuning is for example accomplished by tuning a cavity mode and the loss minimum synchronous over a range equal to the longitudinal mode spacing, then resetting the cavity modes to their original locations, and subsequently tuning the next cavity mode simultaneously with the loss minimum, ...

For dense wavelength division multiplexing (DWDM) applications, a typical requirement for the tuning range is complete frequency coverage across the entire C-band (i.e. roughly from 192 to 196 THz) or L-band (i.e. from 187 to 191 THz). This has so far only been achieved in the quasi-continuous tuning regime, see e.g. [21]-[22]. The number of frequency channels that can effectively be used in these bands is mainly limited by the accuracy with which the laser can be tuned to a particular channel. The present version of ITU-T Recommendation G.692, “Optical interfaces for multi-channel systems with optical amplifiers,” which contains specifications for WDM systems, proposes a channel grid with 50 or 100 GHz channel spacing, anchored at 193.1 THz [23]. At 50 GHz spacing, about 80 channels would be available in both C- and L-band. For these multi-channel systems, a frequency accuracy of ±10% of the channel separation is commonly required. Therefore, if one wants to reduce the channel spacing by a factor N, the frequency accuracy has to be improved by the same amount.

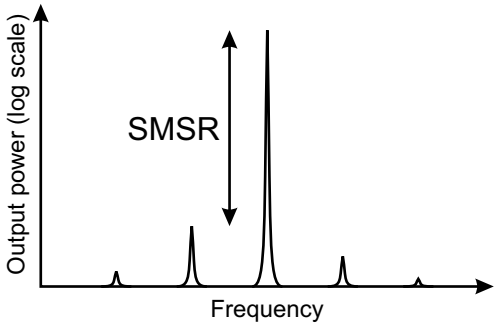

Figure 2.6 Definition of the side-mode suppression ratio (SMSR): ratio of the power in the main (lasing) mode to the power in the strongest side-mode (usually expressed in dB).

In the case of quasi-continuous tuning, the control of a tunable laser can be quite complicated, because two or more parameters have to be adjusted at the same time to change the laser frequency. Therefore, the laser is usually built into a module containing a microprocessor and drive electronics that allow easy, command-based control of the laser frequency and output power. The set-points for the different frequency channels are stored in a look-up table in an EPROM (erasable, programmable read-only memory). When the laser has to be tuned to a particular channel, the microprocessor controller interprets the incoming command, reads the appropriate values from the look-up table and adjust the control currents/voltages accordingly. The initial frequency error is hence mainly limited by the accuracy of the procedure that was used to generate this look-up table (assuming the current/voltage sources have ample resolution and are sufficiently accurate). As mentioned in the introductory chapter, some form of feedback control can also be applied to improve the accuracy and stability of the emission frequency.

2.2.2 Side-mode suppression ratio

Above, we implicitly assumed that the laser was always emitting in a single longitudinal mode. Still, this is only true if all cavity modes other than the lasing mode experience a roundtrip loss that is sufficiently higher than the roundtrip loss of the lasing mode. For applications in optical communication systems, this is an essential requirement because fiber dispersion is proportional to the spectral width of the carrier wave, which means that multi-mode operation would seriously limit the achievable transmission distance. The spectral purity of a laser is quantified by the side-mode suppression ratio (SMSR), which is defined as the ratio of the power in the dominant mode to the power in the strongest side-mode. The SMSR is usually expressed in decibels (Figure 2.6). For telecom applications, a SMSR of at least 30 dB, preferably even 40 dB, is required.

It was already mentioned that semiconductor lasers have a very wide gain bandwidth (several THz). Because typical mode spacings are below 100 GHz (corresponding to a cavity length of 400 μm or more), this means that without any filtering the laser may oscillate in more than one longitudinal mode simultaneously. How this filtering can be implemented will be illustrated in the following sections. Apart from

designing a sufficiently narrow intra-cavity filter, in a tunable laser care also has to be taken that a cavity mode is more or less aligned with the loss minimum of the filter (cf. Figure 2.2). Even with a filter bandwidth comparable to the mode spacing, one can still get two-mode operation, namely in the case when the loss minimum lies halfway between two cavity modes.

2.2.3 Output power

For communication applications, a fiber-coupled power of a few mW is needed. Since all of the tuning mechanisms described in §2.1 not only change the refractive index, but also increase losses to some extent, one additionally has to consider the variation of output power across the tuning range. These variations have to be kept as low as possible, either by cleverly designing the laser or by adjusting the active section drive current (e.g. by using some form of feedback control).

2.2.4 Linewidth

For many applications, the spectral linewidth is an important characteristic of single-mode laser diodes, e.g. for coherent communication systems using optical heterodyne detection (cf. §1.1.2). For coherent systems, a linewidth of no more than a few MHz is required. However, for systems using direct detection, the linewidth can be at least an order of magnitude larger. Of course, a prerequisite for narrow linewidths is that the current and/or voltage sources that drive the laser exhibit low noise levels.

In lasers that use the quasi-continuous or discontinuous tuning schemes, the linewidth can vary strongly. The linewidth is relatively low as long as the lasing mode and the loss minimum are more or less aligned, but singularities in the linewidth arise at the mode boundaries, where frequency jumps occur [24].

With respect to linewidth, the three tuning mechanisms behave quite differently. Thermal and field-induced tuning have negligible effects on the linewidth, provided the lasing mode coincides with the loss minimum. However, when carrier-induced tuning is used, considerable linewidth broadening is observed [25], more than can be expected from the classic Schawlow-Townes-Henry theory [26] (even when taking into account the broadening due to increased losses). This excess broadening is attributed to injection-recombination shot noise in the tuning section(s) [27]. The shot noise of the carrier injection and recombination processes causes carrier density fluctuations, which lead to refractive index and loss variations. These in turn produce fluctuations of the instantaneous laser frequency that finally lead to a broadened spectral line. This broadening can be avoided to a large degree by using a voltage source (low internal resistance) instead of a current source (high internal resistance) to bias the tuning section(s) [28].

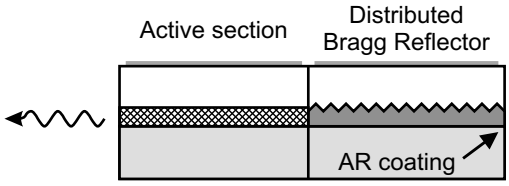

Figure 2.7 Longitudinal cross-section of a 2-section distributed Bragg reflector (DBR) laser.

2.3 Distributed Bragg reflector laser

After the distributed feedback (DFB) laser, the distributed Bragg reflector (DBR) laser is the most common design for a single-mode laser diode [29]. The basic DBR laser consists of two longitudinally integrated sections: an active section and a reflector section (Figure 2.7). The waveguide core of the active section has a band-gap matching the desired emission frequency and hence provides optical gain if sufficient carriers are injected. The core material of the reflector in contrast has a higher band-gap, such that the material is transparent (passive) for the laser light. Along the reflector section, a diffraction grating is embedded in the waveguide, yielding a periodic modulation of the effective refractive index of the waveguide.

This grating can for example be obtained by periodically varying the thickness of the waveguide core. The grating pattern is commonly defined by a holographic process, in which a photo-resist layer is exposed by two interfering beams of ultra-violet light. The angle of the beams is chosen such that an interference pattern with period Λ is generated. Subsequently, the resist is developed and the grating pattern is etched into the semiconductor material. Finally, the etched grating structure is overgrown with the top cladding layer, which has a higher band-gap and a lower refractive index than the core layer. Since the effective index of the waveguide increases with the thickness of the high-index core layer, it exhibits the same periodic variation as the thickness of the core layer.

Because of the grating, the passive section reflects light back in a narrow frequency band. This can be understood intuitively as follows. Every tooth of the grating reflects a small amount of light. Reflections from consecutive teeth of the grating have a phase difference that depends on the ratio of the wavelength in the material λ/n_d to the grating period Λ. Here $\lambda = c/\nu$ is the vacuum wavelength, c is the speed of light in vacuum, and n_d is the average effective index. If the wavelength in the material equals twice the grating period, successive reflections interfere constructively and a strong overall reflection is obtained. This condition defines the Bragg frequency ν_B:

$$\nu_B = \frac{c}{2n_d(\nu_B)\Lambda} \tag{2.10}$$

If there is a mismatch between the frequency of the incident light and the Bragg frequency, the reflection is much lower. To avoid interference between reflections

from the grating and reflections from the end facet, an anti-reflection (AR) coating is usually applied to the facet.

A more quantitative analysis of the reflectivity of a Bragg grating is usually performed using the coupled-mode theory [30]. The modulated effective refractive index is written as

$$n'(z) = n_d + \mathrm{Re}\left[\Delta n_1 e^{j(2\beta_0 z+\phi)}\right] + \ldots \tag{2.11}$$

where $\beta_0 = \pi/\Lambda$, and Δn_1 is first order Fourier component of the refractive index modulation, which is assumed to be much smaller than n_d. The model is based on the scalar wave equation for the electric field

$$\frac{\partial^2 E}{\partial z^2} + \left[(n' + jn'')k_0\right]^2 E = 0 \tag{2.12}$$

where E is the complex amplitude of a field with frequency ν, which is assumed to be independent of the x and y co-ordinates, and $k_0 = 2\pi\nu/c$ is the free-space propagation constant. Assuming that $n'' << n'$ and $\Delta n_1 << n_d$, we have

$$\left[(n' + jn'')k_0\right]^2 \approx \beta^2 + 2j\beta\zeta + 4\beta\,\mathrm{Re}\left[\kappa\, e^{j(2\beta_0 z+\phi)}\right], \tag{2.13}$$

with $\beta = n_d k_0$ the mode propagation constant, $\zeta = n''k_0 = -\alpha/2$ the mode *field* gain coefficient, and κ the so-called coupling coefficient (usually expressed in cm^{-1}):

$$\kappa = \frac{\pi\nu\Delta n_1}{c} \tag{2.14}$$

The coupling coefficient is a measure for the strength of the backward scattering by the grating structure. In principle, the periodic index modulation generates an infinite set of diffraction orders, but in the vicinity of the Bragg frequency, i.e. $\Delta\beta = \beta - \beta_0 << \beta_0$, only two modes are more or less in phase synchronism. These are the two counter-propagating waves, which are coupled due to the Bragg scattering. We can therefore expand the electric field in the forward and backward propagating modes:

$$E(z) = R(z)e^{-j\beta_0 z} + S(z)e^{j\beta_0 z} \tag{2.15}$$

where the functions $R(z)$ and $S(z)$ vary slowly as a function of z, so that their second derivatives in (2.12) can be neglected. If we insert (2.15) into the wave equation (2.12), take into account all of the above assumptions, and collect terms with identical phase factors ($\exp(-j\beta_0 z)$ and $\exp(j\beta_0 z)$ respectively), we obtain the coupled-mode equations:

$$\begin{aligned} -\frac{dR}{dz} + (\zeta - j\Delta\beta)R &= j\kappa^* e^{-j\phi} S \\ \frac{dS}{dz} + (\zeta - j\Delta\beta)S &= j\kappa\, e^{j\phi} R \end{aligned} \tag{2.16}$$

By solving these coupled first-order differential equations, it can be shown that the field reflectivity of a distributed Bragg reflector of length L is given by:

$$r(\nu) = \frac{-j\kappa^* e^{-j\phi}\sinh(\gamma L)}{\gamma\cosh(\gamma L) - (\zeta - j\Delta\beta)\sinh(\gamma L)} \tag{2.17}$$

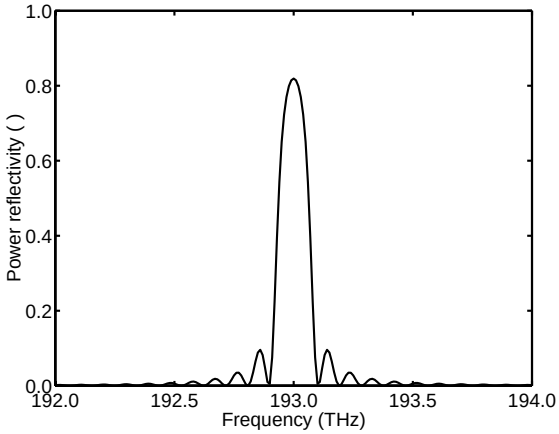

Figure 2.8 Power reflectivity spectrum of a distributed Bragg reflector with $\kappa L = 1.5$.

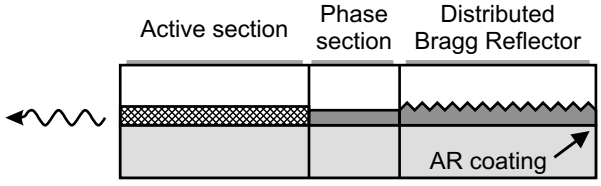

Figure 2.9 Longitudinal cross-section of a 3-section tunable distributed Bragg reflector (DBR) laser.

where
$$\gamma^2 = |\kappa|^2 + (\zeta - j\Delta\beta)^2 \tag{2.18}$$

Figure 2.8 shows a characteristic power reflectivity spectrum $R(\nu) = |r(\nu)|^2$ of a distributed Bragg reflector with $\kappa L = 1.5$.

In 1977, Okuda and Onaka proposed the first integrated tunable laser diode, which was essentially a tunable 2-section DBR laser [31]. Indeed, if the effective refractive index of the DBR section can be changed electronically, the frequency of minimal roundtrip loss (i.e. the Bragg frequency ν_B) can be shifted, thus enabling discontinuous tuning of the laser frequency [32] (cf. Figure 2.2(a)). In order to make quasi-continuous tuning possible an additional phase shifter section is needed [33] (Figure 2.9). This section has the same structure as the DBR, except for the grating. The roundtrip phase condition in this case reads (cf. (2.1)):

$$\frac{2\pi\nu_k}{c}\left(2n_aL_a + 2n_pL_p\right) + \phi_d(\nu_k) = 2\pi k \tag{2.19}$$

Here n_x and L_x are the effective index and length of the active and phase section; $\phi_d = -\arg(r)$ is the phase of the reflection from the grating.

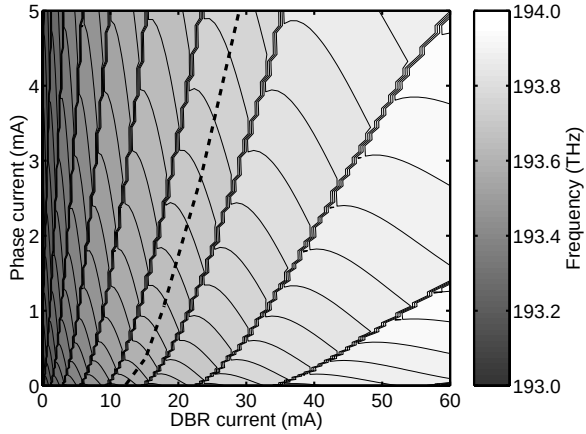

Figure 2.10 Tuning characteristic of a 3-section DBR laser. Contour plot of frequency as a function of DBR and phase current (20 GHz increments). The dashed line indicates a possible trajectory for continuous tuning.

If the laser is biased above threshold, the carrier density in the active section is clamped. Changing the active section current therefore has no effect on the index of the active section (if thermal effects are neglected). The index of the phase section on the other hand can be adjusted electronically, e.g. through current injection. Using this a cavity mode can be tuned to the Bragg frequency.

Figure 2.10 displays a tuning characteristic of such a 3-section DBR laser. The cavity mode hops are easily discernible by the fact that at the hops multiple frequency contours coincide. Continuous tuning is possible along curves that lie approximately halfway between two mode hop contours, as the one indicated by the dashed line. For these points, the SMSR is normally higher than 30 dB. This particular laser has a quasi-continuous tuning range of approximately 1 THz (8 nm), which is a typical value for DBR lasers. The tuning range is limited by the maximum index change Δn_d that can be reached in the DBR section (cf. §2.1.3):

$$\frac{\Delta \nu_{B,max}}{\nu_B} = -\frac{\Delta n_{d,max}}{n_{d,g}(\nu_B)} \tag{2.20}$$

where

$$n_{d,g}(\nu) = n_d(\nu) + \nu \frac{\partial n_d}{\partial \nu} \tag{2.21}$$

represents the group effective index, which includes the dispersion of $n_d(\nu)$ around ν_B. Through careful optimisation of the waveguide structure [3], the tuning range for carrier-induced tuning can be increased to about 2 THz [34]-[35].

Note again that absorption losses in the DBR and phase sections increase with the applied current. If the active section current is kept constant during tuning, the output power from the front facet generally varies by 1 to 2 dB.

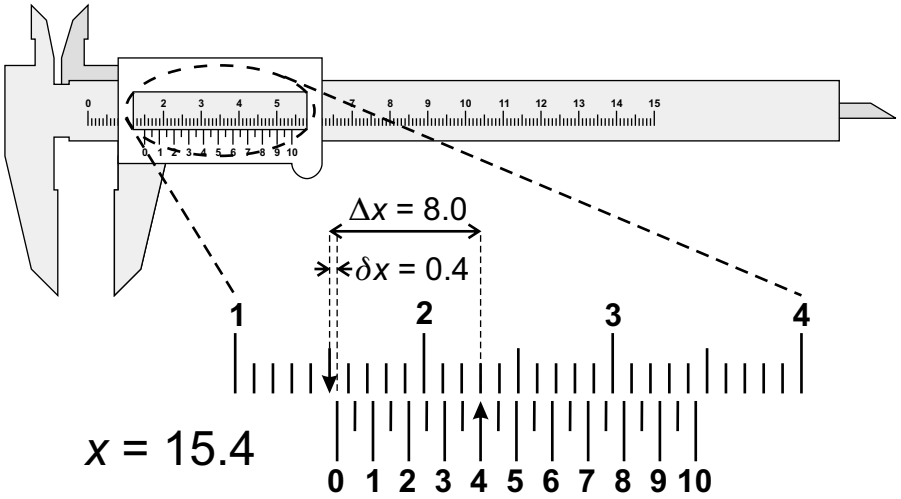

Figure 2.11 A Vernier calliper, using two scales with a pitch difference of 1/20. A shift of the lower scale by an amount δx leads to a shift of the point where tick marks on both scales coincide by an amount $\Delta x = 20 \cdot \delta x$.

2.4 Increasing the tuning range of DBR-type lasers

The tuning ranges of conventional DBR lasers, 1 to 2 THz, are significantly smaller than the available gain bandwidth of MQW semiconductor material (more than 10 THz) and Erbium doped fiber amplifiers (about 4 THz in the C- or L-band). Consequently, a lot of research effort has been put in the development of integrated lasers with extended tuning ranges, beyond the $\Delta\nu/\nu = -\Delta n/n_g$ limit. The basic principle behind all schemes that have been developed for wide tuning is that a refractive index *difference* is changed rather than the index itself. Therefore, the relative frequency change is equal to a relative change in index difference, which can be significantly larger for similar absolute refractive index variations. In the following paragraphs, we will describe the two most common schemes: one using a Vernier effect between two comb reflectors and the other using the broad tunability of a grating assisted co-directional coupler.

2.4.1 Using a Vernier effect between two comb reflectors

The Vernier calliper (invented by the French scientist Pierre Vernier °1580-†1637) is a well-known tool for high-resolution length measurements. The principle is illustrated in Figure 2.11. The calliper consists of two graduated scales, a main scale like a ruler and a second scale, the Vernier, which slides parallel to the main scale. The two scales have a small relative pitch difference, e.g. 1/20, such that a shift of the slider by an amount δx leads to a shift of the point where tick marks on both scales coincide by an amount $\Delta x = 20 \cdot \delta x$. In other words, any change in position is enhanced by a factor equal to the inverse of the relative pitch difference.

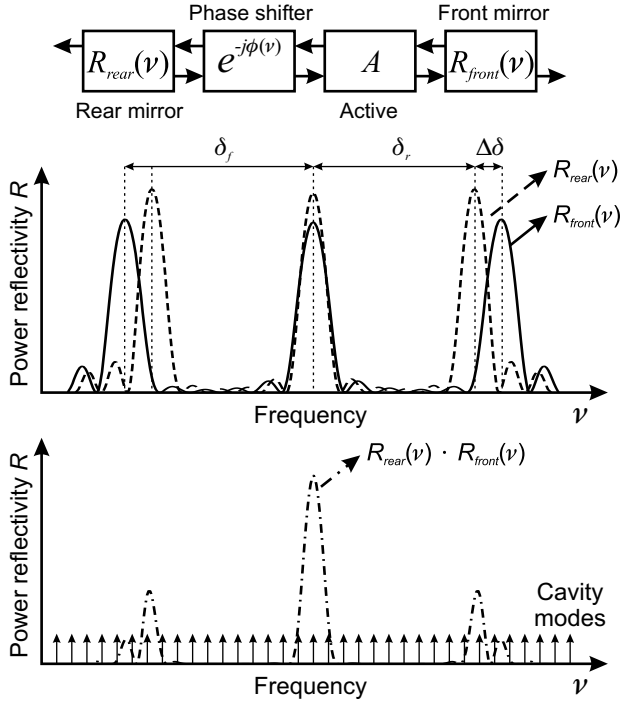

Figure 2.12 Vernier principle applied to a tunable laser, which has two mirrors with comb-shaped reflectivity spectra. Lasing can only occur in the frequency range where reflection peaks coincide.

The same principle can be applied to a tunable laser, if the laser has two mirrors with a comb-shaped reflectivity spectrum [36] (Figure 2.12). The mirrors are designed such that the peak spacing of the front mirror (δ_f) and the rear mirror (δ_r) differ by a small amount $\Delta\delta$. Lasing can then only occur in the frequency range where two peaks coincide, since the cavity roundtrip loss is inversely proportional to the product of both mirror reflectivities. The phase section can again be used to adjust the longitudinal modes, such that a mode can be aligned with the loss minimum.

If one of the mirrors is tuned by $\pm\Delta\delta$, two adjacent peaks coincide and a large change in frequency is obtained. If the phase section is simultaneously adjusted such that a cavity resonance is aligned with the coincident peaks, the frequency changes by an amount δ_f ($-\delta_r$) if the rear (front) mirror is tuned by $\Delta\delta$. Thus, the tuning enhancement is either $F + 1$ or $-F$, where F is defined by:

$$\Delta\delta = \frac{\delta_r}{F} = \frac{\delta_f}{F+1} \tag{2.22}$$

The coincidence of two particular peaks is often called a “super-mode” and the large frequency changes observed when applying the Vernier tuning mechanism are consequently called “super-mode” jumps.

A few simple design criteria for the mirrors can easily be derived:

- The reflection peaks should be sufficiently narrow (relative to the mode spacing $\Delta\nu$) to suppress all cavity modes but one.
- The difference in peak spacing $\Delta\delta$ should be comparable with the width of the reflection peaks. If $\Delta\delta$ is too large, there is a region where the laser frequency is unpredictable during the tuning of a single reflector over an amount $\Delta\delta$. If $\Delta\delta$ is too small, the overlap of adjacent reflector peaks is too large and cavity modes at these frequencies are insufficiently suppressed.
- Care has to be taken that only one pair of peaks coincides at the same time within the gain bandwidth of the laser (especially if F is an integer). This can be done either by designing the mirrors such that strong reflection peaks only occur within a sufficiently limited bandwidth, or by making sure that all other possible coincidences fall outside of the gain bandwidth. Ideal reflectors have a limited number of uniform reflection peaks.

Intermediate tuning, from one longitudinal mode to the adjacent one, is obtained by tuning both reflectors simultaneously. True continuous tuning (fine tuning), requires synchronised adjustment of the two reflectors and the phase section. For full frequency coverage over a wide range (i.e. quasi-continuous tuning), a number of requirements have to be met. The front and rear reflector must be tunable over at least δ_f and δ_r respectively. At the same time, the phase section should allow tuning of the cavity modes by more than the mode spacing $\Delta\nu$.

Practical implementations of this Vernier tuning scheme look much like the 3-section DBR laser in Figure 2.9, but with distributed Bragg reflectors on both sides. The gratings in the DBR sections are modified to obtain multiple reflection peaks. Two examples are discussed below.

Sampled grating DBR

The sampled grating (SG) is technologically the simplest way to obtain a reflectivity spectrum that has periodic maxima [37]. The sampled grating is nothing more than a conventional uniform grating with an appropriate grating pitch Λ, multiplied by a sampling function with period Λ_s, as shown in Figure 2.13. It can be fabricated essentially in the same way as an ordinary Bragg grating. The grating pattern is again defined by exposing a photo-resist layer with the interference pattern of two ultra-violet beams. By periodically masking off part of the photo-resist layer (period Λ_s), the resist is only exposed in the regions with width Λ_g. In the following etch step, the sampled interference pattern is then transferred into the semiconductor.

A qualitative idea of the shape of the reflectivity spectrum can easily be derived from the coupled-mode theory, which says that every spatial Fourier component of the refractive index modulation contributes a peak to the reflection spectrum (cf. §2.3). The Fourier components of the sampled grating are of course obtained by convoluting the Fourier transforms of the uniform grating and the sampling function. The uniform grating has a single Fourier component with a coupling strength κ_u given by (2.14), at a spatial frequency $1/\Lambda$, which corresponds to the Bragg frequency ν_B according to (2.10).

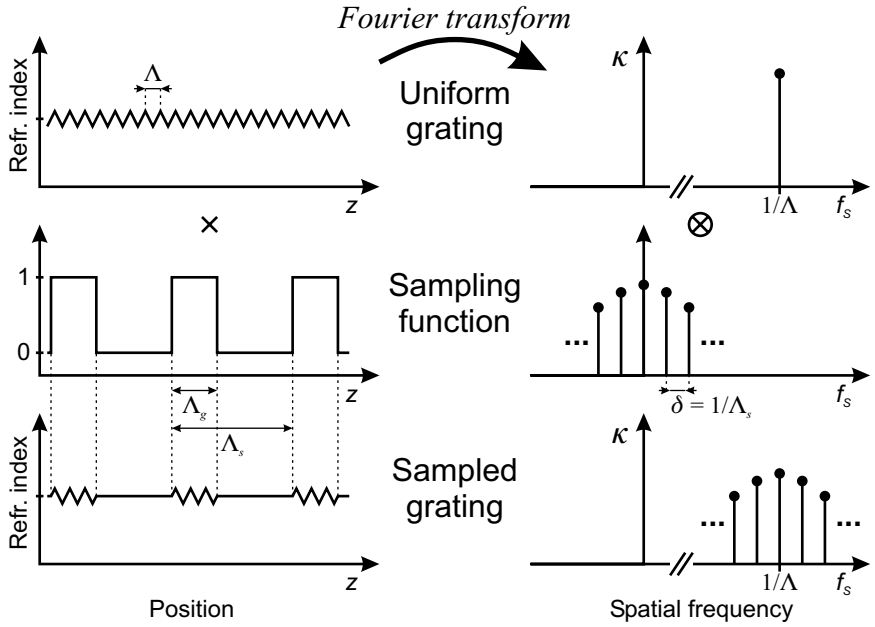

Figure 2.13 Principle of the sampled grating. In real space, the uniform grating is multiplied by a sampling function. In Fourier space, this corresponds to a convolution of the respective spectra. According to the coupled-mode theory, every spatial Fourier component of the refractive index modulation contributes a peak to the reflection spectrum [37].

The Fourier transform of the sampling function on the other hand consists of a comb of peaks with a spatial frequency spacing of $1/\Lambda_s$.

The modulation function is given by (l is an integer):

$$F(z) = \begin{cases} 1 & l\Lambda_s < z < l\Lambda_s + \Lambda_g \\ 0 & l\Lambda_s + \Lambda_g < z < (l+1)\Lambda_s \end{cases} \tag{2.23}$$

From which the amplitudes of the Fourier components are easily obtained as:

$$F_k = \frac{1}{\Lambda_s}\int_0^{\Lambda_s} F(z) e^{-j\frac{2\pi k}{\Lambda_s}z}\,dz = \frac{\Lambda_g}{\Lambda_s}\frac{\sin\left(\pi k\Lambda_g/\Lambda_s\right)}{\pi k\Lambda_g/\Lambda_s} e^{-j\pi k\Lambda_g/\Lambda_s} \tag{2.24}$$

The convolution of both Fourier transforms exhibits peaks centred at $1/\Lambda$, with spacing $1/\Lambda_s$. This leads to strong reflections at frequencies ν_k (cf. (2.10)):

$$\nu_k = \frac{c}{2n(\nu_k)}\left(\frac{1}{\Lambda} + \frac{k}{\Lambda_s}\right) \tag{2.25}$$

The reflection peak spacing is determined by the sampling period Λ_s:

$$\delta = \nu_{k+1} - \nu_k = \frac{c}{2n_g\Lambda_s} \tag{2.26}$$

where n_g is the group refractive index:

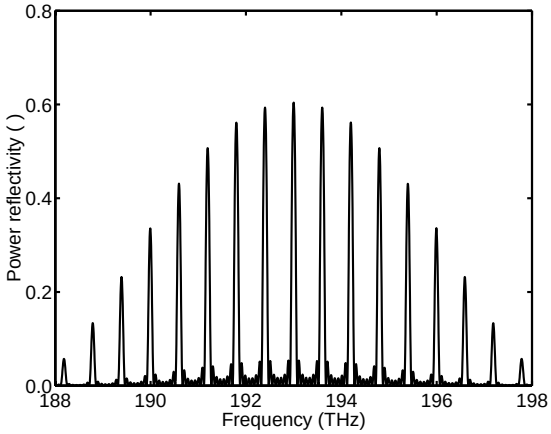

Figure 2.14 Reflection spectrum of a sampled grating DBR, consisting of 8 periods with length $\Lambda_s = 65$ µm. Parameters: sampling duty cycle $\Lambda_g/\Lambda_s = 10\%$, unsampled coupling coefficient $\kappa_u = 200$ cm^{-1}, peak spacing $\delta = 0.6$ THz ($n_g = 3.85$).

$$n_g(\nu) = n(\nu) + \nu \frac{\partial n}{\partial \nu} \tag{2.27}$$

The coupling coefficients at the frequencies ν_k are equal to the product of the coupling coefficient of the unsampled grating κ_u with the Fourier components F_k of the sampling function:

$$\kappa_k = \kappa_u F_k \tag{2.28}$$

If we assume that only one diffracted order is phase matched at any frequency, then the overall reflectivity can be written as the sum of the contributions of the separate Fourier components. In other words, the overall reflectivity is the sum of the reflectivities of individual gratings with Bragg frequencies ν_k and coupling coefficients κ_k (cf. (2.17)):

$$r(\nu) = \sum_k \frac{-j\kappa_k^* \sinh(\gamma_k L)}{\gamma_k \cosh(\gamma_k L) - (\zeta - j\Delta\beta_k)\sinh(\gamma_k L)} \tag{2.29}$$

with

$$\gamma_k^2 = |\kappa_k|^2 + (\zeta - j\Delta\beta_k)^2$$

$$\Delta\beta_k = \frac{2\pi\nu}{c} n(\nu) - \pi\left(\frac{1}{\Lambda} + \frac{k}{\Lambda_s}\right) \tag{2.30}$$

Here L is the length of the sampled grating. A more rigorous calculation of the reflectivity spectrum of sampled gratings using transfer matrices will be presented in Chapter 3. Figure 2.14 shows the result of such a calculation for a sampled grating DBR consisting of 8 periods with length $\Lambda_s = 65$ µm, which leads to a peak spacing $\delta = 0.6$ THz ($n_g = 3.85$).

If waveguide losses are neglected ($\zeta = 0$), then the peak power reflectivity at the frequency ν_k is simply given by:

$$R(\nu_k) = |r(\nu_k)|^2 = \tanh^2(|\kappa_k|L) = \tanh^2(|F_k|\kappa_u L) \tag{2.31}$$

For order zero, and with $L_g = L\Lambda_g/\Lambda_s$ the total length of grating this becomes:

$$R(\nu_0) = \tanh^2(|F_0|\kappa_u L) = \tanh^2(\kappa_u L\Lambda_g/\Lambda_s) = \tanh^2(\kappa_u L_g) \tag{2.32}$$

This is nothing else than the peak reflectivity of a uniform Bragg reflector with coupling coefficient κ_u and length L_g. If $\kappa_u L_g < 0.5$, we can approximate the reflectivity of peak k by $(|\kappa_k|L)^2$. From (2.24) it is clear that the envelope of the reflectivity peaks becomes broader as the sampling duty cycle Λ_g/Λ_s is reduced. For small duty cycles, the number of peaks within the 3 dB bandwidth of the envelope is approximately equal to the inverse of the duty cycle [37]. Reducing the duty cycle requires increasing the unsampled coupling coefficient κ_u to maintain the same peak reflectivity (at constant sampled grating length L). Unfortunately, the technological limit for gratings in InGaAsP/InP waveguides is about 300 cm^{-1}. The example in Figure 2.14 assumes a coupling coefficient $\kappa_u = 200$ cm^{-1} and a sampling duty cycle $\Lambda_g/\Lambda_s = 10\%$, resulting in about 11 peaks within the 3 dB bandwidth.

Super-structure grating DBR

Although it is technologically the simplest way to obtain a comb reflector, the sampled grating does not exhibit the optimum reflection spectrum. As already mentioned, ideally one would have a number of equally spaced, equally strong reflectivity peaks within a limited bandwidth, with close to zero reflectivity outside that bandwidth. The above approach of periodically sampling a uniform Bragg grating in order to obtain multiple reflection peaks around the Bragg frequency can naturally be extended to other types of periodic modulation [38]. Any modulation function that has a comb-shaped Fourier spectrum can be applied. These more general periodically modulated gratings are commonly called super-structure gratings (SSGs). The sampled grating consists of a digital on/off variation of the coupling coefficient κ, so the first option one could think off is a smoother periodic modulation of κ. However, with existing etching technology this is very difficult to implement. A second option is a variation of the grating frequency (or phase). The drawback is that this requires direct writing of the grating pattern on the semiconductor substrate with an electron beam, a slow and hence costly procedure.

The first demonstration of such a super-structure grating consisted of a periodic linear chirp of the grating frequency $f = 1/\Lambda$ [39] (Figure 2.15). Within the super-period of length Λ_s the grating frequency f is varied from $f_a = 1/\Lambda_a$ to $f_b = 1/\Lambda_b$.

$$f(z) = \frac{1}{2}(f_a + f_b) + \frac{z - l\Lambda_s}{\Lambda_s}(f_b - f_a) = f_0 + \frac{z - l\Lambda_s}{\Lambda_s}\Delta f \tag{2.33}$$

for $$(l - \tfrac{1}{2})\Lambda_s < z < (l + \tfrac{1}{2})\Lambda_s$$

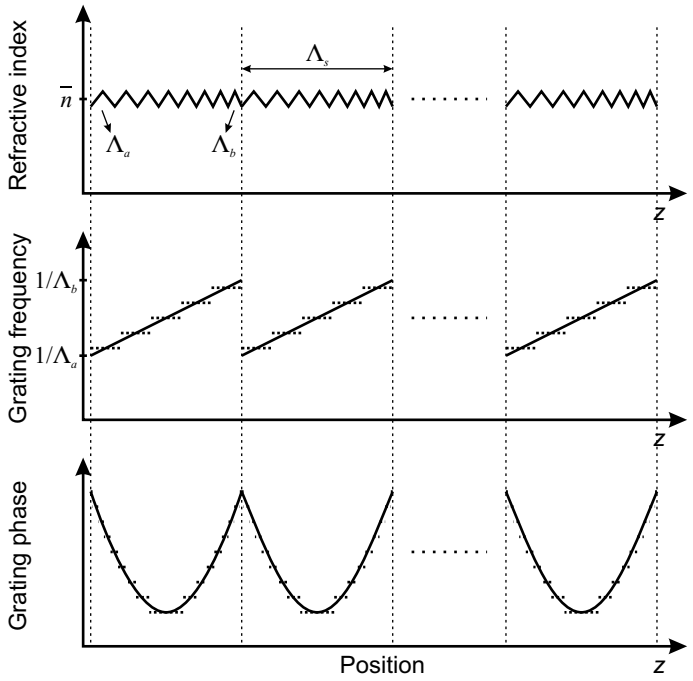

Figure 2.15 Schematic of a linearly chirped super-structure grating. Solid lines indicate the ideal linear frequency chirp, equivalent to a quadratic relative phase variation. Dotted lines indicate practical implementations: discrete frequency changes or discrete phase changes (with uniform grating pitch).

The grating modulation function has a magnitude of one and a quadratic phase term:

$$F(z) = \exp\left[j2\pi\left(f(z) - f_0\right)z\right] = \exp\left[j2\pi\Delta f\,\frac{z - l\Lambda_s}{\Lambda_s}\,z\right] \tag{2.34}$$

As a result, the Fourier coefficients are given in terms of Fresnel integrals [40]:

$$F_k = \frac{1}{\Lambda_s}\int_{-\Lambda_s/2}^{\Lambda_s/2} F(z)e^{-j\frac{2\pi k}{\Lambda_s}z}\,dz = A\int_a^b e^{ju^2}\,du \tag{2.35}$$

where

$$A = \frac{1}{\sqrt{2\pi\Delta f\Lambda_s}}\exp\left[-j\,\frac{(k\pi)^2}{2\pi\Delta f\Lambda_s}\right]$$

$$a = \frac{1}{2}\sqrt{2\pi\Delta f\Lambda_s}\left(-1 - \frac{2\pi k}{2\pi\Delta f\Lambda_s}\right) \tag{2.36}$$

$$b = \frac{1}{2}\sqrt{2\pi\Delta f\Lambda_s}\left(+1 - \frac{2\pi k}{2\pi\Delta f\Lambda_s}\right)$$

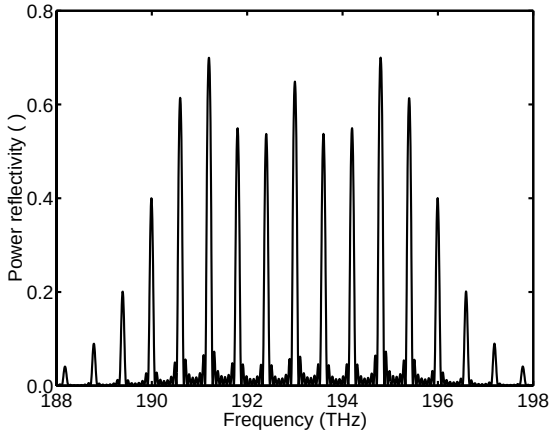

Figure 2.16 Reflection spectrum of a super-structure grating with quadratic phase variation, consisting of 8 periods with length Λ_s = 65 μm. Parameters: peak-to-peak phase variation of 3.05π, coupling coefficient κ_u = 67 cm^{-1}, peak spacing δ = 0.6 THz (n_g = 3.85).

Strong reflection peaks are obtained in the frequency interval determined by the minimal and maximal grating frequency (cf. the Bragg condition (2.10)):

$$f_a < 2n(\nu)\nu / c < f_b \tag{2.37}$$

Due to the limited resolution of the e-beam lithography, a truly continuous chirp can not be accomplished. For this reason, the first super-structure gratings were made by varying the grating frequency in discrete steps [39]-[40], as indicated by the dotted lines in Figure 2.15. For these first implementations, reflection characteristics were rather poor due to the limitations of the e-beam lithography [20]. Fabrication becomes simpler and more reliable if the same grating pitch can be used throughout the SSG. This can be achieved if the discrete frequency steps are replaced by discrete phase-shifts. Indeed, any frequency modulation can also be regarded as a phase modulation.

Above we already noticed that a linear frequency chirp is equivalent to a quadratic change in the phase ϕ of the super-structure grating (measured relative to the phase of a uniform grating with frequency f_0):

$$\phi(z) = \int_{-\Lambda_s/2}^{z} 2\pi\left(f(z') - f_0\right)dz' = \frac{\pi}{4}\Delta f \Lambda_s\left[\left(2z/\Lambda_s - 2l\right)^2 - 1\right] \tag{2.38}$$

In practice, this phase variation is approximated by discrete phase-shifts of e.g. $\pi/10$ with a quadratically varying density [20]. Figure 2.16 shows the reflection spectrum of an 8-period grating with a peak-to-peak phase variation of 3.05π. Note that although the coupling coefficient κ_u is only one third of the value used for the sampled grating in Figure 2.14 and both gratings have the same length L, the 11 reflection peaks within the 3 dB bandwidth are on average stronger for the SSG.

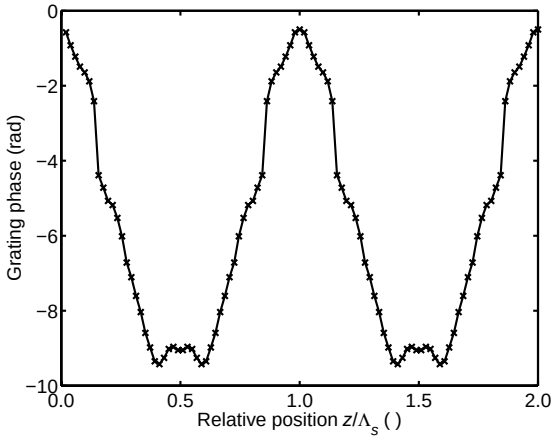

Figure 2.17 Optimised grating phase variation for a multi-phase-shift (MPS) SSG with 11 reflectivity peaks. Discrete phase-shifts were equally spread over the super-period (51 per period), and their values were optimised numerically in order to obtain a rectangular reflectivity envelope.

For a sampled grating, the number of peaks N is inversely proportional to the sampling duty cycle Λ_g/Λ_s, while the peak reflectivities are directly proportional to the duty cycle (for constant length L and coupling coefficient κ_u). In other words, the peak reflectivities of the SG decrease as $1/N$ when the number of peaks N increases. In a frequency- or phase-modulated SSG on the other hand, reflectivities only decrease approximately as $1/\sqrt{N}$, because in this case Parseval's theorem says that:

$$\sum_k \left|F_k\right|^2 = 1 \tag{2.39}$$

In order to get similar reflectivities for the SG as for the SSG (for a given number of peaks N), either the grating length L or the coupling coefficient κ_u has to be increased by roughly $\sqrt{N}$ (i.e. ≈ 3.3 for 11 peaks).

Still, with a quadratic phase variation, the envelope of the reflection peaks is not yet rectangular. To obtain this, the phase variation can be optimised numerically [41]-[42]. The target reflectivity spectrum consists of N uniform peaks, with zero reflectivity outside the band. Because of (2.31) and (2.39), this can be expressed by following trial function (for given length L and coupling coefficient κ_u):

$$C\left(\phi(z)\right) = \sqrt{\frac{1}{N}\sum_k^N \left(1 - \frac{R(\nu_k)}{R_T}\right)^2} \tag{2.40}$$

where

$$R_T = \tanh^2\left(\kappa_u L/\sqrt{N}\right) \tag{2.41}$$

The target reflectivity R_T is the maximum reflectivity that can be achieved for N uniform peaks, and if all N peaks have reflectivity R_T, out-of-band reflectivity will automatically be zero.

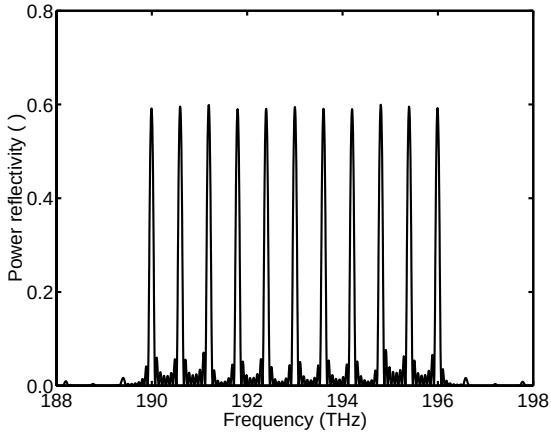

Figure 2.18 Reflection spectrum of the MPS-SSG with phase variations as shown in Figure 2.17, consisting of 8 periods with length $\Lambda_s = 65$ µm. Parameters: coupling coefficient $\kappa_u = 67$ cm^{-1}, peak spacing $\delta = 0.6$ THz ($n_g = 3.85$). The target reflectivity R_T is 0.61.

Figure 2.17 shows the optimised phase variation for $N = 11$. Reflectivity spectra were calculated using a transfer matrix method (cf. Chapter 3). The super-period was divided into 51 sections of equal length, with a discrete phase-shift at each interface. The phase variation was initialised to the parabolic curve used to calculate the spectrum in Figure 2.16. Subsequently, the phase-shifts were optimised numerically using a simulated annealing algorithm, combined with the downhill simplex method of Nelder and Mead [43]-[44]. The optimisation procedure was repeated a few times, and the best result was retained. At first sight, the result in Figure 2.17 looks quite different from the curve in [41]. On closer inspection though, an excellent match is found provided the phase curve is inverted and is shifted by half the super-period. Changing the sign of the phase of course merely corresponds to calculating the reflectivity from the other end of the SSG-DBR (replace z by $-z$ in (2.11)), and should therefore yield the same result.

The corresponding reflection spectrum is plotted in Figure 2.18. The peak reflectivities are clearly highly uniform, and very close to the target value of 0.61. Consequently, the reflectivity is also negligible outside the band of 11 peaks.

SG-DBR and SSG-DBR lasers

The longitudinal cross-section of a SG-DBR laser is sketched in Figure 2.19. Both cavity mirrors consist of sampled grating Bragg reflectors. The difference in reflection peak spacing δ, which is required for the Vernier-tuning, is obtained by applying different sampling periods Λ_s to front and rear reflector (cf. (2.26)). Apart from the specifics of the grating design, the cross-section of a super-structure grating (SSG) DBR laser is evidently identical.

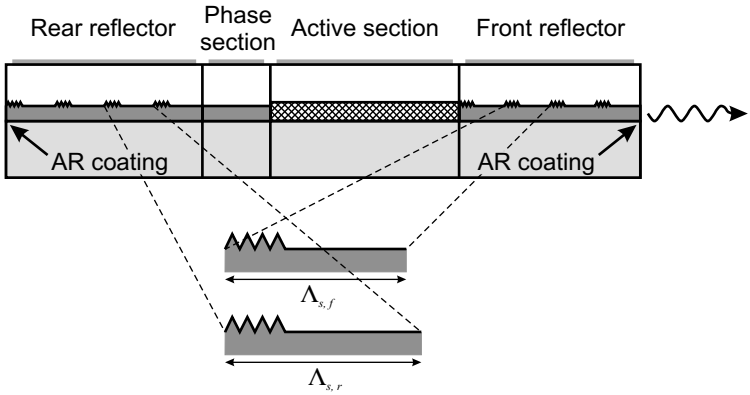

Figure 2.19 Longitudinal cross-section of a tunable sampled grating (SG) DBR laser. Apart from the specifics of the grating design, the cross-section of a super-structure grating (SSG) DBR laser is identical.

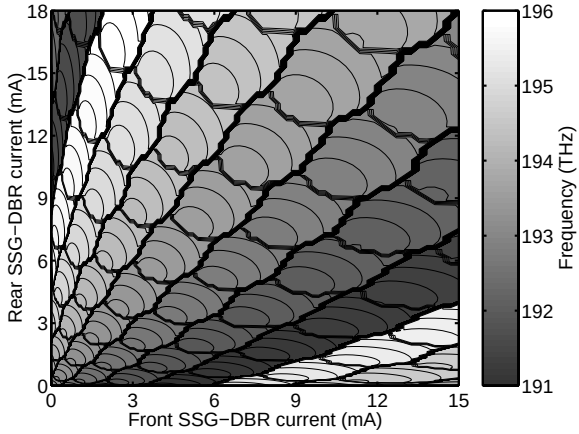

Figure 2.20 Tuning characteristic of a SSG-DBR laser. Contour plot of frequency as a function of front and rear reflector currents (10 GHz increments). Both SSG reflectors have 7 uniform reflection peaks. The dashed line indicates a possible trajectory for simultaneous tuning of both reflectors, where a particular pair of reflection peaks is kept aligned (medium tuning).

Shown in Figure 2.20 is the Vernier-tuning characteristic of a SSG-DBR laser, of which both reflectors have 7 uniform reflectivity peaks. It is clearly visible that if either the front reflector or the rear reflector is tuned, large frequency jumps (super-mode jumps) of about 0.7 THz are obtained. At one particular super-mode jump the frequency jumps from one end of the spectrum to the other. If both reflectors are tuned simultaneously, such that a particular pair of reflector peaks is kept aligned, smaller frequency hops of approximately 50 GHz are observed. These correspond to longitudinal mode hops. If one runs through the diagram from top-left to bottom-right, one finds more or less the same frequency for points which are 7 super-mode jumps apart, consistent with the number of reflectivity peaks.

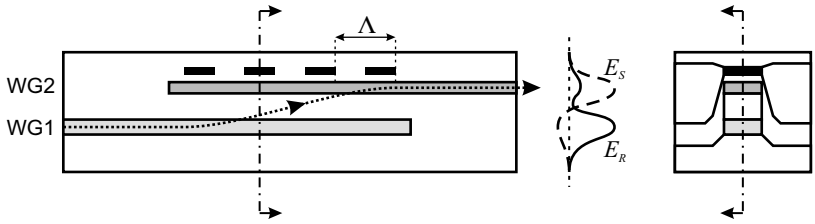

Figure 2.21 Longitudinal and lateral cross-section of a grating-assisted co-directional coupler (GACC) filter. Also shown are the field distributions of the two modes *R* and *S* of the asymmetric dual-waveguide structure.

In order to accomplish quasi-continuous tuning over the depicted range of about 5 THz, one has to add the third tuning dimension: the phase section control. Tuning a SG-DBR or SSG-DBR laser to a particular frequency is hence achieved in three steps. First, either the front reflector or the rear reflector is tuned to align the appropriate pair of reflector peaks (coarse tuning). Then, both reflectors are tuned simultaneously to bring the coincident peaks to the correct frequency (medium tuning). Finally, the phase section current is adjusted to align a cavity mode with the coincident reflector peaks (fine tuning).

2.4.2 Combining a co-directional grating coupler with a comb reflector

Instead of using a Bragg reflector as intra-cavity tunable filter, one could look for alternative filters that are more widely tunable. One option is the grating-assisted co-directional coupler (GACC) filter [45]-[46] (Figure 2.21). This filter consists of two parallel, asymmetric waveguides. The dual-waveguide structure supports two guided modes *R* and *S*. Because of the asymmetry, one mode (*R*) is mainly confined in the lower waveguide, while the other (*S*) has most of its power in the upper waveguide. Parallel to both waveguides, there is a grating layer with a periodically varying refractive index. At the input, mainly mode *R* is excited. Without the grating, there would only be a weak coupling between the two modes, and only little power would be transferred from the lower to the upper waveguide. With the grating, efficient coupling is obtained in a limited frequency band.

In §2.3 we described the coupling in a single waveguide between a right-propagating mode *R* and a left-propagating mode *S*, by a periodic refractive index modulation with period Λ. Both modes have the same transverse field distribution, but opposite propagation constants $\beta_R = -\beta_S = 2\pi\nu n/c$. Efficient coupling between the modes is obtained if the periodic structure provides phase matching between the two modes, i.e. $\beta_S = \beta_R - k_g$, where $k_g = 2\pi/\Lambda$ is the propagation constant of the grating (Figure 2.22(a)). This condition immediately translates to the Bragg condition (2.10).

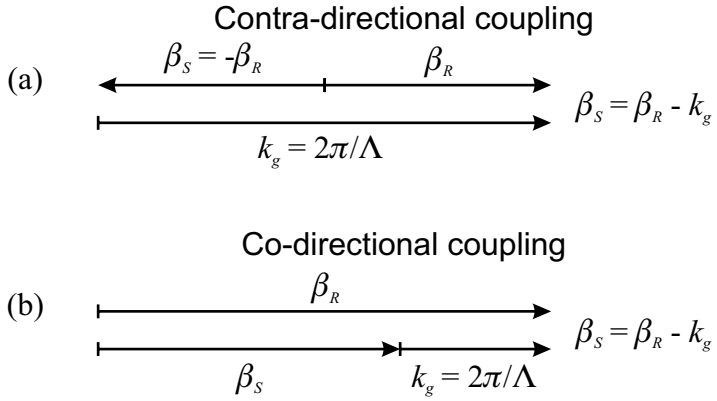

Figure 2.22 Vector diagram for contra-directional (a) and co-directional (b) coupling between two waveguide modes with propagation constants β_R and β_S, by a periodic structure with period Λ (propagation constant $k_g = 2\pi/\Lambda$).

In the co-directional coupler, the periodic structure should provide coupling between the two modes *R* and *S* propagating in the same direction, with different propagation constants $\beta_R = 2\pi\nu n_R/c$ and $\beta_S = 2\pi\nu n_S/c$ (Figure 2.22(b)). Here n_R and n_S are the effective indices of modes *R* and *S*. Phase matching again occurs when $\beta_S = \beta_R - k_g$. The coupling frequency ν_c is hence given by:

$$\nu_c = \frac{c}{\Lambda\left[n_R(\nu_c) - n_S(\nu_c)\right]} \tag{2.42}$$

Because $(n_R - n_S) << n_R$, it is clear that the period Λ required for co-directional coupling is much longer than the period needed for contra-directional coupling. As the power transfer from lower to upper waveguide is only efficient near the coupling frequency, this structure can be used as frequency selective filter. In a laser cavity one could have the light in the upper waveguide reflect back at the facet, while making sure that the light that remains in the lower waveguide is either absorbed or lost through diffraction. In that way, only light with frequencies close to the coupling frequency is efficiently coupled back to the gain section, which in the configuration of Figure 2.21 would be connected to the lower waveguide on the left-hand side.

Since the coupling frequency depends on an index *difference*, a small change of either n_R or n_S can yield a large tuning [46]-[48]:

$$\frac{\Delta\nu_{c,max}}{\nu_c} = -\frac{\Delta\left(n_R - n_S\right)_{max}}{n_{R,g} - n_{S,g}} \tag{2.43}$$

Here $n_{R,g}$ and $n_{S,g}$ are the group effective indices of modes *R* and *S* (cf. (2.27)).

Let us assume that $\Delta(n_R - n_S) = \Delta n_R$ is equal to the effective index change Δn_d in the DBR structure. Then the tuning enhancement factor *F*, i.e. the ratio of the tuning range of the GACC to the tuning range of a DBR (2.20), is found as:

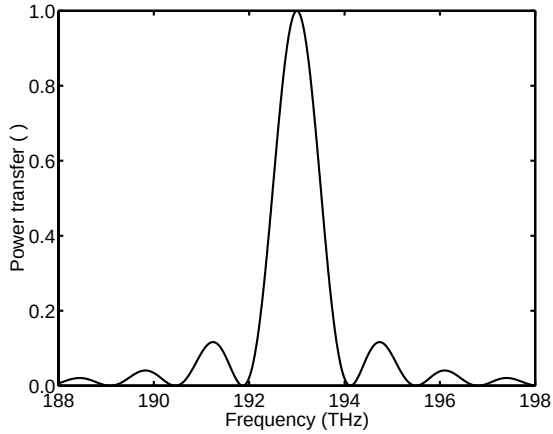

Figure 2.23 Power transfer of a grating-assisted co-directional coupler (GACC) filter. Parameters: $n_R = 3.307$, $n_{R,g} = 3.95$, $n_S = 3.205$, $n_{S,g} = 3.54$, $\nu_c = 193$ THz and $\kappa = 28$ cm^{-1}.

$$F = \frac{n_{d,g}}{n_{R,g} - n_{S,g}} > 1 \tag{2.44}$$

By means of a coupled-mode analysis, it can be shown that the power transfer through the coupler (neglecting absorption and scattering losses) is described by [49]:

$$T(\nu) = \frac{\kappa^2}{\kappa^2 + (\Delta\beta)^2} \sin^2\left[L\sqrt{\kappa^2 + (\Delta\beta)^2}\right] \tag{2.45}$$

where

$$\Delta\beta = \frac{\beta_R - \beta_S}{2} - \frac{\pi}{\Lambda} \tag{2.46}$$

In (2.45) κ represents the grating coupling coefficient. Complete power transfer is possible at zero detuning ($\Delta\beta = 0$), when the grating length is equal to the coupling length L_c:

$$L_c = \frac{\pi}{2\kappa} \tag{2.47}$$

Figure 2.23 shows a typical power transfer characteristic of a GACC. With the parameters used in the figure, and assuming $n_{d,g} = n_{R,g}$, we obtain a tuning enhancement factor F of about 9.6. Unfortunately, the GACC filter bandwidth is also much larger than that of a DBR (compare with Figure 2.8). From (2.45), the filter full width at half maximum (FWHM) bandwidth is calculated as [49]-[50]:

$$\Delta\nu_{FWHM} \approx 0.8\frac{c}{L_c\left(n_{R,g} - n_{S,g}\right)} \tag{2.48}$$

With the parameters from Figure 2.23 this gives a bandwidth of approximately 1 THz. On closer inspection, both the tuning range (2.43) and the 3 dB bandwidth (2.48), are inversely proportional to the group index difference. The ratio of both is:

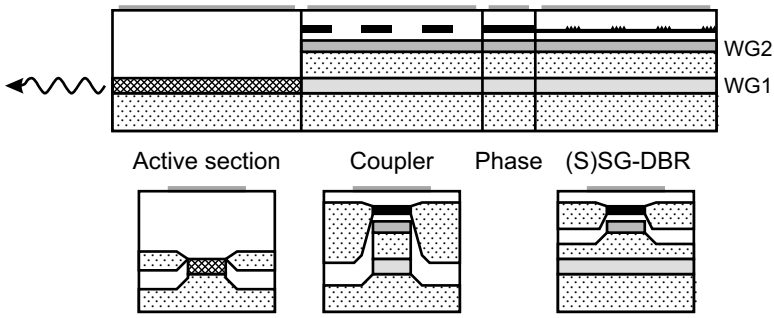

Figure 2.24 Longitudinal and lateral cross-sections of a grating-assisted coupler with rear sampled or super-structure grating reflector (GCSR) laser.

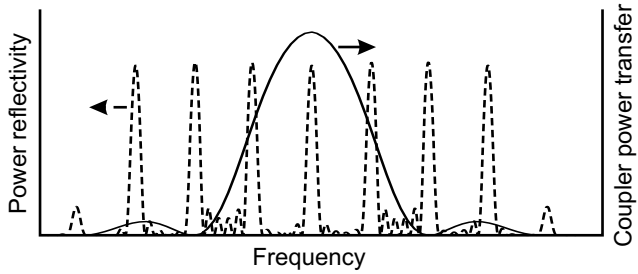

Figure 2.25 Power reflectivity of the super-structure grating DBR and power transfer of the grating-assisted co-directional coupler of a GCSR laser.

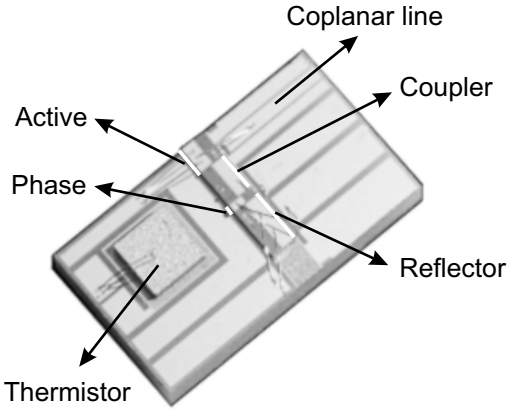

Figure 2.26 Photograph of a GCSR laser on a ceramic carrier with bonding pads for the different laser contacts and a thermistor (for temperature control). The coplanar line can be used to apply a high-frequency modulation signal to the active section. The actual laser chip is about 2 mm long.

$$\frac{\Delta\nu_{FWHM}}{\Delta\nu_{c,max}} \approx -0.8\frac{c}{\nu_c L_c \Delta\left(n_R - n_S\right)_{max}} \tag{2.49}$$

The only parameter that allows reducing the bandwidth without affecting the tuning range is the coupler length L_c. In a laser cavity, the filter bandwidth has to be measured relative to the longitudinal mode spacing. Since increasing the coupler length at the same time reduces the mode spacing, it is difficult to obtain both a large tunability and sufficient mode selectivity in a tunable laser with a GACC filter [49]-[50]. Typically, the side-mode suppression ratio is only about 20 dB.

In order to take advantage of the broad tunability of the GACC filter, without having to trade-off tunability for selectivity, J. Willems proposed to combine the GACC filter with a sampled or super-structure grating DBR [46], [51]-[52]. Due to its broad tunability, the GACC can be used to filter out one of the reflectivity peaks of the SG- or SSG-DBR. The narrow reflectivity peaks on the other hand supply the required selectivity.

When this dual filter structure is integrated into a laser cavity, together with a phase shifter section for fine tuning of the cavity modes, one obtains the so-called GCSR laser depicted in Figure 2.24 [53]. Note that in the phase and reflector sections, the lower waveguide is planar, such that the light that is not coupled to the upper waveguide in the GACC diffracts and can not couple back to the active section. Alternatively, one could replace the lower waveguide core material with absorptive material in those sections. Figure 2.25 plots typical reflection and transmission characteristics of the intra-cavity filters. The photograph in Figure 2.26 shows the laser (with a length of approximately 2 mm) mounted on a ceramic carrier, with bonding pads for the different laser contacts. On the carrier, one also finds a thermistor, which is used in the control loop stabilising the laser temperature. The coplanar line can be used to apply a high-frequency modulation signal to the active section.

As for a SG- or SSG-DBR laser, tuning the GCSR laser to a particular frequency is done in three steps. First, the coupler is tuned to filter out the appropriate reflector peak (coarse tuning). Then, coupler and reflector are tuned simultaneously to bring the reflector peak to the correct frequency (medium tuning). Finally, the phase section current is adjusted to align a cavity mode with the selected reflector peak (fine tuning).

One of the main advantages of the GCSR laser with respect to the SG-and SSG-DBR lasers is the lower variation of the output power across the tuning range. From §2.1.1 we know that when a section is tuned, the absorption losses in that section increase. Since the light generated in a SG- or SSG-DBR laser has to propagate through the front reflector, the output power will vary a lot more with tuning in these lasers. On the other hand, the combination of two narrowband filters in the SG- and SSG-DBR devices provides better suppression of neighbouring cavity modes than the combination of a narrowband and a broadband filter in the GCSR. This effect is enhanced by the fact that the effective cavity length is typically shorter in these lasers (and hence the cavity mode spacing is larger). Another disadvantage of the GCSR laser is that the laser structure is more difficult to fabricate (compare Figure 2.19 and Figure 2.24).

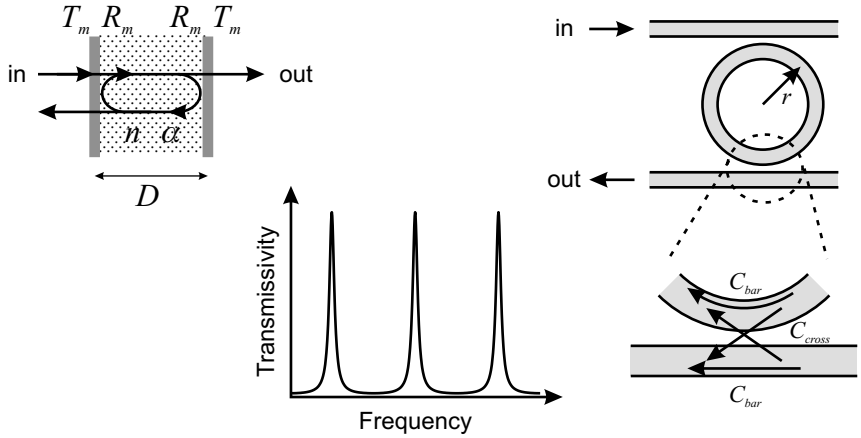

Figure 2.27 Filters with a comb-shaped transmissivity spectrum: a Fabry-Perot etalon (left) and a ring resonator (right).

In a patent application that we recently submitted jointly with J. Buus [54], we propose some alternative designs for widely tunable lasers that try to combine the strengths and avoid the weaknesses of both types of laser considered above. The new lasers employ the Vernier principle to achieve wide tuning ranges with high selectivity, have all filter sections on one side of the cavity to minimise power variations with tuning, and avoid the complexity of the vertically integrated waveguide structure of the GCSR laser. The designs are briefly discussed below. Note however that these lasers have not yet been fabricated or tested.

2.4.3 Alternative designs for widely tunable lasers

Combining a ring or disk resonator and a comb reflector

The most obvious way to use the Vernier tuning mechanism with both filters at the same side of the cavity is by combining a filter with a comb-shaped transmission characteristic with one of the comb reflectors used above. The first suitable transmission filter that comes to mind is a Fabry-Perot etalon (Figure 2.27), of which the transmittance (in the symmetric case) is described by:

$$T(\nu) = \frac{T_m^2 A}{(1 - R_m A)^2 + 4R_m A \sin^2(2\pi\nu n D/c)} \tag{2.50}$$

where

$$A = e^{-\alpha D} \tag{2.51}$$

R_m and T_m are the reflectivity and transmissivity of the mirrors, respectively; n is the refractive index of the etalon material, α is the loss per unit length of the etalon material, and D is the distance between the mirrors. The transfer function has periodic maxima, which are spaced by:

$$FSR = c/(2n_g D) \tag{2.52}$$

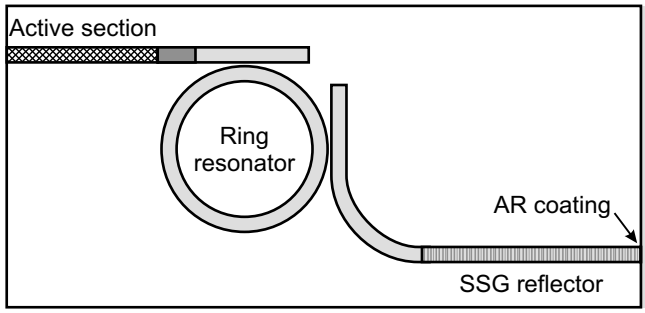

Figure 2.28 Possible layout for a Vernier-tunable laser consisting of an active section, a phase section, a ring resonator and a SG or SSG reflector.

where *FSR* stands for "free spectral range." A high selectivity requires a small value for 1 - R_mA, in which case the bandwidth of the etalon can be approximated by:

$$\Delta\nu = FSR\frac{1-R_mA}{\pi\sqrt{R_mA}} = \frac{FSR}{F} \tag{2.53}$$

The quantity F is called the finesse of the filter.

Unfortunately, the etalon also has a non-zero reflectivity $R(\nu)$, which is high for frequencies ν for which the transmissivity is low ($R(\nu) = 1 - T(\nu)$ if losses are negligible). This will most often yield multi-mode lasing at frequencies where $R(\nu)$ is high. A second, more appropriate option, is the ring resonator sketched on the right side of Figure 2.27 [55]-[56]. The transmittance of the ring resonator is also described by (2.50), provided the distance $2D$ is replaced by the circumference of the ring $2\pi r$, the mirror transmissivity T_m is replaced by C_{cross}, and R_m is replaced by C_{bar}. Here C_{cross} is the cross-coupling ratio of the directional couplers, i.e. the fraction of the input power in one waveguide that will be transferred to the other waveguide at the output. C_{bar} is the fraction of the input power in one waveguide that remains in that waveguide at the output. In a loss-less coupler, we naturally have $C_{cross} + C_{bar} = 1$. The refractive index n in (2.50) should be interpreted as the effective index of the ring waveguide. If the waveguide ends that are not used as input or output are properly terminated, the ring-resonator will have zero reflectivity.

A possible layout for the Vernier-tunable laser with a ring resonator is shown in Figure 2.28. As any curved waveguide, the ring will suffer from radiation losses, which increase with decreasing bend radius r [55]. Higher losses will both reduce the overall transmissivity of the resonator, as well as reduce the selectivity (cf. (2.53)). For the present application, a FSR between 0.5 and 1.0 THz would typically be required, which translates to bend radiuses between 24 and 12 μm (assuming $n_g \approx 4.0$). With such bend radiuses, a very high lateral index contrast is required to avoid excessive radiation losses. This can be achieved by using deeply etched ridge waveguides, as has recently been demonstrated by D. Rafizadeh et al. [57]. They also showed that a somewhat lower loss and hence an improved performance is obtained when the ring is replaced by a disk (or in other words the inner sidewall of the ring structure is eliminated).

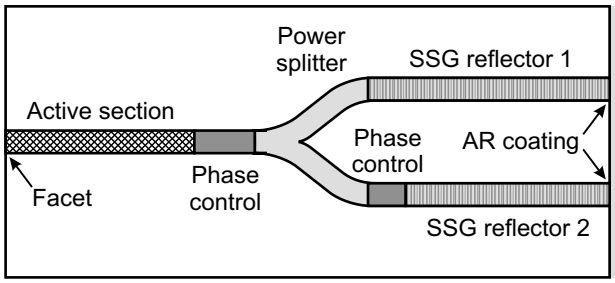

Figure 2.29 Layout of a Vernier-tunable laser with two comb reflectors in a Y-branch configuration.

Table 2.2 Comparison of state-of-the-art tunable laser characteristics. Quasi-continuos tuning range, SMSR, maximum output power (ex-facet) and power uniformity across the tuning range are compared for 3S-DBR, SG-DBR, SSG-DBR, and GCSR lasers. The shaded columns represent values for commercially available devices.

	3S-DBR		*SG-DBR*			*SSG-DBR*			*GCSR*		
	[35], [58]	[59]	[60]	[61]	[62]	[63]	[64]	[65]	[66]	[22]	[67]
QC tuning range (THz)	2.1	1.6	5.5	7.4	>5.0	5.0	7.8	4.2	8.3	5.0	>5.0
SMSR (dB)	>35	>35	>30	>30	>35	>30	>25	>35	>25	>30	>30
Max. output power (dBm)	20	15	10	5	14	3	10	10	6	10	6
Power uniformity (dB)	1.7	2	5	5	5	9	10	8	13	5	2

Combining two comb reflectors in a Y-branch configuration

The two comb reflectors of the SG- or SSG-DBR lasers can be placed at the same side of the cavity if they are put in a Y-branch configuration, as is illustrated in Figure 2.29. In this configuration, the reflectivities of the two reflectors are *added* in stead of *multiplied* (cf. Figure 2.12). This makes the control a bit more complicated. Indeed, to get the laser to emit at a particular frequency, one not only has to tune a reflectivity peak of each reflector to this frequency, but also has to assure that the two reflectivities are added in phase. Therefore, an additional phase control section has to be provided in one of the branches.

2.5 Comparison of state-of-the-art tunable lasers

Table 2.2 summarises state-of-the-art characteristics of the tunable lasers that were introduced above. Both published results and specifications of commercially available lasers are mentioned. SG-DBR, SSG-DBR, and GCSR lasers have demonstrated quasi-continuous tuning ranges exceeding the bandwidth of (either C- or L-band) Erbium doped fiber amplifiers. In the case of 3-section DBR lasers, typically 3 different lasers are required to cover this bandwidth.

All lasers can achieve a side-mode suppression ratio (SMSR) of more than 30 dB across their entire tuning range. The widely tunable lasers (SG-DBR, SSG-DBR, and GCSR) generally have somewhat lower output power than the 3S-DBR. Additionally, the SG-DBR and SSG-DBR have the disadvantage of relatively large output power variation across the tuning range. As was explained above, this is because in these lasers light generated in the active section has to traverse a reflector section in which absorption losses increase with tuning (cf. §2.1).

2.6 Conclusion

This chapter presented the current state-of-the-art on monolithically integrated tunable lasers for WDM applications. The physical mechanisms enabling electronic control of the emission frequency of such a laser were reviewed and it was concluded that carrier-induced tuning offers the best compromise between tuning range, tuning speed, and power consumption.

In §2.2, we summarised the requirements posed on tunable lasers for WDM applications. The ideal tunable laser would have a (quasi-continuous) tuning range of at least 4 THz (covering the C- or the L-band). Any frequency within this range should be reachable with a side-mode suppression ratio of 30 to 40 dB, a linewidth of no more than a few MHz, and with very little variation of the output power.

Section §2.3 covered the "original" tunable laser diode, the distributed Bragg reflector laser. The maximum refractive index change that can be achieved using carrier-induced tuning unfortunately limits the tuning range of this laser to about 2 THz, since $\Delta\nu/\nu = -\Delta n/n_g$.

In §2.4, two mechanisms to enhance the tuning range beyond the $\Delta\nu/\nu = -\Delta n/n_g$ limit were presented. The basic principle in both cases is that a refractive index *difference* is changed rather than the index itself. Therefore, the relative frequency change is proportional to a relative change in index difference, which can be significantly larger for similar absolute refractive index variations. The first method uses a Vernier effect between two comb reflectors. Such a reflector can be obtained by applying a periodic modulation to the grating in a Bragg reflector. This principle is applied in the sampled grating (SG) and super-structure grating (SSG) DBR lasers. The second method uses the broad tunability of a grating assisted co-directional coupler (GACC). In order to provide sufficient selectivity the GACC however has to be combined with a comb reflector. The resulting laser is called the grating coupler with rear sampled (or super-structure) grating reflector laser (GCSR laser). We also introduced two new laser designs that try to combine the strengths of the SSG-DBR and GCSR lasers.

Finally, §2.5 compared the performance of the different lasers presented in this chapter using results published in literature and specifications of commercially available devices.

References

[1] M.-C. Amann, and J. Buus, *Tunable laser diodes*, Artech House, Norwood, MA, USA, 1998.

[2] B.R. Bennett, R.A. Soref, and J.A. Del Alamo, "Carrier-induced change in refractive index of InP, GaAs and InGaAsP," *IEEE J. Quantum Electron.*, vol. 26, no. 1, pp. 113-122, January 1990.

[3] J.-P. Weber, "Optimization of the carrier-induced effective index change in InGaAsP waveguides - Application to tunable Bragg filters," *IEEE J. Quantum Electron.*, vol. 30, no. 8, pp. 1801-1816, August 1994.

[4] M. Asada, A. Kameyama, and Y. Suematsu, "Gain and intervalence band absorption in quantum-well lasers," *IEEE J. Quantum Electron.*, vol. 20, no. 7, pp. 745-753, July 1984.

[5] I. Joindot, and J.L. Beylat, "Intervalence band absorption coefficient measurements in bulk layer, strained and unstrained multiquantum well 1.55 µm semiconductor lasers," *Electron. Lett.*, vol. 29, no. 7, pp. 604-606, April 1993.

[6] A. Sneh, and C.R. Doerr, "Indium Phosphide-based photonic circuits and components," *Chapter 7 in Integrated optical circuits and components*, ed. E.J. Murphy, Marcel Dekker, New York, NY, USA, 1999.

[7] J.E. Zucker, "Linear and quadratic electro-optic coefficients in InGaAsP," *in Properties of lattice-matched and strained Indium Gallium Arsenide*, ed. P. Bhattacharya, INSPEC, the Institution of Electrical Engineers, London, UK, 1993.

[8] D.A.B. Miller, D.S. Chemla, T.C. Damen, A.C. Gossard, W. Wiegmann, T.H. Wood, and C.A. Burrus, "Electric field dependence of optical absorption near the band gap of quantum-well structures," *Phys. Rev. B*, vol. 32, no. 2, pp. 1043-1060, July 1985.

[9] H. Yamamoto, M. Asada, and Y. Suematsu, "Electric-field-induced refractive index variation in quantum-well structure," *Electron. Lett.*, vol. 21, no. 13, pp. 579-580, June 1985.

[10] J.E. Zucker, I. Bar-Joseph, B.I. Miller, U. Koren, and D.S. Chemla, "Quaternary quantum wells for electro-optic intensity and phase modulation at 1.3 and 1.55 µm," *Appl. Phys. Lett.*, vol. 54, no. 1, pp. 10-12, January 1989.

[11] N. Susa, and T. Nakahara, "Enhancement of change in refractive index in asymmetric quantum well," *Appl. Phys. Lett.*, vol. 60, no. 20, pp. 2457-2459, May 1992.

[12] N. Susa, "Electric-field-induced refractive index changes in InGaAs-InAlAs asymmetric coupled quantum wells," *IEEE J. Quantum Electron.*, vol. 31, no. 1, pp. 92-100, January 1995.

[13] J. Hong, M. Cyr, H. Kim, S. Jatar, C. Rogers, D. Goodchild, and S. Clements, "Cascaded strongly gain-coupled (SGC) DFB lasers with 15-nm continuous wavelength tuning," *IEEE Photon. Technol. Lett.*, vol. 11, no. 10, pp. 1214-1216, October 1999.

[14] M. Öberg, S. Nilsson, T. Klinga, and P. Ojala, "A three-electrode distributed Bragg reflector laser with 22 nm wavelength tuning range," *IEEE Photon. Technol. Lett.*, vol. 3, no. 4, pp. 299-301, April 1991.

[15] S.L. Woodward, U. Koren, B.I. Miller, M.G. Young, M.A. Newkirk, and C.A. Burrus, "A DBR laser tunable by resistive heating," *IEEE Photon. Technol. Lett.*, vol. 4, no. 12, pp. 1330-1332, December 1992.

[16] T. Kameda, H. Mori, S. Onuki, T. Kikugawa, Y. Takahashi, F. Tsuchiya, and H. Nagai, "A DBR laser employing passive-section heaters, with 10.8 nm tuning range and 1.6 MHz linewidth," *IEEE Photon. Technol. Lett.*, vol. 5, no. 6, pp. 608-610, June 1993.

[17] M.-C. Amann, "Broad-band wavelength-tunable twin-guide lasers," *Optoelectronics - Devices and Technologies*, vol. 10, no. 1, pp. 27-38, March 1995.

[18] M.-C. Amann, and W. Thulke, "Continuously tunable laser diodes: longitudinal versus transverse tuning scheme," *IEEE J. Selected Areas in Commun.*, vol. 8, no. 6, pp. 1169-1177, August 1990.

[19] P.-J. Rigole, S. Nilsson, L. Bäckbom, T. Klinga, J. Wallin, B. Stålnacke, E. Berglind, and B. Stoltz, "Access to 20 evenly distributed wavelengths over 100 nm using a single current tuning in a four-electrode monolithic semiconductor laser," *IEEE Photon. Technol. Lett.*, vol. 7, no. 11, pp. 1249-1251, November 1995.

[20] H. Ishii, Y. Tohmori, Y. Yoshikuni, T. Tamamura, and Y. Kondo, "Multiple-phase-shift super structure grating DBR lasers for broad wavelength tuning," *IEEE Photon. Technol. Lett.*, vol. 5, no. 6, pp. 613-615, June 1993.

[21] H. Ishii, F. Kano, Y. Tohmori, Y. Kondo, T. Tamamura, and Y. Yoshikuni, "Broad range (34 nm) quasi-continuous wavelength tuning in super-structure grating DBR lasers," *Electron. Lett.*, vol. 30, no. 14, pp. 1134-1135, July 1994.

[22] P.-J. Rigole, S. Nilsson, L. Bäckbom, B. Stålnacke, E. Berglind, J.-P. Weber, and B. Stoltz, "Quasi-continuous tuning range from 1560 to 1520 nm in a GCSR laser, with high power and low tuning currents," *Electron. Lett.*, vol. 32, no. 25, pp. 2352-2354, December 1996.

[23] International Telecommunication Union – Telecommunication Standardization Sector (ITU-T), Recommendation G.692: "Optical interfaces for multichannel systems with optical amplifiers," *Series G: Transmission systems and media, digital systems and networks (Transmission media characteristics – Characteristics of optical components and sub-systems)*, October 1998.

[24] T.L. Koch, U. Koren, R.P. Gnall, C.A. Burrus, and B.I. Miller, "Continuously tunable 1.5 µm multiple-quantum-well GaInAs/GaInAsP distributed-Bragg-reflector lasers," *Electron. Lett.*, vol. 24, no. 23, pp. 1431-1433, November 1988.

[25] Y. Kotaki, and H. Ishikawa, "Spectral characteristics of a three-section wavelength-tunable DBR laser," *IEEE J. Quantum Electron.*, vol. 25, no. 6, pp. 1340-1345, June 1989.

[26] C.H. Henry, "Theory of the linewidth of semiconductor lasers," *IEEE J. Quantum Electron.*, vol. 18, no. 2, pp. 259-264, February 1982.

[27] M.-C. Amann, and R. Schimpe, "Excess linewidth broadening in wavelength-tunable laser diodes," *Electron. Lett.*, vol. 26, no. 5, pp. 279-280, March 1990.

[28] M.-C. Amann, S. Illek, and H. Lang, "Linewidth reduction in wavelength tunable laser diodes by voltage control," *Electron. Lett.*, vol. 27, no. 6, pp. 531-532, March 1991.

[29] K. Kobayashi, and I. Mito, "Single frequency and tunable laser diodes," *J. Lightwave Technol.*, vol. 6, no. 11, pp. 1623-1633, November 1988.

[30] H. Kogelnik, and C.V. Shank, "Coupled-wave theory of distributed feedback lasers," *J. Appl. Phys.*, vol. 43, no. 5, pp. 2327-2335, March 1972.

[31] M. Okuda, and K. Onaka, "Tunability of distributed Bragg-reflector laser by modulating refractive index in corrugated waveguide," *Jpn. J. Appl. Phys.*, vol. 16, pp. 1501-1502, 1977.

[32] M. Yamaguchi, M. Kitamura, S. Murata, I. Mito, and K. Kobayashi, "Wide range wavelength tuning in 1.3 µm DBR-DC-PBH-LDs by current injection into the DBR region," *Electron. Lett.*, vol. 21, no. 2, pp. 63-65, January 1985.

[33] S. Murata, I. Mito, and K. Kobayashi, "Over 720 GHz (5.8 nm) frequency tuning by a 1.5 µm DBR laser with phase and Bragg wavelength control regions," *Electron. Lett.*, vol. 23, no. 8, pp. 403-405, April 1987.

[34] F. Delorme, S. Slempkes, G. Alibert, B. Rose, and J. Brandon, "Butt-jointed DBR laser with 15 nm tunability grown in three MOVPE steps," *Electron. Lett.*, vol. 31, no. 15, pp. 1244-1245, July 1995.

[35] F. Delorme, S. Grosmaire, A. Gloukhian, and A. Ougazzaden, "High power operation of widely tunable 1.55 µm distributed Bragg reflector lasers," *Electron. Lett.*, vol. 33, no. 3, pp. 210-211, January 1997.

[36] L.A. Coldren, "Multi-section tunable laser with differing multi-element mirrors," *US Patent*, no. 4896325, filed August 23, 1988, published January 23, 1990.

[37] V. Jayaraman, Z.-M. Chuang, and L.A. Coldren, "Theory, design and performance of extended tuning range semiconductor lasers with sampled gratings," *IEEE J. Quantum Electron.*, vol. 29, no. 6, pp. 1824-1834, June 1993.

[38] Y. Tohmori, Y. Yoshikuni, H. Ishii, F. Kano, and T. Tamamura, "Distributed reflector and wavelength-tunable semiconductor laser," *US Patent*, no. 5325392, filed March 3, 1993, published June 28, 1994.

[39] Y. Tohmori, Y. Yoshikuni, T. Tamamura, H. Ishii, Y. Kondo, and M. Yamamoto, "Broad-range wavelength tuning in DBR lasers with super structure grating (SSG)," *IEEE Photon. Technol. Lett.*, vol. 5, no. 2, pp. 126-129, February 1993.

[40] H. Ishii, Y. Tohmori, T. Tamamura, and Y. Yoshikuni, "Super structure grating (SSG) for broadly tunable DBR lasers," *IEEE Photon. Technol. Lett.*, vol. 4, no. 4, pp. 393-395, April 1993.

[41] H. Ishii, F. Kano, Y. Tohmori, Y. Kondo, T. Tamamura, and Y. Yoshikuni, "Narrow spectral linewidth under wavelength tuning in thermally tunable super-structure-grating (SSG) DBR lasers," *IEEE J. Selected Topics Quantum Electron.*, vol. 1, no. 2, pp. 401-407, June 1995.

[42] H. Ishii, H. Tanobe, F. Kano, Y. Tohmori, Y. Kondo, and Y. Yoshikuni, "Quasicontinuous wavelength tuning in super-structure-grating (SSG) DBR lasers," *IEEE J. Quantum Electron.*, vol. 32, no. 3, pp. 433-440, March 1996.

[43] W.H. Press, S.A. Teukolsky, W.T. Vetterling, and B.P. Flannery, *Numerical recipes in C: the art of scientific computing*, Cambridge University Press, Cambridge, UK, 1992.

[44] J.A. Nelder, and R. Mead, "A Simplex Method for Function Minimization," *Computer Journal*, vol. 7, pp. 308-313, 1964.

[45] R.C. Alferness, T.L. Koch, L.L. Buhl, F. Storz, F. Heismann, and M.J.R. Martyak, "Grating-assisted InGaAsP/InP vertical codirectional coupler filter," *Appl. Phys. Lett.*, vol. 55, no. 19, pp. 2011-2013, November 1989.

[46] J. Willems, *Modeling and design of integrated optical filters and lasers with a broad wavelength tuning range*, Ph.D. Thesis, University of Gent, January 1995.

[47] R.C. Alferness, L.L. Buhl, U. Koren, B.I. Miller, M.G. Young, T.L. Koch, C.A. Burrus, and G. Raybon, "Broadly tunable InGaAsP/InP buried rib waveguide vertical coupler filter," *Appl. Phys. Lett.*, vol. 60, no. 8, pp. 980-982, February 1992.

[48] R.C. Alferness, L.L. Buhl, T.L. Koch, and U. Koren, "Tunable optical waveguide coupler," *US Patent*, no. 5253314, filed January 31, 1992, published October 12, 1993

[49] Z.-M. Chuang, and L.A. Coldren, "Design of widely tunable semiconductor lasers using grating-assisted codirectional-coupler filters," *IEEE J. Quantum Electron.*, vol. 29, no. 4, pp. 1071-1080, April 1993.

[50] Z.-M. Chuang, and L.A. Coldren, "On the spectral properties of widely tunable lasers using grating-assisted codirectional coupling," *IEEE Photon. Technol. Lett.*, vol. 5, no. 1, pp. 7-9, January 1993.

[51] J. Willems, G. Morthier, and R. Baets, "Novel widely tunable integrated optical filter with high spectral selectivity," *Proc. ECOC '92*, pp. 413-416, paper WeB9.2, Berlin, Germany, September 1992.

[52] J. Willems, and R. Baets, "Integrated tunable optical filter," *European Patent*, no. EP 0613571 B1, filed September 17, 1993, published July 29, 1998.

[53] M. Öberg, S. Nilsson, K. Streubel, L. Bäckbom, and T. Klinga, "74 nm wavelength tuning range of an InGaAsP/InP vertical grating assisted codirectional coupler laser with rear sampled grating reflector," *IEEE Photon. Technol. Lett.*, vol. 5, no. 7, pp. 735-738, July 1993.

[54] G. Sarlet, J. Buus, and R. Baets, "Multi-section widely wavelength tunable integrated semiconductor laser with different reflection or transmission sections," *European Patent Application*, filed in 1999.

[55] E.A.J. Marcatili, "Bends in optical dielectric guides," *Bell Syst. Tech. J.*, vol. 48, no. 9, pp. 2103-2132, September 1969.

[56] B.E. Little, S.T. Chu, H.A. Haus, J. Foresi, and J.-P. Laine, "Microring resonator channel dropping filters," *J. Lightwave Technol.*, vol. 15, no. 6, pp. 998-1005, June 1997.

[57] D. Rafizadeh, J.P. Zhang, R.C. Tiberio, and S.T. Ho, "Propagation loss measurements in semiconductor microcavity ring and disk resonators," *J. Lightwave Technol.*, vol. 16, no. 7, pp. 1308-1314, July 1998.

[58] F. Delorme, "Widely tunable 1.55 µm lasers for wavelength-division-multiplexed optical fiber communications," *IEEE J. Quantum Electron.*, vol. 34, no. 9, pp. 1706-1716, September 1998.

[59] Commercial DBR laser, Alcatel Optronics, Route de Villejust, 91625 Nozay Cedex, France. <http://www.alcatel.com/telecom/optronics/>

[60] F. Delorme, G. Alibert, C. Ougier, S. Slempkes, and H. Nakajima, "Sampled grating DBR lasers with 101 wavelengths over 44 nm and optimised power variation for WDM applications," *Electron. Lett.*, vol. 34, no. 3, pp. 279-281, February 1998.

[61] D.J. Robbins, N.D. Whitbread, P.J. Williams, and J.R. Rawsthorne, "Sampled grating DBR lasers for WDM systems," *Proc. 1998 IEE Colloquium on Multiwavelength Optical Networks: Devices, Systems and Network*, pp. 9/1-9/4, London, UK, June 1998.

[62] Commercial SG-DBR tunable laser, Marconi Caswell Ltd., Caswell, Towcester, Northants NN12 8EQ, UK. <http://www.caswelltechnology.com/>

[63] M. Öberg, P.-J. Rigole, S. Nilsson, T. Klinga, L. Bäckbom, K. Streubel, J. Wallin, and T. Kjellberg, "Complete single mode wavelength coverage over 40 nm with a super structure grating DBR laser," *J. Lightwave Technol.*, vol. 13, no. 10, pp. 1892-1897, October 1995.

[64] H. Ishii, H. Tanobe, F. Kano, Y. Tohmori, Y. Kondo, and Y. Yoshikuni, "Broad-range wavelength coverage (62.4 nm) with superstructure-grating DBR laser," *Electron. Lett.*, vol. 32, no. 5, pp. 454-455, February 1996.

[65] Commercial SSG-DBR laser, NTT Electronics Corporation, 3-1 Morinosato Wakamiya, Atsugi-shi 243-0198, Kanagawa, Japan. <http://www.nel.co.jp/>

[66] P.-J. Rigole, S. Nilsson, L. Bäckbom, B. Stålnacke, T. Klinga, E. Berglind, B. Stoltz, D.J. Blumenthal, and M. Shell, "Wavelength coverage over 67 nm with a GCSR laser. Tuning characteristics and switching speed.," *Proc. XV IEEE Int. Semiconductor Laser Conference*, pp. 125-126, paper W1.1, Haifa, Israel, October 1996.

[67] Commercial GCSR laser, ADC / Altitun, P.O. Box 911, Bruttovägen 7, SE-175 29 Järfälla-Stockholm, Sweden. <http://www.altitun.com/>

Chapter 3

Modelling of integrated tunable lasers with passive tuning sections

The behaviour of most tunable laser diodes is rather complex. The lasers typically consist of three or four different sections, each described by a large number of parameters. A good model of the laser is therefore essential, both to optimise the design as well as to interpret measurement results on manufactured devices. A proper understanding of the tuning behaviour is also crucial when developing the control algorithms and electronics that are needed to translate the frequency and output power requirements to appropriate values of the laser's control parameters (i.e. the currents or voltages driving the different sections).

Since our main interest lies in the tuning characteristics of the laser, the model will be limited to static operation. The laser is considered to be a one-dimensional structure. Hence, all variations of lateral waveguide dimensions or composition are expressed as variations of the effective refractive index. The model consists of two main parts, one describing the active section using the classic laser rate equations (§3.1), and one describing the passive sections using transfer matrices (§3.2). The reflection characteristics of the passive structures left and right of the active section, which obviously are needed as input to the rate equation model, are easily derived from the overall transfer matrices of these structures. Section 3.3 looks at some of the more practical aspects concerning the implementation of the models in software.

The transfer matrix description of the passive sections has also been used in design studies of alternative types of reflectors with comb-shaped reflectivity spectra, which will be discussed in §3.4.

3.1 Cavity model

The complex tunable laser cavity can be described as a Fabry-Perot cavity with frequency-dependent mirror reflectivities [1] (Figure 3.1). The functions $r_L(\omega)$ and $r_R(\omega)$ represent the complex field reflectivities of the passive tuning sections left and right of the active section ($\omega = 2\pi\nu$ is the angular optical frequency). The active section consists of a waveguide structure with core dimensions L (length), w (width), and d (thickness), supporting a single transverse mode with confinement factor Γ (i.e. the ratio of the mode power in the core to the total mode power).

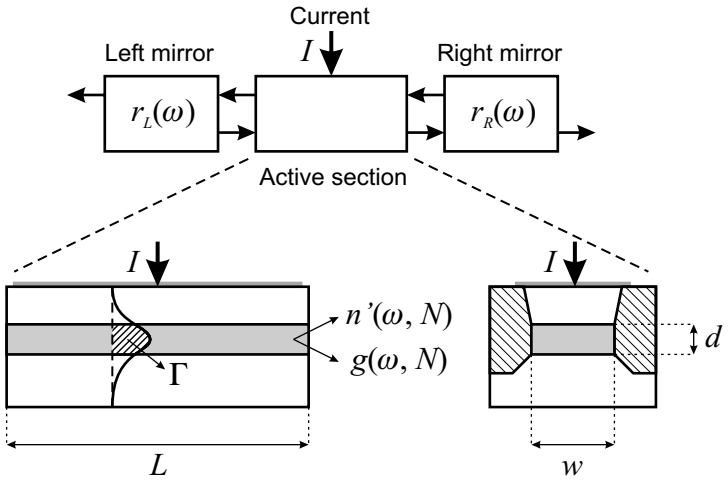

Figure 3.1 Fabry-Perot cavity model for longitudinally integrated tunable lasers with passive tuning sections. The tuning sections are represented by the mirrors with (tunable) frequency-dependent reflectivities $r_L(\omega)$ and $r_R(\omega)$. The active section consists of a waveguide with core dimensions L, w, and d. The core material has a refractive index n' and a gain g, which are changed by injecting a current I.

When a current I is applied, the carrier density in the waveguide core N will increase. For carrier densities above the transparency density $N_{g,0}$, the core layer exhibits gain $g(\omega,N)$ for a limited range of frequencies ω. The mode propagating in the waveguide also experiences scattering losses, described by a constant loss coefficient α_{int}. The net *field* gain of the waveguide mode is hence given by

$$\zeta(\omega, N) = \frac{1}{2}\left[\Gamma g(\omega, N) - \alpha_{int}\right] \tag{3.1}$$

If the spectral variation of the gain coefficient $g(\omega,N)$ is approximated by a parabola, and the change of the peak gain g_p with carrier density is linearised around the transparency carrier density $N_{g,0}$, then the material gain can be described by [1]

$$g(\omega, N) = \frac{\partial g_p}{\partial N}\left(N - N_{g,0}\right) - g_\omega\left(\omega - \omega_p(N)\right)^2 \tag{3.2}$$

Here $2g_\omega$ is the curvature of the parabola and $\omega_p(N)$ is the gain peak frequency, which shifts with the carrier density N due to the band-filling effect.

$$\omega_p(N) = \omega_{p,0} + \frac{\partial \omega_p}{\partial N}\left(N - N_{g,0}\right) \tag{3.3}$$

The effective refractive index $n(\omega,N)$ of the waveguide naturally also depends on the frequency and carrier density. For the frequency dependence we immediately find:

$$\frac{\partial n}{\partial \omega} = \frac{n_g(\omega) - n(\omega)}{\omega} = \frac{n_{g,0} - n_0}{\omega_0} \tag{3.4}$$

where $n_g(\omega)$ is the group index (2.26); $n_{g,0}$ and n_0 are the group and effective indices at $\omega = \omega_0$.

Since the effective index depends linearly on the carrier density (cf. §2.1.1 (2.6)), the function $n(\omega,N)$ can be written as:

$$n(\omega, N) = n_0 + \Gamma \frac{\partial n'}{\partial N}(N - N_0) + (n_{g,0} - n_0)\frac{\omega - \omega_0}{\omega_0} \tag{3.5}$$

where n' is the real part of the refractive index of the core layer and N_0 is a reference carrier density.

3.1.1 Threshold condition

The threshold condition is obtained by requiring that the optical field reproduces itself in magnitude and phase after each roundtrip in the cavity (under continuous-wave operating conditions). This is expressed mathematically as

$$r_L(\omega) r_R(\omega) e^{-j2k(\omega,N)L} = 1 \tag{3.6}$$

Here $k(\omega,N)$ is the complex propagation constant of the waveguide mode given by

$$\begin{aligned} k(\omega, N) &= \beta(\omega, N) + j\zeta(\omega, N) \\ &= \frac{\omega}{c} n(\omega, N) + j\frac{1}{2}\left[\Gamma g(\omega, N) - \alpha_{int}\right] \end{aligned} \tag{3.7}$$

The oscillation condition (3.6) can be separated into two conditions, one for the gain and one for the phase-shift of the field during one roundtrip in the cavity (cf. (2.1)). The gain condition reads:

$$\Gamma g(\omega, N) = \alpha_{int} - \frac{1}{L}\ln\left|r_L(\omega) r_R(\omega)\right| = \alpha_{int} + \alpha_m(\omega) = \alpha_{tot}(\omega) \tag{3.8}$$

where $\alpha_m(\omega)$ is the mirror loss and $\alpha_{tot}(\omega)$ the total roundtrip loss, which should be compensated by the modal gain $\Gamma g(\omega,N)$.

The cavity mode frequencies are determined by the phase condition:

$$2L\frac{\omega}{c} n(\omega, N) - \arg\left[r_L(\omega) r_R(\omega)\right] = 2\pi i, \qquad i \text{ integer} \tag{3.9}$$

From the gain condition (3.8), the carrier density N required in the active section can be calculated as a function of the angular frequency ω. With the above assumption of a parabolic gain spectrum, $N(\omega)$ can be derived analytically as:

$$N(\omega) = N_{g,0} + \frac{b(\omega) - \sqrt{b^2(\omega) - 4ac(\omega)}}{2a} \tag{3.10}$$

where

$$\begin{aligned} a &= \Gamma g_\omega \left(\frac{\partial \omega_p}{\partial N}\right)^2 \\ b(\omega) &= \Gamma\left(2g_\omega(\omega - \omega_{p,0})\frac{\partial \omega_p}{\partial N} + \frac{\partial g_p}{\partial N}\right) \\ c(\omega) &= \Gamma g_\omega(\omega - \omega_{p,0})^2 + \alpha_{tot}(\omega) \end{aligned} \tag{3.11}$$

Substitution of $N(\omega)$ in the phase condition (3.9) results in a condition for the frequency alone.

$$h(\omega) = 2L\frac{\omega}{c}n(\omega, N(\omega)) - \arg\left[r_L(\omega)r_R(\omega)\right] = 2\pi m \tag{3.12}$$

Solving this equation will yield a set of possible lasing modes ω_m. The actual lasing frequency ω_{out} is then found as the frequency ω_m that requires a minimal carrier density $N(\omega_m)$. This condition defines the threshold carrier density N_{th}.

$$N_{th} = \min\left\{N(\omega_m) \mid h(\omega_m) = 2\pi m\right\} \tag{3.13}$$

In order to find the other cavity modes ω_i, (3.9) has to be solved with $N = N_{th}$.

3.1.2 Static solution of the rate equations

The simplest way to study the basic properties of a laser is the rate equation approach [2]-[3]. The equations express the evolution in time of the average carrier density in the cavity N and the number of photons S_i in each cavity mode i, where the mode frequencies ω_i are defined by the carrier density through the phase condition (3.9). Since only the static operation of the laser is considered here, all time derivatives can be set to zero. The carrier density rate equation is:

$$0 = \frac{dN}{dt} = \frac{I}{qV_a} - \left(AN + BN^2 + CN^3\right) - \frac{v_g}{V_a}\sum_i \Gamma g(\omega_i, N)S_i \tag{3.14}$$

It expresses that the carrier density increases due to the injected current I ($V_a = Lwd$ is the volume of the waveguide core), and decreases as a result of non-radiative recombination (AN), spontaneous emission (BN^2), Auger recombination (CN^3) and stimulated emission ($v_g = c/n_g$ is the group velocity). If we assume that at threshold the stimulated emission rate is negligible, then (3.14) can be used to calculate the threshold current I_{th} from the threshold carrier density (3.13).

$$I_{th} = qV_a\left(AN_{th} + BN_{th}^2 + CN_{th}^3\right) \tag{3.15}$$

The rate equation for the number of photons S_i in mode i is:

$$0 = \frac{dS_i}{dt} = \left(v_g\Gamma g(\omega_i, N) - \frac{1}{\tau(\omega_i)}\right)S_i + \beta_{sp}BN^2V_a \tag{3.16}$$

Here $\tau(\omega)$ is the photon lifetime, defined as:

$$\frac{1}{\tau(\omega)} = v_g\left[\alpha_{int} - \frac{1}{L}\ln\left|r_L(\omega)r_R(\omega)\right|\right] = v_g\alpha_{tot}(\omega) \tag{3.17}$$

The last term of (3.16) describes the coupling of a small fraction β_{sp} (typically 10^{-4}) of the spontaneous emission into mode i. For the lasing mode, the photon equation yields that the net gain Γg - α_{tot} is not exactly zero above threshold, but rather slightly negative due to the non-zero β_{sp}. This means that the carrier density N is actually slightly smaller than N_{th} (3.13) above threshold. Still, the difference is so small that the approximation $N \approx N_{th}$ can certainly be used to calculate the mode frequencies from the phase condition (3.9).

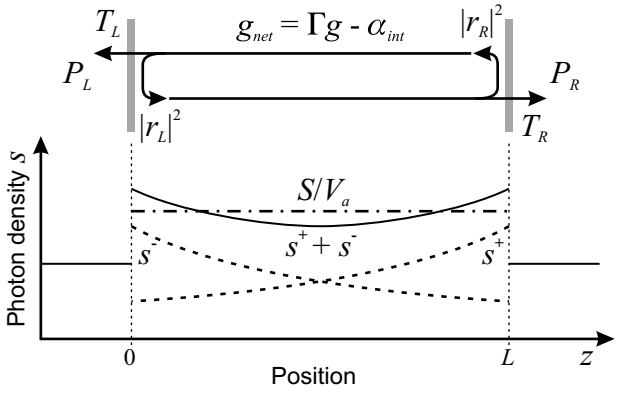

Figure 3.2 Schematic view of a Fabry-Perot cavity. Plot of the photon density distributions of the forward (s^+) and backward (s^-) propagating waves inside the cavity (dashed lines), of the total photon density ($s = s^+ + s^-$, solid line) and of the average photon density in the cavity (S/V_a, dash-dotted line).

The relative intensities of the different modes are obtained by numerically solving the set of equations (3.14) and (3.16) for N and S_i. To solve this set of highly non-linear equations an algorithm based on the one outlined in [4] is used. In the solution of (3.14) and (3.16), not all modes within the gain bandwidth are taken into account in order to speed up the calculation. Typically, only the 3 to 5 modes with lowest values for $N(\omega_i)$ (3.10) are considered, since modes with high $N(\omega_i)$ will have negligible photon numbers S_i.

From the values of N and S_i that are found, a number of other output parameters can be derived. The side-mode suppression ratio (SMSR) can be calculated as the ratio of the photon numbers of the two strongest modes, i.e. the lasing mode and the strongest side-mode. In most cases, the SMSR will be more than 20 dB. Low values are only obtained when two modes have almost equal values of $N(\omega_i)$. If the SMSR is more than 20 dB, only the lasing mode will contribute significantly to the output power of the laser. In those cases, the output power from the left or right side of the cavity can easily be calculated from the photon number of the lasing mode S.

Figure 3.2 shows a schematic representation of a Fabry-Perot cavity, with plots of the photon density distributions of the forward (s^+) and backward (s^-) propagating waves inside the cavity. The output power from the left end of the cavity is proportional to the photon density s^- of the backward propagating wave at $z = 0$.

$$P_L = \hbar\omega\, v_g\, wd\, T_L s^-(0) \tag{3.18}$$

Here $\hbar\omega = h\nu$ is the photon energy, and T_L is the power transmissivity of the left mirror. The total photon density at a position z in the cavity is equal to the sum of the photon densities of the forward and backward propagating waves, and can be expressed as a function of $s^-(0)$:

$$s(z) = s^+(0)e^{(\Gamma g - \alpha_{int})z} + s^-(0)e^{-(\Gamma g - \alpha_{int})z} = \left(|r_L|^2 e^{(\Gamma g - \alpha_{int})z} + e^{-(\Gamma g - \alpha_{int})z}\right)s^-(0) \tag{3.19}$$

In order to relate the density $s^-(0)$ to the total number of photons inside the cavity, the total photon density $s(z)$ has to be integrated over the volume of the active layer.

$$S = wd\int_0^L s(z)dz \tag{3.20}$$

By performing the integration, and taking into account the gain condition (3.8), the output power P_L can be expressed as a function of the photon number S:

$$P_L = \frac{-T_L\left|r_R\right|\frac{1}{L}\ln\left|r_L r_R\right|}{\left(1-\left|r_L r_R\right|\right)\left(\left|r_L\right|+\left|r_R\right|\right)}\hbar\omega\, v_g\, S \tag{3.21}$$

Using the assumption that $N \approx N_{th}$ above threshold, and by inserting (3.15) in (3.14), the photon number S can be evaluated as a function of the injected current:

$$I - I_{th} = qv_g\Gamma gS = qv_g\left(\alpha_{int}+\alpha_m\right)S \tag{3.22}$$

Substitution in (3.21) allows calculating the differential efficiency $\eta_{d,L}$ from the left side of the cavity, i.e. the number of photons emitted from the left side per additional carrier that is injected into the cavity above threshold.

$$\eta_{d,L} = \frac{P_L/\hbar\omega}{\left(I-I_{th}\right)/q} = \frac{\alpha_m}{\alpha_{int}+\alpha_m}\frac{T_L\left|r_R\right|}{\left(1-\left|r_L r_R\right|\right)\left(\left|r_L\right|+\left|r_R\right|\right)} \tag{3.23}$$

The expressions for the output power P_R and the differential efficiency $\eta_{d,R}$ from the right side of the laser are of course immediately obtained from (3.21) and (3.23) by swapping the subscripts L and R.

From the current I and the carrier density N, the voltage V across the active region can also be derived:

$$V = \frac{E_g}{q} + \frac{k_B T}{q}\left[\ln\left(\frac{N^2}{N_C N_V}\right) + C_1 N + C_2 N^2\right] + R_s I \tag{3.24}$$

where $$C_1 = \frac{\sqrt{2}}{4}\left(\frac{1}{N_C}+\frac{1}{N_V}\right) \qquad C_2 = \left(\frac{3}{16}-\frac{\sqrt{3}}{9}\right)\left(\frac{1}{N_C^2}+\frac{1}{N_V^2}\right) \tag{3.25}$$

In (3.24), the last term is the voltage due to the non-zero series resistance of the active section. The first two terms describe the separation of the quasi-Fermi levels [5]. Here E_g is the band-gap energy of the core layer, k_B is the Boltzmann constant, and N_C and N_V are the effective densities of state of the conduction and valence band, respectively. Since the core material becomes transparent when the separation of the quasi-Fermi levels equals the band-gap, the transparency carrier density $N_{g,0}$ can be calculated by solving the equation:

$$\ln\left(\frac{N_{g,0}^2}{N_C N_V}\right) + C_1 N_{g,0} + C_2 N_{g,0}^2 = 0 \tag{3.26}$$

Table 3.1 summarises the various parameters of the active section that have been introduced above, and cites numerical values typical for InGaAsP/InP lasers emitting in the 193 THz window.

Table 3.1 List of active section parameters with values typical for InGaAsP/InP lasers emitting in the 193 THz frequency window [1], [6]-[9].

Parameter	*Symbol*	*Unit*	*Typical value*
length	L	μm	400
width	w	μm	1.50
thickness	d	μm	0.10
confinement factor	Γ	-	0.20
effective refractive index	n	-	
effective refractive index at $N = N_0$, $\omega = \omega_0$	n_0	-	3.30
reference carrier density for effective index	N_0	μm^{-3}	$1.2 \cdot 10^{6}$
reference frequency	ω_0	THz	$2\pi \cdot 193.0$
change of refractive index with carrier density	$\partial n'/\partial N$	μm^{3}	$-2.0 \cdot 10^{-8}$
group effective index ($N = N_0$, $\omega = \omega_0$)	$n_{g,0}$	-	4.00
gain coefficient	g	μm^{-1}	
change of peak gain with carrier density	$\partial g_p/\partial N$	μm^{2}	$3.0 \cdot 10^{-8}$
transparency carrier density	$N_{g,0}$	μm^{-3}	$1.2 \cdot 10^{6}$
gain peak curvature	$2g_\omega$	$\mu m^{-1} \cdot THz^{-2}$	$1.0 \cdot 10^{-4}$
gain peak frequency at transparency	$\omega_{p,0}$	THz	$2\pi \cdot 190.0$
change of gain peak frequency with carrier density	$\partial \omega_p/\partial N$	$\mu m^{3} \cdot THz$	$1.6 \cdot 10^{-6}$
internal loss	α_{int}	μm^{-1}	$2.0 \cdot 10^{-3}$
non-radiative recombination coefficient	A	s^{-1}	$1.4 \cdot 10^{8}$
bimolecular recombination coefficient	B	$s^{-1} \cdot \mu m^{3}$	100
Auger recombination coefficient	C	$s^{-1} \cdot \mu m^{6}$	$7.5 \cdot 10^{-5}$
spontaneous emission coupling factor	β_{sp}	-	10^{-4}
effective density of states of the conduction band	N_C	μm^{-3}	$4.65 \cdot 10^{5}$
effective density of states of the valence band	N_V	μm^{-3}	$8.25 \cdot 10^{6}$
band-gap energy	E_g	eV	0.83
series resistance	R_s	Ω	3.0

3.2 Transfer matrix description of passive sections

The cavity model outlined above assumes the knowledge of the complex field reflectivities of the mirrors on either end of the cavity. According to the examples discussed in Chapter 2, such a mirror could be a simple cleaved facet, a distributed Bragg reflector (DBR), or more complicated structures like the concatenation of a straight waveguide section (phase section) with a DBR, a sampled grating, etc. Common to all these structures is that the electric field can be described as the superposition of a right-propagating wave $E^R(z)$ and a left-propagating wave $E^S(z)$:

$$E(z) = E^R(z) + E^S(z) \tag{3.27}$$

The transfer matrix is a tool that is frequently used to relate the right- and left-propagating waves at one end of such a structure to the right- and left-propagating waves at the opposite end of the structure [10]-[12] (Figure 3.3).

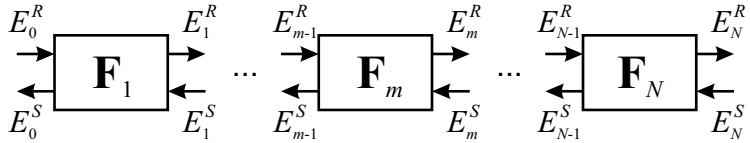

Figure 3.3 Transfer matrix description relating the right- and left-propagating waves at one end of a structure to the right- and left-propagating waves at the opposite end.

If we use the convention

$$E_m^X = E^X(z_m), \quad \text{with} \quad X = R \text{ or } X = S \tag{3.28}$$

then the fields at position $z = z_m$ are related to the fields at $z = z_{m-1}$ by the transfer matrix $\mathbf{F}_m$:

$$\begin{bmatrix} E_m^R \\ E_m^S \end{bmatrix} = \mathbf{F}_m \begin{bmatrix} E_{m-1}^R \\ E_{m-1}^S \end{bmatrix} = \begin{bmatrix} F_{11}^m & F_{12}^m \\ F_{21}^m & F_{22}^m \end{bmatrix} \begin{bmatrix} E_{m-1}^R \\ E_{m-1}^S \end{bmatrix} \tag{3.29}$$

The first obvious property of transfer matrices is that the transfer matrix of a concatenation of different sections m is given by the matrix product of the transfer matrices of the individual sections:

$$\begin{bmatrix} E_N^R \\ E_N^S \end{bmatrix} = \mathbf{F}_N \cdot \mathbf{F}_{N-1} \cdot \ldots \cdot \mathbf{F}_2 \cdot \mathbf{F}_1 \begin{bmatrix} E_0^R \\ E_0^S \end{bmatrix} = \mathbf{F}_{tot} \begin{bmatrix} E_0^R \\ E_0^S \end{bmatrix} \tag{3.30}$$

The complex field reflectivity r and transmissivity t of this compound structure can easily be calculated from the transfer matrix $\mathbf{F}_{tot}$ by setting the left-propagating wave at the right end to zero:

$$E_N^S = 0 \quad \Rightarrow \quad \begin{cases} r = \dfrac{E_0^S}{E_0^R} = -\dfrac{F_{21}^{tot}}{F_{22}^{tot}} \\ t = \dfrac{E_N^R}{E_0^R} = F_{11}^{tot} - \dfrac{F_{12}^{tot} F_{21}^{tot}}{F_{22}^{tot}} \end{cases} \tag{3.31}$$

If the concatenated structure is periodic, i.e. the N sections are identical, then the overall transfer matrix $\mathbf{F}_{tot}$ is the N-th power of the transfer matrix $\mathbf{F}$ of the individual sections.

$$\mathbf{F}_{tot} = (\mathbf{F})^N \tag{3.32}$$

In this case, the overall transfer matrix can be calculated very efficiently by solving the eigenvalue equation for $\mathbf{F}$:

$$\det \begin{bmatrix} F_{11} - \lambda & F_{12} \\ F_{21} & F_{22} - \lambda \end{bmatrix} = 0 \tag{3.33}$$

The solutions are of course:

$$\lambda_{\pm} = \frac{1}{2}\left[F_{11} + F_{22} \pm \left((F_{11} + F_{22})^2 - 4(F_{12}F_{21} - F_{11}F_{22}) \right)^{1/2} \right] \tag{3.34}$$

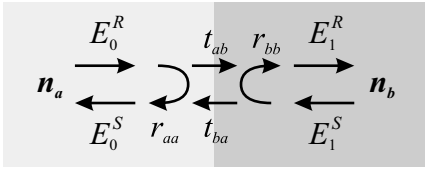

Figure 3.4 Discrete reflection at the interface between two media with dissimilar refractive indices (n_a and n_b respectively).

In general, the N-th power of the matrix $\mathbf{F}$ is then given by

$$\mathbf{F}_{tot} = (\mathbf{F})^N = \frac{\lambda_+^N - \lambda_-^N}{\lambda_+ - \lambda_-}\mathbf{F} - \frac{\lambda_-\lambda_+^N - \lambda_+\lambda_-^N}{\lambda_+ - \lambda_-}\mathbf{1} \tag{3.35}$$

where $\mathbf{1}$ is the unit matrix. In the degenerate case $\lambda_+ = \lambda_- = \lambda$ this becomes:

$$\mathbf{F}_{tot} = N\lambda^{N-1}\mathbf{F} - (N-1)\lambda^N\mathbf{1} \tag{3.36}$$

In the following paragraphs, we will calculate transfer matrices for a number of passive structures used in tunable laser diodes.

3.2.1 Discrete reflection

A very simple passive "section" is the interface between two media with dissimilar refractive indices n_a and n_b (Figure 3.4). In terms of waveguide structures, this can be the interface between two waveguides with different effective refractive indices. The field reflection and transmission coefficients are given by the well-known Fresnel equations (for perpendicular incidence):

$$r_{aa} = r = \frac{n_a - n_b}{n_a + n_b} = -r_{bb} \tag{3.37}$$

$$t_{ab} = \frac{2n_a}{n_a + n_b} = 1 + r \qquad t_{ba} = \frac{2n_b}{n_a + n_b} = 1 - r \tag{3.38}$$

Using these coefficients, the fields propagating away from the interface are easily expressed in terms of the fields incident on the interface:

$$\begin{aligned} E_0^S &= r_{aa}E_0^R + t_{ba}E_1^S \\ E_1^R &= t_{ab}E_0^R + r_{bb}E_1^S \end{aligned} \tag{3.39}$$

from which the transfer matrix can be derived as:

$$\mathbf{F}_{refl}(n_b \mid n_a) = \frac{1}{1-r}\begin{bmatrix} 1 & -r \\ -r & 1 \end{bmatrix} \tag{3.40}$$

where r is given by (3.37). Note that, since the power P is proportional to $n|E|^2$ and not just $|E|^2$, the power transmission coefficient T is not equal to the square of the field transmission coefficients.

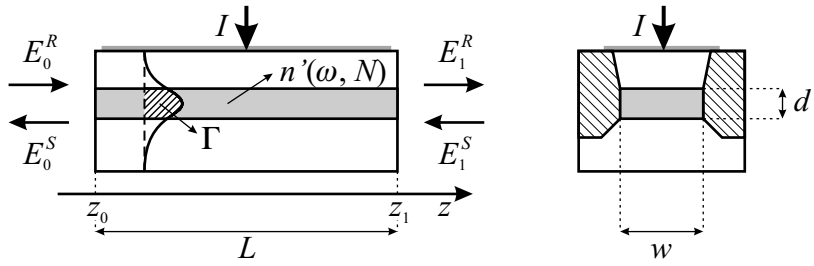

Figure 3.5 Waveguide section with effective refractive index n, which can be tuned through current injection I.

$$T_{ab} = \frac{n_b \left|E_1^R\right|^2}{n_a \left|E_0^R\right|^2} = \frac{n_b}{n_a}\left|t_{ab}\right|^2 = \frac{1-r}{1+r}(1+r)^2 = 1-r^2 = T_{ba} = T \tag{3.41}$$

For the power reflection coefficient on the other hand, we find as expected:

$$R_{aa} = \frac{n_a \left|E_0^S\right|^2}{n_a \left|E_0^R\right|^2} = \left|r_{aa}\right|^2 = r^2 = R_{bb} = R \tag{3.42}$$

3.2.2 Waveguide

Another basic building block is a section consisting of a uniform waveguide (Figure 3.5). We consider a waveguide structure with core dimensions L (length), w (width), and d (thickness), supporting a single transverse mode with confinement factor Γ. The mode has an effective refractive index n and experiences a loss per unit length α. The effective index n can be tuned by injecting a current I, which will affect the carrier concentration N in the core layer according to the carrier rate equation:

$$\frac{I}{qLwd} = AN + BN^2 + CN^3 \tag{3.43}$$

As discussed in §2.1.1, the effective index will decrease linearly as a function of carrier density N. If the dispersion of n is again linearised around a reference optical frequency ω_0, we obtain:

$$n(\omega, N) = n_0 + \Gamma \frac{\partial n'}{\partial N}(N - N_0) + (n_{g,0} - n_0)\frac{\omega - \omega_0}{\omega_0} \tag{3.44}$$

The loss coefficient α will increase linearly with carrier density

$$\alpha(N) = \alpha_0 + \Gamma \frac{\partial \alpha}{\partial N}(N - N_0) \tag{3.45}$$

Since the transfer matrices relate field strengths rather than intensities, it is useful to introduce the field gain coefficient ζ:

Table 3.2 List of waveguide parameters with values typical for InGaAsP/InP waveguides that are transparent in the 193 THz frequency window [1], [6]-[9].

Parameter	*Symbol*	*Unit*	*Typical value*
length	L	μm	
width	w	μm	1.50
thickness	d	μm	0.45
confinement factor	Γ	-	0.50
effective refractive index	n	-	
effective refractive index at $N = N_0$, $\omega = \omega_0$	n_0	-	3.30
reference carrier density for effective index	N_0	μm^{-3}	0
reference frequency	ω_0	THz	$2\pi \cdot 193.0$
change of refractive index with carrier density	$\partial n'/\partial N$	μm^3	$-1.3 \cdot 10^{-8}$
group effective index ($N = N_0$, $\omega = \omega_0$)	$n_{g,0}$	-	3.85
absorption coefficient	α	μm^{-1}	
absorption coefficient at $N = N_0$	α_0	μm^{-1}	$1.0 \cdot 10^{-3}$
change of absorption coefficient with carrier density	$\partial\alpha/\partial N$	μm^2	$3.0 \cdot 10^{-9}$
non-radiative recombination coefficient	A	s^{-1}	$0.50 \cdot 10^{8}$
bimolecular recombination coefficient	B	$s^{-1} \cdot \mu m^3$	100
Auger recombination coefficient	C	$s^{-1} \cdot \mu m^6$	$2.5 \cdot 10^{-5}$

$$\zeta(N) = -\frac{1}{2}\alpha(N) \tag{3.46}$$

In a homogeneous waveguide there is no coupling between left- and right-propagating waves, so the transfer matrix is simply given by:

$$\mathbf{F}_{WG}(L) = \begin{bmatrix} e^{-jkL} & 0 \\ 0 & e^{jkL} \end{bmatrix} \equiv \mathbf{E}(-jkL) \tag{3.47}$$

where $k(\omega,N)$ is the complex propagation constant of the waveguide mode

$$k(\omega, N) = \beta(\omega, N) + j\zeta(N) = \frac{\omega}{c} n(\omega, N) - j\frac{1}{2}\alpha(N) \tag{3.48}$$

and where we have also introduced the notation $\mathbf{E}(u)$ for the "exponential" matrix:

$$\mathbf{E}(u) \equiv \begin{bmatrix} e^{u} & 0 \\ 0 & e^{-u} \end{bmatrix} \tag{3.49}$$

These "exponential" matrices have similar properties as the scalar exponential function:

$$\begin{aligned} \mathbf{E}(u) \cdot \mathbf{E}(v) &= \mathbf{E}(v) \cdot \mathbf{E}(u) = \mathbf{E}(u+v) \\ [\mathbf{E}(u)]^{-1} &= \mathbf{E}(-u) \\ [\mathbf{E}(u)]^{N} &= \mathbf{E}(Nu) \end{aligned} \tag{3.50}$$

Table 3.2 lists all the parameters of the waveguide, with numerical values typical for InGaAsP/InP waveguides that are transparent in the 193 THz frequency window.

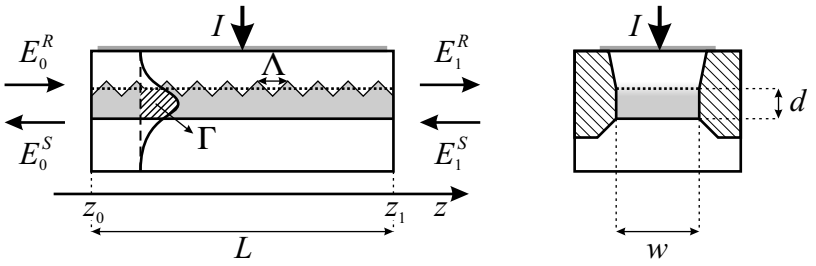

Figure 3.6 Distributed Bragg reflector section with coupling coefficient κ and grating period Λ.

3.2.3 Distributed Bragg reflector

The third elementary building block is the distributed Bragg reflector, which was already briefly discussed in §2.3 (Figure 3.6). The DBR consists of a waveguide structure as presented in the previous paragraph, of which the effective index now fluctuates periodically around its average value $n(\omega,N)$, which is usually obtained by varying the thickness of a layer of high index material. Equations (3.43)-(3.46) hence also apply to the DBR. The only additional parameters of the DBR as compared to the uniform waveguide are the coupling coefficient κ (2.14) and the grating period Λ, which determines the Bragg frequency ν_B (2.10). In the case of a DBR, the separation of the electric field in right- and left-propagating waves is commonly written as:

$$E(z) = E^R(z) + E^S(z) = R(z)e^{-j\beta_0 z} + S(z)e^{j\beta_0 z} \tag{3.51}$$

where $\beta_0 = \pi/\Lambda$ is the Bragg propagation constant. The coupling between the counter-propagating waves is described by the well-known coupled-mode equations (for index-coupled gratings) [13]:

$$\begin{cases} -\dfrac{dR}{dz} + (\zeta - j\Delta\beta)R = j\kappa^* e^{-j\phi} S \\ \dfrac{dS}{dz} + (\zeta - j\Delta\beta)S = j\kappa\, e^{j\phi} R \end{cases} \tag{3.52}$$

where

$$\Delta\beta(\omega, N) = \beta(\omega, N) - \beta_0 = \frac{\omega}{c} n(\omega, N) - \frac{\pi}{\Lambda} \tag{3.53}$$

Because of the phase factor $e^{j\phi}$, we can without loss of generality assume that κ is real, i.e. $\kappa^* = \kappa$. ϕ is the phase of the grating at $z = 0$ (cf. (2.11)). In order to solve these equations, we insert a trial solution:

$$\begin{cases} R(z) = r\, e^{\gamma z} \\ S(z) = s\, e^{\gamma z} \end{cases} \tag{3.54}$$

This yields a set of algebraic equations in r and s:

$$\begin{cases} (\gamma - \zeta + j\Delta\beta)r + j\kappa e^{-j\phi} s = 0 \\ -j\kappa e^{j\phi} r + (\gamma + \zeta - j\Delta\beta)s = 0 \end{cases} \tag{3.55}$$

These equations will only have non-trivial solutions for r and s if the determinant of the set of equations is zero, which requires:

$$\gamma(\omega, N) = \left[\kappa^2 + \left(\zeta(N) - j\Delta\beta(\omega, N)\right)^2\right]^{1/2} \tag{3.56}$$

The general solution of the coupled-mode equations is then:

$$\begin{cases} R(z) = r_+ e^{\gamma z} + r_- e^{-\gamma z} \\ S(z) = s_+ e^{\gamma z} + s_- e^{-\gamma z} \end{cases} \tag{3.57}$$

By solving (3.55) and using the boundary conditions $R(z_0)$, $S(z_0)$ at $z = z_0$ the functions $R(z_1)$ and $S(z_1)$ at any position $z = z_1$ can be calculated as:

$$\begin{bmatrix} R(z_1) \\ S(z_1) \end{bmatrix} = \mathbf{T}(z_1 - z_0, \phi) \begin{bmatrix} R(z_0) \\ S(z_0) \end{bmatrix} \tag{3.58}$$

where
$$\mathbf{T}(z_1 - z_0, \phi) = \frac{1}{1-\rho^2} \begin{bmatrix} a(z_1 - z_0) & -\rho e^{-j\phi} b(z_1 - z_0) \\ -\rho e^{j\phi} b(z_0 - z_1) & a(z_0 - z_1) \end{bmatrix} \tag{3.59}$$

and
$$\begin{aligned} a(u) &= e^{\gamma u} - \rho^2 e^{-\gamma u} \\ b(u) &= e^{\gamma u} - e^{-\gamma u} \\ \rho &= j\kappa/(\gamma + \zeta - j\Delta\beta) \end{aligned} \tag{3.60}$$

Since
$$\begin{bmatrix} E^R(z) \\ E^S(z) \end{bmatrix} = \begin{bmatrix} e^{-j\beta_0 z} & 0 \\ 0 & e^{j\beta_0 z} \end{bmatrix} \begin{bmatrix} R(z) \\ S(z) \end{bmatrix} = \mathbf{E}(-j\beta_0 z) \begin{bmatrix} R(z) \\ S(z) \end{bmatrix}, \tag{3.61}$$

the transfer matrix $\mathbf{F}_{DBR}$, which relates the right- and left-propagating field components E^R and E^S at $z = z_1$ to the right- and left-propagating field components at $z = z_0$, is immediately derived as:

$$\mathbf{F}_{DBR}(z_1 \mid z_0) = \mathbf{E}(-j\beta_0 z_1) \cdot \mathbf{T}(z_1 - z_0, \phi) \cdot \mathbf{E}(j\beta_0 z_0) \tag{3.62}$$

As mentioned, ϕ is the phase of the grating at $z = 0$. In some cases, it is useful to express the transfer matrix $\mathbf{F}_{DBR}$ as a function of the phase θ at the start of the grating, i.e. at $z = z_0$:

$$\theta = \phi + 2\beta_0 z_0 \tag{3.63}$$

With $L = z_1 - z_0$, the transfer matrix $\mathbf{F}_{DBR}$ then becomes:

$$\begin{aligned} \mathbf{F}_{DBR}(L) &= \mathbf{E}(-j\beta_0 L) \cdot \hat{\mathbf{T}}(L, \theta) \\ &= \mathbf{E}(-j\beta_0 L) \cdot \frac{1}{1-\rho^2} \begin{bmatrix} a(L) & -\rho e^{-j\theta} b(L) \\ -\rho e^{j\theta} b(-L) & a(-L) \end{bmatrix} \\ &= \mathbf{E}(-j\theta/2) \cdot \mathbf{E}(-j\beta_0 L) \cdot \hat{\mathbf{T}}(L, 0) \cdot \mathbf{E}(j\theta/2) \end{aligned} \tag{3.64}$$

where we have used the notation $\hat{\mathbf{T}}$ to stress the difference in interpretation of the phase θ in (3.64) as opposed to the phase ϕ in (3.62), although the matrices $\mathbf{T}$ and $\hat{\mathbf{T}}$ essentially have the same form. From the transfer matrix, one can of course immediately derive the reflectivity of the DBR (2.17).

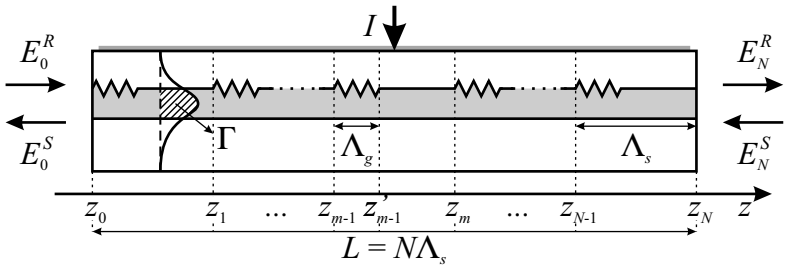

Figure 3.7 Sampled grating DBR section consisting of N periods with sampling period Λ_s and sampling duty-cycle Λ_g/Λ_s.

3.2.4 Sampled grating DBR

In a sampled grating DBR, the grating pattern is periodically interrupted. The sampling period length Λ_s determines the reflectivity peak spacing according to (2.26). As is shown in Figure 3.7, each sampling period m, extending from z_{m-1} to z_m, consists of a short stretch of grating (length Λ_g) followed by a uniform waveguide (length Λ_s - Λ_g). The transfer matrix of a section m is hence immediately found as

$$\begin{aligned}\mathbf{F}_m &= \mathbf{F}_{WG}(z_m - z'_{m-1}) \cdot \mathbf{F}_{DBR}(z'_{m-1} \mid z_{m-1}) \\ &= \mathbf{E}(-jk(z_m - z'_{m-1})) \cdot \mathbf{E}(-j\beta_0 z'_{m-1}) \cdot \mathbf{T}(z'_{m-1} - z_{m-1}, \phi) \cdot \mathbf{E}(j\beta_0 z_{m-1})\end{aligned} \tag{3.65}$$

Here we have used the form (3.62) for the transfer matrix of the grating section, because normally all grating segments will have the same phase ϕ at $z = 0$, since they are defined in a single holographic exposure step. With the notations

$$\begin{aligned}\Lambda_{ng} &= z_m - z'_{m-1} = \Lambda_s - \Lambda_g \\ \Lambda_g &= z'_{m-1} - z_{m-1}\end{aligned} \tag{3.66}$$

the product of the transfer matrices of two successive sections m and m+1 becomes

$$\begin{aligned}\mathbf{F}_{m+1} \cdot \mathbf{F}_m &= \mathbf{E}(-jk\Lambda_{ng}) \cdot \mathbf{E}(-j\beta_0 z'_m) \cdot \mathbf{T}(\Lambda_g, \phi) \cdot \mathbf{E}(j\beta_0 z_m) \cdot \\ &\quad \mathbf{E}(-jk\Lambda_{ng}) \cdot \mathbf{E}(-j\beta_0 z'_{m-1}) \cdot \mathbf{T}(\Lambda_g, \phi) \cdot \mathbf{E}(j\beta_0 z_{m-1}) \\ &= \mathbf{E}(-j\beta_0 z_{m+1}) \cdot \mathbf{E}(-j(k - \beta_0)\Lambda_{ng}) \cdot \mathbf{T}(\Lambda_g, \phi) \cdot \\ &\quad \mathbf{E}(-j(k - \beta_0)\Lambda_{ng}) \cdot \mathbf{T}(\Lambda_g, \phi) \cdot \mathbf{E}(j\beta_0 z_{m-1})\end{aligned} \tag{3.67}$$

From this, the transfer matrix of a sampled grating DBR with N sections can instantly be derived as

$$\mathbf{F}_{SG} = \mathbf{E}(-j\beta_0 z_N) \cdot \left[\mathbf{E}((\zeta - j\Delta\beta)\Lambda_{ng}) \cdot \mathbf{T}(\Lambda_g, \phi)\right]^N \cdot \mathbf{E}(j\beta_0 z_0) \tag{3.68}$$

where we have used

$$-j(k(\omega, N) - \beta_0) = \zeta(N) - j\Delta\beta(\omega, N) \tag{3.69}$$

Here the various waveguide parameters can again be calculated with equations (3.43)-(3.46). Naturally, formula (3.35) can be applied to efficiently calculate the N-th power in (3.68). An example of a reflection spectrum calculated using this transfer matrix was presented in Figure 2.14.

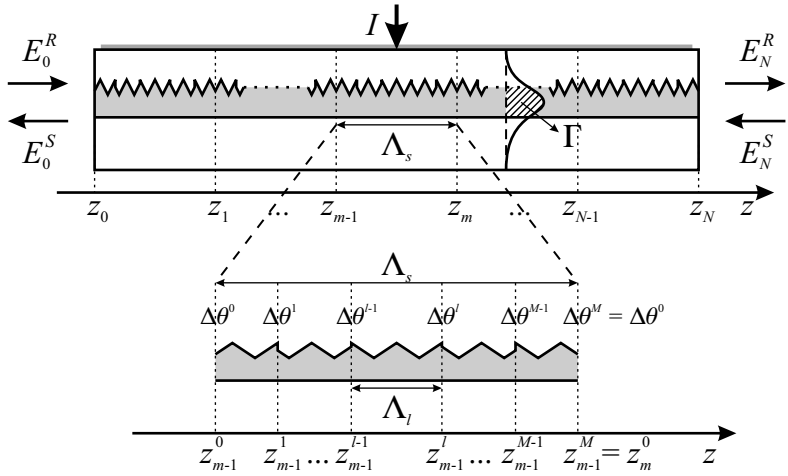

Figure 3.8 Multi-phase-shift super-structure grating DBR section consisting of N periods with super-period Λ_s.

3.2.5 Multi-phase-shift super-structure grating DBR

As mentioned in §2.4.1, a frequency modulated super-structure grating can always be interpreted as a phase modulated SSG. Since in practice continuous phase variations are both difficult to fabricate and difficult to model, we limit our study to super-structure gratings with discrete phase-shifts (MPS-SSG). Each super-period (length Λ_s) is divided into a number of subsections with length Λ_l, with a discrete phase-shift $\Delta\theta^l$ at the interface between two subsections (Figure 3.8). Since here the phase of the grating changes from one subsection to the next, we use the form (3.64) for the transfer matrix of a subsection l of super-period $m + 1$:

$$\mathbf{F}_{m+1}^l = \mathbf{E}\left(-j\theta_m^{l-1}/2\right)\cdot\mathbf{E}\left(-j\beta_0\left(z_m^l - z_m^{l-1}\right)\right)\cdot\hat{\mathbf{T}}\left(\left(z_m^l - z_m^{l-1}\right),0\right)\cdot\mathbf{E}\left(j\theta_m^{l-1}/2\right) \quad (3.70)$$

Here θ_m^{l-1} is the phase of the grating at the start of the subsection, i.e. $z = z_m^{l-1}$. In practice, the length of each subsection l is defined as a fraction x_l of the super-period length Λ_s, where Λ_s determines the reflectivity peak spacing according to (2.26).

$$\Lambda_l = z_m^l - z_m^{l-1} = x_l\Lambda_s \quad (3.71)$$

For the transfer matrix of a single super-period we then find

$$\begin{aligned}\mathbf{F}_{m+1} &= \mathbf{F}_{m+1}^M\cdot\ldots\cdot\mathbf{F}_{m+1}^{l+1}\cdot\mathbf{F}_{m+1}^l\cdot\ldots\cdot\mathbf{F}_{m+1}^1\\ &= \ldots\cdot\mathbf{E}\left(-j\theta_m^l/2\right)\cdot\mathbf{E}\left(-j\beta_0\Lambda_{l+1}\right)\cdot\hat{\mathbf{T}}\left(\Lambda_{l+1},0\right)\cdot\mathbf{E}\left(j\theta_m^l/2\right)\cdot\\ &\quad\ \mathbf{E}\left(-j\theta_m^{l-1}/2\right)\cdot\mathbf{E}\left(-j\beta_0\Lambda_l\right)\cdot\hat{\mathbf{T}}\left(\Lambda_l,0\right)\cdot\mathbf{E}\left(j\theta_m^{l-1}/2\right)\cdot\ldots\\ &= \mathbf{E}\left(-j\theta_{m+1}^0/2\right)\cdot\left\{\prod_{l=1}^{M}\left[\mathbf{E}\left(j\Delta\theta^l\right)\cdot\hat{\mathbf{T}}\left(\Lambda_l,0\right)\right]\right\}\cdot\mathbf{E}\left(j\theta_m^0/2\right)\end{aligned} \quad (3.72)$$

where we have used

$$\theta_m^l = \theta_m^{l-1} + 2\beta_0\Lambda_l + \Delta\theta^l \quad \text{and} \quad \theta_m^M = \theta_{m+1}^0 \quad (3.73)$$

By multiplying N of these matrices, we obtain the transfer matrix of the super-structure grating DBR:

$$\mathbf{F}_{SSG} = \mathbf{E}\left(-j\theta_N^M/2\right)\cdot\left\{\prod_{l=1}^{M}\left[\mathbf{E}\left(j\Delta\theta^l\right)\cdot\hat{\mathbf{T}}\left(\Lambda_l,0\right)\right]\right\}^N\cdot\mathbf{E}\left(j\theta_1^0/2\right) \qquad (3.74)$$

where $$\theta_N^M = \theta_1^0 + N\sum_{l=1}^{M}\left(2\beta_0\Lambda_l + \Delta\theta^l\right) = \theta_1^0 + 2N\beta_0\Lambda_s + N\sum_{l=1}^{M}\Delta\theta^l \qquad (3.75)$$

Again, formula (3.35) can be applied to speed up the calculation of the N-th power in (3.74). Figure 2.16 and Figure 2.18 show examples of reflection spectra that were calculated with (3.74).

3.3 Software implementation

For calculation purposes, the models described in §3.1 and §3.2 were implemented in C++. To begin with, a transfer matrix class *Tmatrix* was defined. An object of class *Tmatrix* contains four variables representing the four matrix elements. These are realised as arrays of complex numbers (type *mwArray*), such that the object can contain the transfer matrix for a range of frequencies ω at once. Naturally, common operations as matrix multiplication, multiplication of a matrix with a scalar and the N-th power of a matrix (cf. (3.35)) were implemented, as well as the calculation of field transmission and reflection coefficients (3.31).

For the passive section models, an abstract base class *Section* was first created.

```
class Section
{
public:
   Section()  {};
   virtual Tmatrix Transfer(const mwArray &omg) = 0;
   // omg:    angular frequency [THz]
};
```

This class has no data members, and a single (pure virtual) member function *Transfer*. From this base class, a number of classes were derived modelling the different types of passive sections discussed in §3.2, according to the hierarchy sketched in Figure 3.9. These classes contain data members for all the relevant parameters and of course an instance of the *Transfer* member function, calculating the transfer matrix of the section as a function of (angular) frequency. Other (protected) member functions calculate section-specific parameters as a function of the input variables, e.g. the refractive index as a function of carrier density and optical frequency. These are obviously called by the *Transfer* function.

Because DBR, SG-DBR and SSG-DBR sections are all based on a waveguide structure, and therefore have many parameters and member functions (e.g. calculating the carrier density N from the current I, cf. (3.43)-(3.46)) in common with the simple waveguide structure, the *DBR*, *SG-DBR*, and *SSG-DBR* classes were derived from the *Waveguide* class. In that way, many of the (protected) member functions of the *Waveguide* class could be re-used.

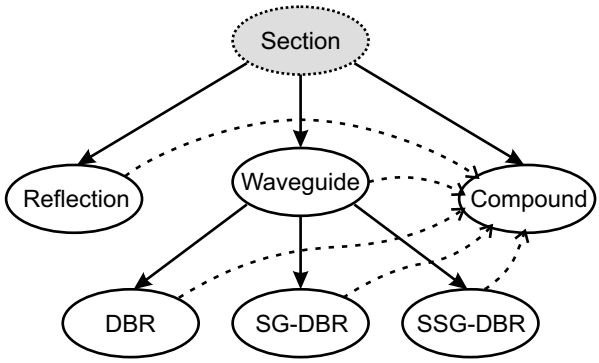

Figure 3.9 Passive section class inheritance graph.

Compound, the last class derived from *Section*, contains an array of pointers to objects of type *Section*. This class can thus represent any concatenation of structures that can be described by an object derived from *Section*, e.g. the concatenation of a *Waveguide* (phase section) and a *DBR*. The transfer matrix of an object of type *Compound* is of course calculated as the product of the transfer matrices of the individual sections.

The active section class (*Laser*), which implements the model from §3.1, has two data members of type *Compound*, one for each mirror, as well as of course data members for all the parameters listed in Table 3.1. The key member function of the *Laser* class is obviously the rate-equation solver. Other member functions calculate various output parameters, as the SMSR, the output power, the voltage, etc.

To calculate the tuning characteristic of a laser, following steps are repeated:

- The control currents of the different subsections of both *Compound* mirrors are set to the appropriate values.
- All solutions ω_m to $h(\omega) = 2\pi m$ (3.12) are located within a pre-defined frequency range $[\omega_{\min}\ \omega_{\max}]$, which should naturally be larger than the expected tuning range. The mirror reflectivities in the expression for $h(\omega)$ are calculated from the transfer matrices of both *Compound* mirrors.
- The threshold carrier density N_{th} and lasing frequency ω_{out} are found by selecting the frequency ω_m that requires a minimal carrier density $N(\omega_m)$ (3.10), (3.13).
- The phase condition (3.9) is solved with $N = N_{th}$ to locate all cavity modes ω_i within the specified frequency range $[\omega_{\min}\ \omega_{\max}]$.
- Subsequently the rate equations (3.14) and (3.16) are solved for the carrier density N and the photon numbers S_i. Only the modes ω_i with lowest values for $N(\omega_i)$ (3.10) are taken into account (typically 3 to 5 modes).
- From N and S_i, various output parameters can be calculated, e.g. output power, voltage, SMSR, …

Two examples were already presented in the previous chapter: the frequency tuning characteristics of a DBR in Figure 2.10 and of a SSG-DBR in Figure 2.20.

3.4 Alternative designs for comb reflectors

The sampled and super-structure grating reflectors that were introduced in Chapter 2 both have their pros and cons. The SG has the advantage that it is fabricated relatively easily using holographic techniques. On the other hand, peak reflectivities are not uniform and high reflectivities are difficult to achieve for a large number of peaks. Strong, uniform reflectivity peaks can be obtained for optimised multi-phase-shift SSGs. The drawback of these gratings is though that high-resolution electron beam lithography is required. Defining phase-shifts on the order of $2\pi/10$ requires writing patterns with a minimum feature size of $\Lambda/10$, where Λ is the grating period which is normally on the order of 240 nm. Since the inscription of a pattern is a sequential process, the exposure time (and cost) scales inversely proportional with the spot-size of the electron beam.

In the following paragraphs, we will discuss two further alternatives, which try to achieve uniform reflectivity combs using holographic techniques. These were studied in collaboration with researchers from Marconi – Caswell Technology (UK).

3.4.1 Multi-wavelength Bragg gratings through multiple holographic exposure

Figure 3.10 shows a typical set-up for the holographic definition of a grating pattern. A photo-resist layer is exposed to the interference pattern of two ultra-violet laser beams, incident at an angle θ to the normal. The grating period Λ is defined by the wavelength of the UV light λ (typically around 350 nm) and the angle θ.

$$\Lambda = \frac{\lambda}{2\sin\theta} \quad \text{or} \quad f = \frac{1}{\Lambda} = \frac{2\sin\theta}{\lambda} \tag{3.76}$$

After development of the resist, the pattern is transferred into the semiconductor substrate by an etch-procedure, either wet chemical etching or reactive ion etching (dry etching). An – at first sight – obvious way of defining a grating with multiple reflectivity peaks would be to expose the resist multiple times at different angles θ_i, thus superimposing sinusoidal fringe patterns with different periods Λ_i.

Such an approach was first demonstrated in silica optical fibers [14], where Bragg gratings are defined in a similar holographic set-up [15]. In the case of glass fiber, however, the fiber itself is exposed to the UV interference pattern, since the refractive index of the glass changes when it is exposed to UV light. For relatively low exposure intensities/durations, the transfer of UV intensity to refractive index change is almost linear. After multiple exposures at different angles θ_i, a refractive index modulation pattern is obtained which contains various frequency components f_i (cf. (3.76)). According to the coupled-mode theory [13], each of these frequency components will give a peak in the reflection spectrum. By choosing appropriate values for the exposure angles θ_i a comb reflector is hence easily fabricated.

In the set-up of Figure 3.10 things are a bit more complicated. First, the response of the photo-resist to the exposure is non-linear (almost digital), so the resist pattern after development will already appear quite different from the linear superposition of the sinusoidal fringe patterns. The non-linearity is further enhanced by the subsequent etch step.

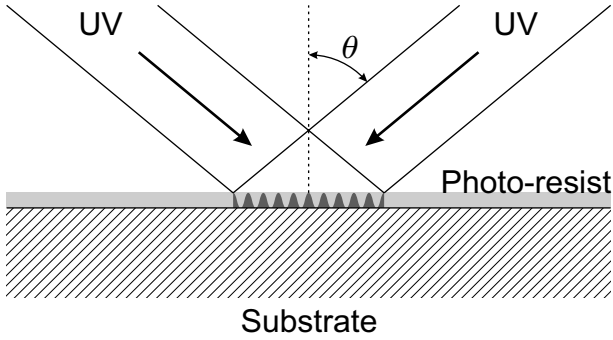

Figure 3.10 Holographic definition of a grating pattern. A photo-resist layer is exposed with the interference pattern of two ultra-violet laser beams, incident at an angle θ to the normal. The grating period is changed by adjusting the angle θ.

Still, experimentally reasonable results have been obtained with a very thin photo-resist layer and wet chemical etching for 4 to 6 superimposed patterns [16]-[17]. Due to the very thin resist, non-linearities are minimised. In addition, since the etch-rate for chemical etching depends on the width of the openings in the resist mask, neither the duty-cycle nor the grating depth are uniform. Through the combination of these effects, the frequency information of the superimposed fringe patterns is sufficiently transferred into the final grating structure. Still, results are often difficult to predict and the approach is certainly limited to only a few (4 to 6) superimposed patterns.

If more conventional dry etching techniques are used, the transfer of exposure intensity (integrated over time) to etch depth looks almost like a step function (Figure 3.11). Consequently, the teeth of the resulting grating are rectangular. The advantage is that in this case the reflection spectrum can be calculated relatively easily using the transfer matrices introduced in §3.2.

If the exposure time is equal for all exposure steps, then the superimposed fringe patterns are described by

$$I(z) = I_0 \sum_{i=1}^{K} \left[1 + \cos(2\pi f_i z + \phi_i)\right] \tag{3.77}$$

where I_0 is the average exposure level of a single step, i.e. the product of the average intensity and the exposure time, $f_i = 1/\Lambda_i$ is the spatial frequency of fringe pattern i and ϕ_i is the phase of this pattern at a reference position $z = 0$. The phases ϕ_i are adjusted by shifting the substrate left or right over an appropriate distance between two subsequent exposure steps. These shifts are obviously very small, only a fraction of the pitch Λ_i.

Since the aim is to fabricate a comb reflector with equidistant reflectivity peaks, we will limit our study to the superposition of fringe patterns with constant frequency spacing:

$$f_{i+1} - f_i = \Delta f \qquad i = 1, \ldots, K-1 \tag{3.78}$$

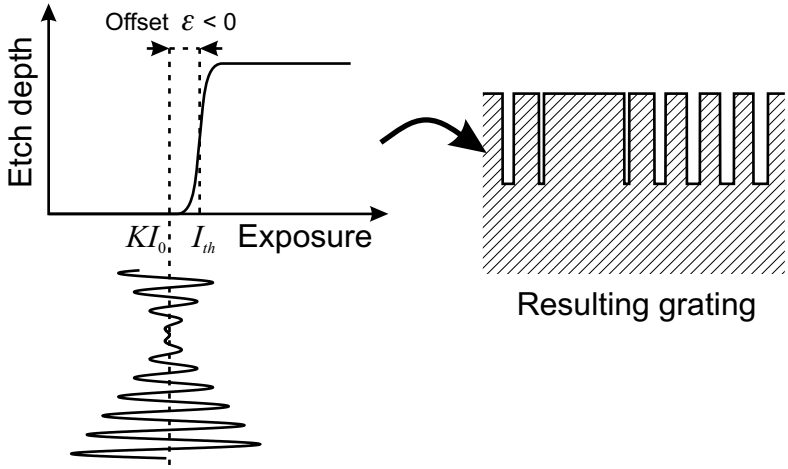

Figure 3.11 Transfer of exposure intensity (integrated over time) to etch depth for dry etch processes. Example of a superimposed fringe pattern and resulting grating. I_{th} is the exposure threshold, ε is the offset between the average exposure level of the superimposed fringes and the threshold.

Furthermore, we will only consider the case where the number of superimposed patterns K is even ($K = 2M$). The case where K is odd can though be treated completely analogously. By numbering the frequencies f_i from $-M$ to -1 and 1 to M, and by defining a central frequency f_c (3.77) then becomes:

$$\begin{aligned} I(z) &= 2MI_0 + I_0 \sum_{i=1}^{M} \left\{ \begin{array}{c} \cos\left[2\pi\left(f_c + \left(i - \tfrac{1}{2}\right)\Delta f\right)z + \phi_i\right] \\ + \cos\left[2\pi\left(f_c - \left(i - \tfrac{1}{2}\right)\Delta f\right)z + \phi_{-i}\right] \end{array} \right\} \\ &= 2MI_0 + 2I_0 \sum_{i=1}^{M} \left\{ \begin{array}{c} \cos\left[2\pi\Delta f\left(i - \tfrac{1}{2}\right)z + \tfrac{1}{2}\left(\phi_i - \phi_{-i}\right)\right] \\ \cdot \cos\left[2\pi f_c z + \tfrac{1}{2}\left(\phi_i + \phi_{-i}\right)\right] \end{array} \right\} \end{aligned} \tag{3.79}$$

The transfer function from exposure I to etch depth t is approximated by:

$$T(I) = \frac{t}{2}\left[1 + \mathrm{sgn}\left(I - I_{th}\right)\right] \tag{3.80}$$

In other words, $T(I) = 0$ for $I < I_{th}$ and $T(I) = \mathrm{t}$ for $I \geq I_{th}$.

In general, this will yield a grating with continuously varying width of the grating teeth, as is illustrated in Figure 3.11. The reflection spectrum of such a grating can be calculated in the layered structure approximation. Let n_a be the effective refractive index of the unetched waveguide, and n_b the effective refractive index of the waveguide which has been etched to a depth t ($n_a > n_b$). The reflection spectrum is then found by calculating the transfer matrix of alternating layers with indices n_a and n_b, with thicknesses determined by (3.79)-(3.80) as the distances between subsequent points where $I - I_{th}$ changes sign. The calculation generally involves the multiplication of several hundreds of matrices of the form:

$$\mathbf{F}_k = \mathbf{F}_{refl}\left(n_a \mid n_b\right) \cdot \mathbf{E}\left(-j\frac{\omega}{c} n_b l_{b,k}\right) \cdot \mathbf{F}_{refl}\left(n_b \mid n_a\right) \cdot \mathbf{E}\left(-j\frac{\omega}{c} n_a l_{a,k}\right) \tag{3.81}$$

This is obviously very time-consuming, and thus impractical for design purposes. In specific cases, however, more efficient transfer matrix descriptions exist. If in (3.79) the phases are chosen anti-symmetrically, i.e. $\phi_i = -\phi_{-i}$, we obtain:

$$I(z) = 2MI_0 + 2I_0 \cos(2\pi f_c z) \cdot E(z) \tag{3.82}$$

where

$$E(z) = \sum_{i=1}^{M} \cos\left[2\pi\Delta f\left(i - \tfrac{1}{2}\right)z + \phi_i\right] \tag{3.83}$$

If the average exposure level is adjusted such that the offset ε between the average exposure level of the superimposed fringes and the threshold is zero ($\varepsilon = 2MI_0 - I_{th} = 0$), then the etch depth as a function of position is found as:

$$T(I(z)) = \frac{t}{2}\left[1 + \operatorname{sgn}(\cos(2\pi f_c z)) \cdot \operatorname{sgn}(E(z))\right] \tag{3.84}$$

This yields a grating with constant spatial frequency f_c, 50% duty-cycle (i.e. the ratio of the width of the etched trenches to the grating period), and phase changes of π at points where the envelope function $E(z)$ changes sign. Note that the envelope function is periodic, with period $1/\Delta f$. The grating length L is therefore chosen to be an integer multiple N of the super-period length. Under these assumptions, the transfer matrix can be calculated as the transfer matrix of a MPS-SSG (3.74) with super-period $1/\Delta f$, where all phase-shifts $\Delta\theta_l$ are π, and where the lengths of the subsections Λ_l (or the fractional lengths x_l) are found by calculating the distances between zero-crossings of $E(z)$ within one super-period. The coupling coefficient κ is proportional to the first order Fourier component of the refractive index modulation Δn_1 (cf. (2.14)). Since the modulation here is a square wave with amplitude $(n_a - n_b)$, we find:

$$\kappa = \frac{\pi\nu\Delta n_1}{c} = \frac{\pi\nu}{c} \cdot \frac{2}{\pi}\left(n_a - n_b\right) = \frac{2\nu}{c}\left(n_a - n_b\right) \tag{3.85}$$

The calculation of the reflection spectrum with (3.74) is of course much more efficient, since it in general only involves the multiplication of $2M$-1 (or less) transfer matrices, and calculating the N-th power of the resultant matrix with (3.35).

Figure 3.12 gives a few examples of calculated reflection spectra of multiple exposure Bragg gratings. The number of super-periods N was 6 in all cases. The horizontal axis represents the normalised frequency $(\nu - \nu_c)/\delta$, where ν_c is the central frequency defined by the Bragg condition (2.9) and δ is the peak spacing (2.25).

$$\nu_c = \frac{cf_c}{n_a + n_b} \quad \text{and} \quad \delta = \frac{c\Delta f}{n_{a,g} + n_{b,g}} \tag{3.86}$$

Figure 3.12(a) shows the spectrum of the simplest case, $2M = 2$, which is sometimes referred to as a Moiré grating [18]. In this case the value of the phases $\phi_{\pm 1}$ obviously does not matter, since a change in these phases only reflects a change in reference position $z = 0$. For $2M > 2$, these phases however play an important role, as can be seen from the examples in Figure 3.12(b)-(d) for $2M = 6$. In (b) all fringe patterns were in phase at the reference point $z = 0$, in (c) a set of phases was arbitrarily chosen, and in (d) the phases were $[\phi_{-3} \ldots \phi_3] = [-\pi\ 0\ 0\ 0\ 0\ \pi]$. It is clear that for application in tunable lasers, (d) is much better than (b) or (c).

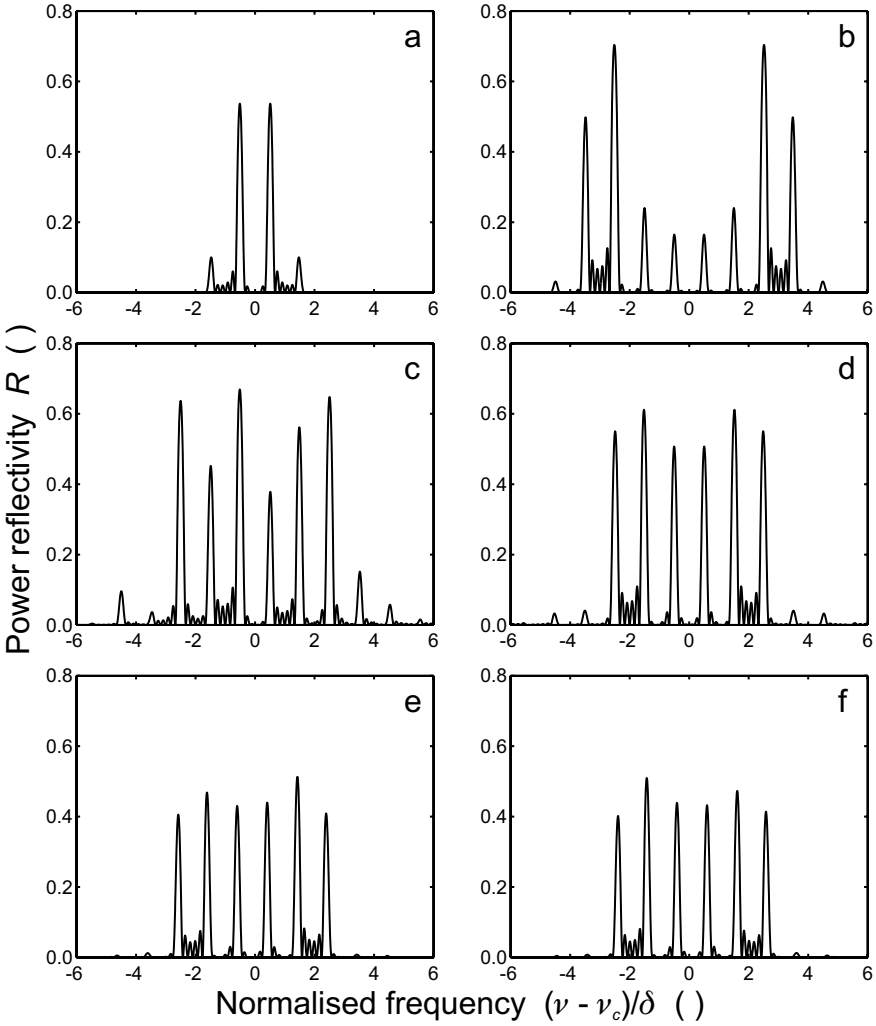

Figure 3.12 Examples of calculated reflection spectra of multiple exposure Bragg gratings: $2M = 2$ (a) or $2M = 6$ (b)-(f). The offset ε between the average exposure level and the exposure threshold I_{th} is 0 in (a)-(d), $-0.2I_{th}$ in (e) and $0.2I_{th}$ in (f). The relative phases ϕ_i of the superimposed fringe patterns are $[\phi_{-1}\ \phi_1] = [0\ 0]$ (a), $[\phi_{-3} \ldots \phi_3] = [0\ 0\ 0\ 0\ 0\ 0]$ (b), $[\phi_{-3} \ldots \phi_3] = [2.83\ -1.68\ 0.67\ -0.09\ 2.46\ 1.65]$ (c). $[\phi_{-3} \ldots \phi_3] = [-\pi\ 0\ 0\ 0\ 0\ \pi]$ (d)-(f).

In (e) and (f) finally, the phases were chosen as in (d), but the average exposure level $2MI_0$ was offset from the threshold level I_{th} by $-0.2I_{th}$ and $0.2I_{th}$, respectively. Because of the negative (positive) offset, the average duty-cycle of the grating is less (more) than 50%, and consequently the average effective index increases (decreases). This leads to a slight red-shift (blue-shift) of the reflectivity peaks, as is apparent from Figure 3.12(e) and (f). At the same time, the average coupling coefficient is reduced, which yields lower peak reflectivities. A negative offset also

increases the reflectivity of the high-frequency peaks relative to low-frequency peaks and vice-versa.

Apparently, the relative phases of the superimposed fringe patterns (at $z = 0$) have to be optimised numerically in order to obtain a uniform reflection comb. The optimisation is limited to the superpositions with anti-symmetric phases, $\phi_i = -\phi_{-i}$, and zero offset ε, because the reflection spectra can be calculated much more efficiently and more importantly because only these cases yield symmetric reflection spectra (cf. Figure 3.12). As trial function we use:

$$C(\phi_i) = \sqrt{\frac{1}{M}\sum_{i=1}^{M}\left(1 - \frac{R_i}{R_T}\right)^2} + W\sqrt{\frac{1}{M}\sum_{i=1}^{M}\left(1 - \frac{R_i}{\langle R\rangle}\right)^2} \tag{3.87}$$

where $$R_T = \tanh^2\left(\kappa L/\sqrt{2M}\right) \quad \text{and} \quad \langle R\rangle = \frac{1}{M}\sum_{i=1}^{M} R_i \tag{3.88}$$

Because of the symmetry only the reflectivities R_i of the peaks with frequencies higher than the central frequency ν_c have to be considered. If the weight factor W is zero, this trial function is the same as (2.40). However, because of the limited number of degrees of freedom, the R_i will not come as close to the target reflectivity R_T as in Figure 2.18. Therefore, the second term is included here to assure sufficient uniformity of the reflectivity peaks (usually with $W = 50$). The phase $\phi_1 = -\phi_{-1}$ can always be set to zero, since adding a value of $\pm(2i - 1)\theta$ to $\phi_{\pm i}$ will yield the same grating, only shifted over a distance $\Delta z = \theta/(\pi\Delta f)$ (cf. (3.83)).

The phases ϕ_i ($i = 2, \ldots, M$) are initialised to randomly selected values. Subsequently, the phase-shifts are optimised numerically using a simulated annealing algorithm, combined with the downhill simplex method of Nelder and Mead [19]-[20]. The optimisation procedure is repeated a few times, and the best result is retained. Figure 3.13 shows optimised spectra for $2M = 6$, 8, 10, and 12. The corresponding phases are listed in Table 3.3. The peak reflectivities are significantly lower than the target reflectivity $R_T = 0.5$, and consequently the reflectivity outside the specified bandwidth is not completely nulled.

In order to estimate the tolerances on the phases, random errors with a Gaussian distribution were repetitively added to the phases and reflection spectra were calculated using the layered structure approximation. The plots in the right column of Figure 3.13 show the 95% probability intervals for the peak reflectivities when the phase errors have a standard deviation of $4\pi\cdot10^{-3}$. The maximum relative deviation from the average peak reflectivity $\langle R\rangle$ when the 5% worst results are discarded, $|\Delta R|_{95\%}/\langle R\rangle$, is listed in the final column of Table 3.3. Actually, for $2M = 10$ a secondary optimum with a slightly higher value of $C(\phi_i)$ was chosen in stead of the true overall optimum, because this last phase distribution was an order of magnitude more sensitive to phase errors. Still, the phases of the superimposed fringe patterns have to be controlled with an accuracy of 0.01 rad or better. This would require controlling the lateral position of the substrate in the holographic set-up (Figure 3.10) with nanometer resolution. At the same time the exposure intensity and duration have to be controlled very well. Therefore, one could doubt whether this solution would be cheaper than using e-beam lithography to define the grating pattern, or even whether it would be feasible at all.

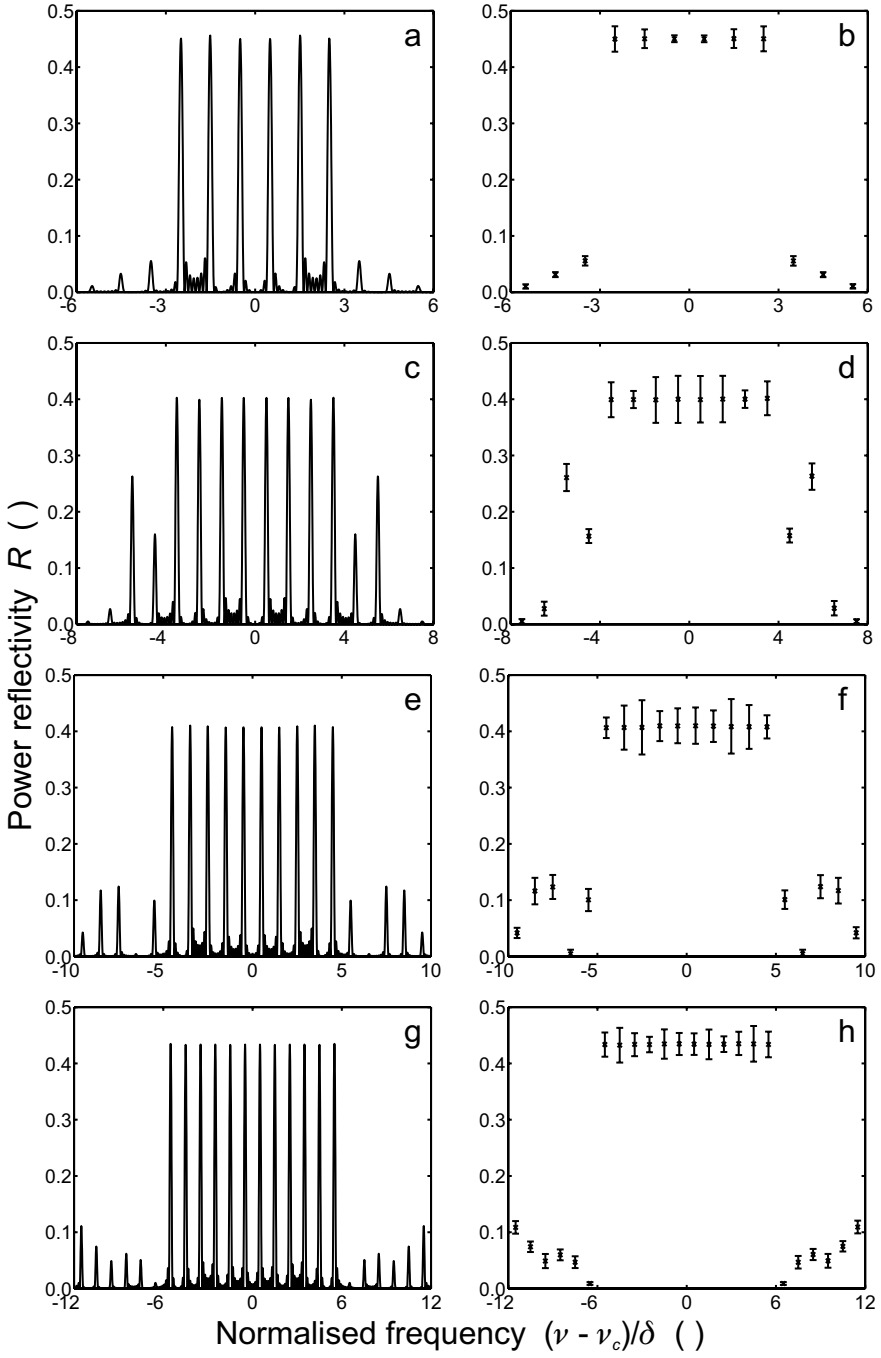

Figure 3.13 Optimised reflection spectra for 6 (a), 8 (c), 10 (e), and 12 (g) superimposed exposures. Error bars (95% probability intervals) for Gaussian errors on the phases $\phi_{\pm i}$ with a standard deviation $\sigma = 4\pi \cdot 10^{-3}$ (b, d, f, h).

Table 3.3 Phases ϕ_i of the superimposed exposures for the optimised reflection spectra ($\phi_{-i} = -\phi_i$). The last column shows the relative deviation $|\Delta R|_{95\%}/<R>$. Here $|\Delta R|_{95\%}$ is the maximum deviation from the average peak reflectivity $<R>$ when Gaussian errors with a standard deviation $\sigma = 4\pi \cdot 10^{-3}$ are added to the phases ϕ_i, if the 5% worst results are discarded.

$K = 2M$	ϕ_1	ϕ_2	ϕ_3	ϕ_4	ϕ_5	ϕ_6	$\lvert\Delta R\rvert_{95\%}/<R>$
2	0						0
4	0	1.7033					0.073
6	0	0.7193	3.0756				0.050
8	0	1.2195	1.3109	1.5591			0.105
10	0	1.6698	-0.8018	2.5047	2.0566		0.120
12	0	1.8903	-1.2502	2.4781	0.8383	1.1876	0.074

3.4.2 MPS-SSG with 180° phase-shifts

In the previous paragraph, the superposition of fringe patterns with anti-symmetric phases ($\phi_i = -\phi_{-i}$) and optimum exposure intensity/duration ($\varepsilon = 0$), yielded a grating with constant spatial frequency f_c, 50% duty-cycle, and phase changes of π at certain designated positions. Evidently, this is a very elaborate procedure to obtain a relatively simple grating structure, so the question arises whether there are no simpler means to fabricate such a MPS-SSG with 180° phase-shifts.

One option is illustrated in Figure 3.14 [21]. Compared to Figure 3.10, a phase-mask has been introduced into the interfering light beams. Additionally, the beams are in this case not only incident at opposite angles in the longitudinal direction of the waveguide, but also in the lateral direction. Because of this, the fringe lines will not be entirely perpendicular to the waveguide. If the lateral angle of incidence is chosen much smaller than the longitudinal angle (as is shown in Figure 3.14), the deviation will however be rather small and will thus have little effect on the reflection characteristics of the grating.

The phase-mask shows surface corrugations in the path of one of the beams, which introduce a phase-shift of π in this beam relative to the other beam. This can be achieved by properly choosing the depth of the corrugation. The corrugations are periodically repeated, with a period length Λ_s. If the distance between the phase mask and the substrate is sufficiently small, these phase-shifts of π will be transferred to the interference fringe pattern. The resulting grating will thus contain a periodic pattern of 180° phase-shifts, at locations corresponding to the edges of the corrugations on the phase mask.

In principle, the location of the trenches on the phase mask can be derived from the envelopes $E(z)$ found above for the optimised fringe superpositions. On the other hand, better solutions can possibly be found if the positions of the 180° phase-shifts are optimised directly. The super-period is divided in Q subsections with fractional lengths x_l, which must of course comply with:

$$\sum_{l=1}^{Q} x_l = 1 \tag{3.89}$$

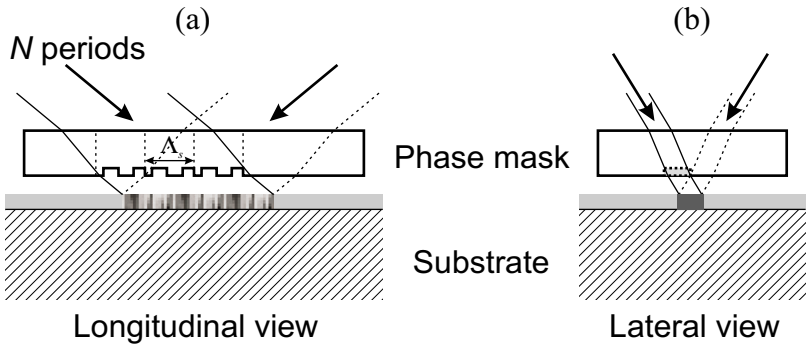

Figure 3.14 Holographic definition of a grating pattern through a phase mask. The phase-mask shows surface corrugations in the path of one of the beams, which introduce a phase-shift of π in this beam relative to the other beam. The corrugations are periodically repeated, with a period length Λ_s. The resulting grating will thus contain a periodic pattern of 180° phase-shifts.

From symmetry arguments, one can immediately derive that Q should be odd for an even number of reflection peaks K, and vice-versa. Indeed, for even K the reflectivity at the Bragg frequency ν_c must be zero, which requires that the reflections of subsequent super-periods interfere destructively. This is achieved for odd Q, since subsequent super-periods then have a 180° phase difference. For odd K, reflections of subsequent super-periods must be in phase, and hence Q should be even.

Since we consider both odd and even numbers of reflection peaks in this case, the trial function should consider all peak reflectivities R_i, where peaks are just numbered from 1 to K, left to right:

$$C(x_l) = \sqrt{\frac{1}{K}\sum_{i=1}^{K}\left(1-\frac{R_i}{R_T}\right)^2} + W\sqrt{\frac{1}{K}\sum_{i=1}^{K}\left(1-\frac{R_i}{\langle R\rangle}\right)^2} \tag{3.90}$$

Of course, the fractional lengths x_l must fulfil (3.89), which reduces the number of independent variables to $Q-1$. Also, negative values of x_l have to be avoided. Therefore, an additional term was added to the cost function:

$$C'(x_l) = C(x_l) + W_{min}\sum_{l=1}^{Q}\left[1-\mathrm{sgn}(x_l - x_{min})\right]\left(1 - x_l/x_{min}\right)^2 \tag{3.91}$$

where we chose $x_{min} = 10^{-5}$ and $W_{min} = 50$.

The fractional lengths are initialised to randomly selected values, and normalised to comply with (3.89). In a first iteration, the number of subsections Q is set to $K+1$. The simulated annealing optimisation procedure is again repeated a few times, and the best result is retained. In most cases, a few of the fractional lengths x_l converged to very low values, sometimes close to x_{min}. Such short subsections will have very little influence on the reflection spectrum, and they can consequently be omitted. The lengths of the two adjacent sections then have to be added, since these grating sections are in phase. As selection criterion we used $x_l > 5\cdot10^{-3}$, since in typical reflector designs:

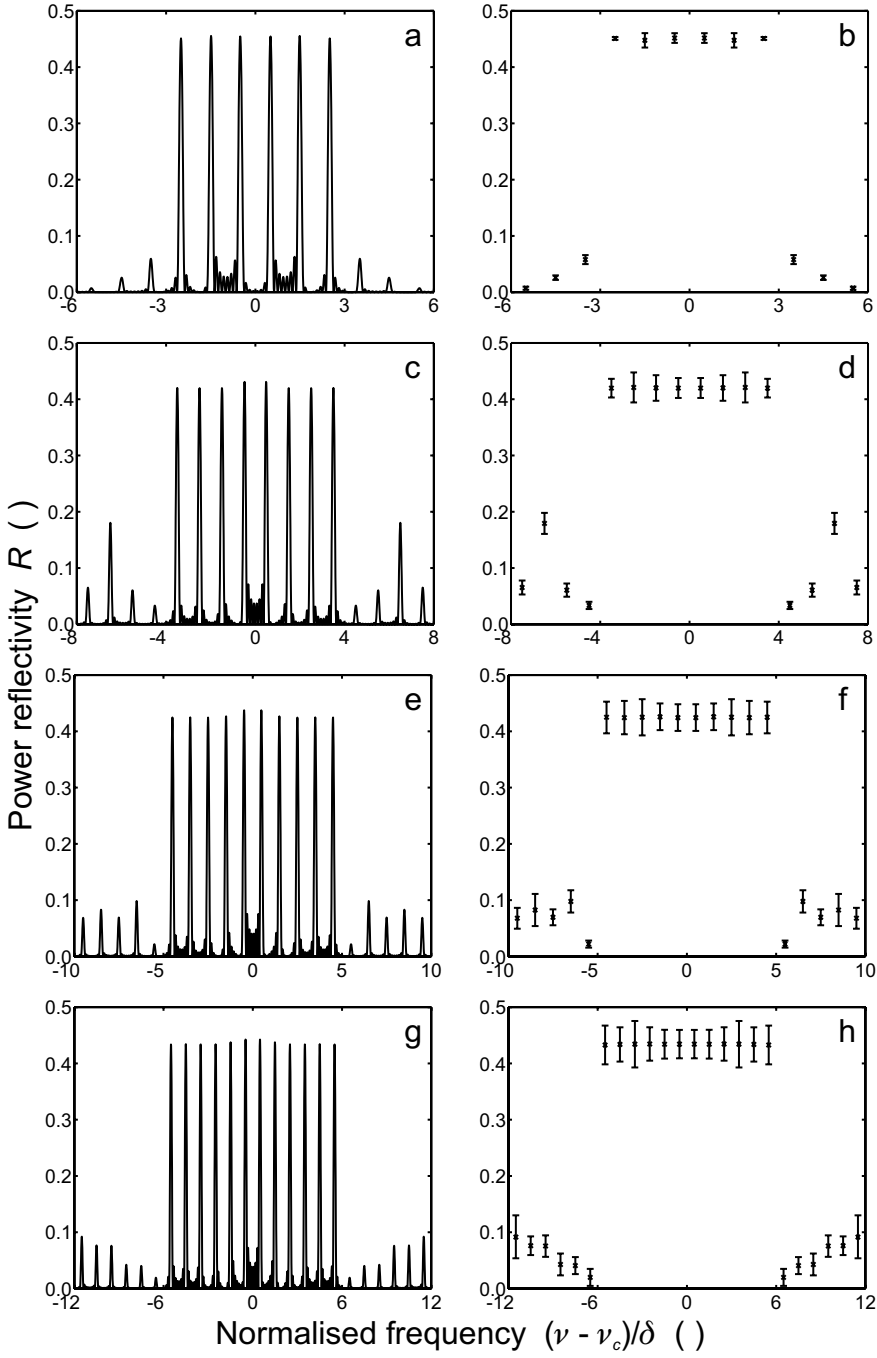

Figure 3.15 Optimised reflection spectra of MPS-SSGs with 180° phase-shifts for 6 (a), 8 (c), 10 (e), and 12 (g) peaks. Error bars (95% probability intervals) for Gaussian errors on the fractional lengths with a standard deviation $\sigma = 2.5 \cdot 10^{-3}$ (b, d, f, h).

Table 3.4 Fractional lengths x_l of the super-period subsections of a MPS-SSG with 180° phase-shifts. The last column shows the relative deviation $|\Delta R|_{95\%}/\langle R\rangle$. Here $|\Delta R|_{95\%}$ is the maximum deviation from the average peak reflectivity $\langle R\rangle$ when Gaussian errors with a standard deviation $\sigma = 2.5\cdot10^{-3}$ are added to the fractional lengths x_l, if the 5% worst results are discarded.

K	x_1	x_2	x_3	x_4	x_5	x_6	x_7	x_8	$\lvert\Delta R\rvert_{95\%}/\langle R\rangle$
3	0.7359	0.2641							0.0234
4	0.4455	0.1094	0.4451						0.0300
5	0.3497	0.2642	0.3477	0.0384					0.0451
6	0.5835	0.1916	0.2249						0.0287
7	0.4751	0.1003	0.1931	0.2315					0.0413
8	0.3645	0.1250	0.2310	0.0642	0.2153				0.0636
9	0.4078	0.1324	0.1716	0.1591	0.0630	0.0661			0.0826
10	0.2685	0.1079	0.1710	0.0850	0.1765	0.0167	0.1744		0.0759
11	0.1433	0.1034	0.1394	0.0579	0.3400	0.1167	0.0098	0.0895	0.1142
12	0.2905	0.0395	0.1344	0.0801	0.1225	0.1213	0.2117		0.0953

$$\frac{\Lambda_s}{\Lambda} = \frac{n\nu_c}{n_g\delta} \approx 200 \tag{3.92}$$

which means that subsections shorter than the grating period Λ are omitted. With this reduced set of fractional lengths x_l, the optimisation is re-run to obtain the final set. Figure 3.15 shows optimised spectra for $K = 6$, 8, 10 and 12. The optimum fractional lengths are listed in Table 3.4. The spectra for $K = 8$ and $K = 10$ are clearly better than those obtained with the multiple exposure approach.

Tolerances were again estimated by adding random errors with a Gaussian distribution to the fractional lengths and recalculating the reflection spectra. Error bars for a standard deviation of $2.5\cdot10^{-3}$ are shown in the right column of Figure 3.15 and $|\Delta R|_{95\%}/\langle R\rangle$ is listed in the final column of Table 3.4. The sensitivity to errors apparently shows a strong correlation to the number of subsections.

Since a fractional length of $2.5\cdot10^{-3}$ typically corresponds to half a grating period $\Lambda/2$, these gratings could also be fabricated using low-resolution e-beam lithography. As already mentioned, reducing the resolution of the e-beam lithography decreases the time needed to inscribe a grating pattern by the same factor. Assume that the electron beam has a spot-size equal to half the grating period. The beam then only needs to scan the surface once per grating trench, after which the beam is displaced over a distance Λ. If a phase-shift of π has to be introduced, the beam is displaced over $\Lambda/2$ or $3\Lambda/2$, depending on the optimum position of the phase-shift. In that way the phase-shift is located with a resolution of $\Lambda/2$, which means the average deviation from the optimum phase-shift position will be $\Lambda/4$ (i.e. an error on the fractional length on the order of 10^{-3}). Consequently, the deviations from the optimum reflection spectrum will certainly be lower than those shown in the right column of Figure 3.15. Naturally, the fact that the phase-shifts can only be positioned with a resolution of $\Lambda/2$ could also be taken into account

during the optimisation by requiring that the x_l are integer multiples of Λ/Λ_s (and Λ_s is an integer multiple of Λ).

3.5 Conclusion

We developed a model to calculate the tuning characteristics of monolithically integrated tunable lasers with passive tuning sections. The tunable laser is described as a Fabry-Perot laser with frequency-dependent mirror reflectivities. These reflectivities are calculated using a transfer matrix description for the passive sections (§3.2). We derived transfer matrices for the most common structures in a tunable laser: a discrete reflection, a uniform waveguide, a distributed Bragg reflector, a sampled grating DBR and a multi-phase-shift super-structure grating DBR. Using these matrices, a wide range of devices can be modelled.

The actual laser cavity is described using the classic rate equations (§3.1). First, the threshold carrier density is calculated from the gain and phase conditions, using the complex mirror reflectivities derived from the transfer matrices of the passive sections. From this value, the lasing mode and the neighbouring cavity modes are computed. Subsequently, the rate equations are solved for the carrier density N and the photon numbers S_i of the modes i. From N and S_i, various output parameters can be calculated, e.g. output power, voltage, SMSR, …

The transfer matrix description was also adopted in design studies of two types of comb reflectors, which try to achieve uniform reflectivity combs using holographic techniques. The first type is fabricated by exposing a photo-resist layer with multiple UV interference patterns, each with a different spatial frequency f_i. From our calculations, we found however that the relative phases of the different fringe patterns have to be adjusted with an accuracy of at least 0.01 rad. This would require controlling the lateral position of the substrate in the holographic set-up with nanometer resolution. It is questionable whether this would be achievable in practice.

The second type of grating is essentially a multi-phase-shift SSG with only 180° phase-shifts, which can be fabricated by holographic exposure through a phase mask (cf. §3.4.2 or [21]). By numerically optimising the position of the phase-shifts, uniform reflectivity combs were obtained. To this end, the position of the 180° phase-shifts has to be controlled with a resolution of about half the grating period. This type of grating could therefore also be fabricated using low-resolution (and hence low-cost) electron beam lithography.

References

[1] X. Pan, H. Olesen, and B. Tromborg, "A theoretical model of multielectrode DBR lasers," *IEEE J. Quantum Electron.*, vol. 24, no. 12, pp. 2423-2432, December 1988.

[2] G.P. Agrawal, and N.K. Dutta, *Long-wavelength semiconductor lasers*, Van Nostrand Reinhold, New York, NY, USA, 1986.

[3] K. Petermann, *Laser diode modulation and noise*, Kluwer Academic Publishers, Dordrecht, Holland, 1988.

[4] T.-P. Lee, C.A. Burrus, J.A. Copeland, A.G. Dentai, and D. Marcuse, "Short-cavity InGaAsP injection lasers: dependence of mode spectra and single-longitudinal-mode power on cavity length," *IEEE J. Quantum Electron.*, vol. 18, no. 7, pp. 1101-1113, July 1982.

[5] W.B. Joyce, "Analytic approximations for the Fermi energy in (Al,Ga)As," *Appl. Phys. Lett.*, vol.32, no. 10, pp.680-681, May 1978.

[6] Y. Kotaki, and H. Ishikawa, "Spectral characteristics of a three-section wavelength-tunable DBR laser," *IEEE J. Quantum Electron.*, vol. 25, no. 6, pp. 1340-1345, June 1989.

[7] N.P. Caponio, M. Goano, I. Maio, M. Meliga, G.P. Bava, G. Destefanis, and I. Montrosset, "Analysis and design criteria of three-section DBR tunable lasers," *IEEE J. Selected Areas in Commun.*, vol. 8, no. 6, pp. 1203-1213, August 1990.

[8] A. Tsigopoulos, T. Sphicopoulos, I. Orfanos, and S. Pantelis, "Wavelength tuning analysis and spectral characteristics of three-section DBR lasers," *IEEE J. Quantum Electron.*, vol. 28, no. 2, pp. 415-426, February 1992.

[9] A. Zatni, and J. Le Bihan, "Analysis of FM and AM responses of a tunable three-electrode DBR laser diode," *IEEE J. Quantum Electron.*, vol. 31, no. 6, pp. 1009-1014, June 1995.

[10] G. Björk, and O. Nilsson, "A new exact and efficient numerical matrix theory of complicated laser structures: properties of asymmetric phase-shifted DFB lasers," *J. Lightwave Technol.*, vol. 5, no. 1, pp. 140-146, January 1987.

[11] M. Yamada, and K. Sakuda, "Analysis of almost-periodic distributed feedback slab waveguides via a fundamental matrix approach," *Appl. Optics*, vol. 26, no. 16, pp. 3474-3478, August 1987.

[12] T. Makino, "Transfer-matrix formulation of spontaneous emission noise of DFB semiconductor lasers," *J. Lightwave Technol.*, vol. 9, no. 1, pp. 84-91, January 1991.

[13] H. Kogelnik, and C.V. Shank, "Coupled-wave theory of distributed feedback lasers," *J. Appl. Phys.*, vol. 43, no. 5, pp. 2327-2335, March 1972.

[14] A. Othonos, X. Lee, and R.M. Measures, "Superimposed multiple Bragg gratings," *Electron. Lett.*, vol. 30, no. 23, pp. 1972-1974, November 1994.

[15] G. Meltz, W.W. Morey, and W.H. Glenn, "Formation of Bragg gratings in optical fibers by a transverse holographic method," *Opt. Lett.*, vol. 14, no. 15, pp. 823-825, August 1989.

[16] A. Talneau, C. Ougier, and S. Slempkes, "Multiwavelength grating reflectors for widely tunable laser," *IEEE Photon. Technol. Lett.*, vol. 8, no. 4, pp. 497-499, April 1996.

[17] A. Talneau, J. Charil, and A. Ougazzaden, "Superimposed Bragg gratings on semiconductor material," *Electron. Lett.*, vol. 32, no. 20, pp. 1884-1885, September 1996.

[18] D.C.J. Reid, C.M. Ragdale, I. Bennion, D.J. Robbins, J. Buus, and W.J. Steward, "Phase-shifted Moiré grating fibre resonators," *Electron. Lett.*, vol. 26, no. 1, pp. 10-12, January 1990.

[19] W.H. Press, S.A. Teukolsky, W.T. Vetterling, and B.P. Flannery, *Numerical recipes in C: the art of scientific computing*, Cambridge University Press, Cambridge, UK, 1992.

[20] J.A. Nelder, and R. Mead, "A Simplex Method for Function Minimization," *Computer Journal*, vol. 7, pp. 308-313, 1964.

[21] D.C.J. Reid, D.J. Robbins, and G. Sarlet, "Multi-wavelength optical reflector," *UK Patent Application*, no. GB 2337135 A, filed May 6, 1998, published November 10, 1999 – *European Patent Application*, no. EP 0955558 A2, filed May 6, 1999, published November 10, 1999.

Chapter 4

Feedback control for frequency and mode stabilisation

During operation, the characteristics of any electronic device will degrade. Still, for fixed-frequency DFB lasers, excellent frequency stability has been demonstrated [1]-[2]. Any residual frequency drift can easily be compensated for by changing the temperature of the laser. Initial studies cast serious doubt on the long-term stability of tunable DBR lasers [3]. More recent experiments have revealed though that, after an appropriate burn-in procedure, degradation is sufficiently slow [4]-[6]. In order to compensate for any remaining drift, a feedback control loop can be applied. This control loop should not only maintain a pre-set frequency and output power, but also ensure a high side-mode suppression ratio (SMSR), since tunable lasers are not inherently single-mode.

Section 4.1 gives an overview of techniques that can be used to stabilise the laser frequency. In most cases, frequency variations are translated into power variations using an optical filter. The frequency error signal can be minimised either by adjusting the laser temperature or by adjusting the phase section current. We chose to adjust the phase current, since the response is intrinsically much faster. Variations of the temperature were on the other hand used to intentionally induce frequency drift. Experimental results presented at the end of §4.1 show that with frequency control alone, the frequency can only be kept constant over a limited temperature range (2 to 3 °C). At larger temperature deviations mode hops occur, which proves the need for a control mechanism that assures stable single-mode operation.

Such mode control mechanisms are the subject of §4.2. In literature, mode stabilisation has been demonstrated on external cavity, cleaved coupled cavity (C^3), DBR, and SSG-DBR lasers by monitoring fluctuations in the output power [7]-[12]. In the integrated tunable lasers we study in this thesis, the feedback signal is however often disturbed by the overall decrease of the output power caused by the tuning (cf. Chapter 2). As an alternative, we proposed to use the voltage across the active section as the feedback signal [13]-[16]. Since this signal comes from inside the cavity, it is generally less sensitive to the increase of absorption losses in the passive sections. In §4.2, we will investigate the limitations of both approaches by studying measurement results for various lasers.

Finally, section 4.3 describes a practical implementation of the frequency and mode control loops and reviews the test results obtained for SSG-DBR lasers.

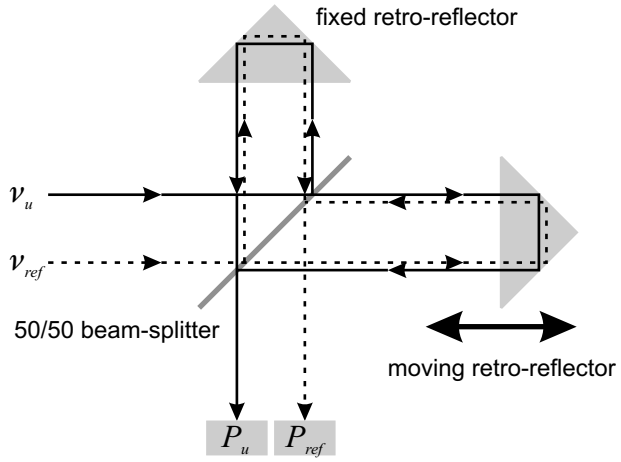

Figure 4.1 Principle of Michelson interferometer frequency meter.

As already mentioned a number of times, tunable lasers should be supplied with microprocessor controller that translates the frequency and output power requirements of the user to the appropriate control parameter values, usually based on a look-up table. If the feedback control is handled by the same microprocessor, the variation over time of the different control currents can easily be logged. Based on this information, alarm signals can be generated to inform the user when a re-calibration of the look-up table is needed[1]. Alternatively, the logged data (for a single operation point) could perhaps be used to recalculate the look-up table for all operation points, without interrupting the operation of the laser. These issues however still require further investigation.

4.1 Frequency stabilisation

Any form of feedback control involves the measurement of an error signal V, from which adjustments of the control parameters are derived. The emission frequency of a laser can be measured directly using a wavelength meter. Such an instrument is generally based on a scanning Michelson interferometer [17] (Figure 4.1). The frequency ν_u of the input light is compared to the frequency of a reference laser ν_{ref}. The reference laser is usually a HeNe gas laser, which has a very stable output frequency. In a typical optical configuration, corner-cube retro-reflectors separate the outgoing and return beams in each arm of the interferometer. In this way, the unknown laser beam and the reference laser beam can be directed along exactly the same path in opposite directions. The interference patterns are detected with two photodiodes. When one of the reflectors is scanned over a certain distance, the powers P_u and P_{ref} will show periodic maxima and minima. If the number of fringes N_u and N_{ref} are counted for both beams, then the unknown laser frequency can be derived from:

[1] How look-up tables can be generated/updated efficiently will be the topic of Chapter 5.

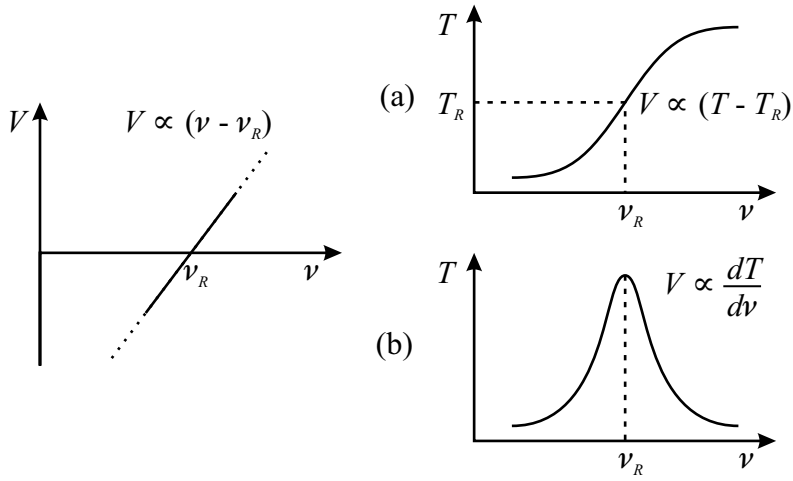

Figure 4.2 Control signal V for frequency stabilisation, generated using a filter edge, which requires an intensity reference (a) or a filter peak, which requires frequency dithering (b).

$$\nu_u = \frac{N_u}{N_{ref}} \nu_{ref} \tag{4.1}$$

By using long scans, or by subdividing the fringes, the unknown laser frequency can typically be determined with a relative accuracy of a few p.p.m. (parts per million). This measurement approach however has a few disadvantages: the interferometer is quite bulky and a single frequency measurement normally takes about one second, which is often too slow for use in a control loop. The advantage is conversely that a direct measurement can be used to stabilise the laser at any desired frequency.

Other techniques to generate a frequency error signal use an optical filter to translate frequency variations into intensity variations. Two possibilities are illustrated in Figure 4.2. In Figure 4.2(a), the edge of a filter transfer characteristic is used, which requires measuring the power of the input light by splitting off part of the light before the filter. The transmission T is the ratio of the power of the filtered light P_f to the power of the unfiltered light P_u. The error signal is then derived by subtracting the value of the transmission T_R at a reference frequency ν_R. Close to the reference frequency one obtains:

$$V = (T - T_R) \propto (\nu - \nu_R) \tag{4.2}$$

A variant of this scheme consists of splitting the light and using two optical filters, of which one has a positive slope around the reference frequency and the other a negative slope. The error signal is then proportional to the difference of the two filtered powers.

In Figure 4.2(b), the laser frequency is stabilised to a transmission peak of a filter. This requires a slight dither of the laser frequency, such that the derivative of the transmissivity to frequency can be measured. The error signal is thus given by:

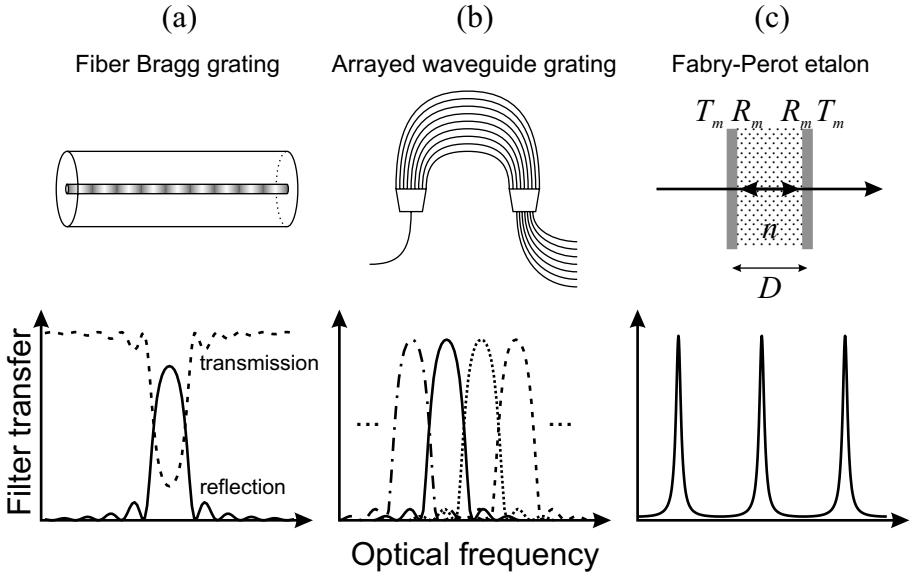

Figure 4.3 Examples of frequency referencing optical filters: a fiber Bragg grating (a) an arrayed waveguide grating (b) or a Fabry-Perot etalon (c).

$$V \propto \frac{dT}{d\nu} \propto (\nu - \nu_R) \tag{4.3}$$

Here the last proportionality only applies close to the peak, where the transfer characteristic can be approximated by a parabola.

If such a filter is to be used as a frequency reference, the centre frequency ν_R must remain very stable over time and must show a very low sensitivity to environmental changes (temperature, humidity). Since the temperature coefficient of the refractive index of semiconductor materials (e.g. InGaAsP/InP) is rather high (about $2 \cdot 10^{-4}$ K^{-1}, cf. §2.1.3), these materials are not used to fabricate referencing filters. Silica (glass) has a refractive index temperature coefficient that is an order of magnitude lower (about $1.3 \cdot 10^{-5}$ K^{-1}), and is hence much more suitable. Still, a silica-based filter is often temperature-controlled to achieve high accuracy and stability. Alternatively, the silica filter can be put into a temperature-compensating package, in which the compressive (tensile) strain on the filter increases (decreases) with temperature, such that the rise in refractive index is compensated by a reduction in length [18]-[19]. Filters are also developed using new materials that have a low temperature coefficient of the refractive index.

Figure 4.3 presents a few examples of filters that can be used as frequency references. Figure 4.3(a) shows a fiber Bragg grating with plots of the reflection and transmission spectrum. The frequency can be stabilised on the edge of the Bragg peak by splitting the light and stabilising the ratio of the power of the filtered light P_f to the power of the unfiltered light P_u [20]. Alternatively, both the transmitted and the reflected power can be measured, and the frequency can be locked to the point where these are equal [21].

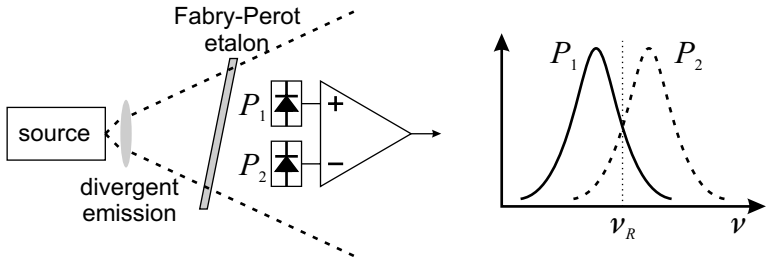

Figure 4.4 Compact frequency discriminator using a tilted Fabry-Perot etalon [24]-[26].

A second option is the arrayed waveguide grating (AWG), which is used as a frequency demultiplexer. Input light will be directed to a particular output port depending on the frequency. Figure 4.3(b) shows an example of the transmission spectra for a number of output ports. The frequency can either be stabilised at the cross-point of the transmissivities of two adjacent ports [11]-[12], [22] or at the peak frequency of a single port by applying a frequency dither [23].

Perhaps the simplest alternative is the Fabry-Perot etalon (Figure 4.3(c)), of which the transmittance (in the symmetric case) is described by:

$$T(\nu) = \frac{T_m^2}{(1 - R_m)^2 + 4R_m \sin^2(2\pi\nu n D/c)} \tag{4.4}$$

R_m and T_m are the reflectivity and transmissivity of the mirrors, respectively; n is the refractive index of the material between the mirrors, and D is the distance between the mirrors. This transfer function has periodic maxima, which are spaced by:

$$\Delta\nu = c/(2n_g D) \tag{4.5}$$

The spacing $\Delta\nu$ is also called the free spectral range (FSR).

In [24], the laser frequency was locked to the transmission peak of a Z-cut quartz etalon. Z-cut quartz exhibits a strong electro-optic effect: its refractive index can be changed by applying an electric field. Therefore, in this case the peak frequency of the etalon can be modulated rather than the laser frequency to generate the error signal V proportional to $dT/d\nu$. This is simply done by applying a sinusoidal voltage to the quartz etalon.

A very compact frequency discriminator that uses a Fabry-Perot etalon was presented in [25]-[26] (Figure 4.4). Here, the etalon is positioned at a certain angle in a diverging beam. If the light is incident on the etalon at an angle θ to the normal, then the distance D in (4.4)-(4.5) has to be replaced by $D/\cos(\theta)$. Behind the etalon, the light is detected by two closely spaced photodiodes acting as apertures (powers P_1 and P_2). Each captures a different portion of the solid angle of the light beam. Thus, two different spectral responses are obtained, offset in frequency according to the angular difference. Since photodiode 2 captures a portion of the emitted light that traversed the etalon at a lower tilt angle θ than the light captured by photodiode 1, its response will peak at a slightly higher frequency. Ideally, the offset is approximately equal to the FWHM of the transmittance peak.

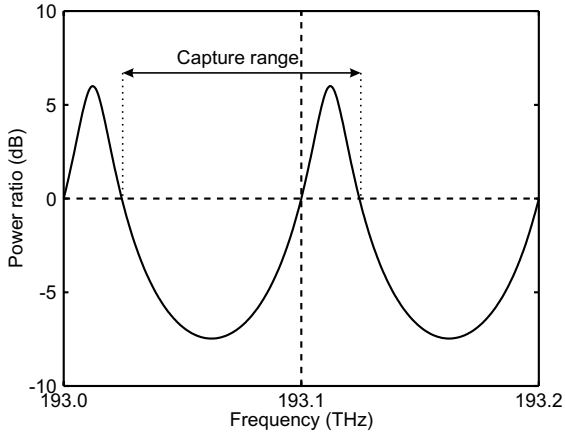

Figure 4.5 Typical transfer characteristic of the Fabry-Perot wavelength locker. Ratio of filtered to unfiltered power (logarithmic scale) as a function of optical frequency. Parameters: mirror reflectivity $R = 1 - T = 0.65$, free spectral range $\Delta\nu = 100.0063$ GHz, splitting ratio 25/75 and calibration factor $\eta = 1.32$.

The frequency is stabilised at the point of equal transmissivity by using the difference in power as the error signal V. The small footprint of this configuration allows its incorporation into a standard laser package [26]. This has the additional advantage that the etalon can be placed on the same thermoelectric cooler as the laser, thus relieving some of the stringent stability requirements.

For wavelength division multiplexing applications, the laser frequency has to be stabilised to an integer multiple of 50 GHz or 100 GHz, as specified by the International Telecommunication Union [27]. In the case of a tunable laser, this of course requires a periodic frequency reference. Consequently, the fiber Bragg grating is not very suitable. Multiple Bragg gratings could be incorporated into a single fiber, either one after the other or superimposed at the same location, but such an approach is not scalable to large channel numbers. The arrayed waveguide grating can be used if it has sufficient output ports (with peak frequencies spaced by 50 GHz or 100 GHz) to cover the tuning range of the laser. The disadvantages are that silica AWGs are rather large (several cm^2), and that different output ports have to be used for each grid frequency. The most suitable reference filter for a tunable laser is the etalon, since it is inherently periodic. By properly choosing the angles and distances in Figure 4.4 for example, this configuration can produce simultaneous locking points for any channel on the ITU grid [25].

We have used a commercially available Fabry-Perot wavelength locker (E-Tek FPWL [28]). In this component, a small fraction (≈ 5%) of the input light is tapped off for frequency monitoring, while the remainder is passed through to the output. The split-off light is then again divided (splitting ratio ≈ 25/75). The smaller fraction is directly detected (power P_1) and the larger is filtered through an etalon with a free spectral range of 100 GHz (power P_2). Figure 4.5 shows a typical plot of $V = 10 \cdot \log(\eta P_2/P_1)$ as a function of frequency around the ITU anchor frequency of 193.1 THz ($\eta \approx 1.32$ is a calibration factor). In fact, the FSR is not exactly 100 GHz,

but has been chosen a few MHz larger to allow locking on the filter edges instead of the filter peaks. Due to the slightly larger FSR, the transmittance peaks are shifted towards higher frequencies. Of course, the offset will vary slightly from channel to channel. This means that if a constant power ratio P_2/P_1 is used to lock the frequency for all ITU channels (i.e. the 0 dB line in Figure 4.5), absolute accuracy can only be achieved for a single channel. Yet, since the FSR is much smaller than the absolute frequency and since the relative deviation on the FSR is also very little, the error on the locking frequencies will be almost negligible across the range of interest (less than ±0.2 GHz between 190 THz and 196 THz with the parameters from Figure 4.5).

The frequency error signal V must be used to adjust the laser frequency, i.e. the frequency of the cavity mode with lowest roundtrip loss. Fine-tuning of this frequency can be done either by changing the temperature of the laser [20]-[21], [26] or by changing the current through the phase section [11]-[12], [22]. When the feedback control is applied to the phase current, then variations of the laser sub-mount temperature can be used to induce frequency drift and test the control loop. Figure 4.6 shows the evolution of the emission frequency of a SSG-DBR laser with sub-mount temperature with and without frequency control. The laser is initially tuned to 193.4 THz at 25 °C. Subsequently the sub-mount temperature is increased or decreased in steps of 0.2 °C.

The dots illustrate the linear decrease of the emission frequency with temperature when no control is applied. The slope is approximately -14.5 GHz/°C. When the error signal from the Fabry-Perot wavelength locker is used to adjust the phase section current, the frequency initially remains locked to the reference value of 193.4 THz. Locking is however only maintained across a limited temperature range, from 23.2 to 25.6 °C. If the temperature is moved out of this range, a mode hop occurs. The feedback loop then quickly saturates the phase current, which means that the frequency is no longer controlled. Evidently, the frequency then again varies linearly with temperature.

Let us look in more detail what happens when the temperature is increased above 25 °C. The feedback loop raises the phase current in order to compensate for the temperature-induced frequency drift. However, no feedback control is applied to the SSG-DBR reflectors. Hence, the reflectivity peaks of these reflectors will shift to lower frequencies. At a certain point, the misalignment between the reflectivity peaks and the lasing mode becomes so large that the side-mode suppression ratio is reduced (Figure 4.7). If the temperature is increased any further, an adjacent cavity mode will see a lower roundtrip loss and will become the preferential mode. The lasing frequency then suddenly jumps downward, in this case by about 45 GHz. The feedback loop tries to correct for this frequency hop by increasing the phase current, but as soon as the lasing frequency comes close to the reference value another mode hop occurs, etc. This goes on until the phase current saturates at its upper limit. Similar observations can be made for decreasing temperatures.

The asymmetry in Figure 4.6 and Figure 4.7 is due to a slight detuning of the cavity mode with respect to the reflectivity peaks at the initial temperature of 25 °C. Optimum alignment is obtained at approximately 24.5 °C. In this case, an alarm signal can of course be generated when the phase current saturates to warn the user that something has gone wrong.

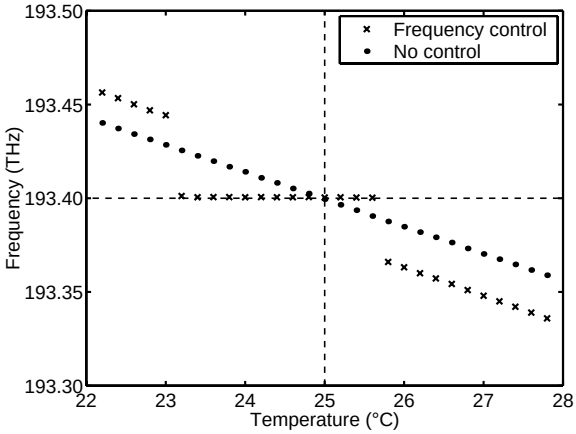

Figure 4.6 Evolution of the emission frequency of a SSG-DBR laser with sub-mount temperature, with and without frequency control. The frequency reference is a Fabry-Perot etalon with a free spectral range of 100 GHz. The laser was initially tuned to 193.4 THz at 25 °C.

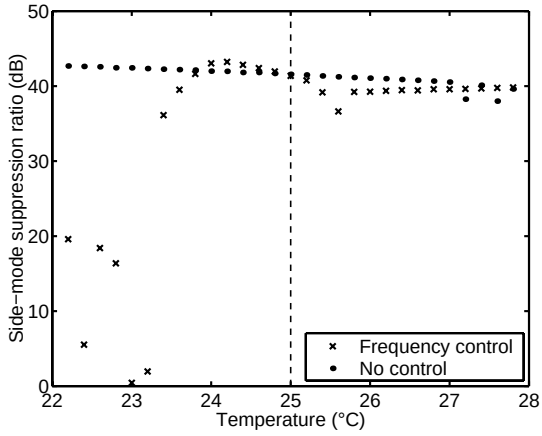

Figure 4.7 Evolution of the side-mode suppression ratio (SMSR) of a SSG-DBR laser with sub-mount temperature, with and without frequency control (compare with Figure 4.6).

If the free spectral range of the reference filter is smaller than 100 GHz, close to the cavity mode spacing of the laser (or even an integer fraction of the mode spacing), the control loop could in some cases stabilise again after the mode hop, albeit at an incorrect frequency. This is illustrated by Figure 4.8, which shows the result of a frequency control experiment where a frequency reference with a FSR of 50 GHz was simulated. This was done by measuring the laser spectrum with an optical spectrum analyser, reading out the data using a PC, and filtering the measured spectrum numerically in order to calculate the necessary correction on the phase current [14]-[15]. Around 25 °C, the frequency again remains locked to the reference value (193.90 THz).

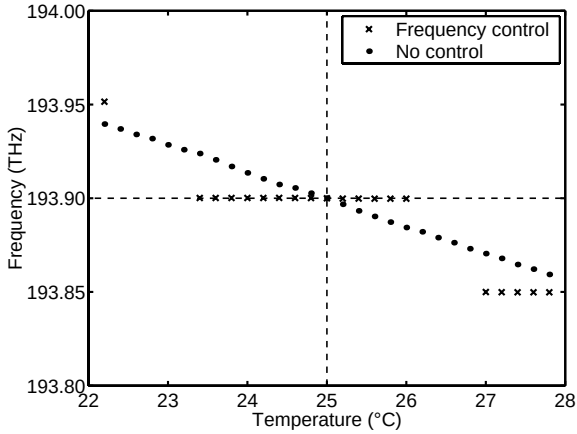

Figure 4.8 Evolution of the emission frequency of a SSG-DBR laser with sub-mount temperature, with and without frequency control. A frequency reference with a free spectral range of 50 GHz was simulated. The laser was initially tuned to 193.9 THz at 25 °C.

At high and low temperatures on the contrary, the frequency is stabilised at the adjacent 50 GHz channel. In the intermediate regions, the frequency is continuously hopping back and forth between the two channels. The reason for this is that the mode spacing (45 GHz) is slightly smaller than the FSR of the filter (50 GHz). Consider again the case of increasing temperatures. After the mode hop, the lasing frequency is somewhat higher than the central frequency of the adjacent channel, 193.85 THz. The feedback loop reduces the phase current to correct for this offset. This however causes the lasing frequency to jump back to the original cavity mode, which shows a slight negative offset with respect to the original reference. That naturally triggers the loop to increase the phase current again, etc. The loop only stabilises when the front and rear reflectivity peaks have drifted close enough to 193.85 THz, i.e. at a temperature of approximately 27 °C.

These experiments amply prove the need for a control mechanism that keeps the laser in a stable single longitudinal mode.

4.2 Mode stabilisation

A tunable laser will only emit light in a single spectral line if the (tunable) intra-cavity filter is more or less aligned with one particular cavity mode and the filter bandwidth is sufficiently narrow, such that all other cavity modes are suppressed. The optimum side-mode suppression ratio is obtained when the gain margin Δg is maximised, where Δg is defined as:

$$\Delta g = \min\left\{\alpha_{tot}(\omega_i) - \Gamma g(\omega_i, N) \,\middle|\, \omega_i \neq \omega_{out}\right\} \tag{4.6}$$

Here, the ω_i are the angular frequencies of all cavity modes, ω_{out} is the lasing frequency, Γ is the confinement factor, g the gain in the active section, and α_{tot} the total roundtrip loss expressed per unit length (cf. §3.1.1).

If a feedback loop has to be devised that keeps the laser in a stable single mode, the first problem to be solved is to find a suitable control signal. The most obvious way to derive a control signal is of course to measure the emission spectrum of the laser directly with an optical spectrum analyser and calculate the SMSR. However, a typical spectral measurement takes several seconds, and an optical spectrum analyser can not exactly be fitted into a transmitter module.

In literature numerous experiments have been described where variations of the output power with tuning are used to determine whether the intra-cavity filter is aligned with a cavity mode or not [7]-[12]. In the integrated tunable laser diodes we study in this thesis, these (small) variations in the output power are however often masked by the overall decrease of the output power caused by the tuning (due to the increase of absorption losses in the passive sections). Therefore, we proposed to use the voltage across the active section as the feedback signal, which in the absence of losses shows similar variations with tuning, and is less affected by the increasing absorption losses [13]-[16]. Still, even the voltage will only provide useful information if certain assumptions are met, as will be illustrated by experimental results presented below.

4.2.1 DBR laser

Simplified DBR laser

We begin by studying a simplified DBR-like laser. The laser consists of a Fabry-Perot cavity with one frequency-independent mirror r_L and one tunable frequency-dependent mirror $r_R(\omega)$ (the DBR). The frequency-dependence of the gain g is initially neglected. The total roundtrip loss $\alpha_{tot}(\omega)$ is approximated by a parabola, and we assume that the loss minimum is initially aligned with a cavity mode. We normalise all frequencies with respect to the frequency of this mode ν_0:

$$\delta\nu = (\nu - \nu_0)/\Delta\nu \,, \tag{4.7}$$

where $\Delta\nu$ is the cavity mode spacing. The gains and losses are normalised with respect to the cavity length L.

$$A = L\alpha_{tot} \quad \text{and} \quad G = L\Gamma g \tag{4.8}$$

If internal losses are neglected ($\alpha_{int} = 0$), the mirror reflectivity $r_R(\delta\nu)$ is related to the roundtrip loss $A(\delta\nu)$ as:

$$r_R(\delta\nu) = \frac{1}{r_L} e^{-A(\delta\nu)} \tag{4.9}$$

We set the minimum normalised loss to a typical value of 1.0 and assume that r_L equals 0.5. In the following paragraphs, we will study what effects the tuning of the frequency of minimum roundtrip loss $\delta\nu_B$ has on the output characteristics of the laser. Figure 4.9 illustrates the tuning of the loss minimum from one cavity mode (mode 0) to the next (mode 1) and the corresponding changes of the modal gains (crosses) and the lasing frequency (vertical line). For the lasing mode, gain of course equals loss. The lasing frequency jumps to mode 1 when the loss minimum has been shifted by half the mode spacing ($\delta\nu_B = 0.5$), because from then on mode 1 experiences a lower loss than mode 0.

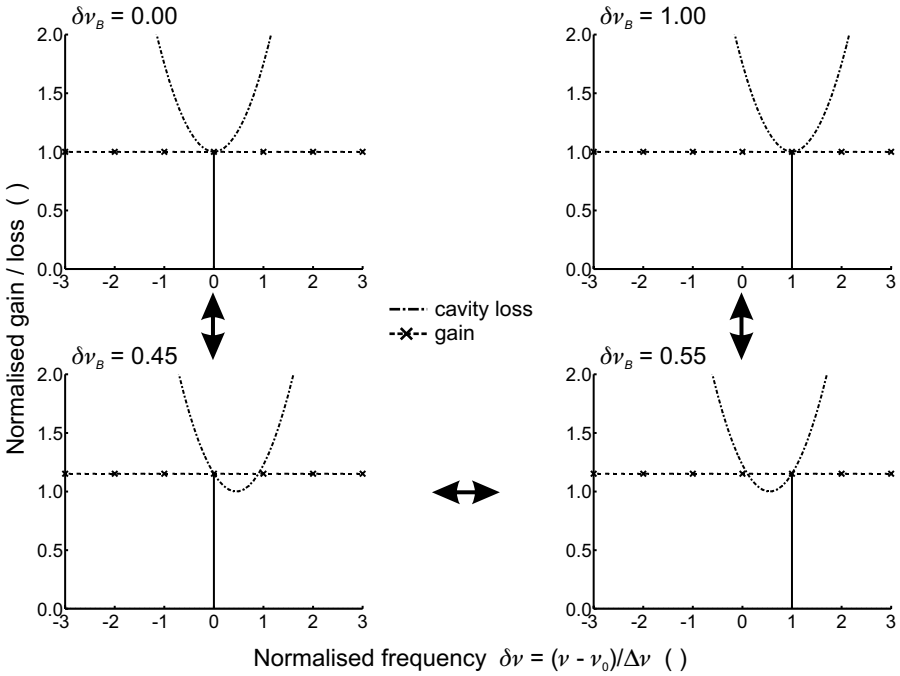

Figure 4.9 Evolution of normalised gain and cavity loss when the frequency of minimum cavity loss $\delta\nu_B$ is tuned from cavity mode 0 to cavity mode 1. Crosses (×) indicate the gain of the different cavity modes. For the lasing mode, indicated by the vertical line, gain of course equals loss.

As was mentioned in §3.1.2, the output power of a laser is proportional to the difference between the drive current I and the threshold current I_{th}, where the slope is determined by the differential efficiency η_d.

$$P_L = \eta_{d,L} \frac{\hbar\omega}{q}(I - I_{th}) \tag{4.10}$$

With the above assumptions the expression for the differential efficiency $\eta_{d,L}$ (3.23) becomes:

$$\eta_{d,L} = \frac{(1 - r_L^2) r_R}{(1 - r_L r_R)(r_L + r_R)} \tag{4.11}$$

The expression for the differential efficiency from the other end of the cavity ($\eta_{d,R}$) is obtained by swapping the subscripts L and R. Since we have neglected internal losses, we have

$$\eta_{d,L} + \eta_{d,R} = 1 \tag{4.12}$$

Figure 4.10 displays the variation of the differential efficiencies and the threshold gain with tuning. When the loss minimum is aligned with a cavity mode, or in other words when a cavity mode experiences a maximum reflectivity r_R, the threshold is lowest (cf. Figure 4.9). At the same time, the left differential efficiency $\eta_{d,L}$ will be maximised (4.11) and the right differential efficiency $\eta_{d,R}$ will be minimised.

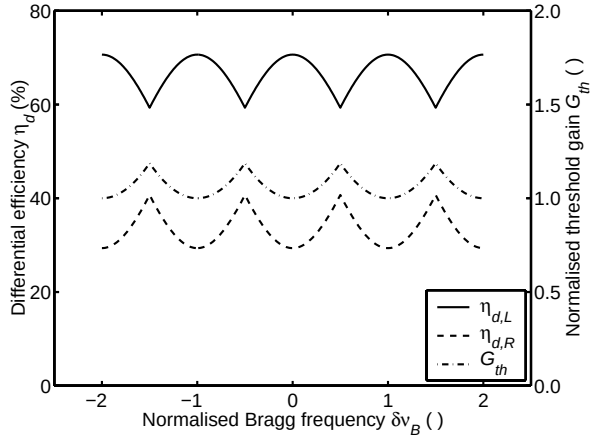

Figure 4.10 Variation of differential efficiency η_d and normalised threshold gain G_{th} with tuning for the idealised DBR-like laser.

If the laser is biased sufficiently above threshold, the variations in output power with tuning will mainly be determined by variations in differential efficiency. The alignment of the reflector peak with a cavity mode can then be detected as a maximum in the left output power P_L or a minimum in the right output power P_R. A high SMSR can therefore be maintained by making sure that the laser remains at the power extremum (with respect to the tuning of the DBR) [10]-[11].

If the laser is biased at a constant current I, then variations in the active section voltage can only be caused by changes in the carrier density (cf. (3.24)). The carrier density is of course determined by the threshold condition. If the threshold gain increases because the reflectivity peak is detuned from the cavity mode (Figure 4.10), then the carrier density must grow to generate sufficient gain, which will in turn raise the active section voltage. To a first order approximation, both the gain at threshold and the active section voltage depend linearly on the carrier density, so the variation of the voltage with tuning will look quite similar to the gain curve in Figure 4.10. The alignment of the reflector peak with a cavity mode can hence also be detected as a minimum in the active section voltage.

It is immediately clear that significant variations in output power and voltage will only be measured if the filter peak is narrow with respect to the cavity mode spacing. On the other hand, a high selectivity is needed anyway to guarantee a high side-mode suppression ratio.

Realistic DBR laser

Figure 4.11 and Figure 4.12 show the results of a calculation for a more realistic DBR laser, using the model presented in Chapter 3. The laser consists of an active section of 300 µm, a phase section of 100 µm, and a DBR of 400 µm length. The coupling coefficient is 25 cm^{-1} ($\kappa L = 1.0$) and the Bragg frequency at zero DBR current is 193.1 THz. Other parameters are as listed in Table 3.1 and Table 3.2.

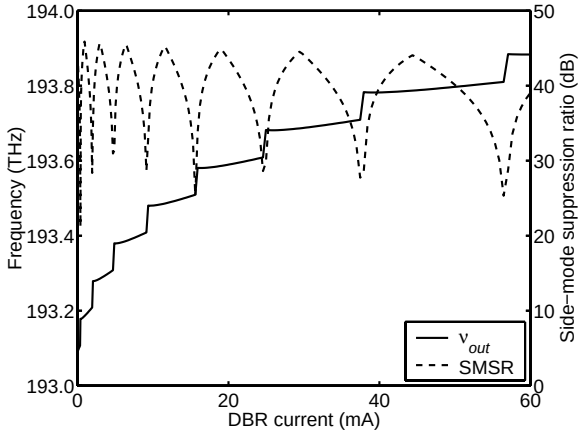

Figure 4.11 Calculated variations of frequency and side-mode suppression ratio as a function of the DBR tuning current. The DBR laser consists of an active section of 300 µm, a phase section of 100 µm and a DBR of 400 µm length. The coupling coefficient is 25 cm^{-1} (κL = 1.0) and the Bragg frequency at zero DBR current is 193.1 THz. Other parameters are as listed in Table 3.1 and Table 3.2.

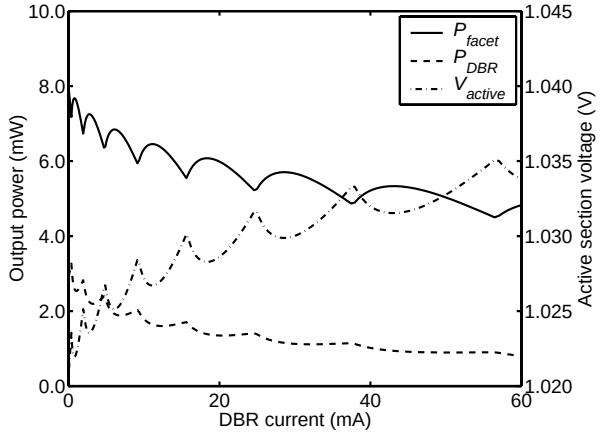

Figure 4.12 Calculated variations of output power and active section voltage with tuning for the DBR laser from Figure 4.11.

Figure 4.11 reveals a plot of the frequency and side-mode suppression ratio as a function of the current through the DBR. The SMSR is maximal approximately halfway between two mode hops, and decreases rapidly close to the mode hops. Near the points of maximal SMSR, extrema are observed in the power emitted from the cleaved facet P_{facet} and in the active section voltage V_{active} (Figure 4.12). The simulation results for the SMSR and the facet output power confirm the experimental results published in [9]-[10]. As the current through the DBR is increased, absorption losses in this section will grow proportional to the carrier density (cf. §2.1.1).

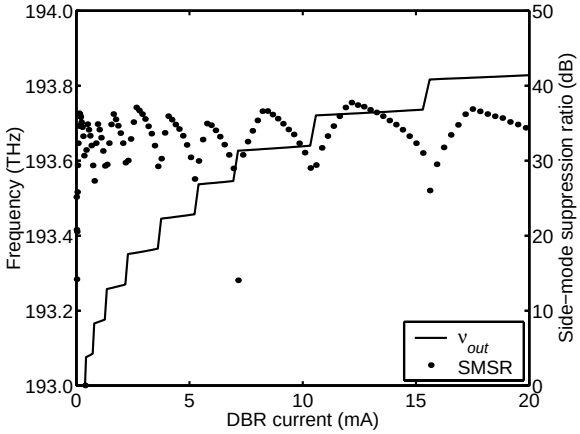

Figure 4.13 Measured emission frequency and side-mode suppression ratio as a function of the DBR tuning current at an active section current of 30 mA ($I_{th} \approx 20$ mA).

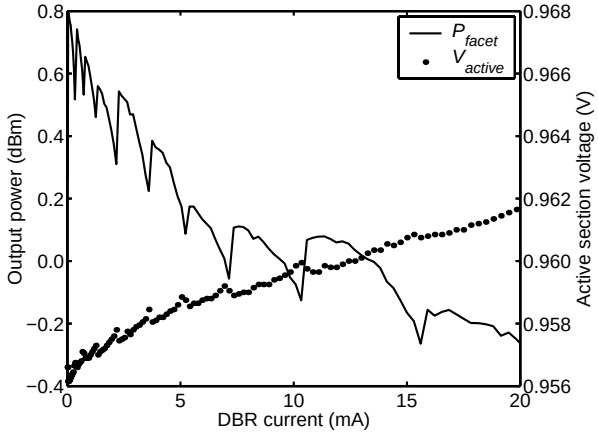

Figure 4.14 Measured output power and active section voltage as a function of the DBR tuning current at an active section current of 30 mA ($I_{th} \approx 20$ mA).

This yields an overall decrease of output power and increase of voltage with tuning, shifting the extrema in P_{facet} and V_{active} somewhat towards lower DBR currents relative to the SMSR maxima. The power emitted from the lossy DBR side is obviously affected much more: the minima shift quite significantly towards higher DBR currents, and even tend to be blurred out at high tuning currents.

Figure 4.13 and Figure 4.14 present measurement results for a DBR laser that consists of an active section of 400 µm, a phase section of 100 µm and a DBR of 500 µm length. Particular to this DBR laser is that the passive sections have a InGaAsP core layer with a band-gap wavelength of 1.48 µm. The band-gap wavelength was chosen that close to the emission wavelength (approximately

1.55 μm) in an attempt to reduce the carrier-induced absorption losses in the phase and DBR sections [29]. To increase the output power from the front facet, the Bragg reflector was also designed with a rather high coupling coefficient ($\kappa L > 2$).

Figure 4.13 plots the variation of the emission frequency ν_{out} and the side-mode suppression ratio with the current through the DBR. The maximum SMSR is only about 35 dB, because the laser is only biased at roughly 50% above the threshold current ($I_{th} \approx 20$ mA) (the reason for this will become clear below). The SMSR maxima occur approximately halfway between two subsequent mode jumps, just as in Figure 4.11. Figure 4.14 presents the corresponding variations of the output power P_{facet} and the active section voltage V_{active}. The measured curves do not look like the calculated curves in Figure 4.12 at all. The output power tends to decrease monotonously, except for the sudden upward steps at the mode hops. In between mode hops, no power maxima are obtained. The active section voltage does not exhibit any clear minima either. Apart from the general upward trend due to the increasing absorption losses, the voltage shows very little variation at all.

A possible explanation lies in the high κL-value, which yields a broad reflectivity peak, combined with a non-uniform gain spectrum, such that adjacent cavity modes experience different gain. In Chapter 3, we assumed a parabolic variation of the gain with optical frequency. Thus, a difference in gain between adjacent cavity modes can for example occur if the Bragg frequency is detuned from the gain peak frequency. The larger the detuning, the greater the difference will be. Locally, the variation of the gain with frequency can be linearised. Let us therefore first return to the simple model of the DBR laser used above, in which we now introduce a linear variation of the gain as a function of the (normalised) frequency (Figure 4.15).

Since the gain is no longer uniform, we now consider the normalised gain G_0 at the reference frequency ν_0 ($\delta\nu = 0$). In the simple parabolic gain model, the entire gain curve just moves up and down with the carrier density (if we neglect the shift of the gain peak with carrier density). Hence, the gain G_0 is linearly related to the carrier density.

Due to the tilt of the gain spectrum (Figure 4.15), the mode hop no longer occurs when the loss minimum is halfway between two cavity modes. The mode hop point is shifted in the direction of decreasing gain. A broader loss curve on the other hand reduces the variations of the differential efficiency $\eta_{d,L}$ and the gain G_0 with tuning. In Figure 4.15, the curvature of the loss $A(\delta\nu)$ has been reduced by a factor of 3 compared to Figure 4.9 (i.e. from 1.5 to 0.5). Figure 4.16 compares the variation of the differential efficiency $\eta_{d,L}$ and the normalised gain G_0 with tuning for uniform gain and for a linearly varying gain with a slope $\partial G/\partial\delta\nu$ of –0.15. In the latter case, the mode hop points are shifted by 0.3, i.e. mode hops occur at $\delta\nu =$ …, -1.2, -0.2, 0.8, 1.8, …

With flat gain, a mode hop occurs when the lasing mode and an adjacent cavity mode experience equal loss A, or in other words when the DBR reflectivity r_R is equal for both modes. Hence, the differential efficiency (4.11) varies continuously. With tilted gain, the mode hop occurs when the difference in loss between the two adjacent modes equals the difference in gain. Since the two modes see a different r_R, the differential efficiency changes discontinuously at the mode hop.

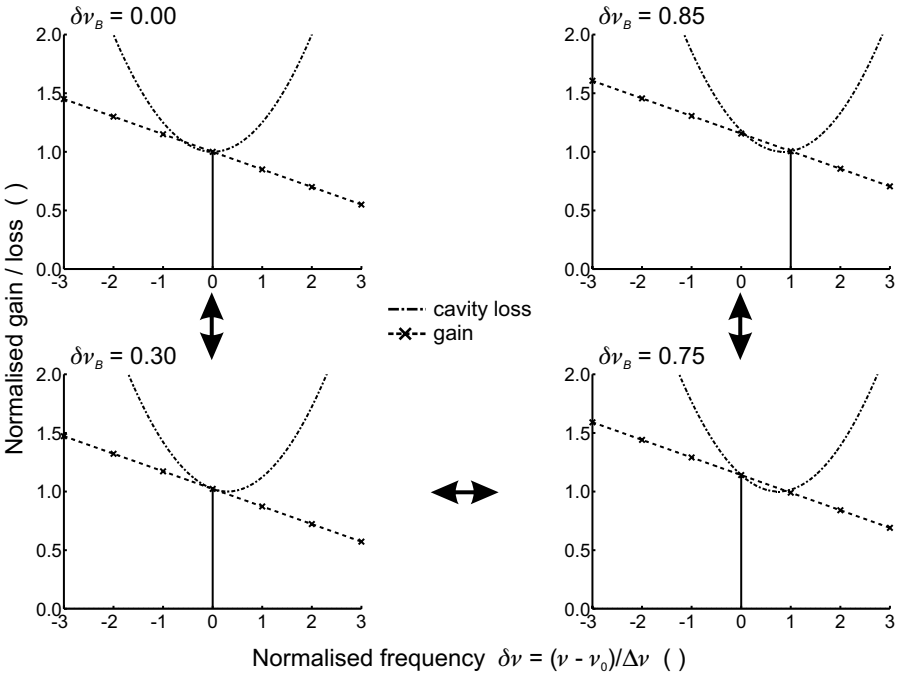

Figure 4.15 Evolution of normalised gain and cavity loss when the frequency of minimum cavity loss $\delta\nu_B$ is tuned from cavity mode 0 to cavity mode 1. Crosses (×) indicate the gain of the different cavity modes. Compared to Figure 4.9, the gain curve has been tilted (slope $\partial G/\partial\delta\nu = -0.15$) and the curvature of the loss curve was reduced by a factor 3 (from 1.5 to 0.5).

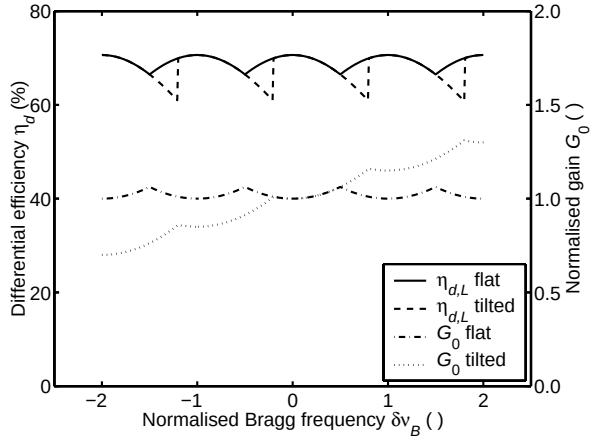

Figure 4.16 Variation of differential efficiency η_d and normalised gain G_0 (i.e. the gain at $\delta\nu = 0$) with tuning for the idealised DBR-like laser, for a flat gain profile and for a tilted gain profile with a slope $\partial G/\partial\delta\nu$ of –0.15. Compared to Figure 4.10, the curvature of the loss curve was reduced by a factor 3.

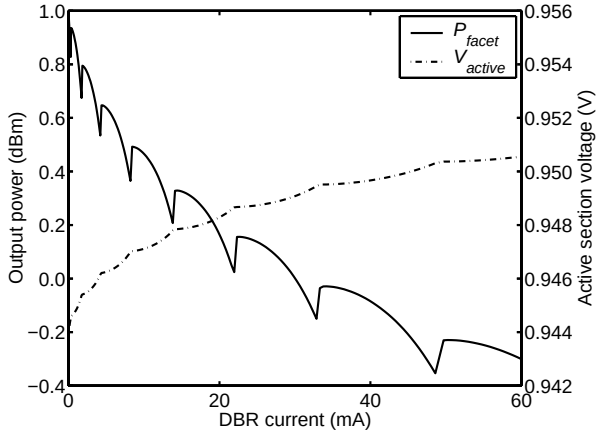

Figure 4.17 Calculated variations of output power and active section voltage as a function of the DBR tuning current. Parameters are as in Figure 4.11, except for: $\kappa = 75$ cm^{-1} ($\kappa L = 3.0$), $\partial\alpha/\partial N = 1.0 \cdot 10^{-9}$ μm^2, and $\omega_{p,0} = 2\pi \cdot 188$ THz.

The normalised gain G_0 at the reference frequency $\delta\nu = 0$ on the other hand varies continuously, because the gain G_0 is equal to the threshold gain of the lasing mode *plus* the gain difference between the lasing mode and mode 0. Due to the negative gain slope, it therefore increases when the loss minimum is tuned to higher frequencies. Again, in a real laser the carrier density and the active section voltage will show a similar variation.

Note that a maximum SMSR, or a maximum gain margin (4.6), is no longer obtained when the lasing mode is aligned with the loss minimum. The points of maximum SMSR are located exactly halfway between two mode jumps (with the numerical values from above that is at $\delta\nu =$ …, -0.7, 0.3, 1.3, …). Hence, these points no longer coincide with the extrema in differential efficiency and gain, which still arise when the lasing mode is aligned with the loss minimum. The difference increases with the width of the loss minimum and the slope of the gain curve. If one wants to use the voltage or the output power for mode control, the reflector peak therefore has to be kept sufficiently narrow (e.g. by reducing the κL-product) and the gain difference between adjacent cavity modes has to be minimised.

Figure 4.17 shows the result of a more realistic simulation. Compared to Figure 4.12 three parameters were changed. In order to better match the design of the DBR from Figure 4.13 and Figure 4.14, the coupling coefficient κ was increased to 75 cm^{-1} ($\kappa L = 3.0$) and the variation of loss with carrier density in the passive sections $\partial\alpha/\partial N$ was reduced to $1.0 \cdot 10^{-9}$ μm^2. To increase the gain difference between adjacent cavity modes around 193 THz, the gain peak frequency at transparency was shifted to 188 THz. This yielded a gain peak frequency of approximately 191 THz at the threshold carrier density. A good qualitative agreement is obtained between Figure 4.17 and Figure 4.14.

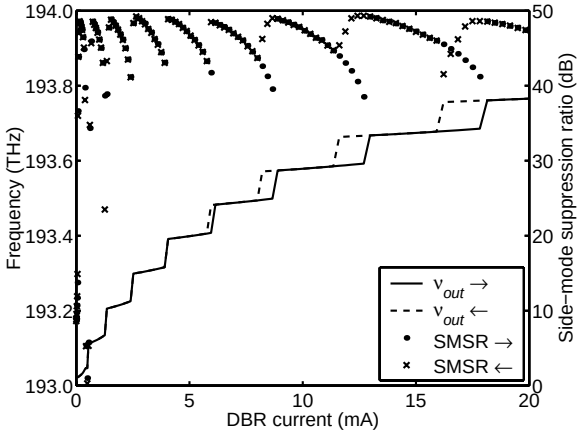

Figure 4.18 Measured emission frequency and side-mode suppression ratio as a function of the DBR tuning current at an active section current of 100 mA ($I_{th} \approx 20$ mA). Plots are shown both for increasing and decreasing DBR current.

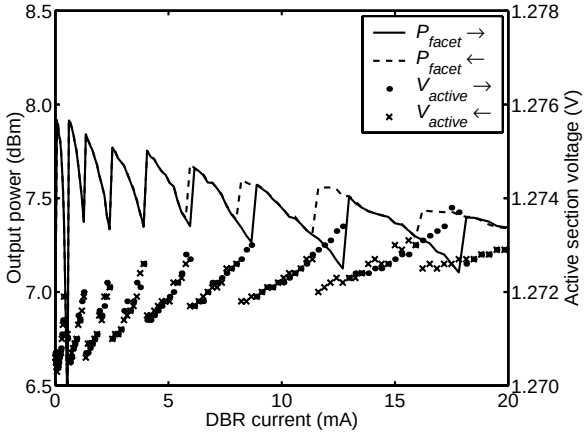

Figure 4.19 Measured output power and active section voltage as a function of the DBR tuning current at an active section current of 100 mA ($I_{th} \approx 20$ mA). Plots are shown both for increasing and decreasing DBR current.

If the active section current of the DBR laser from Figure 4.13 is increased, another phenomenon appears. Figure 4.18 and Figure 4.19 show measurement results at an active section current of 100 mA. Apparently, the mode hops occur at different DBR currents, depending on whether the current is increased or decreased. This hysteresis also widens with the DBR current. When the DBR current is increased, the maximum SMSR is obtained just after a mode hop. The output power shows a similar sawtooth-like behaviour as above, but the shape of the voltage curve has changed dramatically. Now, a sudden jump in voltage is observed at the mode hops, which indicates that the carrier density changes abruptly after a mode hop. The

hysteresis and the voltage jumps can not be explained by the above theory. They are commonly attributed to a non-linear asymmetric gain suppression [30]-[34].

The shape of the gain spectrum around the lasing frequency can be distorted by a number of effects [30]-[32]. The first one is the so-called spectral hole burning. Due to the stimulated emission, carriers at energy levels corresponding to the lasing frequency will recombine at a high rate. The recombined carriers have to be replaced by newly injected carriers, as well as by carriers from adjacent energy levels (through intra-band carrier scattering), in order to keep the gain at a certain level. The replacement of recombined carriers by carriers from adjacent energy levels does however not occur instantaneously. Consequently, the gain for frequencies around the lasing frequency will be suppressed compared to the gain at more distant frequencies. The magnitude of this gain suppression evidently increases with the optical power density in the active material.

In the presence of two or more modes, wave mixing of these modes causes pulsations of the intra-band carrier distribution. Consider for example the case of a lasing mode at frequency ν_0 and an adjacent cavity mode at frequency ν_1. The carrier distribution within the conduction and valence band will then experience a periodic modulation at the beat frequency $\Delta\nu = |\nu_0 - \nu_1|$. This will again affect the gain at the frequencies around the frequency of the lasing mode ν_0. The detailed analysis of these phenomena however falls beyond the scope of this thesis.

A qualitative illustration of the effects leading to tuning hysteresis is shown in Figure 4.20 for the simplified DBR laser model. The gain suppression, which is represented by the dotted line, has a component that is symmetric with respect to the lasing frequency, and a component that is anti-symmetric. These are caused by the spectral hole burning and the carrier pulsations, respectively (cf. [30]-[34]). Although the shape of the gain suppression will normally vary when the side-mode suppression ratio or the output power changes, we will neglect such effects for simplicity. Crosses (×) mark the gain at the cavity mode frequencies and the gain G_0 in absence of non-linear gain saturation is represented by the dashed line. Relative to the gain of the lasing mode, the gain for the adjacent higher frequency mode is strongly suppressed, while the gain for the adjacent lower frequency mode is somewhat enhanced.

The hysteresis is caused by the fact that the gain differences left and right are not equally large. When the loss minimum is tuned to higher frequencies, the mode hop occurs between $\delta\nu_B = 0.70$ and $\delta\nu_B = 0.75$. Without the gain suppression, the mode hop would obviously happen at $\delta\nu_B = 0.50$. When the emission frequency hops, the gain saturation also moves. Consequently, mode 1 suddenly experiences more gain than necessary. The excess gain however causes an enhanced stimulated emission, which quickly consumes the surplus in carriers and brings the gain down to the appropriate level. In other words, the linear gain G_0 and the carrier density are suddenly reduced after the mode hop. This explains the sudden drop of the active section voltage in Figure 4.19. The sudden power upsurge is caused by the combination of two effects: the differential efficiency suddenly increases because r_R is higher after the mode hop (Figure 4.22), and more of the injected carriers contribute to the stimulated emission.

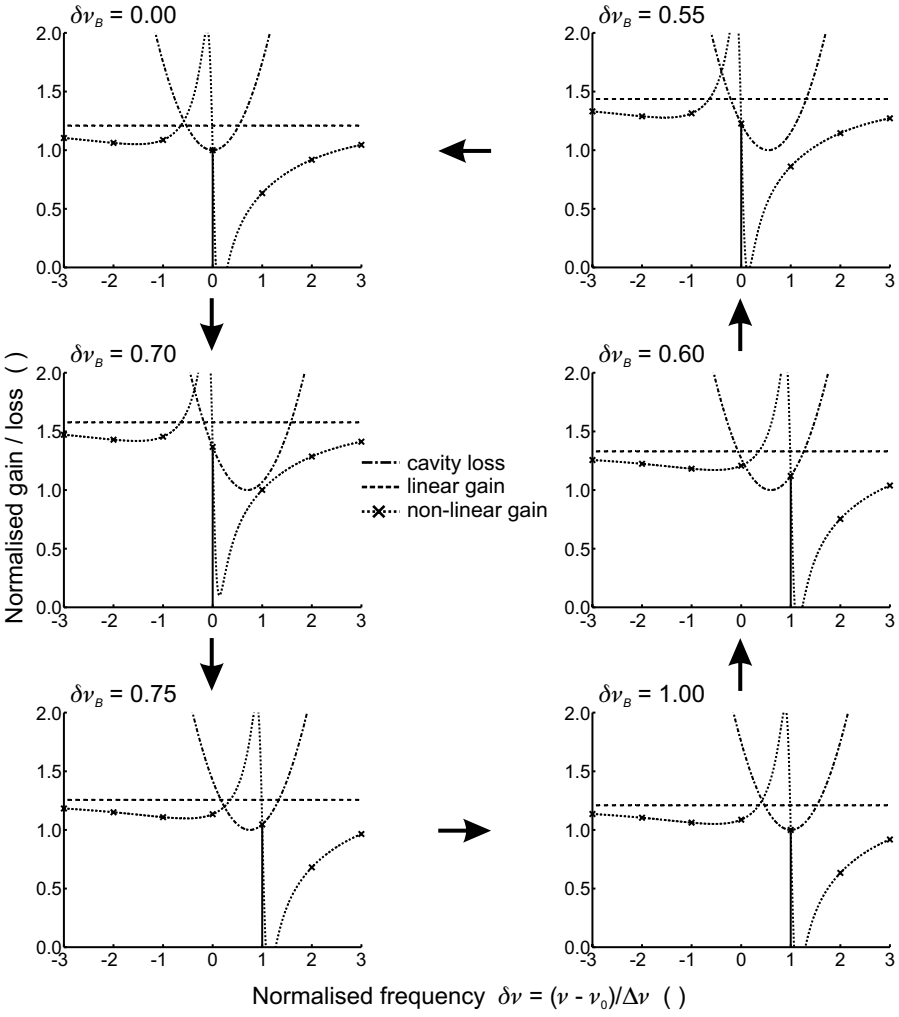

Figure 4.20 Evolution of normalised gain and cavity loss when the frequency of minimum cavity loss $\delta\nu_B$ is tuned from cavity mode 0 to cavity mode 1 and back. The dotted line illustrates the distorted gain spectrum due to non-linear effects, whereas the dashed line shows the equivalent linear gain G_0.

When the loss minimum is tuned in the opposite direction, the gain difference is smaller and hence the mode hop occurs closer to $\delta\nu_B = 0.50$, in this case between $\delta\nu_B = 0.60$ and $\delta\nu_B = 0.55$. Now, the gain of mode 0 is abruptly reduced when it becomes the lasing mode. Hence, the carrier density will have to build up to supply sufficient gain, causing an increase in voltage and a decrease in output power. Note that the lasing frequency will not hop back to mode 1, since the gain of this mode is even more suppressed after the hop to mode 0.

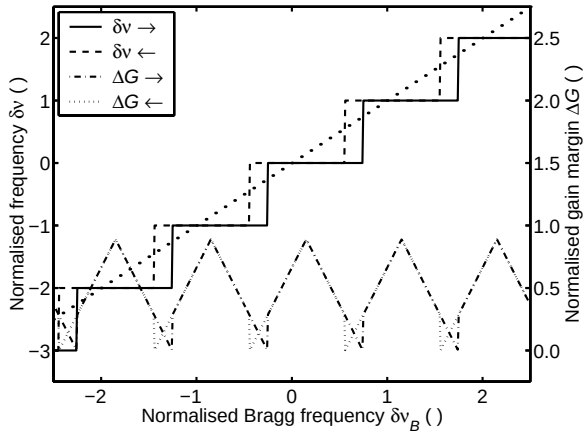

Figure 4.21 Variation of normalised emission frequency $\delta\nu$ and normalised gain margin ΔG with tuning for the idealised DBR-like laser with asymmetric non-linear gain (cf. Figure 4.20). The dotted line represents the Bragg frequency.

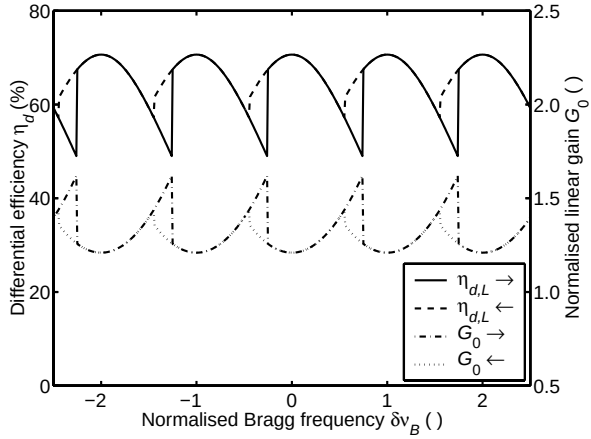

Figure 4.22 Variation of differential efficiency η_d and normalised linear gain level G_0 with tuning for the idealised DBR-like laser with asymmetric non-linear gain (cf. Figure 4.20).

Figure 4.21 and Figure 4.22 plot the variation of the normalised emission frequency $\delta\nu$, the gain margin ΔG, the differential efficiency η_d, and linear gain level G_0 with tuning. The linear gain level G_0 and the differential efficiency η_d still reach extrema for both directions of tuning, namely when the lasing mode is aligned with the loss minimum. These are however not the optimum operation points, since they do not coincide with the points of maximum gain margin ΔG, which lie in the middle of the hysteresis-free regions in the present approximation (Figure 4.21).

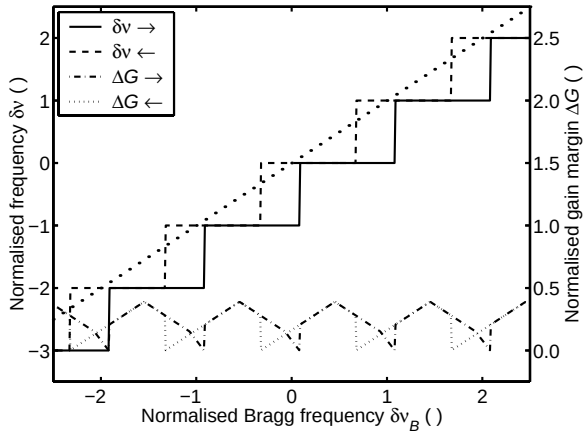

Figure 4.23 Variation of normalised emission frequency $\delta\nu$ and normalised gain margin ΔG with tuning for the idealised DBR-like laser with asymmetric non-linear gain, when the loss minimum has been broadened by a factor 3. The dotted line represents the Bragg frequency.

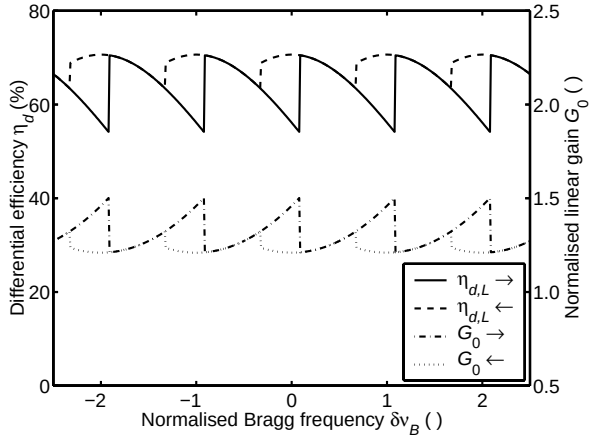

Figure 4.24 Variation of differential efficiency η_d and normalised linear gain level G_0 with tuning for the idealised DBR-like laser with asymmetric non-linear gain, when the loss minimum has been broadened by a factor 3.

If the loss curve becomes broader (or if the gain suppression increases), it can actually happen that during tuning to higher frequencies the second higher cavity mode (mode 2) reaches threshold before the adjacent cavity mode (mode 1). Yet, as soon as mode 2 becomes the lasing mode, mode 1 will experience a negative gain margin ΔG and the lasing frequency will immediately jump to mode 1. This happens for example if the curvature of the parabola in Figure 4.20 is divided by a factor of 3. The resulting variation with tuning of the normalised emission frequency $\delta\nu$, the gain margin ΔG, the differential efficiency η_d, and linear gain level G_0 are plotted in Figure 4.23 and Figure 4.24. When tuning to higher frequencies, the emission

frequency is always lower than the Bragg frequency. In this case, the differential efficiency and the linear gain level no longer reach an extremum (Figure 4.24).

The amount of hysteresis also increases with the width of the loss minimum (compare Figure 4.21 to Figure 4.23) [34]. This could explain why in Figure 4.18 the hysteresis increases with the DBR current. With growing carrier density in the DBR section, the absorption losses increase, which broadens the reflectivity peak of the DBR.

Discontinuous changes of the active section voltage without hysteresis can also be explained by the asymmetric gain suppression. Assume that mode 0 is the lasing mode, and the shape of the gain suppression is such that the gain difference between mode -1 and mode 0 is equal to the gain difference between mode 0 and mode +1. Then the hysteresis disappears, but after a mode hop, the carrier density will still change suddenly because of the abrupt increase/decrease in gain.

To combat these non-linear effects, several measures can be taken. The effects increase with the power density in the active region. Therefore, one could either reduce the output power or increase the cross-section of the waveguide (making sure though that the waveguide remains single-mode). The mixing between the lasing mode and adjacent cavity modes can be reduced by increasing the mode spacing and by improving the suppression of neighbouring cavity modes through better filtering.

In the DBR laser from Figure 4.13 and Figure 4.18, probably a combination of the gain slope effect and the asymmetric gain suppression effect determines the output characteristics. Indeed, at low output powers, the asymmetric gain suppression is low, which can be seen from the fact that almost no jumps occur in the active section voltage (compare Figure 4.14 and Figure 4.19). Even then, significant jumps in output power are observed, which can be explained by the occurrence of a non-zero gain slope combined with a broad reflector peak (cf. Figure 4.17).

The conclusion seems to be that for a DBR laser, both the facet output power and active section voltage in principle provide suitable feedback signals for mode stabilisation. Care has to be taken however that the Bragg reflector is sufficiently selective, which means that high values of the coupling coefficient have to be avoided.

4.2.2 SSG-DBR laser

In the following paragraphs, we will investigate whether a super-structure grating DBR laser can be maintained in a single longitudinal mode by monitoring output power or active section voltage. We will not explicitly mention sampled grating DBR lasers, since these can be considered as a specific subclass of the much broader class of super-structure grating DBR lasers.

Single longitudinal mode operation of a SSG-DBR laser requires that a reflectivity peak of the front reflector, a reflectivity peak of the rear reflector and a cavity mode are aligned. In a properly designed laser, only one pair of reflector peaks can be lined up at the same time. For small deviations from the optimum alignment, the SSG-DBR laser will hence behave largely like a two-sided DBR laser with uniform Bragg reflectors.

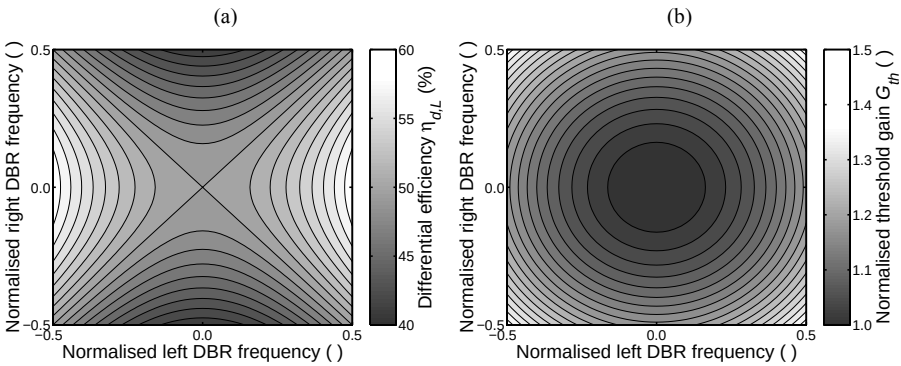

Figure 4.25 Variation of differential efficiency $\eta_{d,L}$ (a) and normalised threshold gain G_{th} (b) with tuning for a two-sided DBR laser.

We can then extend our simple model from §4.2.1 to a laser with two frequency-dependent mirrors $r_L(\delta\nu)$ and $r_R(\delta\nu)$, with their corresponding normalised losses $A_L(\delta\nu)$ and $A_R(\delta\nu)$.

$$r_L(\delta\nu) = e^{-A_L(\delta\nu)} \quad \text{and} \quad r_R(\delta\nu) = e^{-A_R(\delta\nu)} \tag{4.13}$$

If the internal losses are again neglected, then the total loss $A(\delta\nu)$ is given by the sum of the mirror losses $A_L(\delta\nu)$ and $A_R(\delta\nu)$.

Below, we will use the convention that the output power is always measured at the left side of the laser. Referring to the terminology used in Chapter 2, r_L thus represents the reflectivity of the front mirror and r_R is the reflectivity of the rear mirror. We assume that both mirrors are initially aligned with the mode at frequency ν_0, and have an identically shaped (parabolic) loss curve (cf. Figure 4.9).

Figure 4.25 plots the variation of the differential efficiency and the threshold gain if the reflectors are tuned around the point of optimum alignment. As expected, the threshold gain shows a minimum in the centre point. The differential efficiency on the other hand exhibits a so-called saddle point [12]. With respect to the right mirror, the left side efficiency $\eta_{d,L}$ is *maximal* when the mirror is aligned with the cavity mode (cf. $\eta_{d,L}$-curve in Figure 4.10). With respect to the left mirror, the left side efficiency $\eta_{d,L}$ is *minimal* when the mirror is aligned with the cavity mode (cf. $\eta_{d,R}$-curve in Figure 4.10). In the SSG-DBR laser, one hence expects saddle points in the output power and minima in the active section voltage (with respect to the reflector tuning currents) when a pair of reflector peaks is aligned with a cavity mode.

Figure 4.26 shows a calculated map of side-mode suppression ratio as a function of the front and rear reflector currents of a SSG-DBR laser. For both mirrors, a multi-phase-shift SSG design with 7 reflectivity peaks was used (cf. §3.4.2). The coupling coefficient was $5.0 \cdot 10^{-3}$ μm^{-1}. The front (rear) SSG-DBR consisted of 8 (10) super-periods, and the super-period length was chosen so as to obtain a peak spacing of 0.817 THz (0.700 THz). The active section was 400 μm long, and the phase section 150 μm. Initially, the increase of absorption losses with carrier density in the reflectors was neglected ($\partial\alpha/\partial N = 0$). The frequency tuning characteristic of this laser was already presented in Chapter 2 (Figure 2.20).

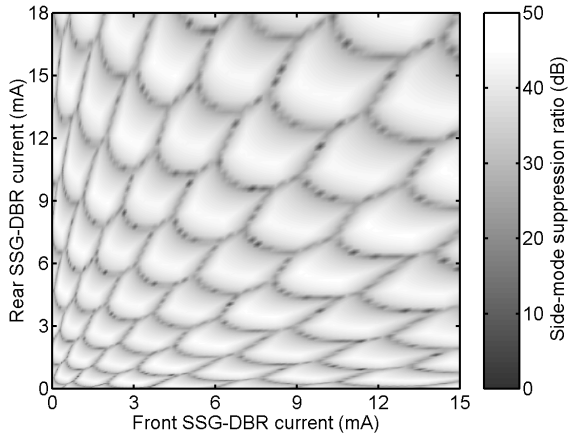

Figure 4.26 Calculated map of side-mode suppression ratio for a SSG-DBR laser as a function of the front and rear reflector currents. The frequency tuning characteristic of this laser can be found in Chapter 2, Figure 2.20.

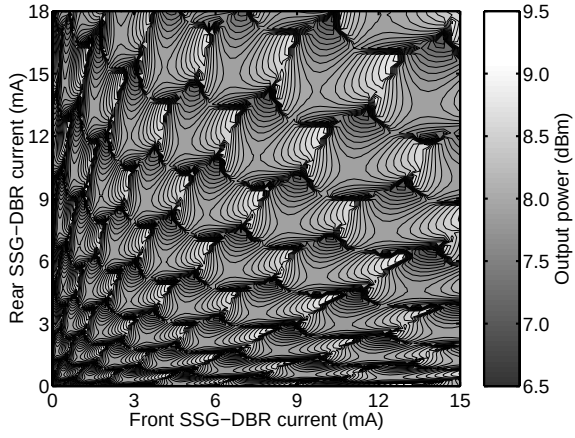

Figure 4.27 Calculated contour map of output power for a SSG-DBR laser as a function of the front and rear reflector currents. Carrier-induced absorption losses in the reflectors were neglected.

Figure 4.27 and Figure 4.28 present the variations of the output power and the active section voltage corresponding to the SMSR map in Figure 4.26. A saddle point in the output power and a local minimum in the active section voltage are indeed observed at the centre of each mode region (i.e. a region in which one particular cavity mode is the lasing mode). At the same locations, a maximum SMSR is obtained in Figure 4.26. In 1997, Ishii et al. demonstrated a control loop for a SSG-DBR laser that maintained a high SMSR by locking the laser to a saddle point in the output power [12]. As we will show below, this method can however not be applied across the entire tuning range of the laser.

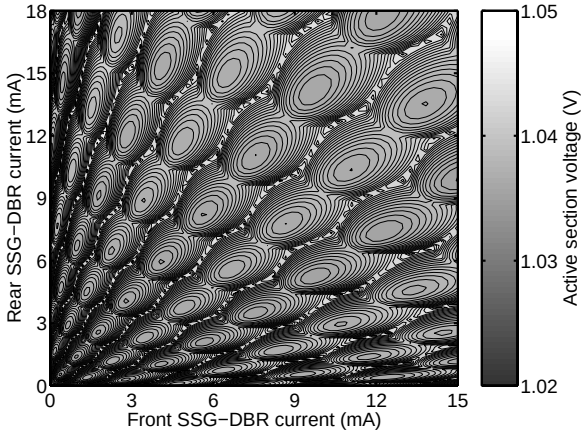

Figure 4.28 Calculated contour map of active section voltage for a SSG-DBR laser as a function of the front and rear reflector currents. Carrier-induced absorption losses in the reflectors were neglected.

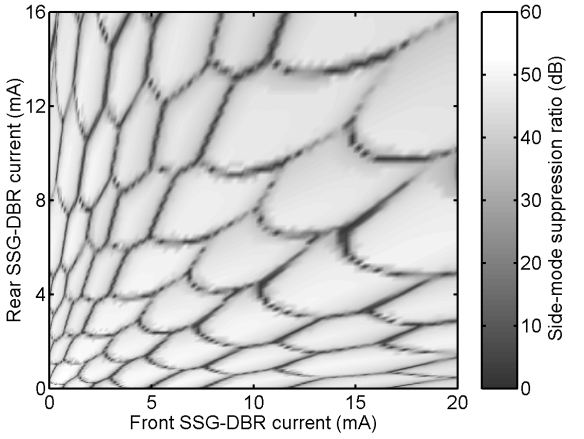

Figure 4.29 Measured map of side-mode suppression ratio for a SSG-DBR laser as a function of the front and rear reflector currents.

Figure 4.29 to Figure 4.32, show measurement results of an actual SSG-DBR laser. The lengths of the front DBR, active, phase, and rear DBR sections are 400 µm, 450 µm, 125 µm, and 600 µm respectively. Both reflectors have 7 reflectivity peaks, with centre frequency and peak spacing chosen such that the laser can be tuned quasi-continuously over the entire C-band (192 to 196 THz). The active section was biased at 80 mA, and no current was applied to the phase section.

The measured output power variations (Figure 4.30) are clearly not as regular as the calculated ones. Saddle points are generally not centred on the mode regions, and in some mode regions, no saddle point is observed at all. The explanation of course lies in the carrier-induced absorption losses, which have been neglected above.

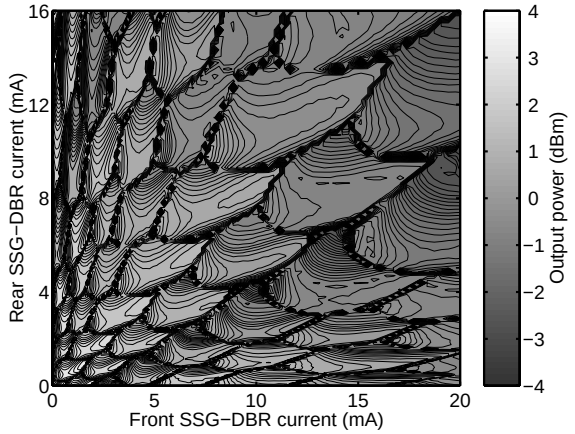

Figure 4.30 Measured contour map of output power for a SSG-DBR laser as a function of the front and rear reflector currents.

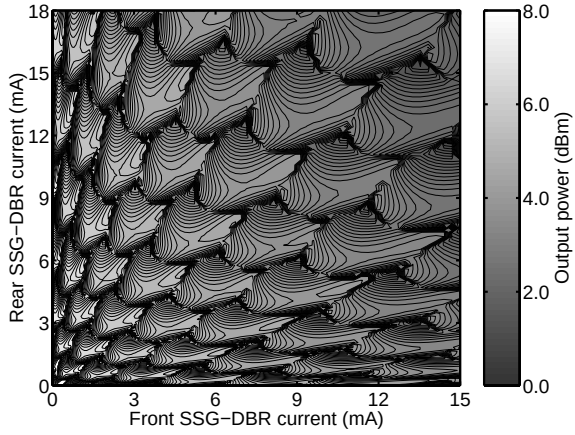

Figure 4.31 Calculated contour map of output power for a SSG-DBR laser as a function of the front and rear reflector currents. For the passive sections, a typical value was assumed for the increase of loss per unit length α with carrier density N ($\partial\alpha/\partial N = 3.0 \cdot 10^{-9}$ μm^2).

It was already noted in the discussion of Figure 4.12 that for a normal DBR laser the output power from the DBR side is not as suitable for mode control as the power from the cleaved facet. The power from the DBR rapidly decreases with tuning due to the carrier-induced losses, and because of this the power minima are shifted significantly towards higher DBR currents, or even disappear. This is also apparent from Figure 4.30, where mainly the minima in output power with respect to the front SSG-DBR current tend to be blurred. The saddle points that can still be discerned are also shifted somewhat towards lower rear SSG-DBR currents, just as the maxima in the facet output power in the ordinary DBR laser were moved a bit towards lower DBR currents.

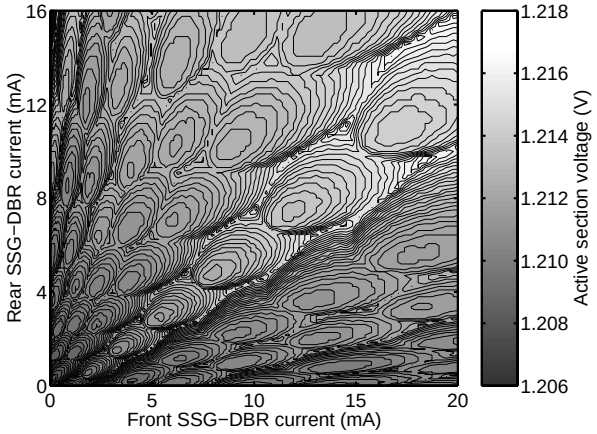

Figure 4.32 Measured contour map of active section voltage for a SSG-DBR laser as a function of the front and rear reflector currents.

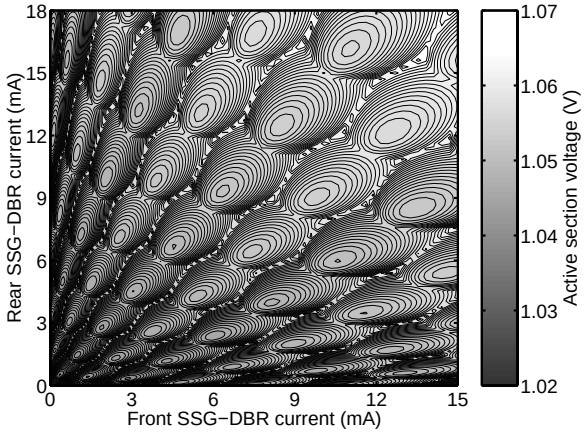

Figure 4.33 Calculated contour map of active section voltage for a SSG-DBR laser as a function of the front and rear reflector currents. For the passive sections, a typical value was assumed for the increase of loss per unit length α with carrier density N ($\partial\alpha/\partial N = 3.0 \cdot 10^{-9}$ µm^2).

One could try to correct the measured power values for the increased losses, but this does not seem very practical, especially since the correction might vary over the lifetime of the laser. Fortunately, the active section voltage still shows the expected minima within each mode region (Figure 4.32). The voltage is less affected by the increased losses in the passive sections because it is only influenced by the reflection characteristics of the two mirrors, and not by the transmissivity as is the case for the output power (cf. (3.23)). Of course, the reflectivity also decreases due to the increased losses, but not to the same degree as the transmissivity. The reduction of the reflectivity does cause an overall increase of the lasing threshold and thus also of the active section voltage. The voltage surface of Figure 4.28 is consequently tilted

to some extent (the upper right corner is lifted), which effectively moves the minimum voltage points towards lower front and rear reflector currents.

These observations are confirmed by the calculation results presented in Figure 4.31 and Figure 4.33. Here the same laser has been considered as above, only now a typical variation of the absorption losses with carrier density has been taken into account ($\partial\alpha/\partial N = 3.0 \cdot 10^{-9}$ μm^2). The saddle points have indeed moved away from the centre of the mode region, and have disappeared at higher front reflector currents. The voltage surface is somewhat tilted – the average voltage level increases from the lower left corner to the upper right corner of the map – but the minima are still clearly discernible.

In total, four different SSG-DBR lasers and one SG-DBR laser have been characterised. All the lasers showed similar variations of output power and voltage. Our results were also confirmed by further measurements on other SSG-DBR lasers at the manufacturer of these devices, NTT Optoelectronics in Atsugi, Japan. The active section voltage should hence be much more suitable as monitoring signal for mode stabilisation than the output power that was used in [12].

None of the studied lasers seemed to be affected by asymmetric non-linear gain suppression, although these lasers have a longer cavity and hence a smaller cavity mode spacing than a typical DBR laser (40-50 GHz vs. 80-90 GHz). No hysteresis was observed, and the voltage always showed smooth variations – no abrupt jumps (Figure 4.32). The explanation lies in the higher selectivity of the intra-cavity filter. Cavity modes adjacent to the lasing mode are better suppressed and consequently the effects of wave mixing between these modes are reduced. Better selectivity is obtained for two reasons. Firstly, the reflectivity peaks of the SSG mirrors are much narrower than the peak of the high-κ Bragg reflector in §4.2.1. Secondly, the filtering action of two reflectivity peaks is combined, which reduces the overall filter bandwidth by a factor of approximately 1.3.

4.2.3 GCSR laser

From an operational point of view, the GCSR laser is very similar to an ordinary DBR laser. Figure 4.34 shows a measured frequency tuning characteristic. The corresponding SMSR map is displayed in Figure 4.35. The active, coupler, phase, and SG-DBR sections of this laser were 400 μm, 600 μm, 150 μm, and 950 μm long, respectively. Let us assume that the coupler transmissivity peak is kept aligned to a particular reflectivity peak of the SG-DBR (the laser is kept in the same super-mode, e.g. along the dashed line in Figure 4.34). Due to the high tuning rate of the coupler, the coupler current only has to be varied very little to track the reflectivity peak. When the current through the reflector is increased, the tuning characteristic resembles the tuning characteristic of a DBR laser with a long phase section between the active section and the DBR. One therefore expects maxima in the front facet output power and minima in the active section voltage with respect to the reflector current at the optimum operation points. When tuning the coupler, one would also expect minimum voltage and maximum output power when the coupler transmissivity peak is aligned with a reflectivity peak.

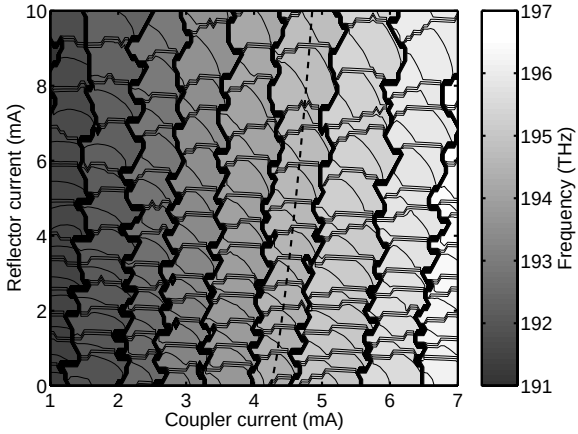

Figure 4.34 Measured contour map of emission frequency for a GCSR laser as a function of the coupler and reflector currents. The dashed line indicates a possible path for simultaneous tuning of coupler and reflector, keeping both filters more or less aligned.

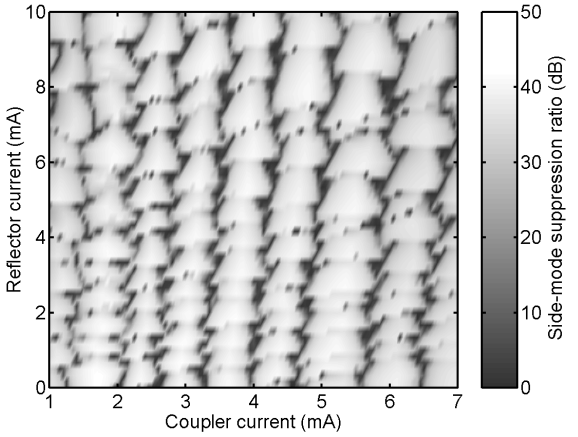

Figure 4.35 Measured map of side-mode suppression ratio for a GCSR laser as a function of the coupler and reflector currents.

Figure 4.36 shows the front facet output power variations with tuning corresponding to Figure 4.34. With respect to the reflector current, the output power shows a similar behaviour as for the DBR laser in §4.2.1. With increasing current, the power decreases monotonously, except for the sudden upward jumps at the mode hops. If the current is decreased, some hysteresis is also observed. With respect to the coupler current, clear maxima are obtained for the second and third super-mode from the left. If the coupler current is increased, the power maxima for subsequent super-modes move closer to the mode boundary. For coupler currents above 4 mA, power maxima are no longer obtained. The power decreases monotonously with coupler current, except for the sudden upward jumps at the super-mode hops.

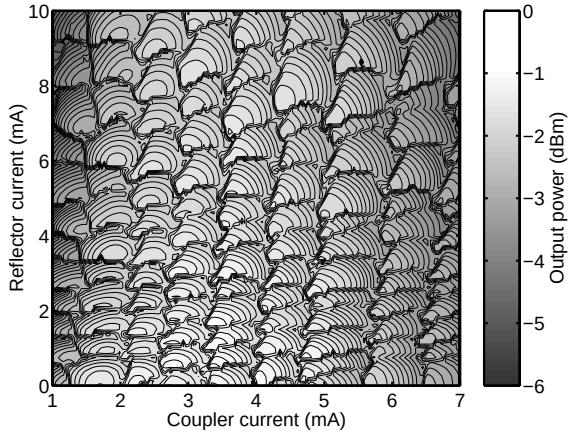

Figure 4.36 Measured contour map of output power for a GCSR laser as a function of the coupler and reflector currents.

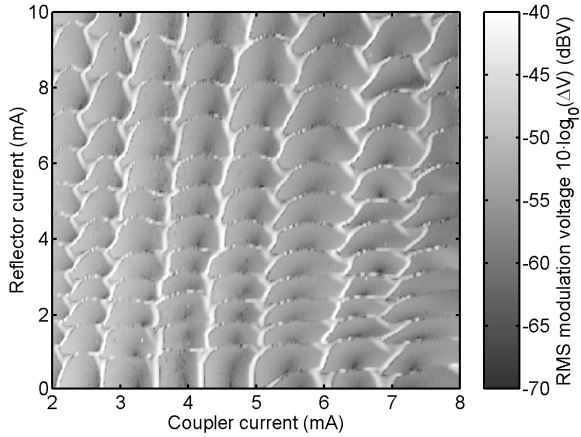

Figure 4.37 Measured map of the norm of the active section voltage gradient for a GCSR laser as a function of the coupler and reflector currents. A small current modulation was added to the coupler and reflector currents and the corresponding voltage modulation components were measured using lock-in amplifiers. These are proportional to the slope in the coupler and reflector direction, respectively. Note that this was measured on a different laser than the results of Figure 4.34 to Figure 4.36.

A similar behaviour is observed in the active section voltage. Figure 4.37 plots the norm of the active section voltage gradient. Note that this was measured on a different laser than the results presented in the previous figures. Small dither signals with equal amplitude were added to the coupler and reflector currents, at frequencies f_1 and f_2 respectively. With two lock-in amplifiers, the in-phase modulation components V_c and V_r of the active section voltage V_a at these two frequencies were determined. These voltages are proportional to the slope of the active section voltage surface in the direction of the coupler and reflector axis, respectively.

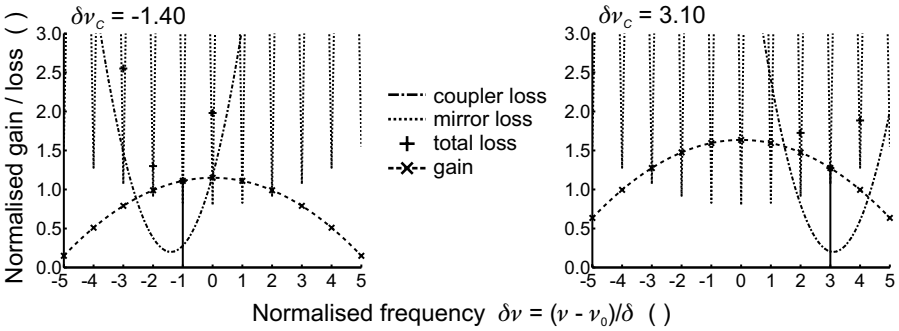

Figure 4.38 Plots of normalised gain and losses for a simplified GCSR laser. Frequencies are normalised with respect to the spacing between reflectivity peaks δ. A cavity mode is assumed to be located at each reflectivity peak.

Plotted in the figure is:

$$10 \cdot \log_{10}(\Delta V) = 10 \cdot \log_{10}\left(\sqrt{V_c^2 + V_r^2}\right) \tag{4.14}$$

where ΔV is a number proportional to the norm of the voltage gradient, which is expressed in dBV.

With respect to the reflector current, the voltage slope is minimal just after a mode hop. No local minima in voltage are hence obtained. The voltage and the voltage slope increase with reflector current, except at a mode hop, where both are abruptly reduced. With respect to the coupler current, voltage minima are observed centrally between the super-mode boundaries between 5 mA and 7 mA. At lower and higher coupler currents, the voltage minima move closer to the super-mode boundary. For coupler currents below 3 mA, voltage minima are no longer observed.

The behaviour of these lasers with respect to the reflector current is again attributed to the non-linear asymmetric gain suppression. Due to the long coupler length, the longitudinal mode spacing is narrow, on the order of 25 to 30 GHz (Figure 4.34). Moreover, there is only one SG-DBR filter. Compared to the SG- and SSG-DBR lasers, the relative filter bandwidth is hence roughly 2.5 times larger. Because of this, the SMSR of these GCSR lasers is typically 10 dB lower (compare Figure 4.35 to Figure 4.29). Both the narrower mode spacing and lower SMSR increase the gain suppression effect [30]-[34].

With respect to the tuning of the coupler, the gain suppression will however play no role, since this effect only changes the gain spectrum locally around the lasing mode. The fact that power maxima and voltage minima are not always centred relative to the super-mode boundaries is due to the non-uniform gain. The effect of a non-zero gain slope was already discussed in §4.2.1 for a normal DBR laser. Similar observations apply here, only now the filter is the coupler (in stead of the DBR), and the tuning occurs between super-modes (in stead of cavity modes). This is illustrated by the simplified representation in Figure 4.38. The frequency is now normalised with respect to the super-mode spacing δ. A parabolic variation of the (normalised) gain is assumed. Two loss terms are plotted separately: the mirror loss (i.e. the loss of the facet and the SG-DBR) and the coupler loss.

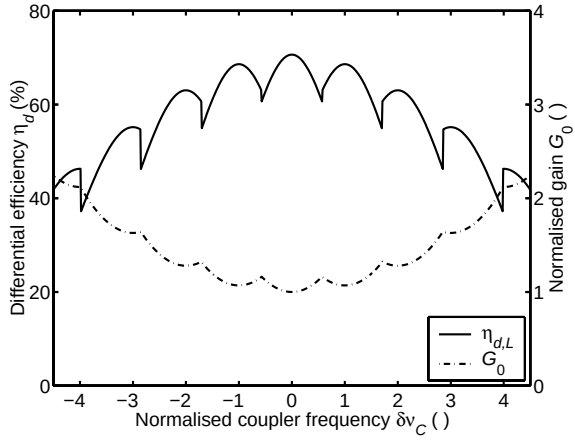

Figure 4.39 Variation of differential efficiency $\eta_{d,L}$ and normalised peak gain level G_0 with tuning of the coupler frequency for the simplified GCSR laser from Figure 4.38.

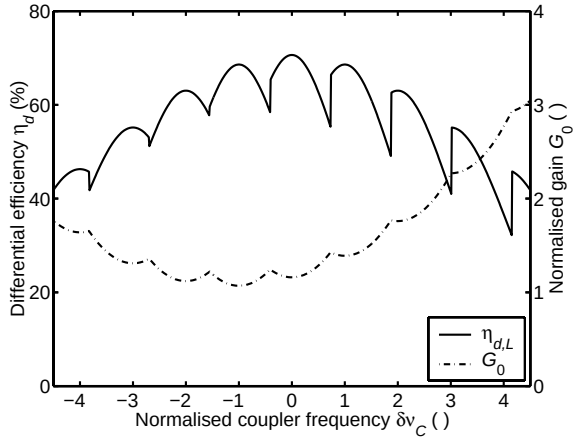

Figure 4.40 Variation of differential efficiency $\eta_{d,L}$ and normalised peak gain level G_0 with tuning of the coupler frequency for the simplified GCSR laser from Figure 4.38. Compared to the previous figure, the gain maximum was moved to $\delta\nu$ = -2.

If we assume that a cavity mode is always aligned with each of the reflectivity peaks of the SG-DBR, then we can calculate the variation of the differential efficiency and the peak gain G_0 as plotted in Figure 4.39. For the central super-mode (mode 0), the differential efficiency and peak gain show the expected extremum centrally between two super-mode hops. When the coupler is tuned away from the gain peak however, the super-mode hop is progressively postponed due to the increasing gain slope. The extrema however always occur when the coupler is aligned to a reflectivity peak. Consequently, these extrema move increasingly closer to the super-mode jumps. Far from the gain peak, the super-mode hop actually occurs after the coupler has been tuned past the reflectivity peak, and neither the peak gain nor the differential

efficiency reaches an extremum anymore. The differential efficiency decreases when the coupler is tuned away from the central frequency because we have assumed a sampled grating reflector, which means that the peak reflectivity declines with the distance from the central peak. The peak gain G_0 on the other hand increases both because of the decreasing reflectivity and because of the increasing detuning from the gain peak.

In Figure 4.39, the super-mode with centrally located differential efficiency and peak gain extrema is also the mode with highest differential efficiency and lowest threshold. On the other hand, in Figure 4.36 the output power is not maximal for the most symmetric super-mode (coupler currents between 1.5 and 2 mA), but rather for coupler currents around 3 mA. In Figure 4.38 and Figure 4.39, we have assumed though that the centre frequency of the SG-DBR coincides with the gain peak. If the gain peak is shifted to lower frequencies, the maximum power will still be obtained for the central peak of the SG-DBR reflector, but this will no longer be the mode with centred power and voltage extrema, as is illustrated by Figure 4.40. By displaying the spectrum of the GCSR laser from Figure 4.36 on an optical spectrum analyser, it was verified that the gain peak was indeed detuned to lower frequencies with respect to the central peak of the SG-DBR reflector.

Obviously, the question arises as to which improvements could be made to the design of the GCSR lasers in order to allow mode stabilisation using either the active section voltage or the output power. First, the effects of non-linear gain suppression should be reduced. This can be achieved by reducing the power density in the active region, by increasing the side-mode suppression and/or by increasing the mode spacing. The last two issues can be tackled in parallel by reducing the cavity length, since increasing the mode spacing will also improve the selectivity of the SG-DBR reflectivity peaks. The power density in the active region can be reduced by using a thicker waveguide core (more quantum wells). However, this can only be done to a limited extent, since the waveguide has to remain single-mode.

To improve the behaviour with respect to the tuning of the coupler, one could try to increase the gain bandwidth. This can be done by proper engineering of the quantum wells in the active section. In [35] for example, tensile strained InGaAs/InGaAsP quantum wells were used. In these quantum wells not only the transitions between the ground states of the electrons in the conduction band and the holes in the valence band contribute to the gain, but also the second order transitions. Alternatively, the bandwidth of the coupler filter could be reduced. Clearly, some trade-off will have to be made between the length, the tuning range, and the bandwidth of the coupler (cf. §2.4.2 (2.49)).

4.3 Feedback control experiments with SSG-DBR lasers

From the previous paragraphs, it should be clear that of all tunable lasers available to us, the SSG-DBR lasers were most suited for feedback control experiments. The hysteresis in the DBR and GCSR lasers would make any feedback control very difficult. As already mentioned, frequency and mode stabilisation of SSG-DBR lasers was first demonstrated in 1997 by locking the laser to saddle points in the output power and using an arrayed waveguide grating as a frequency reference [12].

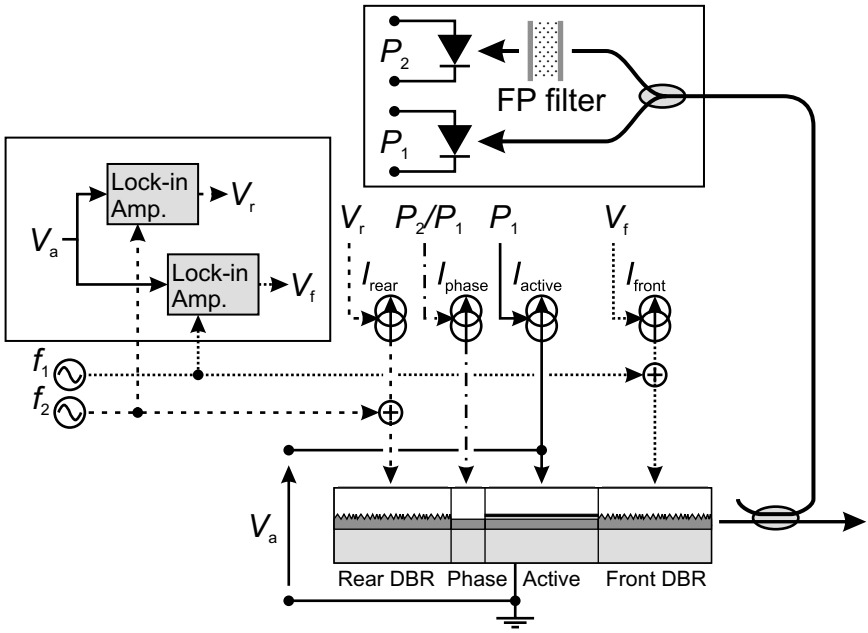

Figure 4.41 Schematic of control circuit for frequency, mode and power stabilisation of a SSG-DBR laser.

The measurement and simulation results presented above have shown however that the active section voltage produces a much more suitable control signal for mode stabilisation. We have hence built a control loop that keeps the SSG-DBR laser at a local minimum in voltage with respect to the reflector currents. For frequency control, the commercial Fabry-Perot wavelength locker (FPWL) that was described in §4.1 is used [28].

4.3.1 Control circuit

Figure 4.41 shows a schematic of the control circuit for frequency, mode and power stabilisation that was developed. Three different feedback loops can be distinguished. For mode stabilisation, small modulation signals (typically 5 μA) are added to the front and rear reflector currents, at frequencies f_1 and f_2 respectively. With two lock-in amplifiers, the in-phase modulation components V_f and V_r of the active section voltage V_a at these two frequencies are measured. These voltages are proportional to the slope of the active section voltage surface (Figure 4.32) in the direction of the front and rear reflector current axis, respectively. At every iteration of the feedback loop, a correction proportional to V_f (V_r) is subtracted from the front (rear) reflector current. Indeed, if the slope is negative, the current must be increased and vice versa. In this way, the laser is stabilised at a local minimum in active section voltage (with respect to the reflector currents).

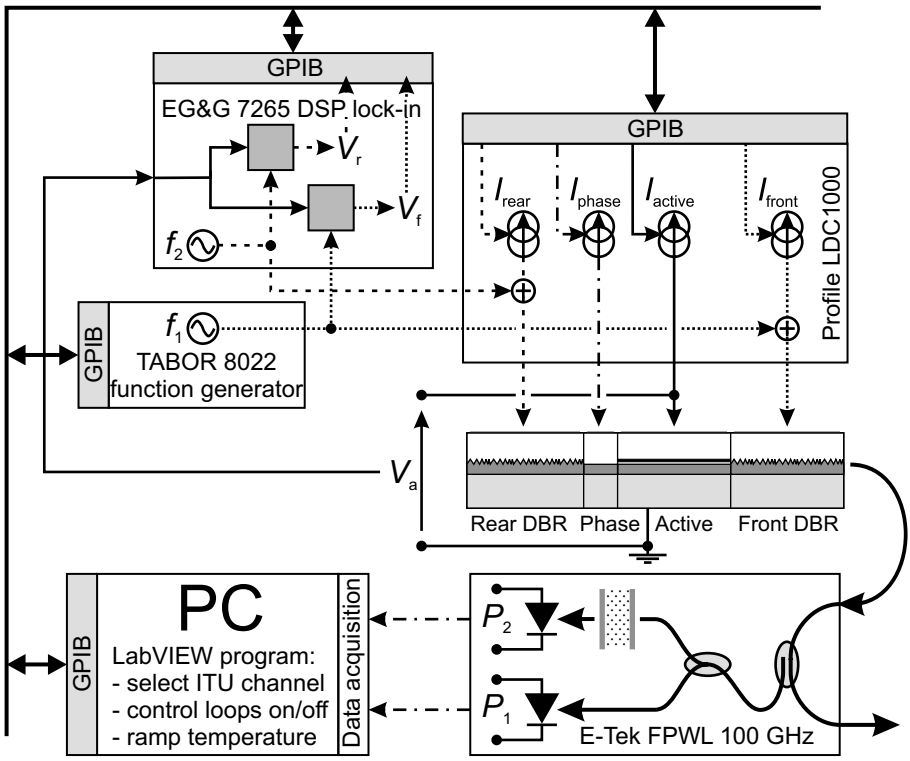

Figure 4.42 Actual configuration of the control circuit schematically drawn in Figure 4.41.

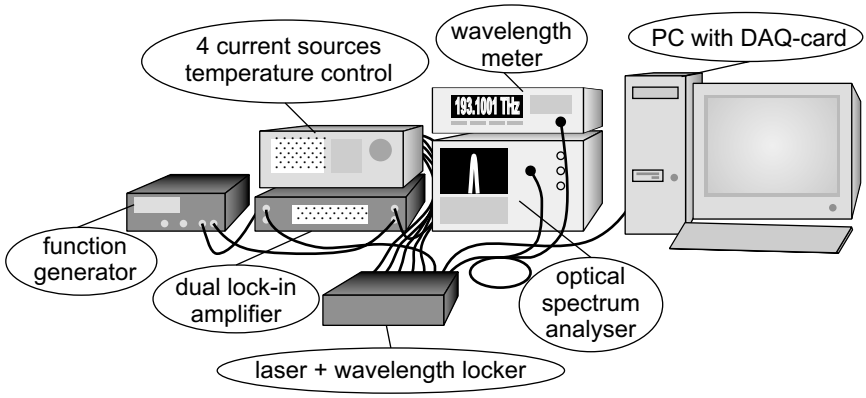

Figure 4.43 View of the feedback control set-up with the various instruments.

For frequency control, corrections proportional to the frequency error signal $V = 10 \cdot \log(\eta P_2/P_1)$ are subtracted from the phase section current. A positive V indicates a too high frequency, hence the phase current has to be reduced (Figure 4.5). For power stabilisation, the active section current is corrected by an amount proportional to $(P_{ref} - P_1)$, where P_{ref} is a reference value proportional to the desired output power.

In practice, the feedback loop is controlled by a LabVIEW program running on a PC, which communicates with different instruments through a GPIB bus (IEEE standard 488). The detailed configuration of the control loop is shown in Figure 4.42, and Figure 4.43 gives an impression of what the set-up looks like in reality. At each iteration of the control loop, the program reads the different control signals from the appropriate instruments, calculates the new drive currents, and sends a command to the modular current source controller (Profile LDC1000) to set these currents. This makes the feedback loop relatively slow, but has the advantage that the currents can be monitored at all times. Additionally, the program can interrupt the operation of the loop at regular intervals to measure frequency, output power, and SMSR and store these measurement results together with the values of the different currents. To this end, the optical output of the wavelength locker is connected to an optical spectrum analyser (HP70951), which monitors the SMSR, and a wavelength meter (HP86120B), which monitors the frequency and output power.

The wavelength locker was mounted on a printed circuit board containing two matched transimpedance amplifiers (Figure 4.44). These convert the current output of the two photodiodes in the FPWL to voltages, which can then be read out by a data acquisition card in the PC.

The two dither signals for front and rear reflector currents (frequencies f_1 and f_2) are generated by a function generator (Tabor 8022) and the internal oscillator of the EG&G 7265 DSP lock-in amplifier, respectively. These signals are connected to the modulator inputs of the current sources, on the rear panel of the LDC1000 controller. A reference TTL signal in phase with the sine wave runs from the function generator to the reference input of the lock-in amplifier. Finally, the active section voltage of the laser is connected to the input of the lock-in amplifier, which is set-up to work in a dual channel mode, locking to both the internal and the external reference alternately. The measured modulation voltages V_f and V_r are read out by the LabVIEW program at every iteration of the feedback loop.

In order to test the control loop, some frequency drift has to be induced. This is done by changing the temperature of the laser sub-mount, which is stabilised by a temperature control module of the LDC1000 controller. The temperature is changed in small steps to simulate gradual ageing of the device. After each temperature step, the feedback loop is left running for a predetermined time, typically 30 to 60 seconds. Subsequently, the frequency, SMSR, and output power are measured.

For all channels on the 100 GHz ITU grid, operation points at a temperature of 20 °C are stored in a look-up table. Initially, the sub-mount temperature is therefore set to 20 °C. When a particular ITU channel is selected on the control panel of the LabVIEW program, the program reads the corresponding current values from the look-up table, and sends commands to the LDC1000 to set these currents.

Figure 4.44 Photograph of the box containing the packaged SSG-DBR laser and the wavelength locker.

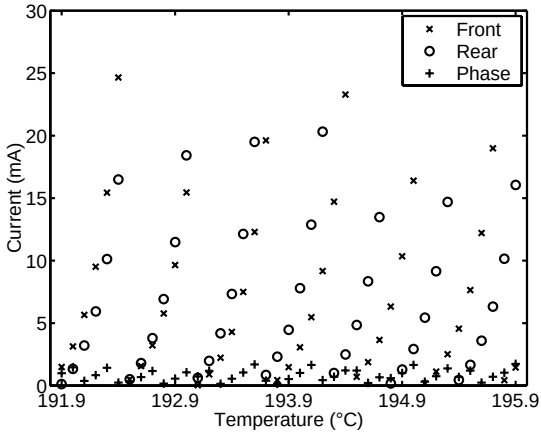

Figure 4.45 Plot of the look-up table of a SSG-DBR laser for all channels on the 100 GHz ITU grid the laser could be tuned to.

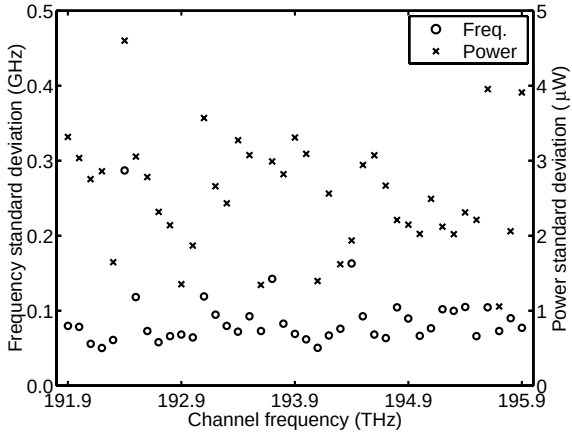

Figure 4.46 Frequency standard deviation and power standard deviation for 41 ITU channels for a temperature sweep from 20 to 30 °C. The output power was stabilised at 0.5 mW.

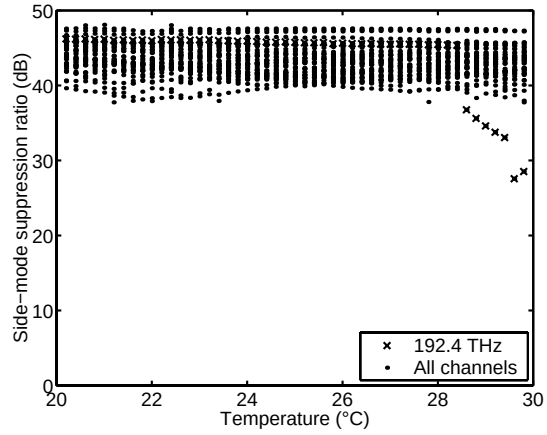

Figure 4.47 Variation of side-mode suppression ratio for 41 ITU channels for a temperature sweep from 20 to 30 °C. Crosses (×) indicate the worst case channel at 192.4 THz.

4.3.2 Static operation

The feedback control set-up was tested extensively on three SSG-DBR lasers [14]-[16]. Results will be presented here for one of them. Tests were performed for all channels on the 100 GHz ITU grid the laser could be tuned to, a total of 41 channels with frequencies ranging from 191.9 to 195.9 THz. The look-up table at 20 °C is plotted in Figure 4.45. During the tests, the temperature of the laser sub-mount was changed from 20 to 30 °C in steps of 0.2 °C. As Figure 4.46 illustrates, the frequency standard deviation across that temperature range was below 0.2 GHz for all channels except 192.4 THz. The maximum frequency variation was less than 1.0 GHz.

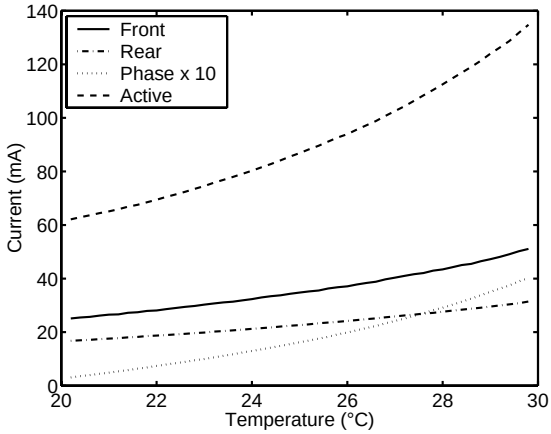

Figure 4.48 Variation of drive currents with temperature for the channel at 192.4 THz.

The frequency standard deviation exhibits some correlation to the look-up table plotted in Figure 4.45. Larger deviations are observed for channels requiring low reflector currents. This is obviously because the tuning efficiency is highest at low currents.

For all channels a SMSR of more than 35 dB was maintained, except again for the 192.4 THz channel where the SMSR decreased for temperatures above 28 °C (Figure 4.47). The output power was stabilised at 0.5 mW and as Figure 4.46 shows, very small power variations were measured.

The larger frequency errors and the decreasing SMSR for the 192.4 THz channel are explained by a thermal runaway effect. At 20 °C this channel requires both a high front and a high rear DBR current, 24.6 mA and 16.6 mA respectively (Figure 4.48). Because of the carrier-induced losses in the tuning sections, this means that also a high active section current is needed to maintain an output power of 0.5 mW. Due to the non-zero thermal resistance between the laser waveguide and the sub-mount, the waveguide temperature is always higher than the sub-mount temperature and the difference is more or less proportional to the injected current. When the sub-mount temperature is ramped up, the phase current has to be increased to counteract the thermal tuning. At the same time, the reflector currents are raised such that the reflector peaks track the cavity mode. This causes higher loss in all three passive sections and consequently the active section current also has to be enlarged. From Figure 4.48, it is clear that the currents increase super-linearly, since the tuning efficiency decreases with current due to Auger recombination and heating effects. All this amounts to a lot of extra heat being generated in the laser waveguide. At a certain point, the waveguide temperature rise due to a further increase in current completely counteracts the electronic tuning and therefore frequency and mode stability are degraded. Note however that at temperatures above 25 °C there is an alternative combination of front DBR, rear DBR and phase currents that will give the same output frequency with much lower currents.

In Figure 4.46, frequency standard deviations were plotted in an attempt to eliminate the errors due to the intrinsic accuracy of the wavelength locker. The commercial wavelength locker [28] used in these experiments has a specified channel accuracy of ±2.5 GHz, and a temperature stability of ±1.0 GHz (0 to 70 °C, without internal temperature control). By properly choosing the calibration factor η in the $V = 10 \cdot \log(\eta P_2/P_1)$ relation, we have however achieved much better accuracies. The circles in Figure 4.49 show the true frequency errors after stabilisation at a sub-mount temperature of 20 °C, with a η-value of 1.32. Clearly, all channels are within ±0.5 GHz of the specified frequency. Note also that the wavelength meter used here (HP86120B) has a resolution of only 0.1 GHz, and a specified absolute frequency accuracy of ±3 p.p.m. (±0.6 GHz) [36].

A possible disadvantage of the control circuit is the fact that small sinusoidal signals (5 μA) are added to the front and rear reflector currents. Since the average tuning efficiency of the reflection peaks of the DBR sections is 25 GHz/mA, the modulation of the reflection peaks is approximately 125 MHz. The corresponding variation of the laser frequency, or in other words the variation of the cavity mode frequency, is however only a fraction of this value [12]. Indeed, the cavity mode frequency is determined by the phase condition:

$$\frac{2\pi\nu_i}{c}\left(2n_aL_a + 2n_pL_p\right) - \arg\left(r_f(\nu_i)\right) - \arg\left(r_r(\nu_i)\right) = 2\pi i \tag{4.15}$$

where L_a and L_p are the lengths of the active and phase section, respectively; n_a and n_p are the corresponding effective indices; and r_f and r_r are the complex field reflectivities of the front and rear SSG mirrors, respectively. If the effective length of a reflector is defined as:

$$L_{x,eff} = -\frac{1}{2}\frac{c}{2\pi n_{g,x}}\frac{\partial}{\partial\nu}\left[\arg\left(r_x(\nu)\right)\right] \tag{4.16}$$

then the phase condition immediately yields that a change of the centre frequency of the front reflector by an amount $\delta\nu$, only causes the cavity modes to shift by an amount $\Gamma_f \cdot \delta\nu$, where:

$$\Gamma_f = \frac{n_{g,f}L_{f,eff}}{n_{g,a}L_a + n_{g,p}L_p + n_{g,f}L_{f,eff} + n_{g,r}L_{r,eff}} \approx \frac{L_{f,eff}}{L_a + L_p + L_{f,eff} + L_{r,eff}} \tag{4.17}$$

Here, $n_{g,x}$ represents the group index of section x. An analogous expression can naturally be derived for the rear reflector. A typical value for Γ_f and Γ_r is 0.2, since the low $\kappa_k L$-values usually found in SSG-DBR reflectors yield an effective length that is about half the physical length of the SSG-DBR section [37]. Here, κ_k is the effective coupling coefficient of a single reflectivity peak k (cf. Chapter 2).

Current modulation on both reflectors thus gives a total frequency modulation on the order of 50 MHz. At the same time, a slight power modulation is added. Measurements have shown however that relative power variations are very small, on the order of 10^{-10} to 10^{-9}. It has to be noted that these frequency and power fluctuations are much slower than typical data rates, so the variation during a single bit period will be negligible.

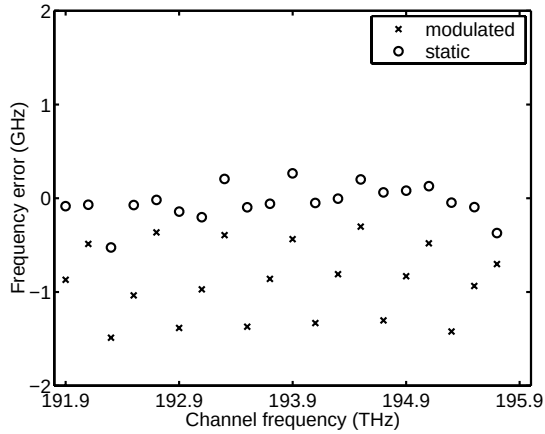

Figure 4.49 Frequency errors after stabilisation of 20 ITU channels at 20 °C, with direct modulation at 1.244 Gbit/s (×) and in static operation (o).

4.3.3 Operation with direct modulation

The frequency and mode control circuits were also tested while the laser was directly modulated. A 2^{23}-1 PRBS signal with a current swing of 60 mA was applied to the active section. The bit-rate was chosen at 1.244 Gbit/s because parasitics in the electrical path limited the small signal bandwidth to approximately 800 MHz. In Chapter 6 we will however present results proving that transmission over 80 km of standard single-mode fiber is feasible with a SSG-DBR laser (with proper electrical contacting) directly modulated at 2.488 Gbit/s. The 2^{23}-1 PRBS signal has a fundamental frequency component:

$$f_0 = \frac{1.244 \cdot 10^9}{2^{23} - 1}\,\text{Hz} = 148.3\,\text{Hz} \tag{4.18}$$

For the mode stabilisation circuit to operate properly the modulation frequencies of the reflector currents (f_1 and f_2, cf. Figure 4.41) have to be chosen away from f_0 and its higher harmonics. The noise on the signals V_f and V_r is also lower at low modulation frequencies. Therefore, we took $f_1 = 1410$ Hz and $f_2 = 960$ Hz. To increase the signal to noise ratio, the current dither was increased to 25 μA. Furthermore, a larger time constant was chosen for the lock-in amplifier. With a true random bit signal, some band-pass filtering might be required in front of the lock-in amplifiers.

Tests were performed for 20 channels at 200 GHz spacing, from 191.9 to 195.7 THz. The laser was roughly tuned to the appropriate channel. Subsequently, the active section bias current was adjusted manually in order to get both a good extinction ratio (typically 10 dB) and a good SMSR. The value of the bias current is quite critical. It should be close to 30 mA above the threshold value for the selected channel. A too low value will reduce the SMSR and cause increased turn-on jitter, whereas a too high value will reduce the extinction ratio (cf. Chapter 6).

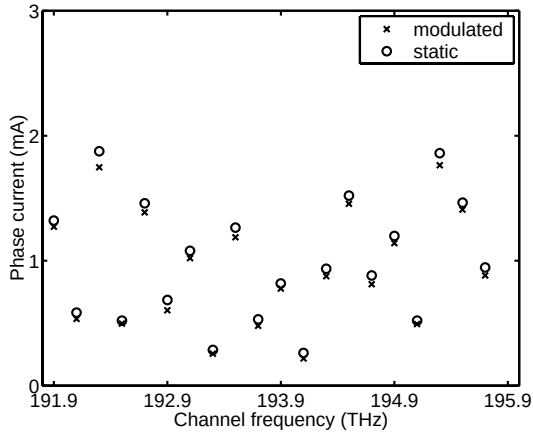

Figure 4.50 Phase currents after stabilisation of 20 ITU channels at 20 °C, with direct modulation at 1.244 Gbit/s (×) and in static operation (o).

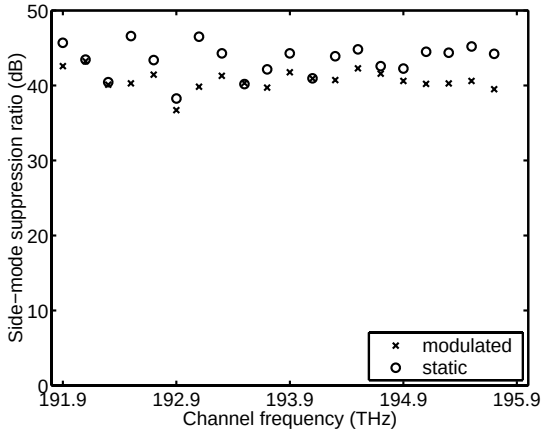

Figure 4.51 Side-mode suppression ratio after stabilisation of 20 ITU channels at 20 °C, with direct modulation at 1.244 Gbit/s (×) and in static operation (o).

After setting the bias current, the frequency and mode stabilisation loops were started. Figure 4.49 shows the time-averaged frequency errors after stabilisation at a sub-mount temperature of 20 °C, both with and without modulation. There is clearly a negative offset of the frequencies when the laser is being modulated (average offset = -0.85 GHz), because the phase current stabilises at a slightly lower value with the modulation switched on (Figure 4.50). This is probably due to the frequency chirp, i.e. the frequency variation caused by the current modulation. This chirp will alter the time-averaged signal detected by the Fabry-Perot wavelength locker.

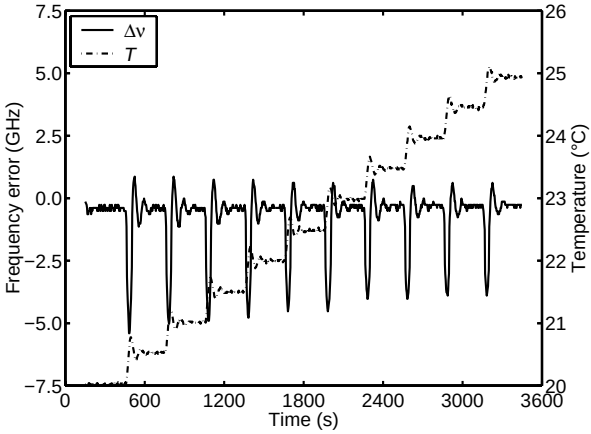

Figure 4.52 Frequency and mode control applied to a directly modulated SSG-DBR laser tuned to 193.9 THz. Evolution of frequency error and sub-mount temperature with time.

With modulation, the SMSR is generally slightly reduced, but it remains above 35 dB for all channels (Figure 4.51). Since a constant current swing was used, the average power varied by about 5 dB across the different channels.

For the 193.9 THz channel, a temperature ramp was again applied. The temperature was changed from 20 to 25 °C in 0.5 °C steps. The evolution of the frequency error and the temperature with time are shown in Figure 4.52. After each temperature step, the frequency stabilises again to within ±0.2 GHz of the initial frequency of 193.895 THz (cf. Figure 4.49). As previously explained, tuning currents increase with temperature and therefore the active section bias current had to be increased manually during the temperature ramp in order to maintain a good SMSR (the threshold current increases due to the additional losses). The current was increased from 39.5 mA at 20 °C to 41.9 mA at 25 °C.

Figure 4.53 shows the eye diagram after the temperature increase. The parasitic-limited rise time of about 460 ps is clearly apparent. Note that no relaxation oscillations are visible after turn-on, because the eye-diagram was measured with a 2.488 Gbit/s reference receiver, which contains a fourth order Bessel-Thompson low-pass filter with a cut-off frequency of 1.8 GHz. If the active section bias current is not adjusted during the temperature ramp, the eye diagram of Figure 4.54 results. Since the current tends to swing below threshold, a higher extinction ratio is obtained (13.3 dB in stead of 10.5 dB), though at the expense of an increased turn-on jitter. Figure 4.55 compares the time-averaged spectra for both cases. A low value of the bias current clearly leads to a poor side-mode suppression ratio.

In order to be able to apply the frequency and mode control loops to a directly modulated laser in a practical system, some mechanism will hence have to be found that automatically adjusts the active section bias to the appropriate level.

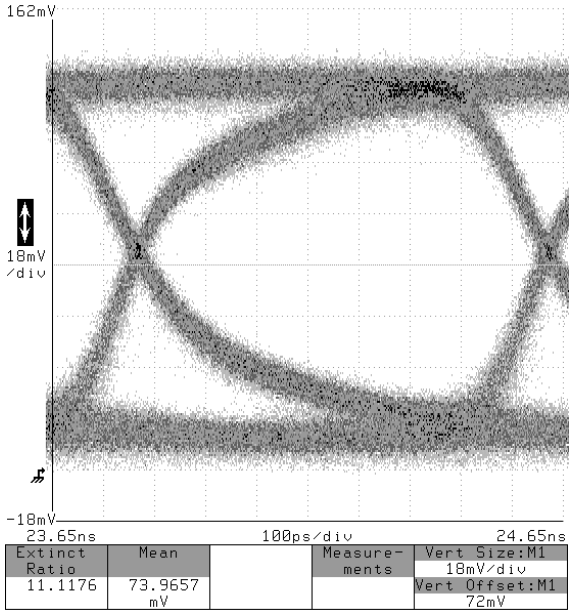

Figure 4.53 Eye diagram of SSG-DBR laser stabilised at 193.9 THz after a temperature ramp to 25 °C *with* manual adjustment of the bias current. The laser was directly modulated at a bit-rate of 1.244 Gbit/s with a 2^{23}-1 PRBS signal. The extinction ratio is 10.5 dB.

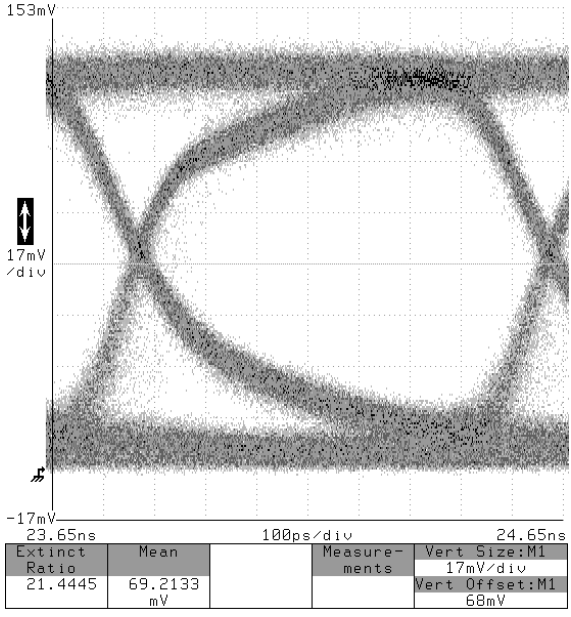

Figure 4.54 Eye diagram of SSG-DBR laser stabilised at 193.9 THz after a temperature ramp to 25 °C *without* manual adjustment of the bias current. The laser was directly modulated at a bit-rate of 1.244 Gbit/s with a 2^{23}-1 PRBS signal. The extinction ratio is 13.3 dB.

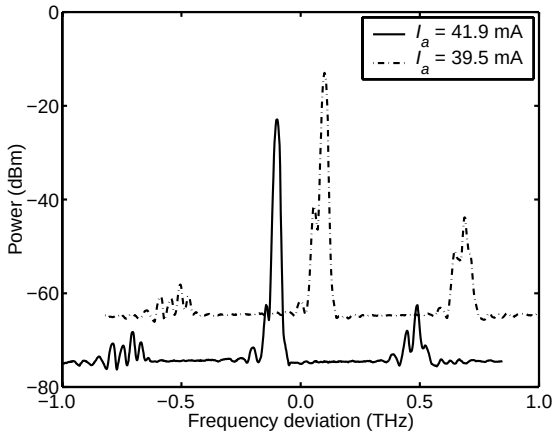

Figure 4.55 Time-averaged optical spectra corresponding to Figure 4.53 (solid line) and Figure 4.54 (dash-dotted line). For clarity, the spectra were offset by ±0.1 THz in frequency and ±5 dBm in power.

4.4 Conclusion

This chapter explored the possibilities for frequency and mode stabilisation of a tunable laser diode. Section 4.1 reviewed the techniques that can be used to stabilise the laser frequency. In most cases, frequency variations are translated into power variations using an optical filter. The frequency error signal can be minimised either by adjusting the laser temperature or by adjusting the phase section current. We chose to adjust the phase current, since the response is intrinsically much faster. Variations of the temperature were on the other hand used to intentionally induce frequency drift. To stabilise the frequency of a tunable laser on a regular grid, a Fabry-Perot etalon seems the most suitable reference filter, due to its inherent periodicity.

Mode control mechanisms were investigated in §4.2. In literature numerous experiments have been described where variations of the output power with tuning are used to determine whether the intra-cavity filter is aligned with a cavity mode or not. In the integrated tunable laser diodes we study in this thesis, these (small) variations in the output power are however often masked by the overall decrease of the output power caused by the tuning. As an alternative, we proposed to use the voltage across the active section as the feedback signal. Experimentally we found that only in the SSG-DBR lasers the voltage provided a suitable feedback signal. In the DBR and GCSR lasers available to us, the filters were not selective enough to provide a good feedback signal. The rather poor selectivity of the Bragg reflectors in both lasers led to non-linear effects, causing tuning hysteresis.

Finally, section 4.3 described a practical implementation of the frequency and mode control loops for SSG-DBR lasers. With the control system, we could maintain frequency errors below ±1.0 GHz and SMSR values above 35 dB across a 10 °C temperature range, and this for 40 frequency channels. Frequency and mode stability could even be maintained when the laser was modulated at a bit-rate of 1.244 Gbit/s.

References

[1] R.S. Vodhanel, M. Krain, R.E. Wagner, and W.B. Sessa, "Long-term wavelength drift of the order of –0.01 nm/yr. for 15 free-running DFB laser modules," *Proc. OFC '94*, vol. 4, pp. 103-104, paper WG5, San Jose, CA, USA, February 1994.

[2] Y.C. Chung, and J. Jeong, "Aging-induced wavelength shifts in 1.5-µm DFB lasers," *Proc. OFC '94*, vol. 4, pp. 104-105, paper WG6, San Jose, CA, USA, February 1994.

[3] S.L. Woodward, P. Parayanthal, and U. Koren, "The effects of aging on the Bragg section of a DBR laser," *IEEE Photon. Technol. Lett.*, vol. 5, no. 7, pp. 750-752, July 1993.

[4] F. Delorme, G. Alibert, P. Boulet, S. Grosmaire, S. Slempkes, and A. Ougazzaden, "High reliability of high-power and widely tunable 1.55-µm distributed Bragg reflector lasers for WDM applications," *IEEE J. Selected Topics Quantum Electron.*, vol. 3, no. 2, pp. 607-614, April 1997.

[5] H. Mawatari, M. Fukuda, F. Kano, Y. Tohmori, Y. Yoshikuni, and H. Toba, "Lasing wavelength changes due to degradation in buried heterostructure distributed Bragg reflector lasers," *J. Lightwave Technol.*, vol. 17, no. 5, pp. 915-923, May 1999.

[6] F. Delorme, G. Terol, H. de Bailliencourt, S. Grosmaire, and P. Devoldere, "Long-term wavelength stability of 1.55-µm tunable distributed Bragg reflector lasers," *IEEE J. Selected Topics Quantum Electron.*, vol. 5, no. 3, pp. 480-486, May 1999

[7] K.R. Preston, "Simple spectral control technique for external cavity laser transmitters," *Electron. Lett.*, vol. 18, no. 25, pp. 1092-1094, December 1982.

[8] N.A. Olsson, W.T. Tsang, and R.A. Logan, "Active spectral stabilisation of cleaved-coupled-cavity (C3) lasers," *J. Lightwave Technol.*, vol. 2, no. 1, pp. 49-51, February 1984.

[9] S.L. Woodward, I.M.I. Habbab, T.L. Koch, and U. Koren, "The side-mode-suppression ratio of a tunable DBR laser," *IEEE Photon. Technol. Lett.*, vol. 2, no. 12, pp. 854-856, December 1990.

[10] S.L. Woodward, T.L. Koch, and U. Koren, "A control loop which ensures high side-mode-suppression ratio in a tunable DBR laser," *IEEE Photon. Technol. Lett.*, vol. 4, no. 5, pp. 417-419, May 1992.

[11] H. Ishii, H. Yasaka, H. Tanobe, and Y. Yoshikuni, "Wavelength stabilisation of a three-electrode distributed Bragg reflector laser with longitudinal mode control," *Electron. Lett.*, vol. 33, no. 6, pp. 494-496, March 1997.

[12] H. Ishii, F. Kano, Y. Yoshikuni, and H. Yasaka, "Mode stabilisation method for superstructure-grating DBR lasers," *J. Lightwave Technol.*, vol. 13, no. 3, pp. 433-442, March 1998.

[13] K.J. Ebeling, and L.A. Coldren, "Wavelength self stabilisation of coupled-cavity semiconductor lasers," *Electron. Lett.*, vol. 20, no. 2, pp.69-70, January 1984.

[14] G. Sarlet, G. Morthier, and R. Baets, "Novel mode stabilisation scheme for widely tunable lasers," *Proc. ECOC '99*, vol. II, pp. 128-129, paper We B3.5, Nice, France, September 1999.

[15] G. Sarlet, G. Morthier, and R. Baets, "Wavelength and mode stabilisation of widely tunable SG-DBR and SSG-DBR lasers," *IEEE Photon. Technol. Lett.*, vol. 11, no. 11, pp. 1351-1353, November 1999.

[16] G. Sarlet, G. Morthier, and R. Baets, "Control of widely tunable SSG-DBR lasers for dense wavelength division multiplexing," *J. Lightwave Technol.*, vol. 18, no. 8, pp. 1128-1138, August 2000.

[17] W.S. Gornall, "Interferometry determines wavelengths precisely," *Laser Focus World*, vol. 33, no. 11, November 1997.

[18] T. Iwashima, A. Inoue, M. Shigematsu, M. Nishimura, and Y. Hattori, "Temperature compensation technique for fibre Bragg gratings using liquid crystalline polymer tubes," *Electron. Lett.*, vol. 33, no. 5, pp. 417-419, February 1997.

[19] J.J. Pan, Y. Shi, and S.X. Li, "Temperature stabilised multi-FBG package with zero-wavelength shift," *Proc. CLEO Europe '98*, pp. 360, paper CFB4, Glasgow, Scotland, UK, September 1998.

[20] S.L. Woodward, V. Mizrahi, T.L. Koch, U. Koren, and P.J. Lemaire, "Wavelength stabilisation of a DBR laser using an in-fiber Bragg filter," *IEEE Photon. Technol. Lett.*, vol. 5, no. 6, pp. 628-630, June 1993.

[21] Y. Park, S.-T. Lee, and C.-J. Chae, "A novel wavelength stabilisation scheme using a fiber Bragg grating for WDM transmission," *IEEE Photon. Technol. Lett.*, vol. 10, no. 10, pp. 1446-1448, October 1998.

[22] M. Teshima, and M. Koga, "100-GHz spaced 8-channel frequency control of DBR lasers for virtual wavelength path cross-connect system," *IEEE Photon. Technol. Lett.*, vol. 8, no. 12, pp. 1701-1703, December 1996.

[23] H. Lee, G.Y. Lyu, S.Y. Park, and J.H. Lee, "Multichannel wavelength locking using transmission peaks of an AWG for multichannel optical transmission," *IEEE Photon. Technol. Lett.*, vol. 10, no. 2, pp. 276-278, February 1998.

[24] M.S. Nakamura, and S. Ohshima, "Frequency-stabilised LD module with a Z-cut quartz Fabry-Perot resonator for coherent communication," *Electron. Lett.*, vol. 26, no. 6, pp. 405-406, March 1990.

[25] B. Villeneuve, H.B. Kim, M. Cyr, and D. Gariépy, "A compact wavelength stabilisation scheme for telecommunication transmitters," *Proc. LEOS Summer Topical Meetings '97*, pp. paper WD2, Montreal, Canada, August 1997.

[26] B. Villeneuve, M. Cyr, and H.B. Kim, "High-stability wavelength-controlled DFB laser sources for dense WDM applications," *Proc. OFC '98*, pp. paper FB5, San Jose, CA, USA, February 1998.

[27] International Telecommunication Union – Telecommunication Standardization Sector (ITU-T), Recommendation G.692: "Optical interfaces for multichannel systems with optical amplifiers," *Series G: Transmission systems and media, digital systems and networks (Transmission media characteristics – Characteristics of optical components and sub-systems)*, October 1998.

[28] Fabry-Perot Wavelength Locker (FPWL), E-Tek Dynamics Inc., 1865 Lundy Avenue, San Jose, CA 95131, USA. <http://www.e-tek.com/>

[29] A.A.M. Staring, J.J.M. Binsma, P.I. Kuindersma, E.J. Jansen, P.J.A. Thijs, T. van Dongen, and G.F.G. Depovere, "Wavelength-independent output power from an injection-tunable DBR laser," *IEEE Photon. Technol. Lett.*, vol. 6, no. 2, pp. 147-149, February 1994.

[30] N. Ogasawara, and R. Ito, "Longitudinal mode competition and asymmetric gain saturation in semiconductor injection lasers. I. Experiment," *Jpn. J. Appl. Phys.*, vol. 27, no. 4, pp. 607-614, April 1988.

[31] N. Ogasawara, and R. Ito, "Longitudinal mode competition and asymmetric gain saturation in semiconductor injection lasers. II. Theory," *Jpn. J. Appl. Phys.*, vol. 27, no. 4, pp. 615-626, April 1988.

[32] A. Uskov, J. Mørk, and J. Mark, "Wave mixing in semiconductor laser amplifiers due to carrier heating and spectral-hole burning," *IEEE J. Quantum Electron.*, vol. 30, no. 8, pp. 1769-1781, August 1994.

[33] I. Maio, G.P. Bava, I. Montrosset, "Mode competition and switching in three section DBR tunable lasers," *IEE Proc.-Optoelectron.*, vol. 138, no. 1, pp. 52-56, February 1991.

[34] P. Ottolenghi, S. Benedetto, and I. Montrosset, "Switching and optical modulation of three-section DBR lasers," *IEEE J. Quantum Electron.*, vol. 60, no. 6, pp. 1381-1388, June 1994.

[35] I. Kim, R.C. Alferness, U. Koren, L.L. Buhl, B.I. Miller, M.G. Young, M.D. Chien, T.L. Koch, H.M. Presby, G. Raybon, and C.A. Burrus, "Broadly tunable vertical-coupler filtered tensile-strained InGaAs/InGaAsP multiple quantum well laser," *Appl. Phys. Lett.*, vol. 64, no. 21, pp. 2764-2766, May 1994.

[36] HP86120B multi-wavelength meter, Agilent Technologies – Test & Measurement, 5301 Stevens Creek Blvd., Santa Clara, CA 95052, USA. < http://www.tm.agilent.com/>

[37] M.-C. Amann, and J. Buus, *Tunable laser diodes*, Artech House, Norwood, MA, USA, 1998.

Chapter 5

Characterisation methods to generate a frequency look-up table

By now, it should be clear that the control of the integrated tunable laser diodes introduced in Chapter 2 is rather complex. In order to tune the laser to a particular frequency with a certain output power, three to four currents have to be adjusted. To make things worse, any change in a single control current will affect both the frequency and the output power. As mentioned in the introductory chapter, tunable lasers nevertheless have many advantages over conventional fixed-frequency lasers for applications in fiber-optic communications. Unless the laser is supplied together with the necessary control electronics, these benefits are however largely outweighed by the disadvantage of the control complexity.

From a user's point of view it should be possible to set the laser to a certain frequency using simple, digital commands. A microprocessor should then translate these into the appropriate values of the laser's control currents. For this, a look-up table of operation points is used, which is stored in an EPROM (erasable, programmable read-only memory). Operation points are typically stored for the frequencies on the ITU-grid [1]. When the frequency has to be changed, the microprocessor interprets the digital commands, reads the appropriate data from the look-up table, and adjusts the control currents accordingly. The circuitry should also include a temperature control loop, since the emission frequency is very sensitive to temperature variations (§2.1.3). Due to fabrication tolerances, a separate look-up table will have to be derived for every individual laser. In this chapter, we will present a number of characterisation methods that can be used to generate these look-up tables.

Section 5.1 first establishes the requirements that a characterisation procedure should fulfil. Of course, a good procedure should yield high frequency accuracy, high side-mode suppression ratio and preferably a high degree of power uniformity across the tuning range. On top of that it should however also be cost-effective.

The first procedure we developed is based on curve fitting to frequency measurements (§5.2). Because of this, the frequency only has to be measured on a rather coarse current grid, which reduces characterisation time significantly. Disadvantages of the approach are that the frequency errors can still be quite large (several GHz) and that intervention of an operator is required to pick good initial estimates for the fit parameters.

In the procedure described in §5.3, the first curve-fitting step of the previous method is used to generate a very coarse look-up table. This table is subsequently updated using the feedback control system from Chapter 4. This yields both a higher frequency accuracy (±1.0 GHz) and a shorter characterisation time. On the other hand, operator intervention is still required and operation points can only be found for a small set of frequencies, determined by the frequency reference in the control loop.

The last method, presented in §5.4, is fully automatic, can generate a look-up table for an arbitrary frequency grid with excellent accuracy (±0.5 GHz) and enables very short characterisation times. In §4.2 and §4.3 we demonstrated that a SSG-DBR laser can be made to emit in a single spectral line by minimising the active section voltage as a function of the front and rear reflector currents. In the algorithm discussed in §5.4 we use this property to map out suitable operation points in the 3-dimensional space of front DBR, rear DBR, and phase currents. In the end, the emission frequency then only has to be measured for these – already optimised – operation points, after which a look-up table can be calculated by straightforward interpolation.

5.1 Requirements for the characterisation procedure

Before describing the procedures that can be used to generate a look-up table, we first need to establish the requirements such a procedure should fulfil. The main criterion is of course frequency accuracy. This can for example be expressed by the root-mean-squared (or maximum) frequency error that is measured when the laser is tuned through all the operation points stored in the table. For WDM applications, errors less than ±10% of the channel spacing are usually demanded. Put the other way around this means that the higher the accuracy is, the denser the channel spacing can become. At a fixed channel separation, a higher frequency accuracy of the transmitter will relieve the requirements on the bandwidth, the pass-band flatness, and the frequency accuracy of the optical filters and (de-)multiplexers in the WDM system.

Of course, the operation points in the look-up table should not only be accurate with respect to frequency; they should also guarantee a sufficient side-mode suppression ratio. Typically, the SMSR should be at least 30 dB, although higher values – 35 to 40 dB – are often preferred.

Another important parameter is the power uniformity, i.e. the variation in output power when the laser is tuned through the operation points in the table. If the active section current is kept at a constant value, the output power can vary by several dB across the tuning range of the laser due to the carrier-induced losses in the passive sections (cf. e.g. Figure 4.30 and Figure 4.36). Therefore, it is often necessary to adjust the active section current. The disadvantage is that the active section current also affects the emission frequency, mainly due to thermal effects. In principle, the carrier density in the active region is clamped for currents above the threshold (if non-linear effects can be neglected). Therefore, the refractive index of this section should not change when the current is varied. However, when the current is increased, extra heat is generated in the active section because of the non-zero series

resistance. Since there is always some thermal resistance between the active region and the Peltier cooler, a small temperature rise will result. This increases the refractive index and hence also the optical length of the cavity, which finally leads to a decline of the emission frequency. To compensate for this drift, the tuning currents have to be adjusted. Requiring a constant output power across the tuning range hence adds another degree of complexity to the control.

Frequency accuracy, SMSR, and power uniformity are all criteria that are of immediate concern to the end user. For the manufacturer of the tunable transmitter module, the cost of generating the look-up table is also crucial. At first sight, the single most important parameter affecting the cost is simply the characterisation time. A few refinements have to be made however. Longer measurement times could for example be allowed for when the procedure is a self-calibration procedure, which only uses the electronics and other components contained within the transmitter module. In that case, large numbers of transmitter modules could indeed be processed in parallel.

What should certainly be minimised is the amount of time expensive (external) instruments, such as an optical spectrum analyser or a wavelength meter, are used. For example, until recently NTT used a full-automatic trial-and-error procedure to generate a look-up table for their SSG-DBR lasers, which only exploited direct frequency and SMSR measurements. This would not necessarily be a problem if the characterisation time were limited to a few minutes. However, to generate a look-up table of 400 operation points, with a frequency increment of 10 GHz, it typically took 2 to 3 days, since a single frequency or SMSR measurement usually takes at least 1 second [2]-[3]. This is of course unacceptable for volume production.

In addition, the amount of operator intervention needed should be kept as low as possible. Ideally, the procedure should run completely automatically from beginning to end.

5.2 Parameter fitting of measured tuning characteristics

For all the tunable lasers introduced in Chapter 2, two conditions have to be fulfilled in order to obtain emission at a particular frequency. Firstly, one or more intra-cavity optical filters have to be tuned to this frequency. Secondly, the optical length of the cavity has to be adjusted to obtain phase resonance at the desired frequency.

The procedure described below first derives the tuning characteristics of the individual intra-cavity filters by measuring the emission frequency of the laser as a function of the current through the intra-cavity filters. Curve fitting is used to reduce the number of frequency measurements that is required. By inverting these curves, we can then derive the currents that should be applied to the filters to tune the cavity loss minimum to any particular frequency. In order to obtain the phase section current that is required to align a cavity mode with the loss minimum at any of those frequencies, a second set of frequency measurements is needed. Again, curve fitting is applied to limit the number of measurements. Inverting the final set of fitted curves yields the phase current for any selected emission frequency (with the associated values for the filter tuning currents determined by the first set of fitted curves).

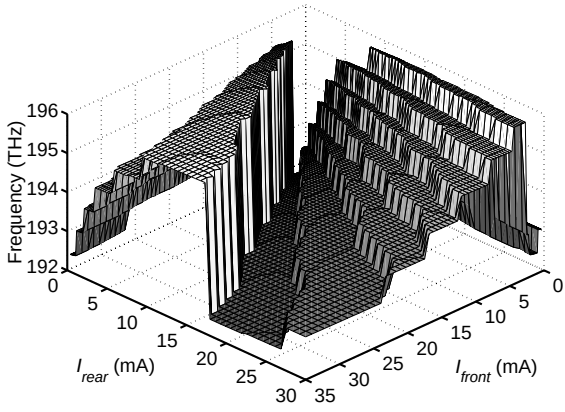

Figure 5.1 Emission frequency of a SSG-DBR laser measured as a function of the front and rear reflector currents, at fixed phase current I_{phase} = 0 mA and active section current I_{active} = 60 mA.

5.2.1 SSG-DBR laser

Tuning of the reflectors

As a first example, we consider the SSG-DBR laser. Figure 5.1 plots the emission frequency ν of a SSG-DBR laser, measured as a function of the front (I_{front}) and rear (I_{rear}) reflector currents. The front DBR, active, phase, and rear DBR sections are 400 µm, 450 µm, 125 µm, and 600 µm long, respectively. Both reflectors have 7 reflectivity peaks, with centre frequency and peak spacing chosen such that the laser can be tuned quasi-continuously over the entire C-band (192 to 196 THz). The active section was biased at 60 mA, and no current was applied to the phase section. On the frequency surface, several plateaux are apparent, each corresponding to the coincidence of a particular pair of reflectivity peaks of the two SSG mirrors. Along the plateaux, smaller frequency hops can be observed, corresponding to cavity mode jumps.

Figure 5.2 plots the same frequency data, but now represented as a function of only the rear reflector current. This graph can in other words be seen as the projection of the data points in Figure 5.1 on the (ν, I_{rear})-plane. The plateaux in Figure 5.1 now appear as parallel bands of measurement points. These bands represent the tuning of the reflectivity peaks of the rear SSG mirror with current. Bands are obtained in stead of lines because of the frequency discretisation imposed by the roundtrip phase condition. The width of the bands is therefore approximately equal to the cavity mode spacing. The actual peak frequencies of the rear SSG reflector are located at the centre of each band.

If it were possible to describe the peak frequency curves with an analytical function $\nu_k(I)$, then the current needed to tune a reflectivity peak to a certain frequency ν could easily be calculated (k is the ordinal number of the curve). The peak frequencies ν_k are determined by the effective refractive index n of the waveguide (cf. (2.25)).

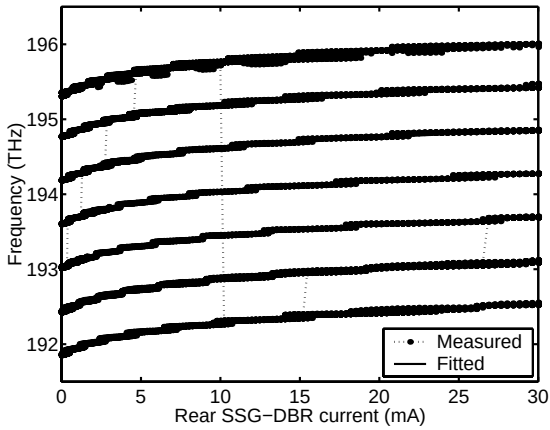

Figure 5.2 Frequency values measured as a function of I_{rear} and I_{front} (150×150 matrix), plotted as a function of I_{rear} only (dots). Fitted tuning characteristic of the rear SSG reflector (solid lines).

The index is changed by injecting a current I into the section. This has two effects: the carrier density N is increased, and the temperature of the waveguide is raised. The index changes are described by [4]:

$$n(\nu, N, T) = n_r + \Gamma \frac{\partial n'}{\partial N} N + \frac{\partial n}{\partial T}\left(T_a - T_r + R_{th} V_j I\right) + \frac{\partial n}{\partial \nu}\left(\nu - \nu_r\right) \qquad (5.1)$$

Here, n_r, T_r, and ν_r are reference values of the effective index, the waveguide temperature and the optical frequency, respectively. n' is the refractive index of the waveguide core material and Γ is the confinement factor (cf. §2.1). Lastly, T_a is the ambient temperature (the temperature of the laser sub-mount) and $R_{th}V_jI$ describes the increase of the waveguide temperature relative to the environment, due to the non-zero thermal resistance R_{th} (V_j is the junction threshold voltage).

The carrier density N is determined by the current I according to the carrier rate equation:

$$\frac{I}{qLwd} = AN + BN^2 + CN^3 \qquad (5.2)$$

For typical parameter values (cf. Chapter 3), the variation of the effective index n with current I can be fitted very well by a relationship of following form:

$$\Delta n(I) = sI_0^{1/3} - s\left(I + I_0\right)^{1/3} + tI \qquad (5.3)$$

Since the relative refractive index variation is small, the corresponding change of the peak frequencies ν_k is easily derived from (2.25) as:

$$\nu_k(I) = \nu_0(0) - aI_0^{1/3} + a\left(I + I_0\right)^{1/3} - bI + k\delta \qquad (5.4)$$

Here $\nu_0(0)$ is the frequency of peak 0 at zero current, and δ is the peak spacing (2.26). If K is the total number of peaks, then we number the peaks according to:

$$k = -\left\lfloor \tfrac{1}{2}(K-1) \right\rfloor, \ldots, 0, \ldots, \left\lceil \tfrac{1}{2}(K-1) \right\rceil \qquad (5.5)$$

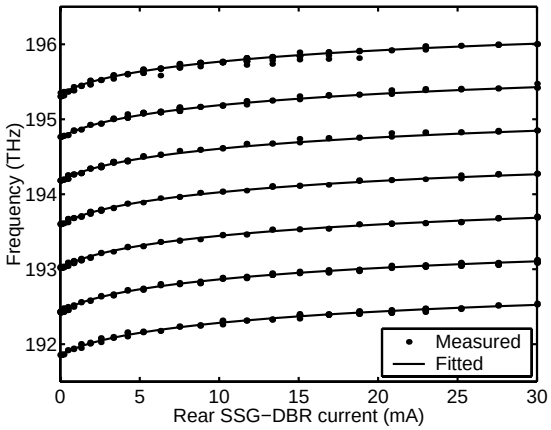

Figure 5.3 Frequency values measured as a function of I_{rear} and I_{front} (25×25 matrix), plotted as a function of I_{rear} only (dots). Fitted tuning characteristic of the rear SSG reflector (solid lines).

Table 5.1 Fitted parameters for the rear reflector tuning characteristic, for the full set of data points (150×150) plotted in Figure 5.2 and for the reduced set of points (25×25) plotted in Figure 5.3.

# points	$\nu_0(0)$ (THz)	a ($mA^{-1/3}$)	b (mA^{-1})	I_0 (mA)	δ (THz)
150×150	193.5919	0.3995	$6.479 \cdot 10^{-3}$	0.8982	0.5806
25×25	193.5890	0.4000	$6.372 \cdot 10^{-3}$	0.9013	0.5805

The parameters $\nu_0(0)$, a, b, I_0, and δ can be calculated by numerically fitting relation (5.4) to the measurement data shown in Figure 5.2. As cost function for the optimisation the sum of squared errors is used, where for each data point the error is defined as the distance to the closest fitting curve. The cost function was minimised by applying the downhill simplex method of Nelder and Mead [5].

The same matrix of measured frequencies can also be plotted as a function of the front reflector current alone. Obviously, a similar graph is obtained, which can again be fitted by (5.4) to obtain the parameter set describing the tuning of the front mirror reflectivity peaks.

A few comments have to be made concerning Figure 5.1 and Figure 5.2. Since the tuning efficiency decreases with current, a higher current resolution is required at low currents than at high currents. Therefore, the currents are increased as:

$$I_m = \left(\frac{m}{M}\right)^p I_{max} \quad \text{where} \quad m = 0, 1, 2, \ldots, M\text{-}1, M \tag{5.6}$$

where p is usually set to 2.

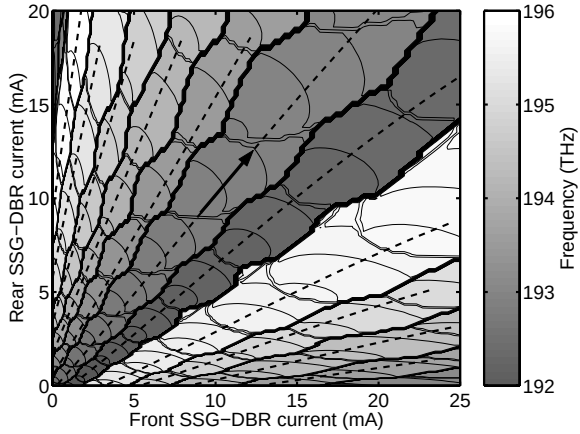

Figure 5.4 Measured contour map of the emission frequency as a function of the front and rear reflector currents. The dashed lines indicate the (I_{front}, I_{rear})-pairs calculated from the parameter fits, for all frequencies within the tuning range of the laser (from 191.9 to 196.0 THz).

To generate the surface in Figure 5.1, the emission frequency was measured on a dense two-dimensional grid of reflector currents (150×150 points). For the parameter fit, a much coarser grid can be used (e.g. 25×25 points). This yields a significant reduction in measurement time (by a factor of 36), without degrading the accuracy of the fit, as is illustrated by Figure 5.3 and the parameter values in Table 5.1.

When the parameter sets for the two reflectors have been determined, the frequency versus current characteristics of the reflectors can easily be inverted. For any frequency within the tuning range (from 191.9 to 196.0 THz in Figure 5.2), front and rear SSG-DBR currents can be calculated, which will tune a reflectivity peak of the respective mirror to that frequency. For some frequencies, multiple solutions exist for one of the reflector currents. Since absorption losses increase with current, the solution that requires minimal current is usually retained. The dashed lines in Figure 5.4 represent the (I_{front}, I_{rear})-pairs that were calculated in this manner for all frequencies within the tuning range. They have been superimposed on a contour plot of the frequency data from Figure 5.1. The dashed lines clearly follow tracks along the frequency plateaux that are situated more or less halfway between the super-mode jumps, indicating that a pair of reflectivity peaks remains reasonably well aligned along these tracks.

Close to a cavity mode hop the calculated (I_{front}, I_{rear})-trace sometimes almost touches a super-mode boundary. In that case, the lasing mode is obviously not very well aligned with the two reflectivity peaks that have the largest overlap. If the peaks are also not perfectly aligned, it could then occur that a cavity mode at the neighbouring loss minimum, produced by the adjacent pair of reflectivity peaks, becomes the preferential mode. Consequently, a super-mode hop will arise. This explains the zigzag behaviour of the super-mode boundaries, where the distance between two adjacent super-mode boundaries is minimal close to a longitudinal mode hop. Some of the asymmetries could be explained by differences in reflectivity

between the various peaks of the mirrors. Super-modes that correspond to weaker SSG-DBR peaks will be suppressed by adjacent super-modes that have stronger reflectivity peaks.

The fact that the (I_{front}, I_{rear})-traces come close to the super-mode boundary near a longitudinal mode hop is however not necessarily a problem. In principle, the phase current should in any case be adjusted such that the laser emits in a stable single mode. Adjusting the phase current to tune the laser away from a longitudinal mode hop will simultaneously push the super-mode boundary away. We can therefore assume that the first condition for laser operation at a particular frequency – tuning the loss minimum to that frequency – is fulfilled by picking the appropriate (I_{front}, I_{rear})-pair on the curves from Figure 5.4.

Adjusting the phase section current

In a second stage, the phase current that should be applied to tune a cavity mode to the loss minimum has to be determined. This requires a second set of measurements. (I_{front}, I_{rear})-pairs are calculated for a uniform frequency grid that covers the desired tuning range and uses a frequency step that is less than the cavity mode spacing $\Delta\nu$ (usually about $0.5 \cdot \Delta\nu$). For each of these (I_{front}, I_{rear})-pairs, the phase current is increased step-wise according to (5.6) and the frequency is measured. Subsequently, the set of data points corresponding to each individual trace in the (I_{front}, I_{rear})-plane is considered separately. Figure 5.5 plots the frequency as a function of the phase and rear reflector currents for one such set, linked to the (I_{front}, I_{rear})-trace indicated by the arrow in Figure 5.4. Obviously, a similar surface would appear if the data was represented as a function of the phase and front reflector currents, since the front and rear reflector currents are uniquely related by the trace in Figure 5.4. Again, a number of plateaux are obtained, which now however correspond to individual longitudinal modes. If the data is represented as a function of only the phase current (Figure 5.6), these plateaux emerge as bands of frequency points.

The situation here is however not entirely the same as for the tuning of the reflectors. In Figure 5.1, the tuning of the front mirror had no influence on the peak frequencies of the rear mirror and vice versa. In this case, a cavity mode frequency not only shifts due to changes in the phase current but also due to the (simultaneous) tuning of the reflectors. The dotted lines in Figure 5.6 illustrate the frequency tuning as a function of phase current for a few selected (I_{front}, I_{rear})-pairs, calculated for frequencies ν spaced by 100 GHz. The slope of these lines is clearly lower than the slope of the bands. Hence, at some point the frequency hops to an adjacent band. This proves that the gap between adjacent bands is equal to the cavity mode spacing. On the other hand, when the front and rear reflectivity peaks are simultaneously tuned by an amount $\delta\nu$, the cavity modes will shift by $\Gamma_{fr} \cdot \delta\nu$. The fraction Γ_{fr} can be derived from the phase condition:

$$\frac{2\pi\nu_i}{c}\left(2n_aL_a + 2n_pL_p\right) - \arg\left(r_f(\nu_i)\right) - \arg\left(r_r(\nu_i)\right) = 2\pi i \qquad (5.7)$$

where L_a and L_p are the lengths of the active and phase section, respectively; n_a and n_p are the corresponding effective indices; and r_f and r_r are the complex field reflectivities of the front and rear SSG mirrors, respectively.

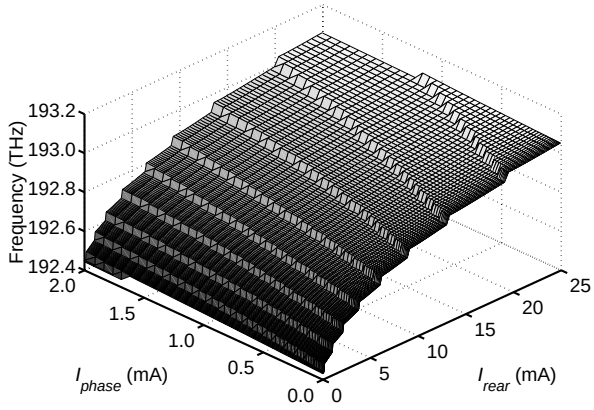

Figure 5.5 Emission frequency of a SSG-DBR laser measured as a function of the phase and rear reflector currents, along the (I_{front}, I_{rear})-trace indicated by the arrow in Figure 5.4. The active section current was kept constant: I_{active} = 60 mA.

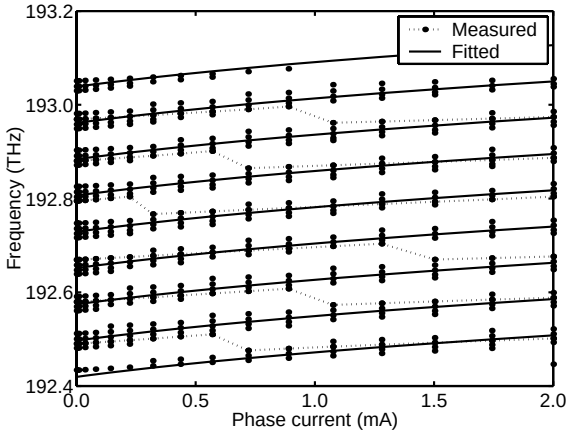

Figure 5.6 Frequency values measured as a function of I_{phase} and I_{rear}, plotted as a function of I_{phase} only (dots). The front and rear reflector currents were related by the curve indicated by the arrow in Figure 5.4. Fitted tuning curves of the individual cavity modes (solid lines).

If the effective length of a reflector is defined as:

$$L_{x,eff} = -\frac{1}{2}\frac{c}{2\pi n_{g,x}}\frac{\partial}{\partial \nu}\left[\arg\left(r_x(\nu)\right)\right] \tag{5.8}$$

then the phase condition immediately yields [6]:

$$\Gamma_{fr} = \frac{n_{g,f}L_{f,eff} + n_{g,r}L_{r,eff}}{n_{g,a}L_a + n_{g,p}L_p + n_{g,f}L_{f,eff} + n_{g,r}L_{r,eff}} \approx \frac{L_{f,eff} + L_{r,eff}}{L_a + L_p + L_{f,eff} + L_{r,eff}} \tag{5.9}$$

Here, $n_{g,x}$ represents the group index of section x.

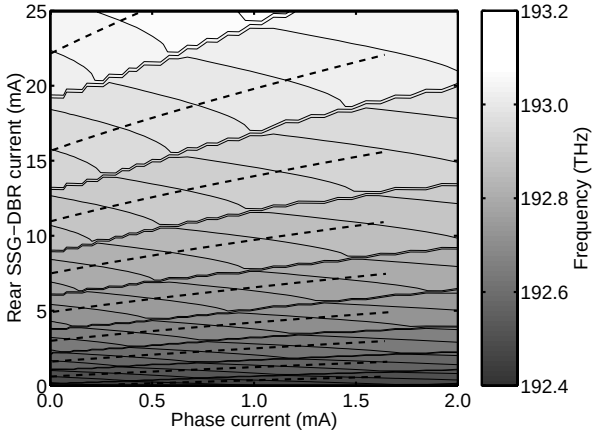

Figure 5.7 Measured contour map of the emission frequency as a function of the phase and rear reflector currents, along the (I_{front}, I_{rear})-trace indicated by the arrow in Figure 5.4. The dashed lines indicate the tuning trajectories calculated from the parameter fits.

Typical values for Γ_{fr} lie in the range from 0.4 to 0.5, since the low $\kappa_k L$-values usually found in SSG-DBR reflectors yield an effective length that is about half the physical length of the SSG-DBR section [7]. Here, κ_k is the effective coupling coefficient of a single reflectivity peak k (cf. Chapter 2). The combination of both tuning effects yields the frequency bands of Figure 5.6. Operation points with high side-mode suppression ratio are located at the central lines of the plateaux in Figure 5.5, as far away from the mode hops as possible. Tuning the laser along these lines requires simultaneous adjustment of I_{front}, I_{rear}, and I_{phase}.

Due to the combined tuning action, the tuning rate of an individual cavity mode will be enhanced by a factor $(1 + \Gamma_{fr})$ compared to the case where only the phase current is adjusted. Everything occurs as if the frequency axis was stretched by the factor $(1 + \Gamma_{fr})$. The front and rear reflector currents can be calculated using the previously obtained parameter sets. In order to derive the phase current, relation (5.4) is fitted to the data in Figure 5.6. In this case, δ will be equal to the mode spacing $\Delta\nu$ multiplied by the tuning enhancement factor $(1 + \Gamma_{fr})$.

In the end, I_{front}, I_{rear}, and I_{phase} can be calculated as a function of frequency using the respective parameter sets. The frequencies obviously have to be limited to the range that can be covered by the current (I_{front}, I_{rear})-track from Figure 5.4. Figure 5.7 shows the (I_{phase}, I_{rear})-combinations that have been obtained in this way, superimposed on a contour plot of the frequency data from Figure 5.5 (remember that the front reflector current is uniquely related to I_{rear}). If multiple solutions existed for the phase current, the lowest value was retained. The tuning traces are indeed located roughly halfway between two mode hops, so these operation points should yield a high SMSR. In order to calculate a look-up table covering the full tuning range of the laser, this has to be repeated for each of the (I_{front}, I_{rear})-tracks in Figure 5.4.

Table 5.2 Excerpt from the table of calculated (I_{front}, I_{rear})-pairs, illustrating how short (I_{front}, I_{rear})-traces can be avoided. Currents were calculated for frequencies from 191.9 to 196.0 THz in 20 GHz steps.

Frequency	Minimal currents		Second best pair			Final choice	
	I_{front} (mA)	I_{rear} (mA)	I_{front} (mA)	I_{rear} (mA)		I_{front} (mA)	I_{rear} (mA)
191.90	1.79	0.45				1.79	0.45
191.92	2.09	0.65				2.09	0.65
191.94	2.42	0.88				2.42	0.88
…	…	…	…	…		…	…
192.98	16.76	17.03				16.76	17.03
193.00	18.40	18.62				18.40	18.62
193.02	20.23	0.09	20.23	20.36		20.23	20.36
193.04	22.29	0.25	22.29	22.26		22.29	22.26
193.06	24.65	0.44	24.65	24.35		24.65	24.35
193.08	0.08	0.64	0.08	26.66		0.08	0.64
193.10	0.24	0.86	0.24	29.22		0.24	0.86
…	…	…	…	…		…	…

An accurate set of fit parameters for the phase current can only be obtained if the measurement data set contains sufficient points. If the only criterion for selecting a (I_{front}, I_{rear})-pair among multiple solutions is the requirement of minimal current, some of the (I_{front}, I_{rear})-traces that are obtained after the first step are found to be very short. For those traces, only a small number of (I_{front}, I_{rear})-pairs will be considered in the second measurement step. As a result, the frequency versus phase current plot (cf. Figure 5.6) will only show one or two bands with a limited number of measurement points. Obviously, this makes it impossible to obtain an accurate parameter fit.

An example is illustrated in Table 5.2, which shows an excerpt from a table of (I_{front}, I_{rear})-pairs calculated for a frequency grid from 191.9 to 196.0 THz in 20 GHz steps (i.e. steps of somewhat less than $0.5 \cdot \Delta\nu$). The second and third columns list the current values that would be used if minimal currents would always be demanded. The fourth and fifth column list the second best (I_{front}, I_{rear})-pair (if it exists). At 191.9 THz, only one solution exists. As the frequency increases, the required currents grow (cf. Figure 5.3). At some point, a second, lower solution will appear for the front or rear reflector current. Assume for example that this is the case for I_{front}. If one only requires minimal currents, the algorithm will pick this lower value for I_{front} and hence move to another (I_{front}, I_{rear})-trace. Subsequently, the currents will again increase with frequency, until a lower solution for the rear reflector current appears, etc. It is possible however, that two subsequent trace changes lie close to each other, as is illustrated by the shaded rows in Table 5.2. For this particular trace only three (I_{front}, I_{rear})-pairs would be used in the second measurement step, and the data set for the phase current fit would hence only consist of $3 \times M_{phase}$ frequency values ($M_{phase} = 16$ in Figure 5.6). Moreover, the frequency range corresponding to this trace is only slightly larger than the cavity mode spacing $\Delta\nu \approx 45$ GHz. Consequently, only one or two frequency bands will appear in the frequency versus

phase current plot (cf. Figure 5.6). This is not enough to guarantee sufficient accuracy of the parameter fit.

To avoid such problems, a second selection criterion was added. This criterion demands that the frequencies corresponding to two subsequent trace hops are separated by at least $2 \cdot \Delta\nu$. If this is not the case, the first of the two trace hops is disregarded and the second best current pair is used for the frequency range concerned. At the next trace switch, both currents then jump to a lower value simultaneously. With this additional criterion the currents listed in the final two columns of Table 5.2 are obtained.

In summary, the procedure consists of following steps:

- Measure the emission frequency on a two-dimensional grid of front and rear reflector currents, where currents are increased according to (5.6). Typically between 20 and 30 steps are used for each of the currents. Phase and active section currents are kept at a constant value.
- Calculate the parameter sets describing the tuning of the reflectivity peaks of the front and rear mirrors by fitting relation (5.4) to the measured data.
- Generate a table of front and rear reflector currents for a uniform frequency grid, which covers the desired tuning range and uses a frequency step that is less than the cavity mode spacing $\Delta\nu$ (usually about $0.5 \cdot \Delta\nu$). This table defines a number of tracks in the (I_{front}, I_{rear})-plane. If multiple solutions exist, the (I_{front}, I_{rear})-pair with lowest total current is retained, except when this choice would lead to a short trace, with insufficient points (cf. above). For each row of this table, the frequency is measured as a function of the phase current. The active section current is kept at the same level as previously. The measurement data is grouped per (I_{front}, I_{rear})-trace.
- Calculate the parameter set describing the tuning as a function of the phase current for each of the (I_{front}, I_{rear})-traces, by fitting relation (5.4) to the measurement data for this trace.
- Generate the look-up table for all required frequencies using the calculated parameter sets.

Experimental results

The look-up table generated for the laser from the previous figures is plotted in Figure 5.8. Currents were calculated for frequencies from 191.9 to 196.0 THz in 1 GHz increments. The accuracy of the look-up table was verified by tuning the laser to each of the operation points from the table and measuring the frequency and the side-mode suppression ratio. The results are represented in Figure 5.9. The SMSR is always above 40 dB, as could be expected from Figure 5.4 and Figure 5.7. The frequency errors are however relatively high. The maximum error is 8.2 GHz, and the root-mean-squared error is 2.6 GHz. This level of accuracy is insufficient to allow a WDM channel spacing below 100 GHz. A further drawback is that the active section current was kept at a constant level. This causes the output power to vary by about 7 dB across the tuning range. Similar results were obtained for several other SSG-DBR lasers (both by us and by NTT) and one SG-DBR laser [2]-[3], [8].

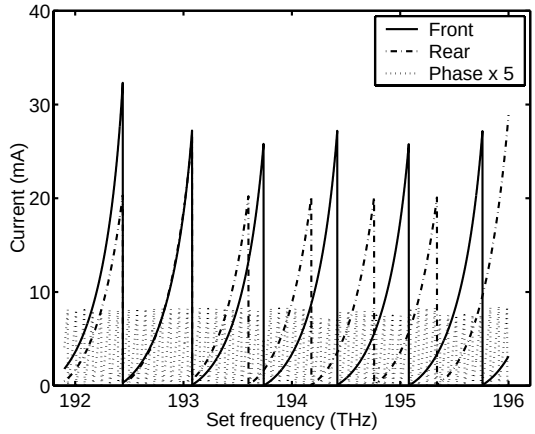

Figure 5.8 Plot of the look-up table calculated from the fitted parameter sets. Currents were calculated for frequencies ranging from 191.9 to 196.0 THz in 1 GHz increments.

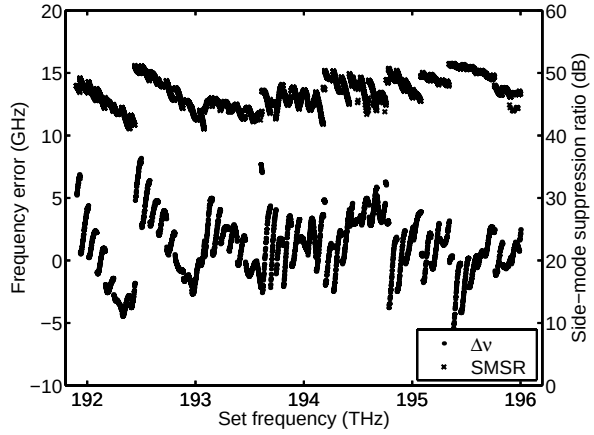

Figure 5.9 Frequency errors (·) and side-mode suppression ratios (×) measured for the look-up table plotted in Figure 5.8.

One important prerequisite to obtain reasonable results is that the laser should exhibit a regular tuning behaviour. Hence, some device selection is required prior to characterisation to reject lasers with certain irregularities in the tuning.

The characterisation time is significantly reduced with this procedure compared to the 2 to 3 days originally needed by NTT. In total $25\times25 + 206\times16 = 3921$ frequency measurements were needed. At a rate of one measurement per second, this would yield a characterisation time of little more than one hour. Compare this also to the $150\times150 = 22500$ points needed to generate Figure 5.2 and Figure 5.4. Still, the procedure relies purely on frequency measurements, which require an expensive wavelength meter.

An additional disadvantage is that some operator intervention is required to initialise the fit parameters $\nu_0(0)$, a, b, I_0, and δ (cf. (5.4)) with suitable values, before having these optimised numerically. If several devices from a same batch are characterised one after the other, the parameters will obviously be very similar. Yet, for example the centre frequency $\nu_0(0)$ can vary significantly across devices originating from the same wafer due to differences in material composition. The numerical fit procedure will only converge rapidly to meaningful values for the parameters if the initial values are chosen such that already a reasonable fit is obtained. This is mainly due to the fact that multiple curves have to be fitted to the data.

A program with a graphical user interface was developed to allow easy manual adjustment of the fit parameters. After a change to any of the parameters, the graph as shown in Figure 5.3 or Figure 5.6 is redrawn and the value of the cost function is displayed. Using this program, an experienced user can find good starting values in less than a minute. If the parameters from a previous fit on a similar device are loaded first, this only takes a few seconds. Another problem is that often multiple optima exist. Some hands-on experience is required to decide whether a particular set of fitted parameters will yield good results or not.

5.2.2 GCSR laser

Tuning of the coupler and the reflector

The procedure outlined above for the SSG-DBR laser has also been applied to GCSR lasers. In this case, the coupler and reflector currents take over the role of the front and rear SSG-DBR currents. Figure 5.10 plots the emission frequency ν of a GCSR laser, measured as a function of the coupler ($I_{coupler}$) and reflector (I_{refl}) currents. The active, coupler, phase, and SG-DBR sections are 400 µm, 600 µm, 150 µm, and 950 µm long, respectively. The active section was biased at 60 mA, and no current was applied to the phase section.

Each of the plateaux in Figure 5.10 represents the tuning of a single reflectivity peak of the SG-DBR mirror. If the frequency data is plotted as a function of the reflector current, a graph similar to Figure 5.2 is obtained. Consequently, (5.4) can once more be used to derive a parameter set for the SG-DBR mirror. If the data is represented as a function of the coupler current on the other hand, a single, broad band of data points appears (Figure 5.11), since the coupler filter only has a single transmission peak. This band can be fitted by (5.4) if the last term is omitted.

As is evident from Figure 5.11, the coupler current was increased with a fixed increment ($p = 1$ in (5.6)), because the coupler frequency varies almost linearly with current. On the other hand, it is very important that the reflector current is ramped super-linearly, in order to achieve a sufficiently accurate fit for the coupler. Indeed, with a fixed current increment for the reflector more measurement points are located at the high frequency end of the coupler bandwidth, since the frequency increases with current and the tuning efficiency decreases with current. If relation (5.4) is then fitted to the data, the fitted curve is not entirely centred on the band in Figure 5.11, but is rather shifted to higher frequencies. As a result, the coupler current will be underestimated when the relationship is inverted. In practice, a quadratic variation was used for the reflector current ($p = 2$ in (5.6)).

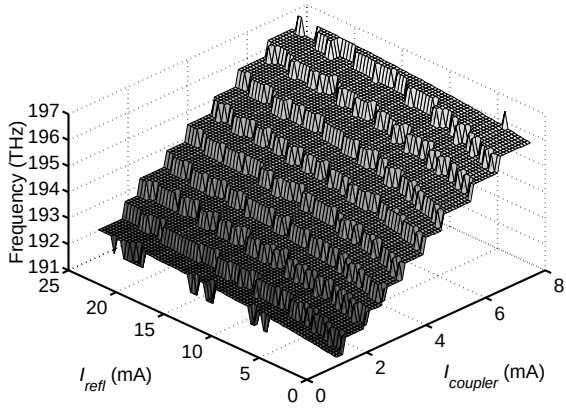

Figure 5.10 Emission frequency of a GCSR laser measured as a function of the coupler and reflector currents, at fixed phase current I_{phase} = 0 mA and active section current I_{active} = 60 mA.

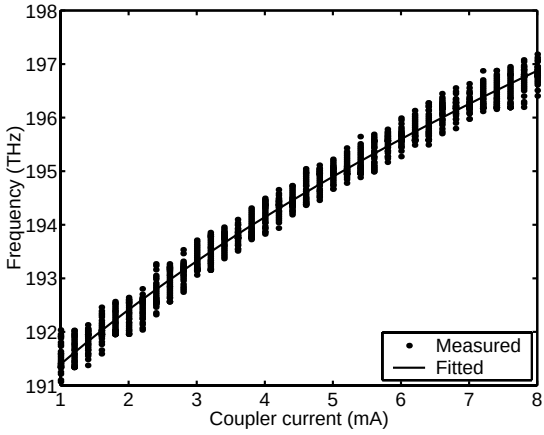

Figure 5.11 Frequency values measured as a function of $I_{coupler}$ and I_{refl} (36×30 matrix), plotted as a function of $I_{coupler}$ only (dots). Fitted tuning characteristic of the grating coupler (solid line).

Figure 5.12 shows the ($I_{coupler}$, I_{refl})-tracks that were calculated from the parameter sets for the coupler and the reflector. The tracks have been superimposed on a contour plot of the frequency data from Figure 5.10 to illustrate that they mostly yield adequate alignment of the coupler transmissivity peak to the reflector peaks. In this case, there is no risk of finding a ($I_{coupler}$, I_{refl})-track that is too short, since the coupler current varies continuously. The criterion of minimal total current is hence sufficient. One of the tracks passes very close to the super-mode boundaries near a cavity mode hop. As was explained for the SSG-DBR laser, this is not necessarily a problem since the super-mode boundary will be pushed away if the phase current is properly adjusted.

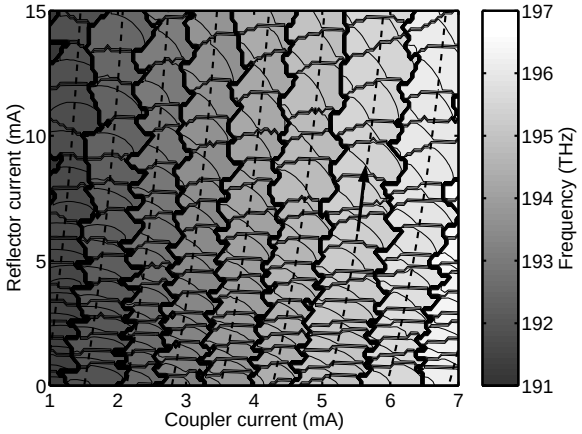

Figure 5.12 Measured contour map of the emission frequency as a function of the front and rear reflector currents. The dashed lines indicate the ($I_{coupler}$, I_{refl})-pairs calculated from the parameter fits, for frequencies ranging from 191.4 to 196.6 THz.

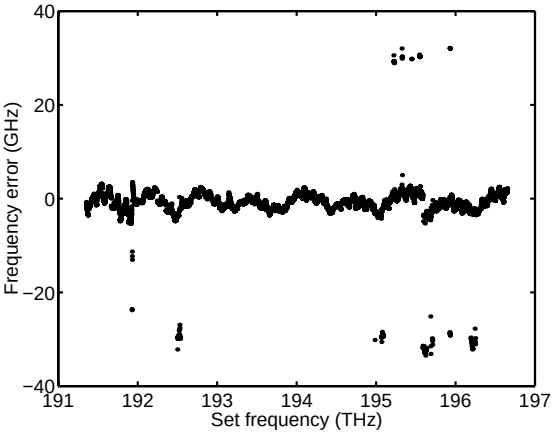

Figure 5.13 Measured frequency errors for the look-up table generated for the GCSR laser from Figure 5.10. Currents were calculated for frequencies ranging from 191.4 to 196.6 THz in 1 GHz increments.

Adjusting the phase section current

The second part of the procedure is entirely the same as for the SSG-DBR laser. A number of points are picked on each of the ($I_{coupler}$, I_{refl})-traces, corresponding to a uniform frequency grid that covers the desired tuning range and uses a frequency step of about half the cavity mode spacing $\Delta\nu$. In each of the points the frequency is measured as a function of the phase current. The data sets for the different traces are fitted by relation (5.4) in order to calculate the phase current as a function of frequency.

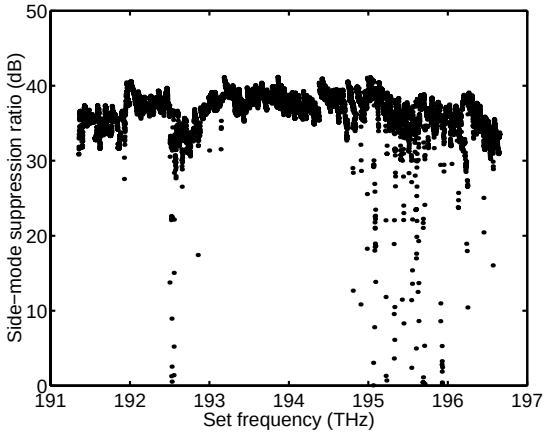

Figure 5.14 Measured side-mode suppression ratios for the look-up table generated for the GCSR laser from Figure 5.10.

Experimental results

Figure 5.13 and Figure 5.14 present the results of the look-up table verification. In general, the frequency errors are comparable to the errors measured for the SSG-DBR lasers. Yet, the side-mode suppression ratio is on average 10 dB lower. As was already mentioned in Chapter 4, the lower SMSR is explained by the narrower mode spacing relative to the SG-DBR peak bandwidth, which is a result of the long cavity. At low and high frequencies, sometimes very large errors occur because the emission frequency jumps to a cavity mode adjacent to the designated lasing mode. This is due to irregularities in the tuning behaviour.

On closer inspection of Figure 5.12 (and Figures 4.34 to 4.36), it becomes apparent that some mode regions are very narrow compared to adjacent mode regions. Similar observations also apply to the phase current tuning bands plotted in Figure 5.15, which correspond to the ($I_{coupler}$, I_{refl})-track indicated by the arrow in Figure 5.12. Some of the bands (indicated by the dotted lines) contain only few measurement points, and show gaps for certain phase current ranges. These observations indicate that it is difficult to tune the laser to these particular longitudinal modes. This phenomenon can probably be attributed to internal reflections in the laser cavity, either at an interface between two sections [9] or within the grating assisted co-directional coupler [10].

The first situation is illustrated by Figure 5.16, which shows the tuning characteristic of the DBR laser in two cases. In the first case, the reflectivity at the interface between the active section and the phase section was set to zero (cf. Figure 4.11), whereas in the second case this reflectivity was assumed to be 1% of the peak reflectivity of the DBR $R_{DBR}(\nu_B)$. Clearly, in the latter case the cavity mode around 193.5 THz is strongly suppressed. The effect of course becomes more important as the strength of the internal reflection increases relative to the DBR reflectivity. It will also be enhanced when the selectivity of the DBR is reduced, either by increasing the DBR bandwidth or by reducing the mode spacing.

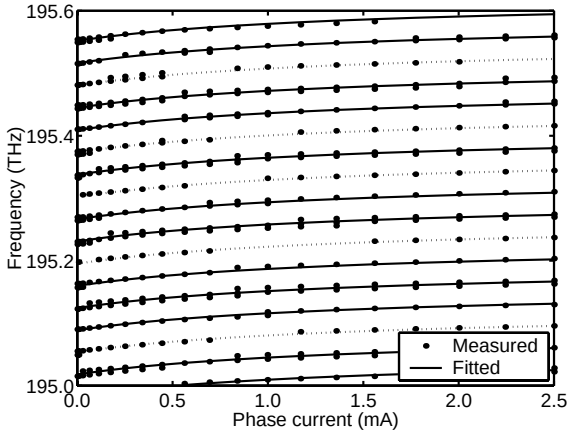

Figure 5.15 Frequency values measured as a function of I_{phase} and I_{refl}, plotted as a function of I_{phase} only (dots). The coupler and reflector currents were related by the curve indicated by the arrow in Figure 5.12. Fitted tuning curves of the individual cavity modes (solid and dotted lines). The dotted lines indicate cavity modes that are difficult to reach.

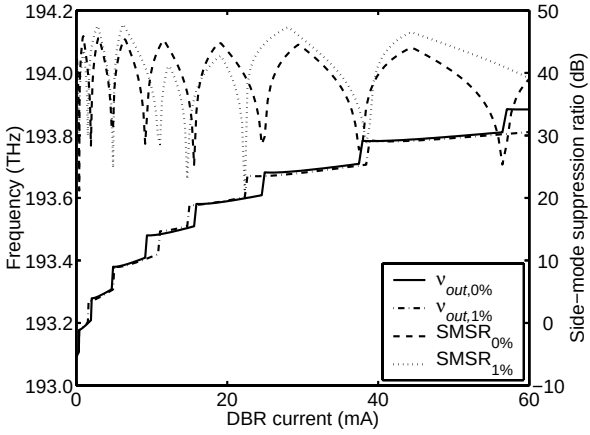

Figure 5.16 Calculated variations of frequency and side-mode suppression ratio as a function of the DBR tuning current, for a DBR laser with negligible reflection at the interface between active and phase sections and for a DBR laser with a reflection of $0.01 \cdot R_{DBR}(\nu_B)$ at this interface (cf. also Figure 4.11).

In the GCSR laser, the rear reflectivity (as seen from the active section) is rather low because of the modest reflectivity of the sampled grating and because of the absorption and scattering losses in the coupler. Typically, the reflectivity is no more than 10%. As already mentioned the selectivity of the SG-DBR peaks is also limited due to the narrow mode spacing. Hence, a small index mismatch (a few percent) between the waveguides in the active and coupler sections could be sufficient to cause some modes to be suppressed. That the effect mainly appears at low and high

frequencies (or in other words low and high coupler currents) is of course due to the envelope of the SG-DBR peaks.

5.3 Combining parameter fitting and feedback control

The largest fraction of the measurement time in the above procedure is used up in the second stage, where the phase current is determined as a function of frequency. The characterisation time will hence be reduced drastically if this second stage can be eliminated. When the laser is supplied with a feedback control circuit as described in Chapter 4 (Figure 4.41), the fine-tuning of the laser can be left to this control loop. In order to tune the laser to a particular channel, the emission frequency only has to be brought within the locking range of the frequency control loop. Since the control system only worked for the SG-DBR and SSG-DBR lasers, only these lasers will be considered here.

Following procedure was devised. The first characterisation stage is essentially the same as above. The frequency is measured on a two-dimensional grid of front and rear reflector currents. Since the highest accuracy is however no longer required, a lower-resolution frequency measurement should now be sufficient. The wavelength meter used in our experiments has two resolution settings [11]. In high-resolution mode, frequencies are measured with a resolution of 0.1 GHz, at a rate of 1 second per point. In low-resolution mode, frequencies are measured at a rate of 0.33 seconds per point, with 1 GHz resolution. Consequently, the measurement time for this first stage can already be reduced by a factor of 3. With the same number of grid points as above, the measurement time becomes $25 \times 25 \times 0.33$ s ≈ 200 s. The measurement data is again fitted by relation (5.4) to calculate the front and rear reflector currents for the channel frequencies. Since the wavelength locker only provides reference points at integer multiples of 100 GHz, only these frequencies will be considered here.

For each channel, the phase current is then scanned across a few values (typically 5). The frequency is measured at each point in order to determine a suitable starting value for the phase current, which is calculated through linear interpolation between the measurement points. This measurement step only takes about 2 seconds per channel. Hence, a crude look-up table is found in a matter of a few minutes.

To obtain a more accurate look-up table, the laser is sequentially tuned to each of the operation points calculated above. Subsequently, the control loop described in §4.3 is started and is left running until the control currents stabilise. With the present (slow) implementation of the control circuit, this takes 20 to 30 seconds per channel. The currents obtained after stabilisation replace the original estimated values in the look-up table. An important added benefit is that output power can now be equalised to a pre-set value. The control loop can monitor the output power and adjust the active section current accordingly so as to compensate for the absorption losses in the tuning sections.

Figure 5.17 shows an example of the look-up table that is obtained after the automatic update of the initial approximate table. Operation points were found for 41 channels on the 100 GHz ITU grid, with frequencies ranging from 191.9 to 195.9 THz. The output power was equalised at approximately 0.5 mW.

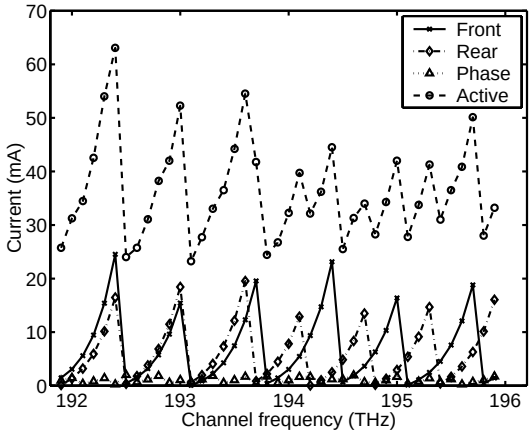

Figure 5.17 Plot of the look-up table obtained after stabilisation at each channel using the feedback loop from §4.3. Operation points were found for 41 channels on the 100 GHz ITU grid, with frequencies ranging from 191.9 to 195.9 THz and with an output power of approximately 0.5 mW.

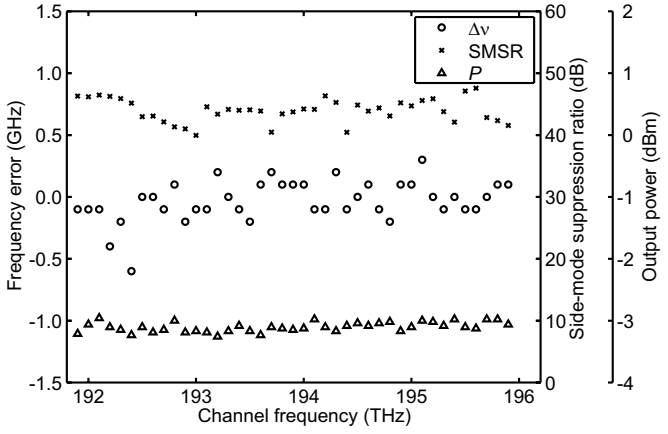

Figure 5.18 Frequency errors (○), side-mode suppression ratios (×) and output powers (Δ) measured for the look-up table plotted in Figure 5.17.

Figure 5.17 clearly reveals the strong correlation between the active section current and the tuning currents. Figure 5.18 plots the frequency errors, side-mode suppression ratios, and output powers measured for the operation points from Figure 5.17. The frequency errors are significantly lower than 1.0 GHz and the SMSR is always above 40 dB. The frequency accuracy is in this case of course largely determined by the accuracy of the wavelength locker in the control system. Although the specified accuracy of the locker is only ±2.5 GHz, we managed to reduce that to less than ±1.0 GHz through calibration of the locker response (cf. Chapter 4).

The output power varies by less than 0.5 dB across the different channels. This is obviously much lower than the 7 dB power variation that was measured in the previous section when the active section current was kept at a constant level. The remaining power variation is probably due to the frequency dependence of the photodiode P_1 and the two power splitters inside the wavelength locker (cf. Figure 4.41).

The procedure however still has a few drawbacks. Operator intervention is still required in the first stage to initialise the fit parameters from (5.4) with suitable values. Also, operation points can only be found for frequencies that lie on the grid determined by the wavelength locker in the control loop.

5.4 Locating operation points by minimising the active section voltage

According to the results from Chapter 4, minimising the active section voltage of a SSG-DBR laser as a function of the front and rear reflector currents guarantees that the laser's emission spectrum will be single-mode. In the algorithm described below we use this property to map out suitable operation points in the 3-dimensional space of front DBR, rear DBR, and phase currents. Actual frequency measurements are only performed for the resultant set of optimised operation points, which are grouped per cavity mode. Finally, the tuning currents for any frequency within the tuning range of the device can be calculated by interpolating between the stored operation points.

Figure 5.19 gives a schematic overview of the procedure. In the following paragraphs we will discuss each of the steps in more detail.

Initialisation

The algorithm requires the knowledge of three initialisation parameters. First, an estimate is needed of the maximum currents that will have to be applied to the front and rear DBR sections in order to achieve full frequency coverage ($I_{front,max}$ and $I_{rear,max}$). Secondly, the phase current required to get a 2π phase-shift has to be determined ($I_{phase,2\pi}$). In other words, this phase current tunes all cavity modes over a distance equal to the mode spacing. Reasonable estimates for these currents can be derived from fairly simple measurements (Figure 5.20).

Full frequency coverage requires that the rear (front) reflector is at least tuned over a range equal to its reflectivity peak spacing. The current $I_{rear,max}$ ($I_{front,max}$) needed to do so is found by setting the front and rear reflector currents to 0 and then gradually increasing the rear (front) reflector current, while monitoring the emission frequency. The frequency will then increase (decrease) step-wise with jumps of about 0.6 THz as subsequent pairs of reflector peaks become aligned (cf. Figure 5.1). At a certain point, the frequency jumps down (up) to the other end of the tuning range, after which it starts increasing (decreasing) again. The current $I_{rear,max}$ ($I_{front,max}$) is reached when the frequency has again crossed its initial value (i.e. at zero tuning currents, Figure 5.20(a)).

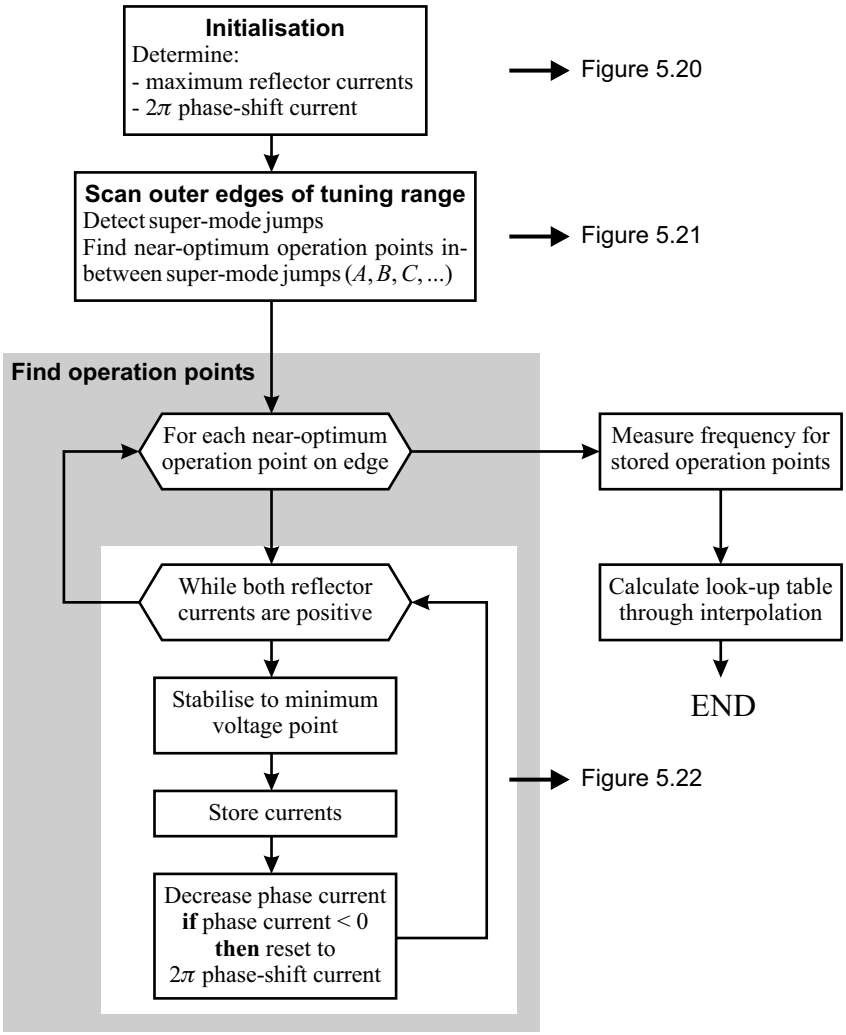

Figure 5.19 Flow-chart of the look-up table generation routine based on minimisation of the active section voltage.

In principle, the frequency can be measured with a wavelength meter. This is however certainly not necessary, since a frequency resolution of 0.2 to 0.3 THz would be more than sufficient and no absolute frequency accuracy is required at all. To speed up the measurements, it would therefore be advantageous to translate the frequency variations into power variations using a fairly simple frequency-discriminating filter and use (much faster) power measurements to detect the super-mode hops [12]. It is often a good idea to increase the value of $I_{rear,max}$ ($I_{front,max}$) obtained in this way by e.g. 10%. A larger value will indeed only yield some redundancy, whereas a too small value will result in gaps in the tuning range.

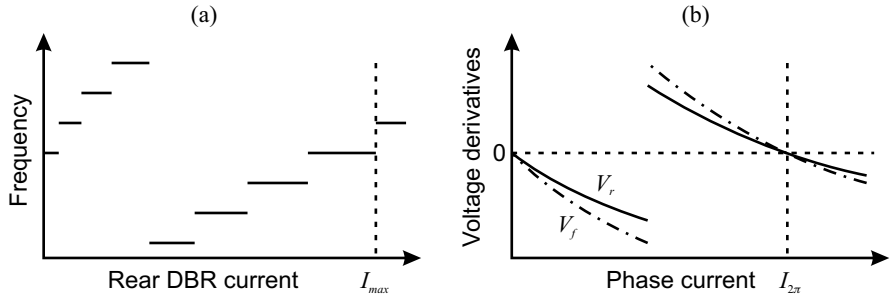

Figure 5.20 Initialisation of the procedure: determine the maximum front and rear reflector currents $I_{front,max}$ and $I_{rear,max}$ (a) and the 2π phase-shift current $I_{phase,2\pi}$ (b).

To determine the 2π phase-shift current, the phase current is first set to zero and the reflector currents are initialised to a local minimum in active section voltage somewhere in the middle of the tuning range. This point can for example be obtained by setting the front and rear reflector currents to half their maximum values, and have the voltage feedback loop stabilise the reflector currents on the closest voltage minimum, which requires that the voltage modulation components V_f and V_r (cf. Figure 4.41) are brought to zero[1]. Subsequently, the feedback loop is switched off and the phase current is gradually increased, while monitoring the signals V_f and V_r (Figure 5.20(b)). The cavity mode will then move away from the aligned reflector peaks towards higher frequencies, which means that the signals V_f and V_r will become negative ($|V_f|$ and $|V_r|$ will increase). At a certain point, an adjacent cavity mode will become the preferential mode and a mode hop will occur, causing the signals V_f and V_r to suddenly change sign. From that moment on, $|V_f|$ and $|V_r|$ will decrease again with increasing phase current. The 2π phase-shift current is reached when V_f and V_r reach zero again. As for the reflector currents, some error margin can be built-in by taking a value for $I_{phase,2\pi}$ that is somewhat larger than the value found in the measurement.

Scanning the outer edges of the tuning range

After determining the maximum tuning currents, the outer edges of the tuning range are scanned to locate the super-mode jumps, i.e. frequency jumps of more than 0.5 THz (cf. Figure 5.1). The rear reflector current is set to $I_{rear,max}$ and the front reflector current is increased stepwise from 0 to $I_{front,max}$. Subsequently, I_{front} is kept constant and I_{rear} is reduced stepwise to 0 (Figure 5.21). In every point, the frequency is measured at zero phase current. At present, a wavelength meter is used, but since the only purpose is to locate the super-mode jumps, a coarse frequency measurement with a frequency-discriminating filter would again be sufficient.

For each super-mode a good starting point is then located, i.e. a point where a cavity mode and the two reflector peaks corresponding to that super-mode are more or less aligned.

[1] Remember that the signals V_f and V_r, are proportional to the derivatives of the active section voltage with respect to the front and rear reflector current, respectively.

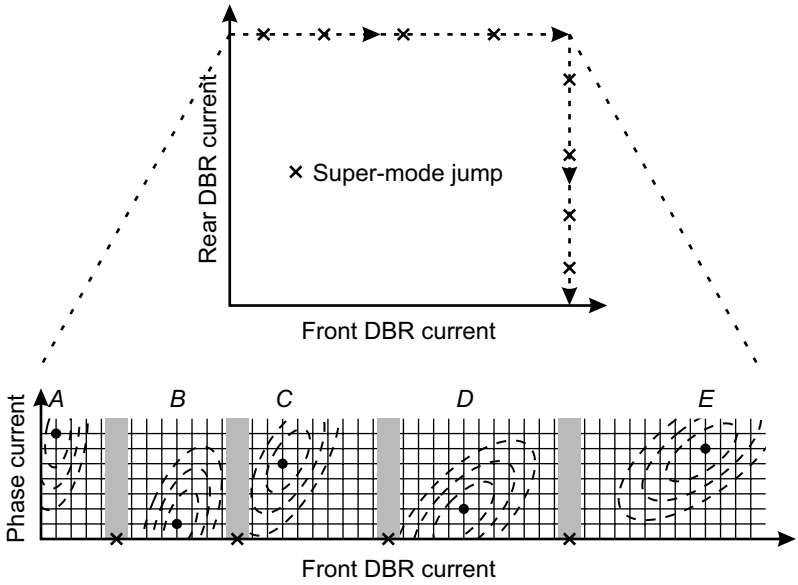

Figure 5.21 Scanning the outer edges of the tuning range to locate good starting points within each super-mode. In between super-mode jumps the combination of phase and reflector current is selected which minimises the misalignment between the lasing mode and the two reflectivity peaks for that super-mode (schematically represented by the contour plot at the bottom).

Since either the front or the rear reflector current is fixed, the two degrees of freedom are the phase current and the variable reflector current. For each value of the variable reflector current in between two super-mode jumps, the phase current is scanned from 0 to $I_{phase,2\pi}$ and the voltage modulation components V_f and V_r are measured (for the SSG-DBR lasers considered here, the phase current was varied from 0.01 to 1.90 mA in 0.27 mA steps). Among the (I_{front}, I_{rear}, I_{phase})-triplets belonging to a particular super-mode the algorithm then selects the point that minimises following trial function (cf. Figure 5.21):

$$T\left(I_{front}, I_{rear}, I_{phase}\right) = I_{front} \cdot V_f^2 + I_{rear} \cdot V_r^2 \tag{5.10}$$

This function was chosen because V_f can be calculated as:

$$V_f = \frac{\partial V_{active}}{\partial I_{front}} \Delta I_{front} = \frac{\partial V_{active}}{\partial \nu_{front}} \frac{\partial \nu_{front}}{\partial N_{front}} \frac{\partial N_{front}}{\partial I_{front}} \Delta I_{front} \tag{5.11}$$

Here, ν_{front} is the frequency of the selected front mirror reflectivity peak, N_{front} is the carrier density in the front reflector section, and ΔI_{front} is the modulation component of the front reflector current. Near the point of optimum alignment, the variation of the active section voltage as a function of the misalignment between the cavity mode and the reflectivity peaks ($\Delta\nu_f$ and $\Delta\nu_r$ respectively) can be approximated by a parabola.

$$V_{active} = V_0 + a\left[\left(\Delta\nu_f\right)^2 + \left(\Delta\nu_r\right)^2\right] \tag{5.12}$$

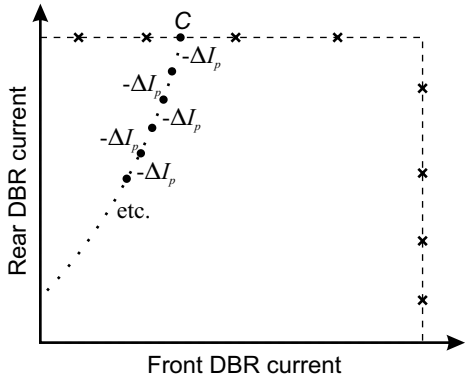

Figure 5.22 Tracking cavity modes in the (I_{front}, I_{rear})-plane with decreasing phase current. When the phase current reaches 0, it is reset to the 2π phase-shift value, such that the adjacent lower-frequency cavity mode is aligned with the coincident reflectivity peaks and becomes the lasing mode.

As a result, $\partial V_{active}/\partial \nu_{front}$ is proportional to the frequency misalignment between the cavity mode and the reflectivity peak $\Delta\nu_f$:

$$\frac{\partial V_{active}}{\partial \nu_{front}} \propto \Delta\nu_f \tag{5.13}$$

Since $\partial \nu_{front}/\partial N_{front}$ can be assumed constant, and to a good approximation $I_{front} \propto (N_{front})^2$, we finally obtain:

$$V_f = C_f \cdot \Delta\nu_f \frac{\Delta I_{front}}{\sqrt{I_{front}}} \tag{5.14}$$

Here C_f is a constant. An analogous relation can be written down for V_r. If $C_f \approx C_r \approx C$ and $\Delta I_{front} = \Delta I_{rear} = \Delta I$, (5.10) becomes:

$$T\left(I_{front}, I_{rear}, I_{phase}\right) \approx (C\Delta I)^2 \left[\left(\Delta\nu_f\right)^2 + \left(\Delta\nu_r\right)^2\right] \tag{5.15}$$

This function should obviously be minimised to obtain a good operation point.

If this search procedure is repeated for all the regions between two subsequent super-mode hops, a number of near-optimum operation points *A*, *B*, *C*, ... is obtained on the outer edge of the tuning range (Figure 5.21).

Find operation points

In the core part of the algorithm (Figure 5.19), an iterative procedure is started for each of these near-optimum points *A*, *B*, *C*, ... The tuning currents are initialised to the selected values and the voltage minimising feedback loop is started. The following steps are then repeated until either I_{front} or I_{rear} reaches the lower limit of 0.1 mA:

- Wait until I_{front} and I_{rear} have stabilised.
- Store the values of the different currents.

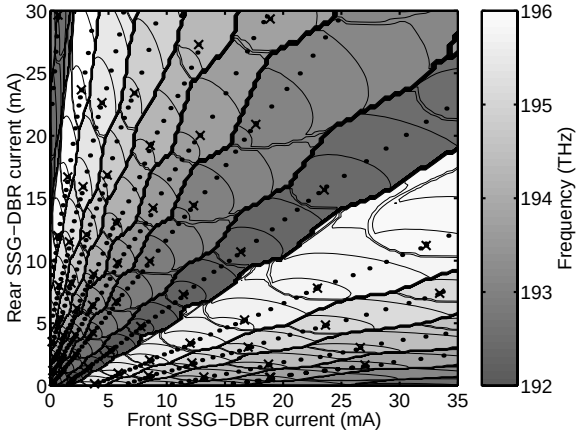

Figure 5.23 Scatter plot of optimum operation points in the (I_{front}, I_{rear})-plane for various phase currents (·) and zero phase current (×), superimposed on a frequency contour map measured at zero phase current. The active section current was kept constant at 60 mA.

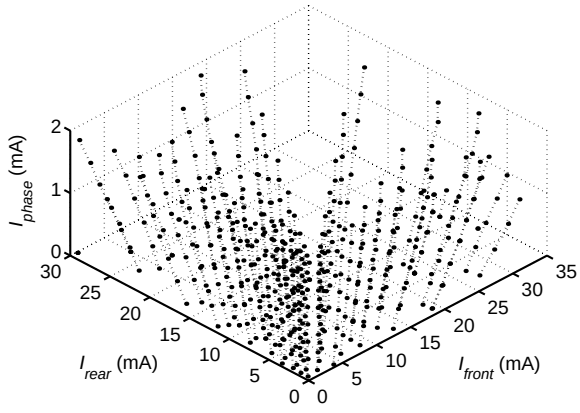

Figure 5.24 Scatter plot of optimum operation points in the three-dimensional space of front reflector, rear reflector, and phase currents. The dotted lines connect operation points belonging to the same cavity mode.

- Reduce the phase current (e.g. by 0.27 mA). If I_{phase} would become negative, then reset it to $I_{phase,2\pi}$ (≈ 1.90 mA).

In this way, a cavity mode is tracked in the (I_{front}, I_{rear})-plane as the phase current is decreased (Figure 5.22). When the phase current reaches 0, it is reset to the 2π phase-shift value, such that the adjacent lower-frequency cavity mode is aligned with the coincident reflectivity peaks and becomes the lasing mode. In the end, a table of optimum operation points covering the entire tuning range of the laser is obtained. Figure 5.23 shows a scatter plot of these points in the (I_{front}, I_{rear})-plane, superimposed on a frequency contour map measured at zero phase current (crosses

indicate the operation points with $I_{phase} = 0$ mA). The acquired points nicely line up to build tracks between two super-mode jumps. In the 3D space of tuning currents, they form tracks describing the continuous tuning of individual cavity modes (Figure 5.24). The ensemble of these cavity modes covers the entire tuning range of the device.

Building the look-up table

In the final stage, the emission frequency is measured for all the points plotted in Figure 5.23 and Figure 5.24. The look-up table is then derived from the measured values as follows. The operation points that were found are grouped per individual cavity mode and stored in a table together with the measured frequencies. For a given frequency, all the cavity modes that can be tuned to this frequency are searched, which is done by verifying whether the desired frequency lies between the minimal and maximal frequency measured for a certain cavity mode. If multiple solutions are found, the cavity mode that can be tuned to the desired frequency with minimal total tuning current is retained, since a minimal sum of the tuning currents will yield the lowest absorption losses. The actual values of the tuning currents are obtained by interpolating between the operation points of the selected mode that are stored in the measurement table. Since the frequency varies sub-linearly as a function of the tuning currents, a cubic interpolation scheme is applied.

Actually, the procedure can be taken one step further. As it is described above, the algorithm implicitly assumes a fixed active section current. This means that the look-up table that is generated will show large output power variations across the different operating points due to the carrier-induced losses in the passive sections. However, since the algorithm uses feedback control to find optimum operation points, a power control loop can easily be added. This loop can run in parallel with the voltage-minimising loop and continually adjust the active section current to maintain a pre-set output power (cf. Figure 4.41).

Experimental results

Figure 5.25 shows an example of a look-up table that was generated using the procedure outlined above, with power equalisation included. The output power was stabilised at approximately –3 dBm. Currents were calculated for frequencies from 191.9 to 196.1 THz in 1 GHz steps. Due to the power equalisation, the active section current varies quite significantly, from 20 to 75 mA. There is an evident correlation between the active section current and the three tuning currents, of which the front reflector current has the strongest effect. For the (I_{front}, I_{rear}, I_{phase})-triplets in the table, the threshold currents range from 7 to 19 mA.

When the look-up table is verified, excellent frequency accuracy and side-mode suppression ratio are obtained for all points. Frequency errors are less than ±0.5 GHz and the SMSR is always above 35 dB, mostly even above 40 dB (Figure 5.26). The root-mean-squared frequency error is typically less than 0.15 GHz. With such low errors, applications in DWDM systems with a channel separation of 25 GHz or even 10 GHz become feasible.

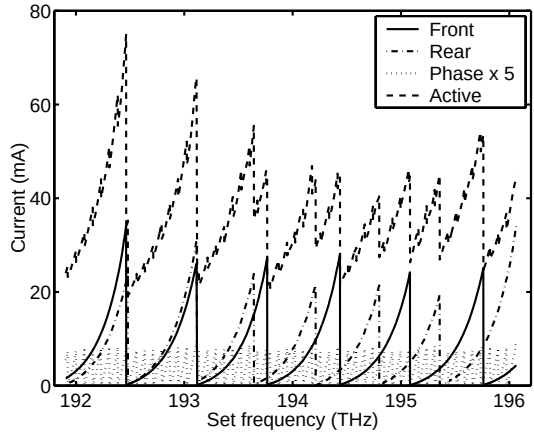

Figure 5.25 Plot of an automatically generated look-up table. Currents were calculated for frequencies ranging from 191.9 to 196.1 THz in 1 GHz increments.

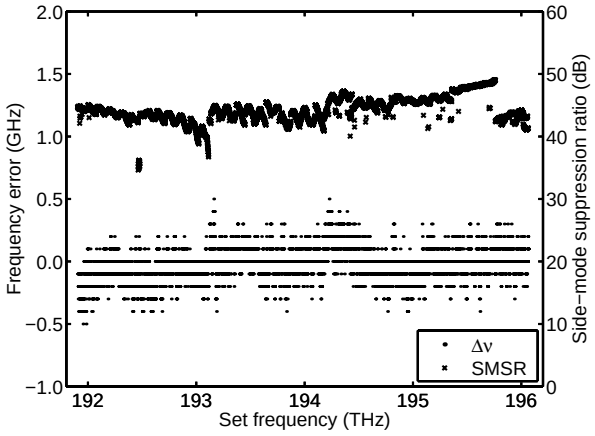

Figure 5.26 Frequency errors and side-mode suppression ratios measured for the look-up table plotted in Figure 5.25.

The measured frequency accuracy is mostly limited by the wavelength meter used in the experiments (HP86120B multi-wavelength meter [11]). It is already evident from Figure 5.26 that the resolution of the wavelength meter is only 0.1 GHz. The data-sheet of the instrument specifies an absolute accuracy of ±3 p.p.m. (±0.6 GHz), and a differential accuracy of ±2 p.p.m. (±0.4 GHz).

Nevertheless, low frequency errors also require a very accurate temperature control, which completely counteracts variations of the environmental temperature. A temperature variation of the laser of only 0.02 °C would already yield a frequency difference of about 0.25 GHz.

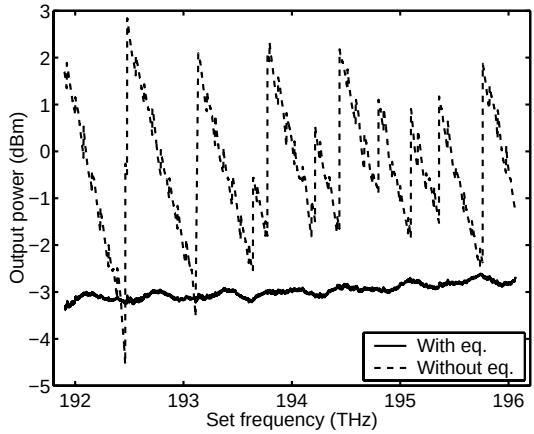

Figure 5.27 Output powers measured for the look-up table plotted in Figure 5.25, i.e. with power equalisation (solid line), as well as for a look-up table that was generated without power equalisation (dashed line). In the latter case, the active section current was kept constant at 60 mA.

It was noted for example that measurements of the same look-up table at different times of the day could yield an average frequency error anywhere in the range from –0.3 GHz to +0.3 GHz. Typically, the ambient temperature in the lab varied by several degrees over a period of 24 hours. Even if the temperature control of the laser would reduce the temperature variations inside the laser package by a factor of 100, these ambient temperature variations would cause sufficient tuning to explain the measured variations of the average frequency error.

It is also essential to use the current sources that will eventually drive the laser in the finished module already at the characterisation stage, in order to eliminate errors due to inaccuracies of the current sources as much as possible. The current sources used in the experiments have a resolution of 3 μA for the phase current, and 8 μA for the reflector currents. Multiplied by the tuning efficiencies at low currents this leads to frequency resolutions on the order of 0.2 GHz. When Figure 5.26 is compared to Figure 5.25, it is clear that the largest frequency errors are obtained when the tuning currents are lowest.

As Figure 5.27 illustrates, the power variation has been reduced to less than 0.8 dB; a reduction by almost a factor of ten compared to the situation where no power control is applied. The remaining power variation is again probably due to the frequency dependence of the photodiode P_1 and the two power splitters inside the wavelength locker (cf. Figure 4.41).

The characterisation time needed to generate a full look-up table is currently about 150 minutes with power control and 100 minutes without. However, as mentioned in Chapter 4, the present feedback loop is still relatively slow since discrete instruments are used, which are controlled by a program running on a PC. It is expected that characterisation time will be drastically reduced if these instruments are replaced by electronic circuitry integrated on a single board and controlled by a microprocessor.

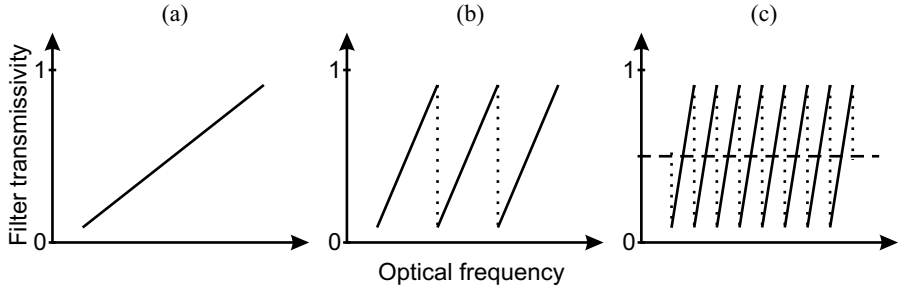

Figure 5.28 Frequency referencing filters with increasing resolution.

The first stage of the procedure, where operation points are located using the control loop, can then in principle run completely autonomously. As mentioned in §5.1, the measurement time is in that case not so critical, since many devices can be processed in parallel. Still, we estimate that with properly designed electronics, a measurement time of less than 30 minutes is certainly feasible.

In the end, the main limitation will be the time needed for frequency measurements. In general, the procedure generates a list of 500 to 600 operation points for which the frequency has to be measured. Since a frequency measurement takes 1 second, the lower limit for the characterisation time is 10 minutes.

The characterisation procedure described here could be extended into a fully automatic calibration procedure, where all frequency measurements are replaced by filtered optical power measurements using a set of filters with transmissivities as sketched in Figure 5.28. The first filter provides a coarse frequency measurement, as is needed to identify super-mode hops. Subsequent filters are periodic and have a decreasing free spectral range. These will hence provide a progressively higher frequency resolution, although the previous filters will be needed to be able to discern between the different periods of the filter. The highest resolution filter has the same periodicity as the desired frequency grid. This could for example be the wavelength locker used in Chapter 4. Using such filters, the look-up table for the desired frequency grid could be derived in a straightforward way from the set of operation points that was found by the algorithm (Figure 5.23 and Figure 5.24).

5.5 Conclusion

In this chapter three characterisation procedures for the generation of a frequency look-up table were presented. Section 5.1 defined the criteria by which the different algorithms should be compared. The generated look-up tables should naturally yield high frequency accuracy, high side-mode suppression ratio and preferably a high degree of power uniformity across the tuning range. Additionally, characterisation time and operator intervention should be minimised to allow the production of low-cost tunable laser modules.

In the first procedure, we tried to reduce the number of frequency measurements by applying curve fitting (§5.2). This brought the total characterisation time down to about one hour. This approach however still has quite some disadvantages: a wavelength meter is needed throughout the entire procedure, intervention of an operator is required to pick good initial estimates for the fit parameters and the frequency errors are still quite large (several GHz).

In the procedure described in §5.3, the first curve-fitting step of the previous method is used to generate a very coarse look-up table. This table is subsequently updated using the feedback control system from Chapter 4. This yields both a higher frequency accuracy (±1.0 GHz) and a shorter characterisation time. On the other hand, operator intervention is still required and operation points can only be found for a small set of frequencies, determined by the frequency reference in the control loop.

By using the mode stabilisation loop developed in Chapter 4 to map out suitable operation points in the 3-dimensional space of front DBR, rear DBR, and phase currents, the characterisation can be made entirely automatic (§5.4). In the end, the emission frequency then only has to be measured for these – already optimised – operation points, after which a look-up table can be calculated by straightforward interpolation. With this method, we have demonstrated excellent frequency accuracy (less than ±0.5 GHz) for any arbitrary frequency grid, with SMSR values of at least 35 dB. We believe that the measured frequency accuracy is mainly limited by the accuracy of our wavelength meter, so there is possibly still room for improvement. Moreover, the algorithm allows equalising the output power across the tuning range, with measured power variations well below 1 dB. With the current configuration of the feedback control system (cf. Chapter 4), the procedure is still rather slow. By developing dedicated control electronics, it should however be possible to reduce the total characterisation time to less than 30 minutes – the ultimate limit being the 10 minutes required for frequency measurements.

References

[1] International Telecommunication Union – Telecommunication Standardization Sector (ITU-T), Recommendation G.692: "Optical interfaces for multichannel systems with optical amplifiers," Series G: Transmission systems and media, digital systems and networks (Transmission media characteristics – Characteristics of optical components and sub-systems), October 1998.

[2] G. Sarlet, G. Morthier, T. Farrell, J. Dunne, P.-J. Rigole, H. Ishii, and D.J. Robbins, "Feasibility demonstration of control methods for modules in the network demonstrator," Project Deliverable ACTS-AC329 ACTUAL, CEC deliverable no. AC329/IMEC/UG/DR/L/002/b1, December 1998.

[3] G. Sarlet, G. Morthier, H. Ishii, T. Farrell, and P.-J. Rigole, "Report on comparison of advanced look-up table and feedback based control methods," Project Deliverable ACTS-AC329 ACTUAL, CEC deliverable no. AC329/IMEC/UG/DR/P/007/b1, October 1999.

[4] N.P. Caponio, M. Goano, I. Maio, M. Meliga, G.P. Bava, G. Destefanis, and I. Montrosset, "Analysis and design criteria of three-section DBR tunable lasers," *IEEE J. Selected Areas in Commun.*, vol. 8, no. 6, pp. 1203-1213, August 1990.

[5] J.A. Nelder, and R. Mead, "A Simplex Method for Function Minimization," *Computer Journal*, vol. 7, pp. 308-313, 1964.

[6] H. Ishii, F. Kano, Y. Yoshikuni, and H. Yasaka, "Mode stabilization method for superstructure-grating DBR lasers," *J. Lightwave Technol.*, vol. 13, no. 3, pp. 433-442, March 1998.

[7] M.-C. Amann, and J. Buus, *Tunable laser diodes*, Artech House, Norwood, MA, USA, 1998.

[8] G. Sarlet, G. Morthier and R. Baets, "A characterisation-efficient procedure for setting the wavelength of widely tunable lasers," *Proceedings IEEE/LEOS Benelux Symposium '98*, pp. 21-24, Gent, Belgium, November 1998.

[9] A. Tsigopoulos, T. Sphicopoulos, I. Orfanos, and S. Pantelis, "Wavelength tuning analysis and spectral characteristics of three-section DBR lasers," *IEEE J. Quantum Electron.*, vol. 28, no. 2, pp. 415-426, February 1992.

[10] W.M. Steffens, and M.-C. Amann, "Effect of internal reflections on wavelength access in widely tunable laser diodes," *IEEE J. Quantum Electron.*, vol. 34, no. 9, pp. 1698-1705, September 1998.

[11] HP86120B multi-wavelength meter, Agilent Technologies – Test & Measurement, 5301 Stevens Creek Blvd., Santa Clara, CA 95052, USA. < http://www.tm.agilent.com/>

[12] T. Farrell, J. Dunne, and R. O'Dowd, "Complete wavelength control of GCSR lasers over EDFA band," *Proc. LEOS '99*, pp. 329-330, paper TuY1, San Francisco, CA, USA, November 1999.

[13] G. Sarlet, G. Morthier, and R. Baets, "Control of widely tunable SSG-DBR lasers for dense wavelength division multiplexing," *J. Lightwave Technol.*, vol. 18, no. 8, pp. 1128-1138, August 2000.

Chapter 6

Modulation properties of tunable lasers

In most present-day fiber-optic communication systems digital data is transmitted by simple on/off keying of an optical carrier wave generated by a laser diode. The data can be encoded on the carrier wave either by direct modulation of the laser's gain current or by using an external modulator.

The obvious advantage of the first approach is the lower cost. Unfortunately, modulation of the current not only yields a variation of the output power, but also of the optical frequency (frequency chirp). Significant frequency excursions occur at the leading and trailing edges of an optical pulse generated through direct modulation. Due to the dispersion of the optical fiber, i.e. the frequency-dependence of the propagation velocity, different parts of the emitted pulses will therefore travel at different speeds. The pulses will broaden with distance, eventually leading to transmission errors when a pulse representing a digital one spills over into a digital zero. As a rule of thumb, dispersion adversely affects a data stream linearly with the transmission distance, but as a square of the bit-rate [1]. Direct modulation is therefore only applied for modest bit-rates (up to 2.5 Gbit/s) and transmission distances (less than 100 km).

On the other hand, external modulators exist than can vary the intensity of a light-beam essentially without adding any chirp. This second solution is hence preferred for higher bit-rates and longer transmission distances.

Obviously, the bit-rates achievable with direct modulation are also limited by the modulation bandwidth of the laser diode. For DFB lasers modulation bandwidths of more than 30 GHz have been demonstrated [2]-[3], which should in principle allow direct modulation at speeds of 10 Gbit/s and more. For tunable lasers, it is expected however that the longer cavity will lead to reduced modulation bandwidths. So far, only few results have been published on the modulation characteristics of tunable lasers [4]-[11]. In this chapter, first some theoretical calculations on the small-signal behaviour of these lasers are presented. Subsequently, experimental results obtained for SSG-DBR and GCSR lasers, both for small-signal and (digital) large-signal modulation, are summarised.

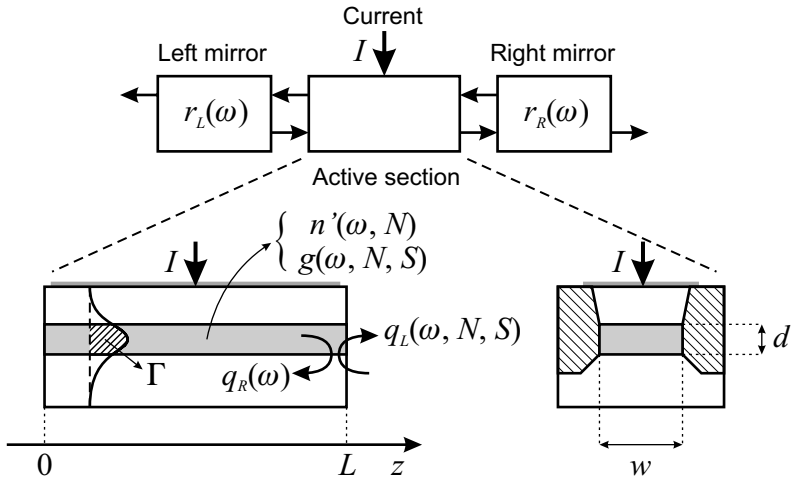

Figure 6.1 Cavity model for longitudinally integrated tunable lasers with passive tuning sections (cf. Chapter 3). $q_L(\omega,N,S)$ and $q_R(\omega)$ represent the effective reflection coefficients for the left- and right-propagating wave at the reference plane, which is located at the right end of the active section just before the interface with the passive section ($z = L^-$).

6.1 Theoretical analysis

6.1.1 Small-signal rate equations

The goal in this section is to derive a set of rate equations describing the small-signal modulation behaviour of a (tunable) laser diode with integrated passive sections. The approach followed here is based on the analysis presented in [12]-[13]. As in Chapter 3, the complex tunable laser cavity is described as an active section that is bounded by two mirrors with frequency-dependent reflectivities $r_L(\omega)$ and $r_R(\omega)$ (Figure 6.1). We assume that the active section waveguide only guides the fundamental transverse mode $\phi_0(x,y)$. Furthermore, it is assumed that the laser oscillates in a single longitudinal mode. The Fourier transform of the electric field $E(x,y,z,t)$ can then be written as:

$$E_\omega(z)\phi_0(x,y) = \int_{-\infty}^{+\infty} E(x,y,z,t)e^{-j\omega t}dt \tag{6.1}$$

The field $E_\omega(z)$ can be decomposed into left- and right-travelling fields:

$$E_\omega(z) = E_\omega^+(z) + E_\omega^-(z) \tag{6.2}$$

A reference plane is chosen at the right end of the active section, just before the interface with the passive section ($z = L^-$). If we define $q_L(\omega,N,S)$ and $q_R(\omega)$ as the effective reflection coefficients for the left- and right-propagating wave at this plane, we find:

$$E_\omega^-(L) = q_R(\omega)E_\omega^+(L) = r_R(\omega)E_\omega^+(L) \tag{6.3}$$

and
$$\begin{aligned} E_\omega^+(L) &= q_L(\omega, N, S)E_\omega^-(L) + F_L(\omega) \\ &= r_L(\omega)e^{-j2Lk(\omega,N,S)}E_\omega^-(L) + F_L(\omega) \end{aligned} \tag{6.4}$$

where
$$k(\omega, N, S) = \frac{\omega}{c}n(\omega, N) + \frac{j}{2}\left[\Gamma g(\omega, N, S) - \alpha_{\text{int}}\right] \tag{6.5}$$

and $F_L(\omega)$ is a Langevin noise term, which accounts for the spontaneous emission in the active section. Compared to (3.2), we have included the possibility of a gain non-linearity by making the gain g dependent on the number of photons in the active section S. In general, the gain will be reduced at high photon numbers (due to spectral hole-burning, carrier heating, ... [2]-[3]), which is commonly described as:

$$g(\omega, N, S) \approx \frac{g(\omega, N, 0)}{1 + \varepsilon_S S} \approx g(\omega, N, 0)(1 - \varepsilon_S S) \tag{6.6}$$

Here ε_S is the gain-suppression coefficient related to the photon number S. The photon number dependence of the gain can be linearised, since the term $\varepsilon_S S$ is much smaller than 1. Often, the gain suppression is expressed as a function of the average power inside the active section P, with a gain-suppression coefficient ε_P that is related to ε_S as:

$$\varepsilon_S = v_g \hbar\omega \frac{1}{L}\varepsilon_P \tag{6.7}$$

A typical value for ε_P is 2 W^{-1}. By combining the boundary conditions (6.3) and (6.4), we find the basic field equation:

$$\left[1 - q_L(\omega, N, S)q_R(\omega)\right]E_\omega^+(L) = F_L(\omega) \tag{6.8}$$

In steady state (above threshold), the noise term can be neglected, which yields the oscillation condition for the stationary solution (ω_s,N_s,S_s):

$$q_L(\omega_s, N_s, S_s)q_R(\omega_s) = 1 \tag{6.9}$$

Under dynamic conditions, the frequency, the carrier density, and the photon number are assumed to be close to their stationary values, such that we can use a first order Taylor-expansion for $q_L \cdot q_R$ in (6.8):

$$\begin{aligned} & q_L(\omega, N, S)q_R(\omega) - 1 \\ & \approx \left(\frac{\partial q_L}{\partial \omega}q_R\bigg|_s + q_L\frac{\partial q_R}{\partial \omega}\bigg|_s\right)\Delta\omega + \frac{\partial q_L}{\partial N}q_R\bigg|_s \Delta N + \frac{\partial q_L}{\partial S}q_R\bigg|_s \Delta S \\ & = \frac{\partial \ln(q_L q_R)}{\partial \omega}\bigg|_s \Delta\omega + \frac{\partial \ln(q_L)}{\partial N}\bigg|_s \Delta N + \frac{\partial \ln(q_L)}{\partial S}\bigg|_s \Delta S \end{aligned} \tag{6.10}$$

where $\Delta X = X - X_s$. The limitations of this approximation will be discussed in the next section by comparing the results derived with the present analysis to results obtained with a more rigorous dynamic laser model [14]-[15]. In what follows the notation $|_s$, indicating that partial derivatives should be calculated in the stationary operation point, is omitted. If we define the (complex) time constant τ as:

$$\frac{\partial \ln(q_L q_R)}{\partial \omega} = -j\tau \tag{6.11}$$

then (6.8) becomes

$$\left[j\tau\Delta\omega - \frac{\partial \ln(q_L)}{\partial N}\Delta N - \frac{\partial \ln(q_L)}{\partial S}\Delta S \right] E_\omega^+(L) = F_L(\omega) \tag{6.12}$$

Next, the envelope function $A^+(t)$ of the right travelling wave at the reference plane and the noise function $F(t)$ are defined as follows:

$$A^+(t)e^{j\omega_s t} = \frac{1}{2\pi}\int_{-\infty}^{+\infty} E_\omega^+(L)e^{j\omega t}d\omega \tag{6.13}$$

$$F(t)e^{j\omega_s t} = \frac{1}{2\pi\tau}\int_{-\infty}^{+\infty} F_L(\omega)e^{j\omega t}d\omega \tag{6.14}$$

In the quasi-stationary approximation, i.e. assuming that A^+, N, and S vary slowly relative to the optical frequency ω, (6.12) then can be converted to:

$$\frac{dA^+}{dt} - \frac{1}{2}(Q_N\Delta N + Q_S\Delta S)A^+ = F(t) \tag{6.15}$$

where

$$Q_X = \frac{2}{\tau}\frac{\partial \ln(q_L)}{\partial X} = Q_{X,r} + jQ_{X,i} \tag{6.16}$$

Here $Q_{X,r}$ and $Q_{X,i}$ are the real and imaginary part of Q_X. In [4] it was shown that the photon number S and the envelope function A^+ are related as:

$$S(t) = \sigma(\omega_s, N_s, S_s)\left|A^+(t)\right|^2 \tag{6.17}$$

or

$$\sqrt{\sigma}\,A^+(t) = \sqrt{S(t)}e^{j\varphi(t)} \tag{6.18}$$

where σ is a proportionality factor that depends on the stationary solution (ω_s,N_s,S_s). By multiplying (6.15) with 2σ times the complex conjugate of A^+ we find:

$$\frac{dS}{dt} + 2jS\frac{d\varphi}{dt} - (Q_N\Delta N + Q_S\Delta S)S = R_{sp}(N) + F_S(t) + 2jSF_\varphi(t) \tag{6.19}$$

As in [16], the noise term has been decomposed as follows:

$$2\sigma F(t)\left[A^+(t)\right]^* = R_{sp}(N) + F_S(t) + 2jS(t)F_\varphi(t) \tag{6.20}$$

where $F_S(t)$ and $F_\varphi(t)$ are (real) Langevin functions with zero mean and R_{sp} is the average spontaneous emission rate into the lasing mode. By separating (6.19) into the real and the imaginary part, and complementing it with the carrier rate equation (cf. (3.14), for a single longitudinal mode and with an added carrier noise term $F_N(t)$), we finally obtain following set of equations:

$$\begin{aligned} \frac{dS}{dt} - (Q_{N,r}\Delta N + Q_{S,r}\Delta S)S &= R_{sp}(N) + F_S(t) \\ \frac{d\varphi}{dt} - \frac{1}{2}(Q_{N,i}\Delta N + Q_{S,i}\Delta S) &= F_\varphi(t) \\ \frac{dN}{dt} + R(N) + G\frac{S}{V_a} &= \frac{I}{qV_a} + F_N(t) \end{aligned} \tag{6.21}$$

where

$$G = v_g\Gamma g(\omega_s, N, S) \tag{6.22}$$

and $$R(N) = AN + BN^2 + CN^3 \qquad R_{sp}(N) = \beta_{sp} BN^2 V_a \tag{6.23}$$

It is usually assumed that the laser system is Markovian, i.e. that the random forces F_p have no memory and their auto-correlation function is a delta function [16]:

$$\left\langle F_p(t) F_q^*(t') \right\rangle = 2D_{pq}\delta(t - t') \tag{6.24}$$

The coefficients D_{pq} are the so-called diffusion coefficients.

6.1.2 Small-signal AM and FM frequency response

From the rate equations (6.21) we will now derive the small-signal amplitude- and frequency modulation (AM and FM) responses. To this end, we write the drive current I as the sum of the stationary value I_s and a small modulation $\delta I(t)$:

$$I(t) = I_s + \delta I(t) \tag{6.25}$$

Similarly, the state variables S, φ, and N are written as:

$$\begin{aligned} S &= S_s + \delta S(t) & \varphi &= \delta\varphi(t) \\ N &= N_s + \delta N(t) & \frac{d\varphi}{dt} &= 2\pi\delta\nu(t) = \delta\omega(t) \end{aligned} \tag{6.26}$$

Finally, the gain coefficient G is expanded around its stationary value G_s:

$$G(\omega_s, N, S) = G_s + G_N \delta N + G_S \delta S \tag{6.27}$$

with $$G_s = G(\omega_s, N_s, S_s) \qquad G_N = \left.\frac{\partial G}{\partial N}\right|_s \qquad G_S = \left.\frac{\partial G}{\partial S}\right|_s \tag{6.28}$$

If these relations are inserted into (6.21), the stationary values are eliminated and subsequently the Fourier transform is taken, then the following set of equations is found:

$$\begin{bmatrix} j\Omega - Q_{S,r}S_s & 0 & -Q_{N,r}S_s - \dfrac{dR_{sp}}{dN} \\ -\dfrac{1}{2}Q_{S,i} & 1 & -\dfrac{1}{2}Q_{N,i} \\ (G_s + G_S S_s)\dfrac{1}{V_a} & 0 & j\Omega + G_N \dfrac{S}{V_a} + \dfrac{dR}{dN} \end{bmatrix} \cdot \begin{bmatrix} \delta S \\ \delta\omega \\ \delta N \end{bmatrix} = \begin{bmatrix} \hat{F}_S(\Omega) \\ \hat{F}_\varphi(\Omega) \\ \hat{F}_N(\Omega) + \dfrac{\delta I}{qV_a} \end{bmatrix} \tag{6.29}$$

To derive the small-signal AM and FM frequency response, the noise terms are set to zero. The AM response is found by eliminating δN from the first and third equation in (6.29):

$$\frac{\delta S}{\delta I} = \frac{1}{qV_a} \frac{H(\Omega)}{\Omega_r^2} \left(Q_{N,r} S_s + \frac{dR_{sp}}{dN} \right) \tag{6.30}$$

with $$H(\Omega) = H(2\pi f) = \frac{\Omega_r^2}{-\Omega^2 + j\gamma\Omega + \Omega_r^2} \tag{6.31}$$

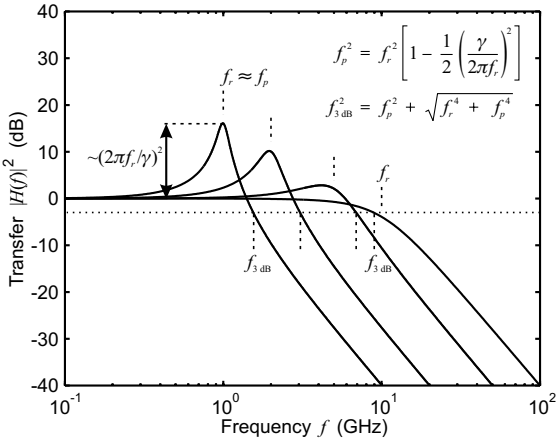

Figure 6.2 Sketch of the transfer function of a second order low-pass filter $|H(f)|^2$ for increasing values of the resonance frequency f_r and the damping γ. Also shown are expressions for the peak frequency f_p and the 3 dB cut-off frequency $f_{3\,\mathrm{dB}}$.

Here $H(f)$ is the normalised transfer function of a second order low-pass filter with resonance frequency $f_r = \Omega_r/(2\pi)$ and damping γ. Figure 6.2 illustrates the general behaviour of $|H(f)|^2$. The resonance frequency is given by:

$$\Omega_r^2 = \frac{1}{V_a}\left(G_s + G_S S_s\right)\left(Q_{N,r}S_s + \frac{dR_{sp}}{dN}\right) - Q_{S,r}S_s\left(G_N\frac{S_s}{V_a} + \frac{dR}{dN}\right) \tag{6.32}$$

and the damping is:

$$\gamma = \frac{dR}{dN} + \left(G_N - Q_{S,r}V_a\right)\frac{S_s}{V_a} \tag{6.33}$$

Similarly, the FM response can be calculated as:

$$\frac{\delta\omega}{\delta I} = \frac{1}{2qV_a}\frac{H(\Omega)}{\Omega_r^2}\left[Q_{N,i}\left(j\Omega - Q_{S,r}S_s\right) - Q_{S,i}\left(Q_{N,r}S_s + \frac{dR_{sp}}{dN}\right)\right] \tag{6.34}$$

In the following paragraphs, we will study the AM response in more detail for a few examples.

Fabry-Perot laser

As a first example, a simple Fabry-Perot laser is considered. Obviously, the assumption that such a laser is oscillating in a single longitudinal mode will not be entirely fulfilled in practice. It will however allow us to compare the results derived from expression (6.30) with the results obtained using a more rigorous dynamic laser model (*i-CLADISS* [14]-[15]), without having to take into account some of the more complex effects that occur in e.g. DBR lasers (cf. further on). For a Fabry-Perot laser the mirror reflectivities are simply given by:

$$r_L(\omega) = r_R(\omega) = r_0 \tag{6.35}$$

Hence, the reflectivities at the reference plane become:

$$q_L = e^{-j2Lk(\omega,N,S)} r_0 \qquad q_R = r_0 \tag{6.36}$$

The partial derivatives of $\ln(q_L)$ with respect to carrier density and photon number are then easily found as (with α_H the chirp parameter defined in (2.7)):

$$\begin{aligned} \frac{\partial \ln(q_L)}{\partial N} &= -j2L\frac{\partial k}{\partial N} = -j2L\left[\frac{\omega}{c}\Gamma\frac{\partial n'}{\partial N} + \frac{j}{2}\Gamma\frac{\partial g}{\partial N}\right] \\ &= L\Gamma\frac{\partial g}{\partial N}\left[1 + j\alpha_H\right] = \frac{L}{v_g}G_N\left[1 + j\alpha_H\right] \end{aligned} \tag{6.37}$$

$$\frac{\partial \ln(q_L)}{\partial S} = -j2L\frac{\partial k}{\partial S} = -L\Gamma g\varepsilon_S = -\frac{L}{v_g}\varepsilon_S G_s = \frac{L}{v_g}G_S \tag{6.38}$$

The complex time constant τ is in this case given by:

$$\begin{aligned} \tau &= j\frac{\partial \ln(q_L q_R)}{\partial \omega} = 2L\frac{\partial k}{\partial \omega}\bigg|_s \\ &= 2L\left[\frac{1}{c}n(\omega_s, N_s) + \frac{\omega_s}{c}\frac{\partial n}{\partial \omega}\bigg|_s + \frac{j}{2}\Gamma\frac{\partial g}{\partial \omega}\bigg|_s\right] = 2L\left[\frac{n_g}{c} + \frac{j}{2}\Gamma\frac{\partial g}{\partial \omega}\bigg|_s\right] \\ &= \frac{2L}{v_g}\left[1 + \frac{j}{2}v_g\Gamma\frac{\partial g}{\partial \omega}\bigg|_s\right] = \frac{2L}{v_g}\left[1 + \frac{j}{2}G_\omega\right] \approx \frac{2L}{v_g} \end{aligned} \tag{6.39}$$

The dimensionless parameter G_ω depends on the dispersion of the gain in the active section. At the gain peak it is zero, but even when the lasing mode is detuned from the gain peak it is usually much smaller than 1 and can therefore be neglected (cf. Table 3.1). With this approximation, τ becomes equal to the roundtrip time in the cavity. The parameters Q_N and Q_S then become:

$$\begin{aligned} Q_N &= \frac{2}{\tau}\frac{\partial \ln(q_L)}{\partial N} = G_N(1 + j\alpha_H) \\ Q_S &= \frac{2}{\tau}\frac{\partial \ln(q_L)}{\partial S} = G_S = -\varepsilon_S G_s \end{aligned} \tag{6.40}$$

which finally yields for the resonance frequency:

$$\Omega_r^2 = G_s G_N\frac{S_s}{V_a} + \frac{1}{V_a}\left(G_s + G_S S_s\right)\frac{dR_{sp}}{dN} - G_S S_s\frac{dR}{dN} \approx G_s G_N\frac{S_s}{V_a} \tag{6.41}$$

This is a well-known expression, which has been derived in many textbooks on laser diodes, e.g. [2]-[3]. Using the static solution to the carrier rate equation in (6.21), this can also be written as:

$$\Omega_r^2 = G_N\left(\frac{I_s}{qV_a} - R(N_s)\right) \approx G_N\frac{I_s - I_{th}}{qV_a} \tag{6.42}$$

where the last approximation is valid if the carrier density above threshold N_s does not deviate significantly from the carrier density at threshold N_{th}, which is true when the gain suppression is low ($I_{th} = R(N_{th})$, cf. (3.15)).

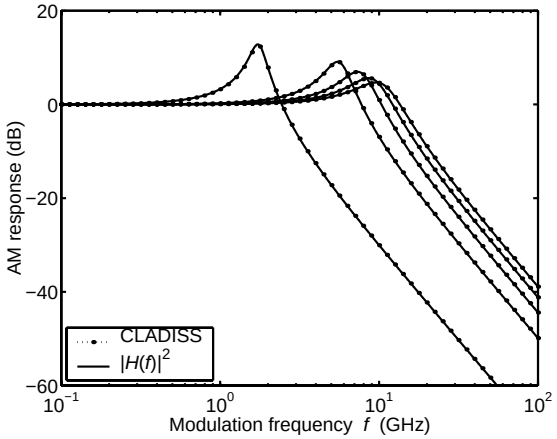

Figure 6.3 Normalised AM frequency response of a Fabry-Perot laser for increasing drive currents I (15, 40, 65, 90, and 115 mA), calculated both with *i-CLADISS* and with (6.30). The parameters were chosen as listed in Table 3.1, with a facet reflectivity $r_0 = 0.567$ and gain-suppression coefficient $\varepsilon_P = 2$ W^{-1}. This yielded a threshold current I_{th} of 12.4 mA.

For the damping we find

$$\begin{aligned}\gamma &= \frac{dR}{dN} + \left(G_N - G_S V_a\right)\frac{S_s}{V_a} \\ &\approx \frac{1}{\tau_d} + \left(\frac{1}{G_s}G_N + \varepsilon_S V_a\right)\frac{I_s - I_{th}}{qV_a} \approx \frac{1}{\tau_d} + \left(\frac{1}{G_s} + \frac{\varepsilon_S V_a}{G_N}\right)\Omega_r^2\end{aligned} \tag{6.43}$$

where

$$\tau_d = \left(\frac{dR}{dN}\right)^{-1} \tag{6.44}$$

is the differential carrier lifetime. The damping hence increases linearly with current. Well above threshold, the damping is approximately proportional to the square of the resonance frequency:

$$\gamma \approx K f_r^2 \tag{6.45}$$

If the resonance frequency and the damping are measured for a number of different bias currents, this relationship can be used to estimate the ultimate modulation bandwidth f_{max} of the laser [17]-[18]. According to (6.42) and (6.43), both the square of the resonance frequency and the damping increase linearly with current. If the damping is plotted as a function of the resonance frequency squared, then K and τ_d can be determined by fitting a linear curve to the data. From the expressions in Figure 6.2, we derive that the maximum bandwidth for a given f_r is achieved when

$$\gamma = 2\pi\sqrt{2} f_r \tag{6.46}$$

which together with (6.45) yields

$$f_{max} = \frac{2\pi\sqrt{2}}{K} \tag{6.47}$$

If the bias current is increased beyond the point where (6.46) applies, the 3 dB bandwidth will decrease again slightly and will finally saturate at $2\pi/K$.

Figure 6.3 compares the normalised AM response calculated using the above expressions to the results obtained with *i-CLADISS*. The laser parameters were chosen as listed in Table 3.1, with a facet reflectivity $r_0 = 0.567$ and gain-suppression coefficient $\varepsilon_P = 2\ \mathrm{W}^{-1}$. This yielded a threshold current I_{th} of 12.4 mA. The AM response is plotted for five values of the drive current I (15, 40, 65, 90, and 115 mA). Clearly, an excellent match is obtained between both results.

Fabry-Perot laser with passive section

All tunable lasers described in Chapter 2 contain a phase section for fine tuning of the cavity mode frequencies. As a first extension of the simple Fabry-Perot laser, we therefore consider a laser with an added passive waveguide section. In the following, we will use the subscript *a* for parameters referring to the active section and *p* for parameters referring to the passive section. If the reflection at the interface between the two sections is negligible, then the reflectivities r_L and r_R are given by:

$$r_L(\omega) = r_0 \qquad r_R(\omega) = e^{-j2L_p k_p(\omega)}\, r_0 \tag{6.48}$$

where

$$k_p(\omega) = \frac{\omega}{c} n_p(\omega) - \frac{j}{2}\alpha_p \tag{6.49}$$

is the complex propagation constant in the passive waveguide. This yields for the time constant τ:

$$\begin{aligned} \tau &= 2L_a \left.\frac{\partial k_a}{\partial \omega}\right|_s + 2L_p \left.\frac{\partial k_p}{\partial \omega}\right|_s = \frac{1}{c}\left[2L_a n_{g,a} + 2L_p n_{g,p}\right] + j2L_a\Gamma \left.\frac{\partial g}{\partial \omega}\right|_s \\ &= \frac{2L_a}{v_{g,a}}\left[\frac{L_a n_{g,a} + L_p n_{g,p}}{L_a n_{g,a}} + \frac{j}{2}G_\omega\right] \approx \frac{2L_a}{\Gamma_z v_{g,a}} \end{aligned} \tag{6.50}$$

where

$$\Gamma_z = \frac{n_{g,a}L_a}{n_{g,a}L_a + n_{g,p}L_p} < 1 \tag{6.51}$$

is a longitudinal confinement factor. Again, (the real part of) τ is equal to the roundtrip time in the cavity. Compared to the simple Fabry-Perot laser, the parameters Q_N and Q_S are now reduced by the factor Γ_z:

$$\begin{aligned} Q_N &\approx \Gamma_z G_N (1 + j\alpha_H) \\ Q_S &\approx \Gamma_z G_S = -\Gamma_z \varepsilon_S G_s \end{aligned} \tag{6.52}$$

Obviously, the same applies to the square of the resonance frequency:

$$\Omega_r^2 \approx \Gamma_z G_s G_N \frac{S_s}{V_a} \approx \Gamma_z G_N \frac{I_s - I_{th}}{qV_a} \tag{6.53}$$

The expression for the damping becomes:

$$\gamma \approx \frac{1}{\tau_d} + \left(\frac{1}{G_s} G_N + \Gamma_z \varepsilon_S V_a\right)\frac{I_s - I_{th}}{qV_a} \approx \frac{1}{\tau_d} + \left(\frac{1}{\Gamma_z G_s} + \frac{\varepsilon_S V_a}{G_N}\right)\Omega_r^2 \tag{6.54}$$

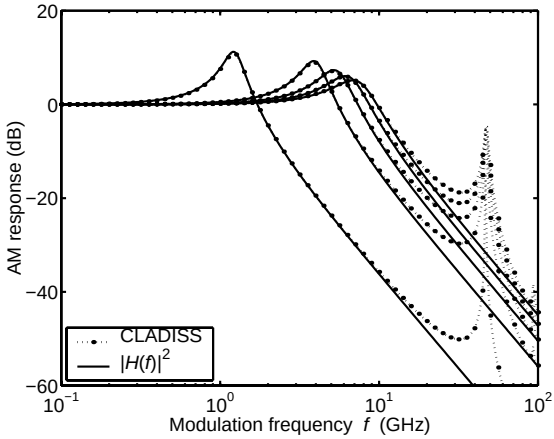

Figure 6.4 Normalised AM frequency response of a Fabry-Perot laser with a passive section of 415.6 µm for increasing active section currents I (15, 40, 65, 90, and 115 mA), calculated both with *i-CLADISS* and with (6.30). The parameters of the active section were chosen as in Figure 6.3. The passive section parameters were as in Table 3.2, except for the loss, which was set to zero in order to obtain the same threshold current as previously. These parameters yield a longitudinal confinement $\Gamma_z = 0.5$.

The K-factor turns out to be somewhat larger, which means that the maximum bandwidth will be reduced. The extent of the reduction depends on the ratio of the two terms between the brackets in (6.43). If the gain-suppression term is dominant, as is the case in the example considered above, the reduction will be rather small.

An advantage on the other hand is that the chirp will be reduced by the factor Γ_z compared to the simple Fabry-Perot laser. The variations of the cavity mode frequency ν and the active section effective index n_a are indeed related as [4]:

$$\frac{\Delta\nu}{\nu} = \frac{\Delta\omega}{\omega} = -\Gamma_z \frac{\Delta n_a}{n_{g,a}} \tag{6.55}$$

Figure 6.4 plots the normalised AM response for a laser with $\Gamma_z = 0.5$. The active section parameters were chosen as in Figure 6.3. The parameters of the 415.6 µm long passive section were chosen as in Table 3.2, except for the loss, which was set to zero in order to obtain the same threshold current as previously. The AM response is plotted for the same values of the drive current I. Compared to Figure 6.3, the resonance peaks have moved to somewhat lower frequencies, as is expected from (6.53). Up to frequencies of 10 to 15 GHz a very good match is also obtained between the curves calculated using the analytical expression (6.30) and the curves obtained from *i-CLADISS*. However, at higher frequencies the last set of curves shows additional resonance peaks. Upon closer inspection, these resonances occur at integer multiples of the cavity roundtrip frequency $f = 1/\tau$ (which is also equal to the cavity mode spacing, i.e. in this case about 46.8 GHz). This can be understood intuitively, since a kind of standing wave pattern will be generated in the cavity at these modulation frequencies. The main conclusion is however that the expression (6.30) describes the AM response of lasers with a passive section very well up to frequencies of about 0.20 to 0.25 times the cavity roundtrip frequency.

DBR laser

In this third and final example, the right facet mirror is replaced by a distributed Bragg reflector, which yields the reflectivities:

$$r_L(\omega) = r_0 \qquad r_R(\omega) = e^{-j2L_p k_p(\omega)}\, r_{DBR}(\omega) \tag{6.56}$$

The time constant τ then becomes:

$$\begin{aligned}\tau &= 2L_a \frac{\partial k_a}{\partial \omega}\bigg|_s + 2L_p \frac{\partial k_p}{\partial \omega}\bigg|_s - \frac{\partial \arg(r_{DBR})}{\partial \omega} + j\frac{\partial \ln(|r_{DBR}|)}{\partial \omega} \\ &\approx \frac{1}{c}\left[2L_a n_{g,a} + 2L_p n_{g,p} + 2L_{eff,d} n_{g,d}\right] + j\frac{\partial \ln(|r_{DBR}|)}{\partial \omega} \\ &= \frac{2L_a}{v_{g,a}}\frac{1}{\Gamma_z}(1 + jx)\end{aligned} \tag{6.57}$$

where

$$L_{eff,d} = -\frac{c}{2n_{g,d}}\frac{\partial \arg(r_{DBR})}{\partial \omega} \tag{6.58}$$

is the effective length of the Bragg reflector and $n_{g,d}$ is the group index of the DBR waveguide, yielding a longitudinal confinement factor:

$$\Gamma_z = \frac{n_{g,a}L_a}{n_{g,a}L_a + n_{g,p}L_p + n_{g,d}L_{eff,d}} \tag{6.59}$$

We have also introduced the dimensionless parameter x:

$$x = \frac{c\Gamma_z}{2n_{g,a}L_a}\frac{\partial \ln(|r_{DBR}|)}{\partial \omega} \tag{6.60}$$

which is proportional to the slope of the reflectivity amplitude with respect to frequency and therefore is equal to zero when the lasing mode is located at the peak frequency of the DBR. With this, we find for Q_N and Q_S:

$$\begin{aligned}Q_N &= \Gamma_z \frac{1 + \alpha_H x + j(\alpha_H - x)}{1 + x^2} G_N \\ Q_S &= \Gamma_z \frac{1 - jx}{1 + x^2} G_S = -\Gamma_z \frac{1 - jx}{1 + x^2} \varepsilon_S G_s\end{aligned} \tag{6.61}$$

Finally, this yields following expressions for the resonance frequency and damping:

$$\Omega_r^2 \approx \Gamma_z \frac{1 + \alpha_H x}{1 + x^2} G_s G_N \frac{S_s}{V_a} \approx \Gamma_z \frac{1 + \alpha_H x}{1 + x^2} G_N \frac{I_s - I_{th}}{qV_a} \tag{6.62}$$

$$\begin{aligned}\gamma &\approx \frac{1}{\tau_d} + \left(\frac{1}{G_s} G_N + \Gamma_z \frac{1}{1 + x^2}\varepsilon_S V_a\right)\frac{I_s - I_{th}}{qV_a} \\ &\approx \frac{1}{\tau_d} + \left(\frac{1 + x^2}{\Gamma_z G_s} + \frac{\varepsilon_S V_a}{G_N}\right)\frac{\Omega_r^2}{1 + \alpha_H x}\end{aligned} \tag{6.63}$$

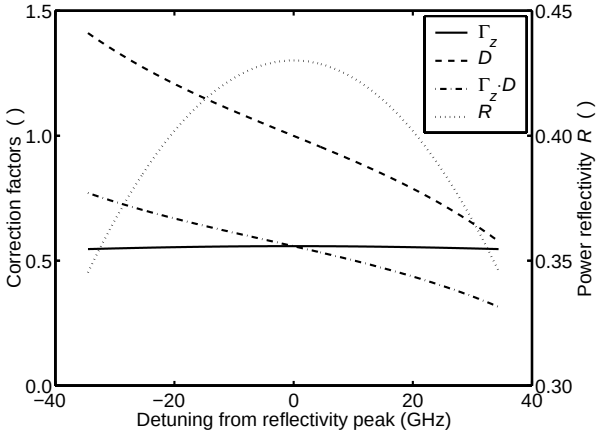

Figure 6.5 Effect of detuned loading on the modulation characteristics of a DBR laser. Plot of longitudinal confinement factor Γ_z and detuning factor D as a function of the detuning of the lasing mode relative to the peak frequency of the DBR. As a reference, the reflectivity R of the DBR is also shown.

These results are in perfect agreement with the expressions obtained in [19]-[20] for lasers coupled to an external resonator.

Compared to the expression (6.42) for the resonance frequency of the simple Fabry-Perot laser, there are now two correction factors. The first is the longitudinal confinement factor Γ_z (6.59), which also appeared in the expression for the Fabry-Perot laser with a passive section (6.53). The second is the detuning factor

$$D = \frac{1 + \alpha_H x}{1 + x^2} \tag{6.64}$$

which depends on the detuning of the lasing mode relative to the peak frequency of the Bragg reflector. Both correction factors are plotted in Figure 6.5 as a function of the detuning for a typical DBR laser (cf. §4.2.1, Figure 4.11 and Figure 4.12). For obvious reasons, the detuning was limited to plus or minus half the cavity mode spacing. The effective length of the DBR increases when the lasing mode is detuned from the peak, but overall the changes to the longitudinal confinement factor Γ_z are rather limited. The linewidth enhancement factor α_H is in this case about 5.4 (cf. (2.7) and Table 3.1). From the curve in Figure 6.5 we can then conclude that even at strong detuning x^2 is very small and can therefore be neglected. With this approximation the expressions for resonance frequency and damping become:

$$\Omega_r^2 \approx \Gamma_z D \cdot G_N \frac{I_s - I_{th}}{qV_a} \qquad \gamma \approx \frac{1}{\tau_d} + \left(\frac{1}{\Gamma_z G_s} + \frac{\varepsilon_S V_a}{G_N} \right) \frac{\Omega_r^2}{D} \tag{6.65}$$

If the lasing mode is detuned to the low frequency side of the Bragg peak, the resonance frequency will be enhanced, although it always remains below the value for the simple Fabry-Perot laser ($\Gamma_z \cdot D < 1$). The K-factor of the DBR laser can however be decreased below the value for the Fabry-Perot laser, due to the presence of the factor D in the denominator.

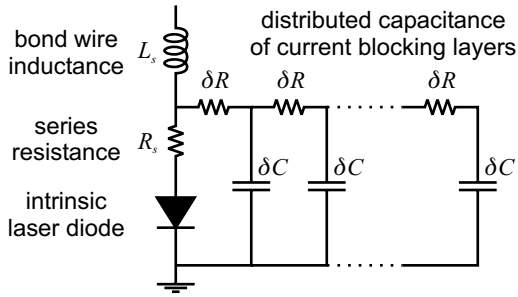

Figure 6.6 Equivalent circuit model for a laser diode including parasitic elements [2].

In other words, the maximum modulation bandwidth of the DBR laser can be significantly enhanced by detuning the lasing mode to lower frequencies [21]-[22]. In general however, a tunable laser will be operated with the lasing mode as close as possible to the Bragg peak in order to maximise the side-mode suppression ratio (cf. Chapter 4 and Chapter 5). In that case, D is approximately equal to one and the modulation characteristics are those of a Fabry-Perot laser with a passive section with length $L_p + L_{d,eff}$. The extension of these results to GCSR, SG-DBR and SSG-DBR lasers is of course rather straightforward.

So far, we have considered the modulation response of an idealised laser diode. Figure 6.6 depicts an equivalent circuit model of a realistic laser diode [2]. A few parasitic elements can immediately be identified. The first is the series resistance of the laser diode, which usually takes on a value of a few Ohm. The bond wire from the laser chip to the mounting pad will have a certain inductance L_s, on the order of one nanohenry per millimetre of bond wire length. Finally, the current blocking layers, which prevent the current from leaking parallel to the active layer, cause a distributed parasitic capacitance. For most practical purposes, the effect of these parasitics on the AM response of the laser can be described sufficiently accurately by multiplying (6.30) with the transfer function of a first order (RC) low-pass filter:

$$H_{RC}(\Omega) = \frac{\Omega_{RC}}{j\Omega + \Omega_{RC}} \tag{6.66}$$

If no special care is taken in the design of a laser diode to achieve low parasitic capacitance and inductance, the maximum achievable modulation bandwidth of the laser f_{max} will often be limited by the parasitics:

$$f_{max} = \frac{\Omega_{RC}}{2\pi} < \frac{2\pi\sqrt{2}}{K} \tag{6.67}$$

Even with low parasitics, the bandwidth is sometimes limited to a value below the estimated maximum value (6.47) due to thermal effects [23]. The heat generated by the injected current can cause the resonance frequency to saturate at a value $f_{r,therm}$. In that case, the maximum bandwidth becomes:

$$f_{max} = \sqrt{1+\sqrt{2}}\, f_{r,therm} \tag{6.68}$$

6.1.3 Relative intensity noise

From the set of equations (6.29) we can also derive the noise properties of the laser diode by setting the current modulation δI to zero. If the equations are then solved for the photon number fluctuations δS, we find:

$$\begin{aligned}\delta S &= \frac{H(\Omega)}{\Omega_r^2}\left[\left(j\Omega + G_N\frac{S_s}{V_a} + \frac{dR}{dN}\right)\hat{F}_S + \left(Q_{N,r}S_s + \frac{dR_{sp}}{dN}\right)\hat{F}_N\right] \\ &= \frac{H(\Omega)}{\Omega_r^2}\left[(j\Omega + \gamma_S)\hat{F}_S + \gamma_N\hat{F}_N\right]\end{aligned} \tag{6.69}$$

Here $H(\Omega)$ is again given by (6.31)-(6.33). The noise in the output power of a laser diode is usually quantified using the relative intensity noise (RIN), which is defined as the ratio of the spectral density of the photon number fluctuations to the square of the average photon number [2]-[3], [24]. The relative intensity noise is commonly expressed in dB/Hz. With the above expression for δS, we can immediately calculate the RIN as:

$$\begin{aligned}RIN(\Omega) &= \frac{\langle \delta S(\Omega)\delta S^*(\Omega)\rangle}{S_s^2} = \frac{|H(\Omega)|^2}{S_s^2\Omega_r^4}\left\langle\left|(j\Omega + \gamma_S)\hat{F}_S + \gamma_N\hat{F}_N\right|^2\right\rangle \\ &= \frac{1}{S_s^2}\frac{(\Omega^2 + \gamma_S^2)2D_{SS} + \gamma_N^2 2D_{NN} + 2\gamma_S\gamma_N 2D_{SN}}{(\Omega_r^2 - \Omega^2)^2 + \gamma^2\Omega^2}\end{aligned} \tag{6.70}$$

where we have used (cf. (6.24)):

$$\langle \hat{F}_p(\Omega)\hat{F}_q^*(\Omega)\rangle = 2D_{pq} \tag{6.71}$$

Note that the denominator in expression (6.70) for the relative intensity noise is the same as the denominator in $|H(\Omega)|^2$, describing the normalised AM response of the laser diode. The resonance frequency (6.32) and damping (6.33) can therefore be extracted from a measurement of the RIN spectrum, by fitting the following function to the measured data:

$$RIN(\Omega) = A\frac{\Omega^2 + \tilde{\gamma}^2}{(\Omega_r^2 - \Omega^2)^2 + \gamma^2\Omega^2} \tag{6.72}$$

It is often easier to determine the resonance frequency and damping from measurements of the RIN spectrum than from direct measurements of the AM response [23], [25]. The latter require connecting a high-frequency electrical modulation signal to the laser, and the measurement results will obviously be affected by the parasitic elements sketched in Figure 6.6, which might impede an accurate determination of Ω_r and γ. For RIN measurements, on the other hand, only a DC bias current needs to be applied to the laser, and the obtained spectra only depend on the parameters of the intrinsic laser diode. If the resonance frequency and damping are extracted from the RIN spectra for different bias currents, the *K*-factor and the intrinsic maximum modulation bandwidth can be determined using (6.45) and (6.47).

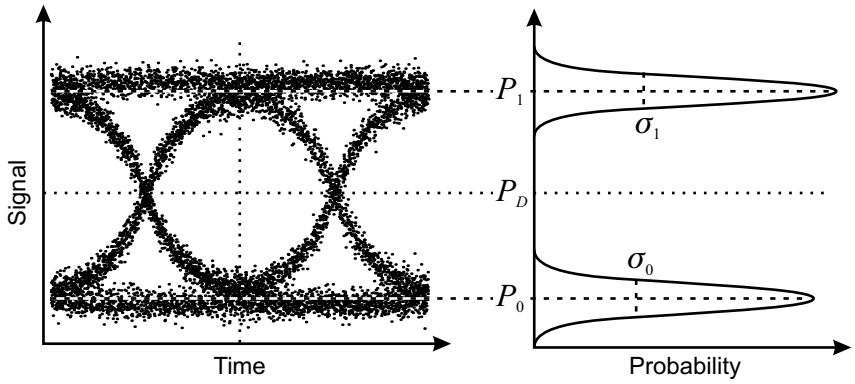

Figure 6.7 Eye diagram and probability density distributions for 0 and 1 bits.

6.1.4 Large-signal digital modulation

So far, only small variations of the drive current have been considered. In most practical systems, the laser diode will however be modulated with a binary pulse-code modulated signal. The drive current is then switched between two levels, I_0 and I_1, which causes the output power to switch from P_0 (representing a digital 0) to P_1 (representing a digital 1). Obviously, the small-signal modulation bandwidth will impose an upper limit on the achievable bit-rate (typically about 1.5 to 2 times the small-signal bandwidth). Whether a reliable data-link can be set up over a certain length of optical fiber at a given bit-rate however also depends on a number of other factors.

The quality of a digital communication link is usually determined by measuring the bit error rate (BER), defined as the probability of an incorrect identification of a bit by the decision circuit at the end of the link. This decision circuit compares the inbound signal to a threshold level, at sampling times determined by a clock-recovery circuit, and decides whether the signal corresponds to a 0-bit or a 1-bit. Figure 6.7 shows a typical shape of the signal at the input of the decision circuit, represented as an eye diagram, i.e. the superposition of multiple 2-bit sequences in the random bit stream on top of each other. The best sampling time is obviously located at the centre of the figure, where the opening of the eye is largest (indicated by the vertical dotted line). The graph on the right shows the probability density distribution of the signal at the selected sampling time. This distribution can be described as the superposition of two Gaussian distributions, one corresponding to the 1-bits (average level P_1 and variance σ_1) and one corresponding to the 0-bits (average level P_0 and variance σ_0). The BER is defined as:

$$BER = \mathrm{P}(1)\mathrm{P}(0 \mid 1) + \mathrm{P}(0)\mathrm{P}(1 \mid 0) \tag{6.73}$$

where P(1) and P(0) are the probabilities of receiving bits 1 and 0, respectively, P(0|1) is the probability of deciding 0 when 1 was transmitted, and P(1|0) is the probability of deciding 1 when 0 was transmitted. Since 1 and 0 bits are equally likely to occur, P(1) = P(0) = 1/2, and the BER becomes:

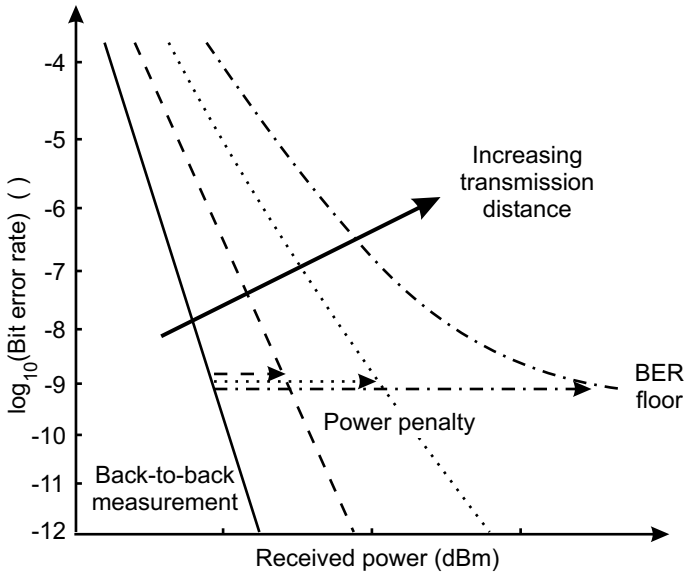

Figure 6.8 Illustration of a bit error rate measurement.

$$BER = \frac{1}{2}\left[\mathrm{P}(0 \mid 1) + \mathrm{P}(1 \mid 0)\right] \tag{6.74}$$

The probabilities P(0|1) and P(1|0) of course depend on the choice of the threshold level P_D. The optimum occurs when [26]:

$$P_D = \frac{\sigma_0 P_1 + \sigma_1 P_0}{\sigma_0 + \sigma_1} \tag{6.75}$$

When the variances are equal this yields the obvious choice $P_D = (P_0 + P_1)/2$. The BER for the optimum choice of the decision threshold is given by [26]:

$$BER = \frac{1}{2}\,\mathrm{erfc}\left(\frac{Q}{\sqrt{2}}\right) \approx \frac{\exp\left(-Q^2/2\right)}{Q\sqrt{2\pi}} \tag{6.76}$$

where

$$Q = \frac{P_1 - P_0}{\sigma_1 + \sigma_0} \tag{6.77}$$

The approximate form of the BER is reasonably accurate for $Q > 3$. Typically, a BER of less than 10^{-9} is required ($Q > 6$).

A common method to test a communication link is to measure the BER as a function of the average received power $(P_0 + P_1)/2$ (Figure 6.8). The input power at the receiver is changed by inserting a variable attenuator. In most cases, the noise in the signal at the input of the decision circuit is dominated by thermal noise generated in the receiver. Therefore, when the average received power is decreased, the Q-factor will be reduced and the bit error rate will increase. The BER measurement for a certain link is subsequently compared to a back-to-back measurement, where the transmitter (the laser) is directly connected to the variable attenuator. If the signal is

in any way degraded during the transmission through the fiber link, the received power required to obtain a certain BER will increase. This increase is referred to as the power penalty (Figure 6.8). Typically, the power penalty is evaluated at a BER of 10^{-9}. In some cases, the BER will not keep on decreasing when the average received power is increased, but will saturate at a certain level, which is commonly called the BER floor.

In this case, we are interested in the performance of the directly modulated laser diode. Therefore, we will now investigate which laser parameters affect the operation of a link in which this laser is used as the transmitter. As already mentioned in the introduction, an important disadvantage of using a directly modulated laser is the frequency chirp caused by the current modulation. Due to the dispersion of the fiber, pulses emitted from the laser will broaden with distance, which will eventually lead to inter-symbol-interference and increase the BER rate at a given received power. The influence of the frequency chirp can be investigated by comparing BER measurements for different lengths of fiber.

Of course, dispersion effects would be worse if the laser does no longer emit light in a single longitudinal mode when it is directly modulated. If the mode selectivity of the intra-cavity filter(s) is not sufficient, or if the main lasing mode is not properly aligned with the intra-cavity filter(s), the side-mode suppression can be severely degraded when the laser is directly modulated. A reduced SMSR not only increases the laser linewidth and thus causes enhanced dispersion effects, but also increases the noise in the optical signal (due to mode partition noise [2]). Typically, a side-mode suppression ratio (under direct modulation) of at least 30 dB is required to achieve low bit error rates ($< 10^{-10}$) [6]. Since BER measurements are very time consuming, the first step in the evaluation of a laser for direct modulation should be a measurement of the time-averaged optical spectrum.

A very important parameter is the 0-level current I_0. Ideally, one would have zero output power for a 0-bit. This would require $I_0 = 0$, which is however not tolerable for a number of reasons. If the active section current of a laser is switched from a value I_0 below the threshold current I_{th} to a value I_1 above threshold, the output power will only start to increase after a certain turn-on delay t_{on} (Figure 6.9). The reason is that the carrier density first has to build up to the threshold value. The turn-on delay can be estimated as [2]:

$$t_{on} = \tau_d \ln\left(\frac{I_1 - I_0}{I_1 - I_{th}}\right) \tag{6.78}$$

where τ_d is the carrier lifetime. Since τ_d is on the order of several nanoseconds, one obtains a turn-on delay of a similar order of magnitude if I_0 is below the threshold. This can obviously not be tolerated for transmission at Gbit/s rates. Moreover, if the laser is switched from below the threshold, the large carrier density fluctuations cause a significant frequency chirp and possibly a reduced side-mode suppression ratio.

On the other hand, I_0 should not be chosen to large, since this will reduce the extinction ratio, defined as the ratio of the average power for a 1-bit (P_1) to the average power for a 0-bit (P_0). It can be shown that a non-infinite extinction ratio leads to a receiver power penalty ΔP (expressed in dB) given by [26]:

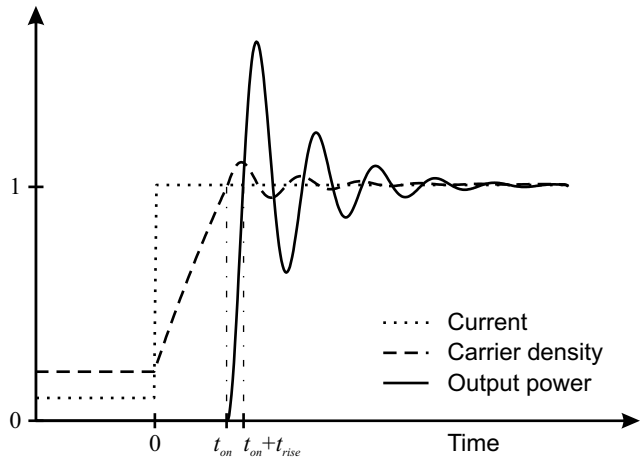

Figure 6.9 Large-signal modulation of a laser diode. Evolution of current, carrier density and output power when the laser is switched from below threshold (at $t = 0$). The parameters were normalised to their steady-state values.

$$\Delta P = 10 \log_{10}\left(\frac{P_1/P_0 + 1}{P_1/P_0 - 1}\right) \tag{6.79}$$

A power penalty of less than 1 dB requires an extinction ratio of at least 9.4 dB. The extinction ratio also affects the rise time t_{rise} of the optical pulse [2]:

$$t_{rise} = \frac{1}{2\pi f_r}\sqrt{2\ln\left(\frac{P_1}{P_0}\right)} \tag{6.80}$$

where f_r is the resonance frequency at the 1-level ($I = I_1$). Enhancing the extinction ratio will hence increase the rise time. The dependence of the rise time on the extinction ratio is however rather weak. As long as the resonance frequency is sufficiently high, this should therefore not be a limiting factor. For example, for a resonance frequency of 5 GHz and an extinction ratio of 10 dB, we find a rise time of somewhat less than 70 ps, which is more than sufficient for 2.5 Gbit/s transmission. Similar observations apply to the turn-on jitter, i.e. the noise on the rise time [2]. In the end, a good compromise seems to be to adjust the 0-level current such that an extinction ratio of about 10 dB is obtained, which requires that I_0 is close to, but slightly above the threshold current I_{th}.

After the laser turns on, the output power will exhibit a relaxation oscillation (Figure 6.9). In order to ensure error-free transmission, this oscillation should be suppressed in the signal that serves as an input to the receiver decision circuit. This is done by passing the signal that comes from the photo-detector through a low-pass filter, typically a fourth-order Bessel-Thompson filter with a cut-off frequency at 0.75 times the bit-rate.

Based on the above observations, we adopted following procedure to evaluate a tunable laser for large-signal digital modulation.

- Tune the laser to a particular frequency (with good SMSR).

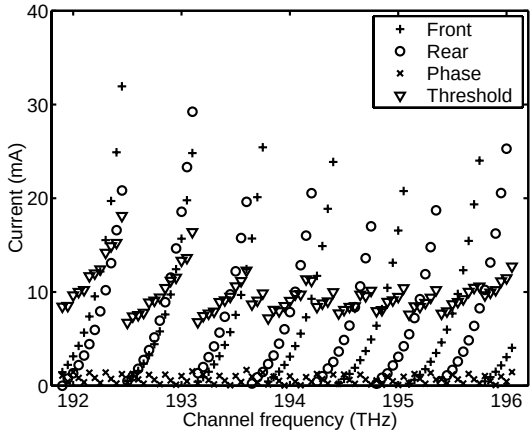

Figure 6.10 Tuning currents for RIN measurements at 84 (50 GHz-spaced) channels of a SSG-DBR laser.

- Apply the modulation signal.
- Adjust the active section bias current such that an extinction ratio of approximately 10 dB is obtained. This is done by displaying the eye diagram of the optical signal on a high-speed oscilloscope (back-to-back).
- Measure the time-averaged optical spectrum and extract the SMSR. If necessary, adjust the tuning currents to increase the SMSR (while keeping the emission frequency constant).
- If the SMSR is sufficiently high, measure the BER as a function of the average received power for different fiber lengths. Determine the power penalty.

6.2 Results for the SSG-DBR laser

6.2.1 RIN measurements

Relative intensity noise measurements were performed on a SSG-DBR laser for 84 channels, from 191.90 THz to 196.05 THz in 50 GHz increments. Figure 6.10 shows the tuning currents for these channels, which were obtained using the algorithm described in §5.4. The output power was equalised across the channels to approximately 0.5 mW. Subsequently, the active section current I_a was decreased for every channel in order to determine the threshold current $I_{a,th}$ (Figure 6.10). When changing the active section current, no adjustments were made to the tuning currents, although the lasing frequency increased somewhat due to the decrease in (waveguide) temperature. For each channel, RIN spectra were then measured at following active section currents:

$$I_a = I_{a,th} + \Delta I = I_{a,th} + \left(\frac{k}{10}\right)^2 \cdot 60\,\text{mA} \qquad k = 1, 2, \ldots, 10 \qquad (6.81)$$

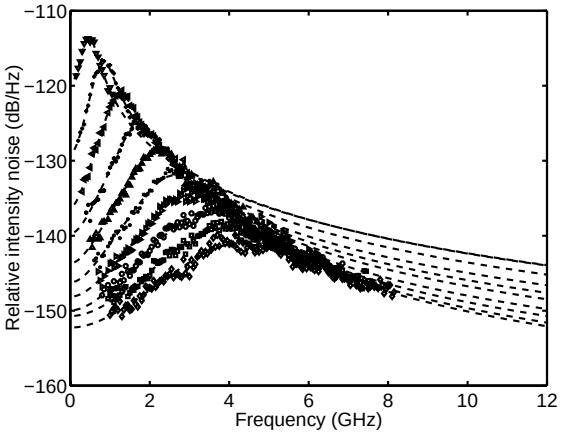

Figure 6.11 RIN spectra measured for increasing bias current for the channel at 192.45 THz (symbols). Fitted curves according to (6.72) (dashed lines).

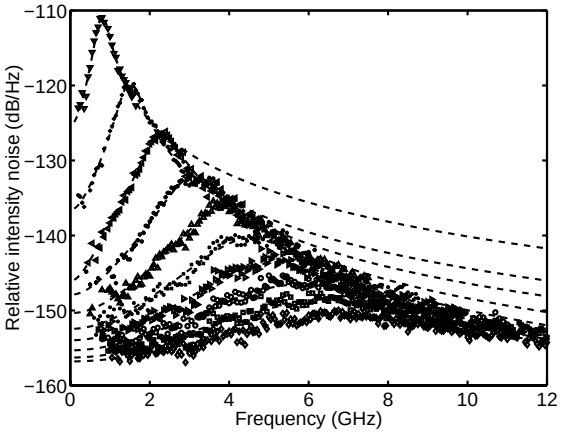

Figure 6.12 RIN spectra measured for increasing bias current for the channel at 195.45 THz (symbols). Fitted curves according to (6.72) (dashed lines).

Figure 6.11 and Figure 6.12 show the results for two channels, 192.45 THz and 195.45 THz. The resonance frequency and damping clearly increase much faster with the drive current for the latter channel. Relation (6.72) was fitted to each of the measured RIN spectra (840 in total) in order to extract the resonance frequency f_r and the damping γ. In Figure 6.13 the resonance frequency is plotted as a function of the square root of ΔI for the two channels considered above. In agreement with (6.62), the resonance frequency is proportional to $\Delta I^{1/2}$. All other channels showed a similar proportionality between f_r and $\Delta I^{1/2}$, with slopes that lie between the two extremes plotted here. No evidence of thermal saturation of the resonance frequency was observed.

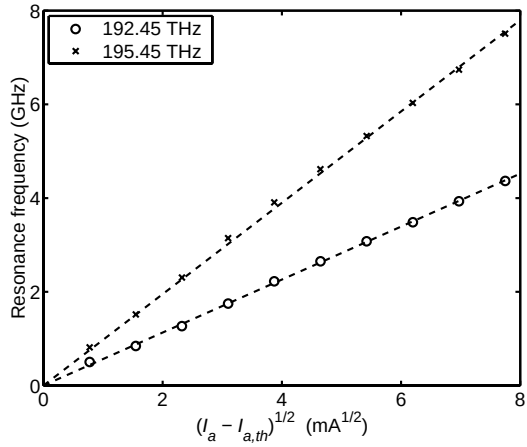

Figure 6.13 Resonance frequency extracted from RIN spectra plotted as a function of the square root of the drive current minus the threshold current, for the channels at 192.45 THz and 195.45 THz.

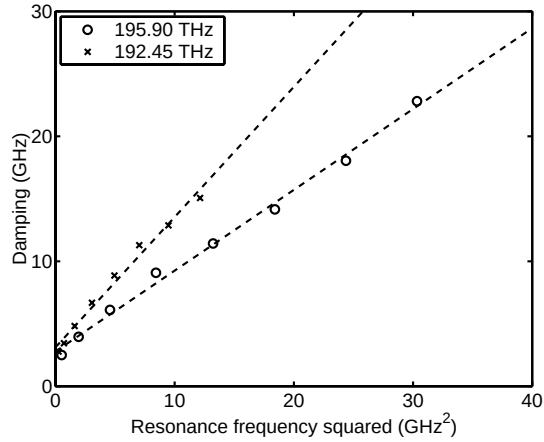

Figure 6.14 Damping plotted as a function of the resonance frequency squared, for the channels at 195.90 THz and 192.45 THz.

According to (6.63), the damping is a linear function of the square of the resonance frequency. The slope yields the *K*-factor from which the maximum intrinsic modulation bandwidth f_{max} can be derived according to (6.47). Figure 6.14 plots the damping as a function of the resonance frequency squared for the channels at 195.90 THz and 192.45 THz, which respectively yielded the minimal and maximal *K*-factor. The results of the parameter extraction for all channels are summarised in Figure 6.15, which plots f_{max} and the resonance frequency f_r at 50 mA above the threshold current for all 84 channels. The derived values for f_{max} lie above 10 GHz for most channels. The minimum value is about 8 GHz, for the 192.45 THz channel. This would indicate that modulation at 10 Gbit/s is, at least in theory, feasible.

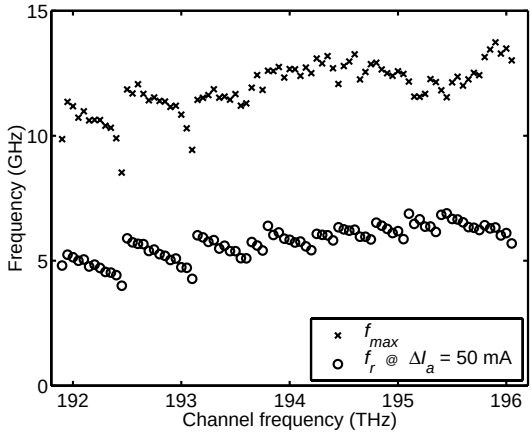

Figure 6.15 Maximum intrinsic modulation bandwidth f_{max} and resonance frequency f_r at 50 mA above threshold for all 84 (50 GHz-spaced) channels.

On the other hand, the resonance frequency at 50 mA above the threshold current is on average only about 5.5 GHz (and varies between 4.0 GHz and 6.9 GHz). Still, direct modulation at a bit-rate of 2.488 Gbit/s should certainly be possible, provided the parasitic capacitance and inductance are kept sufficiently low.

The observed variations in resonance frequency can be explained by variations in the differential gain G_N with tuning (cf. (6.65)). When the carrier density in the active region is raised, the overall gain increases, but the gain peak also shifts to higher frequencies. This means that at a given carrier density level, the differential gain G_N will be larger at higher optical frequencies. On the other hand, at a particular optical frequency, the differential gain G_N decreases with increasing carrier density. Both phenomena can be illustrated using the simple parabolic gain model (3.2):

$$G_N = \Gamma v_g \frac{\partial g}{\partial N} = \Gamma v_g \left[\frac{\partial g_p}{\partial N} + 2 g_\omega \left(\omega - \omega_p \right) \frac{\partial \omega_p}{\partial N} \right] \tag{6.82}$$

where

$$\omega_p = \omega_{p,0} + \frac{\partial \omega_p}{\partial N} \left(N - N_{g,0} \right) \tag{6.83}$$

Comparison of Figure 6.10 and Figure 6.15 clearly reveals the strong correlation between the threshold current and the resonance frequency at 50 mA above threshold. As the threshold goes up, the carrier density in the active section increases and the differential gain diminishes. Consequently, the resonance frequency at a certain current level ΔI above the threshold decreases (cf. (6.65)). The overall rising trend of f_r is of course attributable to the increase of G_N with frequency.

The correlation between the maximum bandwidth and the threshold current is not as clear. From (6.47) and (6.65) we find:

$$f_{max} = \frac{D\sqrt{2}}{2\pi} \left(\frac{1}{\Gamma_z G_s} + \frac{\varepsilon_S V_a}{G_N} \right)^{-1} \tag{6.84}$$

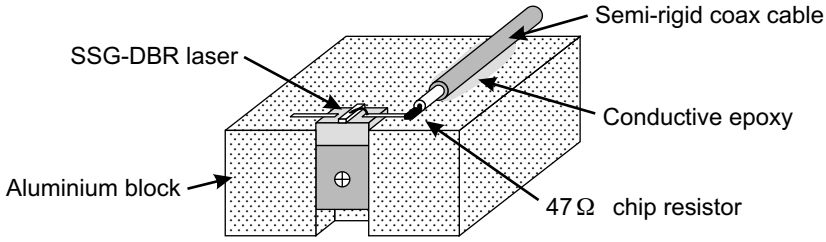

Figure 6.16 Mounting of the SSG-DBR laser for direct modulation measurements.

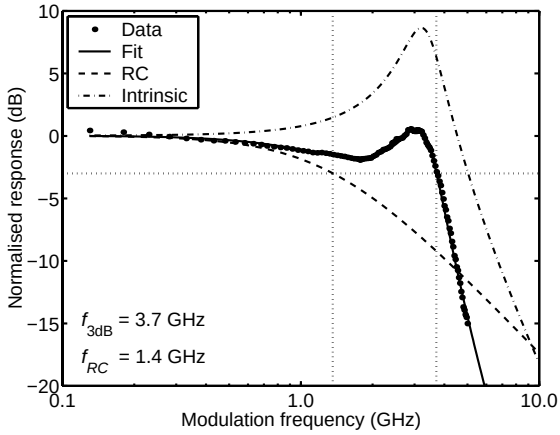

Figure 6.17 Small-signal response of a SSG-DBR laser at a bias current of 18 mA, with no current applied to the tuning sections. Calculated intrinsic response of the laser and parasitic *RC*-like roll-off.

When the threshold current increases, the steady-state gain G_s goes up, but at the same time the differential gain G_N goes down. The net effect on the maximum bandwidth f_{max} will hence depend on the ratio of the two terms between the brackets.

6.2.2 Small-signal modulation response

For the direct modulation measurements, a semi-rigid coaxial cable was connected to a SSG-DBR laser (Figure 6.16). A 47 Ω chip resistor was connected in series with the active section for impedance matching between the series resistance of the laser (typically a few Ohm) and the characteristic impedance of the coax cable (50 Ω). The active section bias current and the sinusoidal modulation signal were combined using a bias-T. With our set-up at the University of Gent, we measured a parasitic-limited small-signal modulation bandwidth of 750 MHz with the SSG-DBR laser biased well above threshold. Using a similar mounting and contacting technique, researchers at NTT Optoelectronics in Atsugi, Japan managed to achieve much better bandwidths. Figure 6.17 shows the small-signal modulation response they

measured at a bias current of 18 mA, with no current applied to the tuning sections. By fitting:

$$F(f) = A - 10 \cdot \log_{10}\left(\left|\left(f_r^2 - f^2 + j\frac{\gamma}{2\pi}f\right)(jf + f_{RC})\right|^2\right) \tag{6.85}$$

to the measurement data, we could extract the resonance frequency f_r = 3.3 GHz, the damping γ = 7.8 GHz and the corner frequency due to the parasitics f_{RC} = 1.4 GHz. Figure 6.17 also plots the derived intrinsic response of the laser and the parasitic *RC*-like roll-off separately. Due to the resonance peak of the laser's intrinsic response, the overall 3 dB bandwidth is enhanced to 3.7 GHz.

6.2.3 Large-signal digital modulation

Eye diagrams

Since the small-signal bandwidth in our set-up was only 750 MHz, the bit-rate for the large-signal measurements had to be limited to 1.244 Gbit/s. A 3 V peak-to-peak non-return to zero (NRZ) data signal was combined with the active section bias current using a bias-T. The current swing between a 0-bit and a 1-bit was therefore approximately equal to 60 mA. The data signal consisted of a 2^{23}-1 pseudo-random bit sequence (PRBS). Large-signal measurements were performed for 20 channels spaced by 200 GHz, from 191.9 THz to 195.7 THz.

The laser was initially tuned to the selected channel with a relatively high bias current. The tuning currents were obtained using the algorithm from §5.3. The optical signal was directed to a 2.488 Gbit/s optical reference receiver (containing a fourth-order Bessel-Thompson low-pass filter with a cut-off frequency at 1.88 GHz) and the resulting electrical signal was displayed on a high-speed oscilloscope. After the modulation signal was switched on, the bias current was optimised to achieve an extinction ratio of approximately 10 dB. With a current swing of 60 mA, the optimum bias current for a particular channel of course lies approximately 30 mA above the threshold current for that channel (cf. §6.1.4). Figure 6.18 shows a typical eye diagram that was obtained in this way.

By changing the modulation signal to a square wave with a longer period (typically a few nanoseconds), we could also measure the rise time of the laser (Figure 6.19). The displayed value of 462 ps is in excellent agreement with the previously measured small-signal bandwidth of 750 MHz, since for a first-order system both are related by:

$$f_{3\,\mathrm{dB}} \approx \frac{0.35}{t_{rise}} \tag{6.86}$$

The tuning currents and the optimised active section bias for all 20 channels are plotted in Figure 6.20. It has to be noted that the value of the bias current is quite critical. Typically, the current has to be controlled with a resolution of ±0.1 mA. A higher value of the bias current will reduce the extinction ratio, whereas a lower value will cause the drive current to swing below the threshold, causing increased chirp and turn-on jitter and reduced side-mode suppression ratio (cf. §6.1.4).

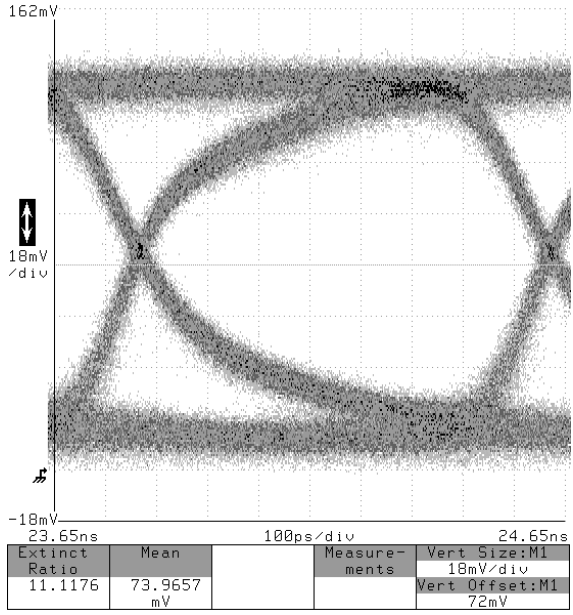

Figure 6.18 Eye diagram measured for a SSG-DBR laser modulated at 1.244 Gbit/s. The transmitter configuration had a parasitic-limited bandwidth of approximately 0.75 GHz. No relaxation oscillations are visible in the signal because the receiver contained a fourth-order Bessel-Thompson low-pass filter with a cut-off frequency at 1.88 GHz.

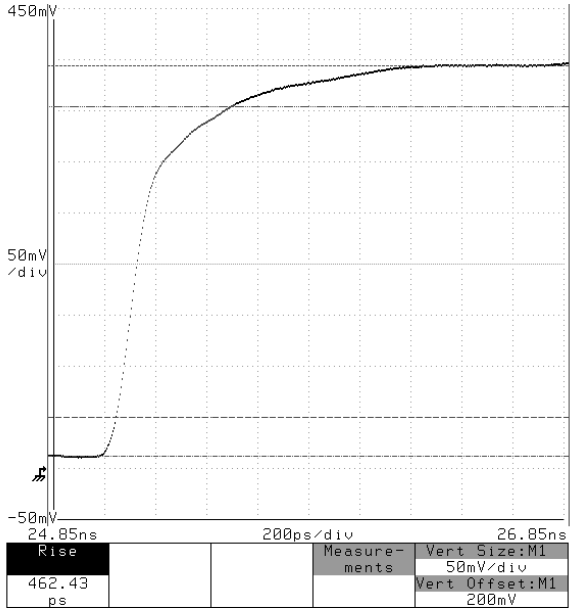

Figure 6.19 Measurement of the parasitic-limited rise time of a SSG-DBR laser.

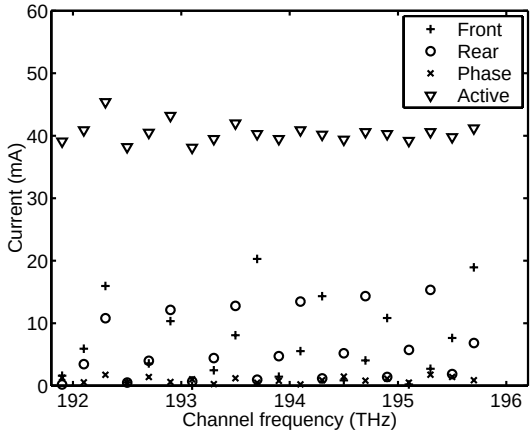

Figure 6.20 Tuning currents and active section bias current for large-signal modulation measurements for 20 (200 GHz-spaced) channels of a SSG-DBR laser.

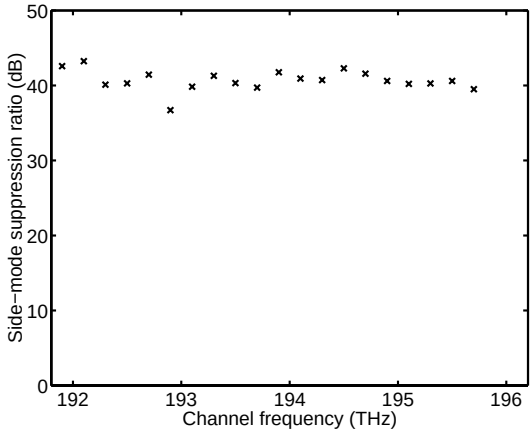

Figure 6.21 Side-mode suppression ratio with direct modulation at 1.244 Gbit/s, for 20 (200 GHz-spaced) channels of a SSG-DBR laser.

Time-averaged optical spectra

The time-averaged optical spectrum of the modulated light was measured for each of the operation points plotted in Figure 6.20 and the side-mode suppression ratio was extracted. The results are summarised in Figure 6.21. For all channels, the SMSR was above 35 dB; in most cases, it was even close to 40 dB. Similar results were already presented in Chapter 4 §4.3.3, where frequency- and mode control were applied to the directly modulated laser.

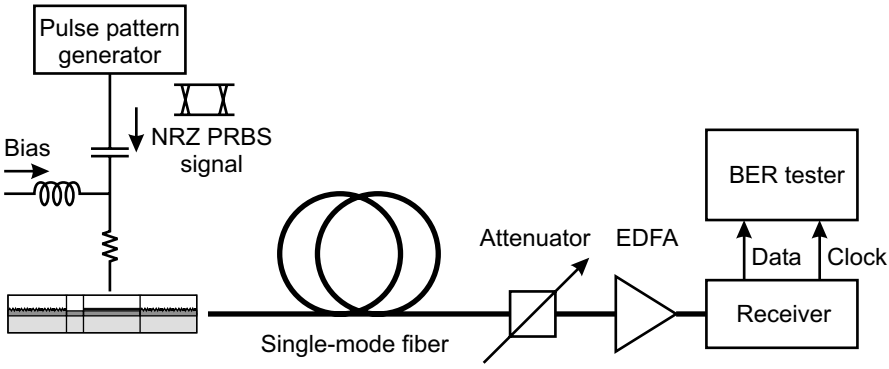

Figure 6.22 Measurement set-up for bit error rate measurements with a directly modulated SSG-DBR laser.

Bit error rate

We were not able to perform bit error rate measurements at the University of Gent, because we did not have a suitable receiver (which should include circuitry for clock recovery and pulse reshaping). For completeness, we will however summarise some of the results obtained by NTT Optoelectronics. Figure 6.22 illustrates the measurement set-up that was used. The laser was modulated with a pseudo-random non-return to zero (NRZ) signal at a bit-rate of 2.488 Gbit/s. The emitted light was transmitted through a standard single-mode fiber (with a dispersion of 17 ps/nm/km). The input power to the receiver was changed using a variable attenuator. An Erbium-doped fiber amplifier (EDFA) was used as an optical pre-amplifier to increase the sensitivity. In the receiver, the optical signal is converted to an electrical signal by a high-speed photodiode and a transimpedance amplifier. The electrical signal is passed through a fourth-order Bessel-Thompson low-pass filter (bandwidth 1.88 GHz), which filters out the relaxation oscillations. Subsequently, some pulse reshaping is performed using a limiting amplifier and the clock signal is extracted. Both the reshaped data signal and the clock signal were connected to the bit error rate tester, which counted the number of incorrectly received bits.

BER characteristics were measured for 21 frequency channels from 192.1 THz to 196.1 THz, with a channel separation of 200 GHz. Figure 6.23 and Figure 6.24 plot the BER as a function of the average received power for all 21 channels, before and after transmission over 60 km of standard fiber, respectively. The active section bias current was optimised for each channel individually, since the BER is very sensitive to the bias condition. For all channels, error-free operation was obtained after transmission over 60 km. The average received power required for a BER of 10^{-9} was around -39 dBm before transmission and -36 dBm after transmission. In other words, a mean power penalty of 3 dB resulted after transmission over 60 km. The required sensitivity varied by about 5 dB between the different channels, probably due to variations in chirp and extinction ratio across the tuning range.

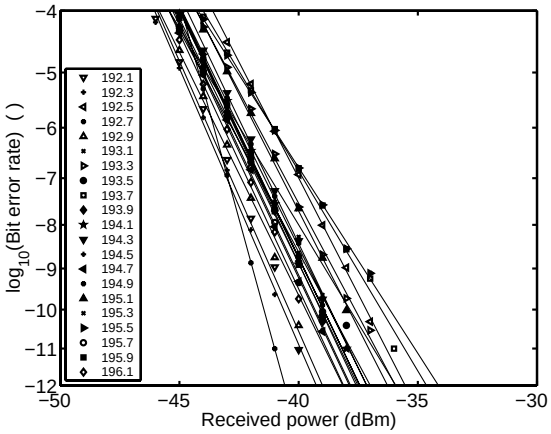

Figure 6.23 Bit error rates as a function of the average received power for 21 channels (200 GHz spacing) of a directly modulated SSG-DBR laser. Back-to-back measurement. The signal parameters were as follows. Bit-rate: 2.488 Gbit/s. Data signal: 2^{11}-1 pseudo-random bit sequence. Modulation format: non-return to zero (NRZ).

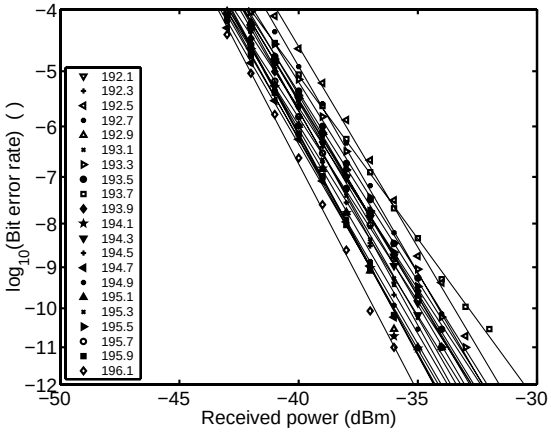

Figure 6.24 Bit error rates as a function of the average received power for 21 channels (200 GHz spacing) of a directly modulated SSG-DBR laser. Measurement after transmission over 60 km of standard single-mode fiber. For the signal parameters, cf. Figure 6.23.

Figure 6.25 shows the eye diagrams for one particular channel after transmission over 0, 40 and 80 km. The first eye diagram was measured without the fourth-order low-pass filter, which normally suppresses the relaxation oscillations. After 80 km, the eye diagram began to degrade due to dispersion, and therefore the transmission distance could not be increased any further. A similar conclusion can be drawn from the BER curves plotted in Figure 6.26 (for the 194.9 THz channel). After 60 km, a power penalty of about 3 dB was measured. After 80 km, the power penalty increased to 5 dB.

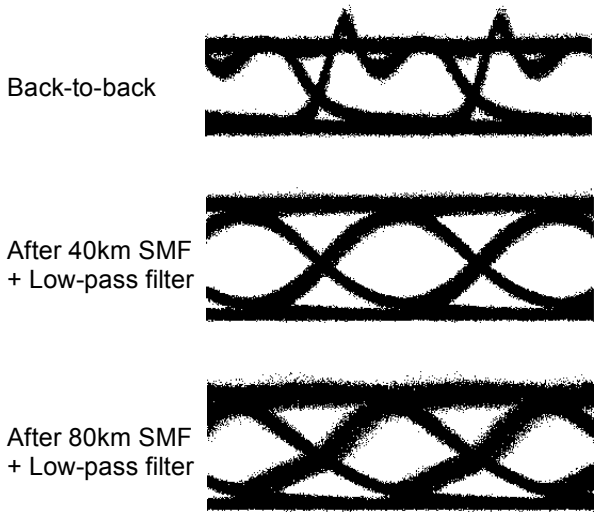

Figure 6.25 Eye diagrams after transmission over 0, 40, and 80 km of standard single-mode fiber. The first eye diagram was measured without the fourth-order low-pass filter, which normally suppresses the relaxation oscillations.

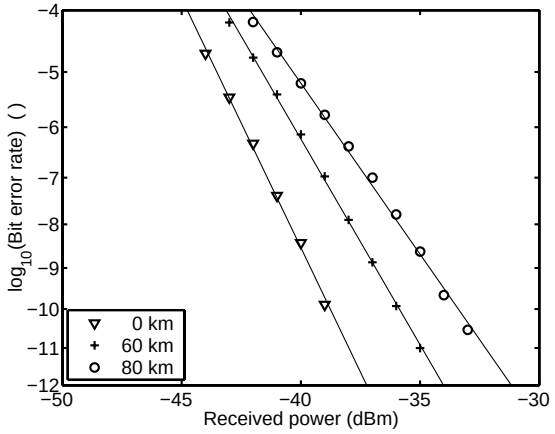

Figure 6.26 Bit error rates after transmission over 0, 60, and 80 km of standard single-mode fiber, with a 2.488 Gbit/s NRZ signal from a directly modulated SSG-DBR laser (channel at 194.9 THz).

With a conventional DFB laser, transmission over more than 100 km of standard single-mode fiber can usually be achieved with direct modulation [27]-[29]. The lower transmission distance is probably caused by the difference in chirp characteristics between a DFB laser and a SSG-DBR laser. Figure 6.27 and Figure 6.28 show the results of a chirp measurement on a SSG-DBR laser and a DFB laser, respectively. The lasers were modulated with a 2.5 Gbit/s pattern of alternating 0- and 1-bits. The graphs plot both the frequency and the intensity variations.

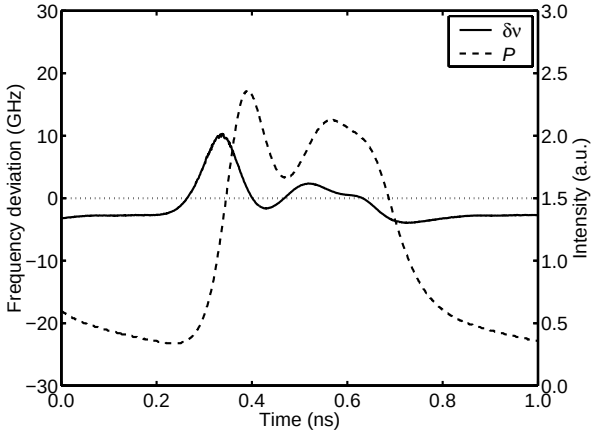

Figure 6.27 Chirp measurement of a SSG-DBR laser.

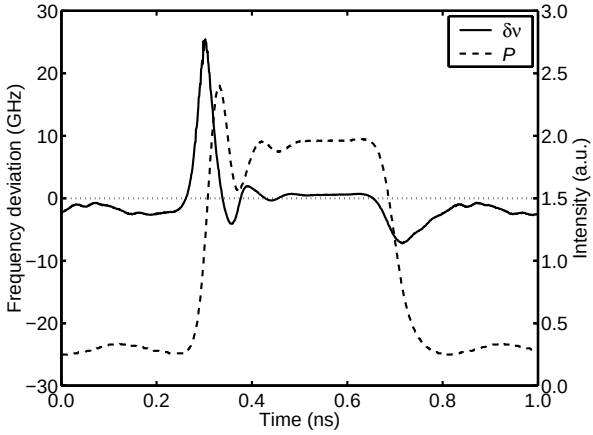

Figure 6.28 Chirp measurement of a DFB laser.

These measurements reveal that, although the amplitude of the chirp is much lower for the SSG-DBR (as expected from (6.55)), the frequency fluctuates for the entire duration of the pulse. For the DFB laser, the frequency deviations are much larger, but they affect only the edges of the pulse (mainly the leading edge). The difference can of course be explained by the higher modulation bandwidth of the DFB laser. From these results, one can expect that the DFB pulse will be less affected by fiber dispersion, allowing longer transmission distances.

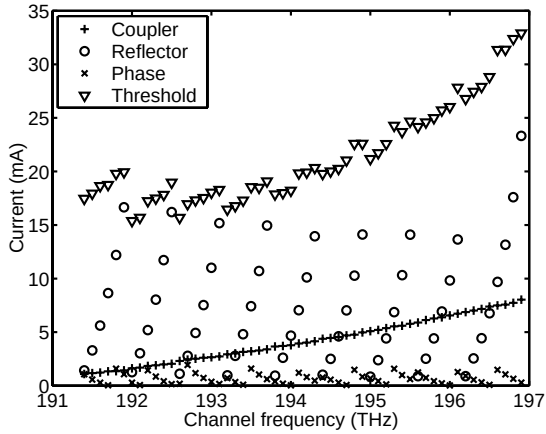

Figure 6.29 Tuning currents and threshold current for RIN measurements at 56 (100 GHz-spaced) channels of a GCSR laser.

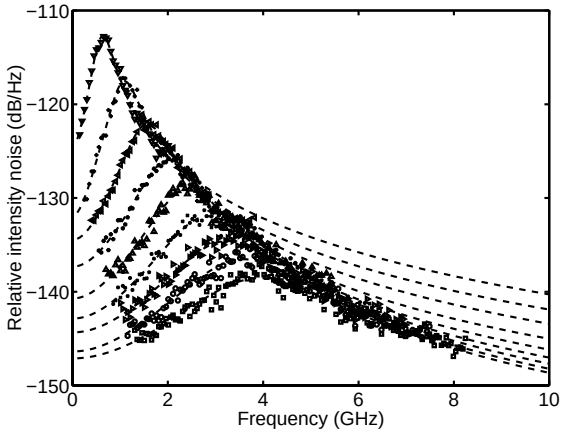

Figure 6.30 RIN spectra measured for increasing bias current for the channel at 193.60 THz (symbols). Fitted curves according to (6.72) (dashed lines).

6.3 Results for the GCSR laser

6.3.1 RIN measurements

For the GCSR laser, relative intensity noise measurements were performed for 56 channels, from 191.5 THz to 196.9 THz in 100 GHz increments. Figure 6.29 reveals the tuning currents and the threshold current for these channels. Initial estimates for the tuning currents were obtained using the algorithm described in §5.2. Some minor adjustments were subsequently made to ensure single-mode operation for active section currents ranging from the threshold to 40 mA above the threshold.

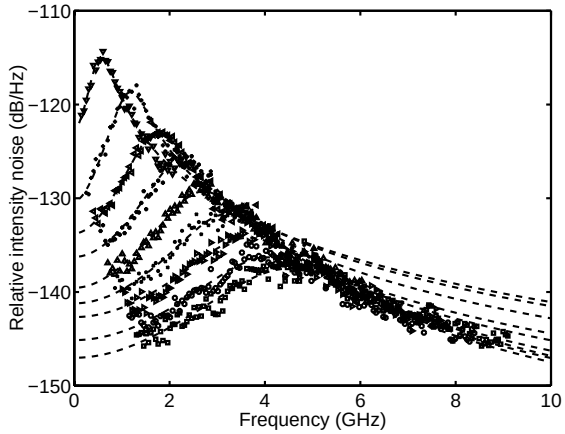

Figure 6.31 RIN spectra measured for increasing bias current for the channel at 195.90 THz (symbols). Fitted curves according to (6.72) (dashed lines).

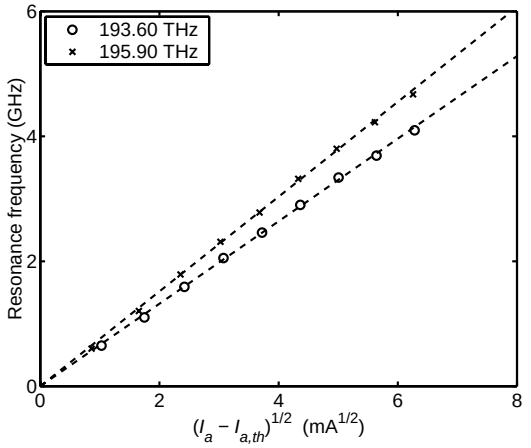

Figure 6.32 Resonance frequency extracted from RIN spectra plotted as a function of the square root of the drive current minus the threshold current, for the channels at 193.60 THz and 195.90 THz.

Figure 6.30 and Figure 6.31 show the results of the RIN measurements for two channels, 193.60 THz and 195.90 THz. Again, relation (6.72) was fitted to each of the RIN spectra in order to extract the resonance frequency f_r and the damping γ. In Figure 6.32 the resonance frequency is plotted as a function of the square root of ΔI for the two channels considered above. As for the SSG-DBR laser, the resonance frequency increases proportional to $\Delta I^{1/2}$. All other channels showed a similar proportionality between f_r and $\Delta I^{1/2}$, with slopes that lie between the two extremes plotted here. Compared to the SSG-DBR laser (Figure 6.13), the variation in the slope of the resonance frequency curves is much smaller.

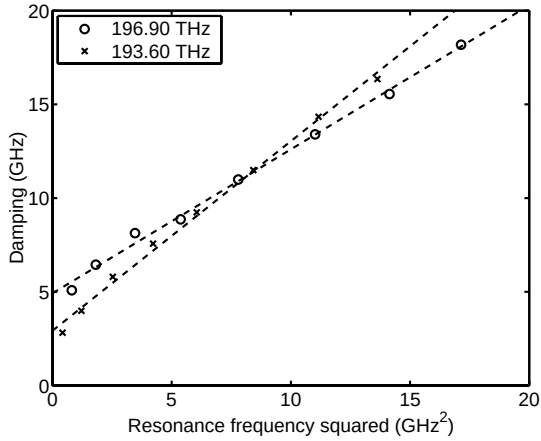

Figure 6.33 Damping plotted as a function of the resonance frequency squared, for the channels at 193.60 THZ and 196.90 THz.

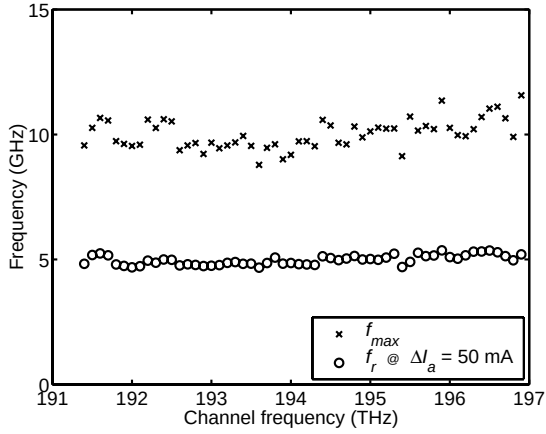

Figure 6.34 Maximum intrinsic modulation bandwidth f_{max} and resonance frequency f_r at 50 mA above threshold for all 56 (100 GHz-spaced) channels.

The same applies to the *K*-factor, as can be seen from Figure 6.33, which plots the damping as a function of the resonance frequency squared for the channels yielding the minimal and the maximal *K*, respectively. The variation of the maximum intrinsic modulation bandwidth f_{max} and the resonance frequency f_r at 50 mA above the threshold across the different channels is shown in Figure 6.34. The derived values for f_{max} are in general somewhat lower than for the SSG-DBR laser, although they still lie above 8 GHz. The lower bandwidth can be attributed to the longer effective length of the passive sections in the GCSR laser (mainly due to the coupler section), cf. (6.65). A detailed comparison is difficult however, since the GCSR and SSG-DBR lasers have a different design of the multi-quantum well (MQW) active

layer, which will obviously affect the material gain and (lateral) confinement factor Γ.

At 50 mA above the threshold, the resonance frequency is always about 5 GHz, again somewhat lower than for the SSG-DBR laser. As already mentioned, the variation of f_r across the different channels is much lower for the GCSR laser. This can probably be explained by the fact that the increase of the differential gain G_N with frequency is largely counteracted by the decrease of G_N due to the increasing threshold (Figure 6.29).

Still, the main conclusion is that direct modulation at a bit-rate of 2.488 Gbit/s should also be possible for the GCSR laser (again provided the parasitic capacitance and inductance can be kept sufficiently low).

6.3.2 Small-signal modulation response

Since the carrier of the GCSR laser contains a short stretch of co-planar line connected to the active section (Figure 2.26), a modulation signal can be applied by probing the co-planar line directly with a GS microwave probe. In order to match the resistance of the laser diode (a few Ohm) to the characteristic impedance of the coax cable (50 Ω), a custom made probe with a 45 Ω series resistor was used. The active section bias current and the sinusoidal modulation signal were combined using a bias-T. With the set-up described above, a parasitic-limited small-signal modulation bandwidth of 750 MHz was measured when the GCSR laser was biased well above threshold.

6.3.3 Large-signal digital modulation

Eye diagrams and time-averaged spectra

Due to the low small-signal bandwidth, the bit-rate for the large-signal measurements was again limited to 1.244 Gbit/s. The same modulation signal was applied as for the SSG-DBR laser. Large-signal measurements were performed for 25 channels spaced by 200 GHz, from 192.1 THz to 196.9 THz.

After tuning the laser to a particular channel, the bias current was again adjusted to obtain an extinction ratio of approximately 10 dB. A typical eye diagram is shown in Figure 6.35. Figure 6.36 shows the result of a rise time measurement. The value of 474 ps agrees quite well with the small-signal bandwidth of 750 MHz (cf. (6.86)).

Unfortunately, when the time-averaged spectrum was measured, the side-mode suppression appeared to be very low for many channels. Even when the tuning currents were carefully optimised to maximise the SMSR, many channels did not achieve the minimum required SMSR of 30 dB. The only way to bring the SMSR to the required level was to increase the bias current, which of course drastically reduced the extinction ratio. Figure 6.37 plots the maximum SMSR that could be achieved for all channels if the extinction ratio was kept at approximately 10 dB. A possible explanation of the low SMSR lies in the lower selectivity of the intra-cavity filters compared to the SSG-DBR laser (there is only a single DBR and the mode spacing is narrower).

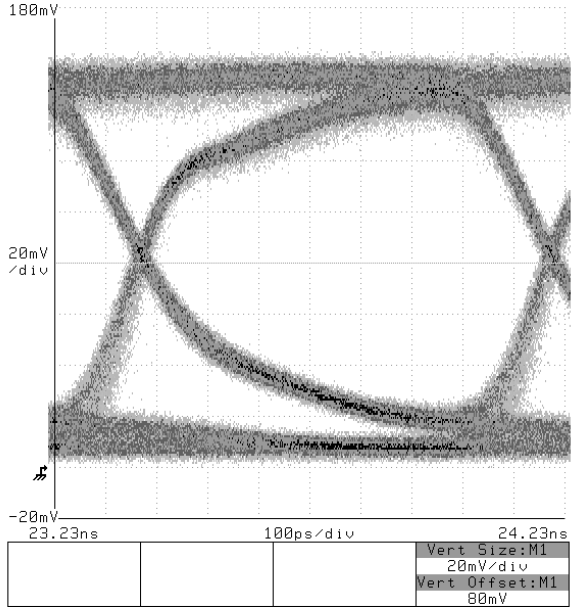

Figure 6.35 Eye diagram for a GCSR laser tuned to 192.7 THz, modulated at 1.244 Gbit/s. The transmitter configuration had a parasitic-limited bandwidth of approximately 0.75 GHz. No relaxation oscillations are visible in the signal because the receiver contained a fourth-order Bessel-Thompson low-pass filter with a cut-off frequency at 1.88 GHz.

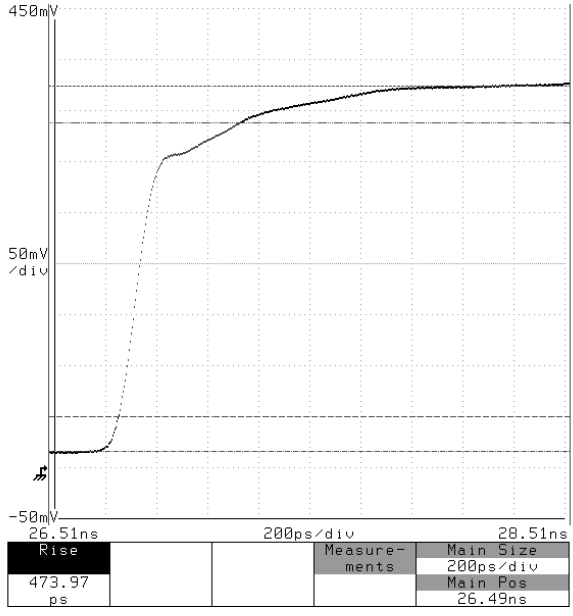

Figure 6.36 Measurement of the parasitic-limited rise time of a GCSR laser.

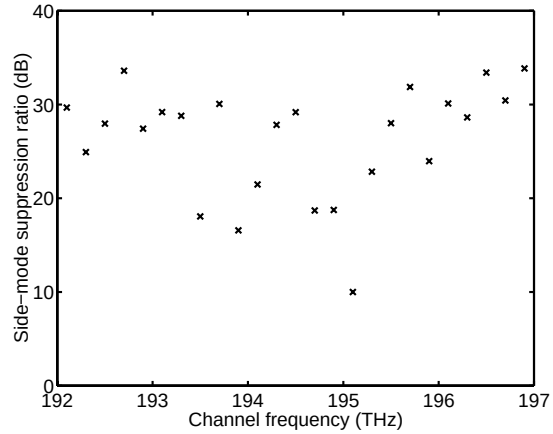

Figure 6.37 Side-mode suppression ratio with direct modulation at 1.244 Gbit/s, for 25 (200 GHz-spaced) channels of a GCSR laser. The tuning currents were optimised to maximise the SMSR, while maintaining an extinction ratio of approximately 10 dB.

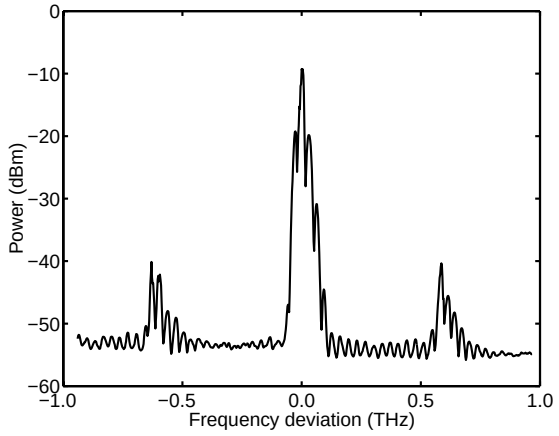

Figure 6.38 Time-averaged spectrum with direct modulation at 1.244 Gbit/s, for the channel at 195.1 THz.

.

From the chirp measurements on the SSG-DBR laser, we know that the peak-to-peak frequency variation is more than 10 GHz. Since we can expect similar values for the GCSR laser, this means that the frequency variations are close to half the cavity mode spacing (approximately 30 GHz, compared to 45 GHz for the SSG-DBR laser). From Chapter 5, we also know that the selectivity for some channels can be further reduced due to internal reflections in the cavity. If this occurs, the modulation will cause the lasing frequency to hop back and forth between different cavity modes.

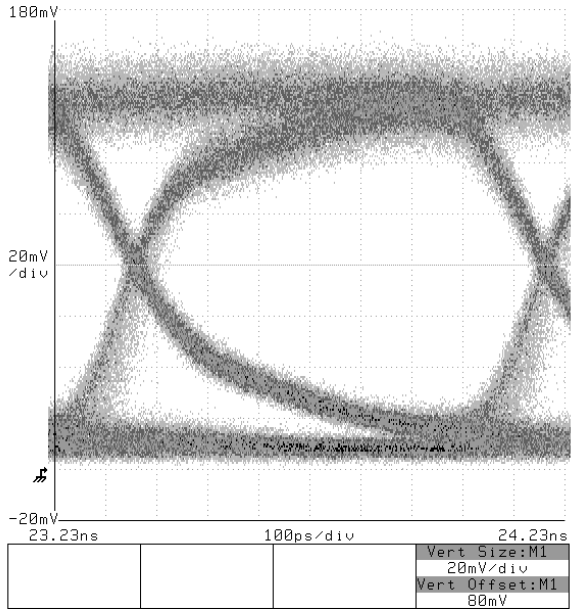

Figure 6.39 Eye diagram for the GCSR laser tuned to 195.1 THz, modulated at 1.244 Gbit/s.

The fact that internal reflections reduce the selectivity for some channels, but improve the selectivity for others could explain the large differences in SMSR in Figure 6.37. In order to improve the behaviour, the cavity probably has to be shortened and more care has to be taken to avoid internal reflections at the transition between the different sections.

The optical spectrum for the worst case channel, 195.1 THz, is displayed in Figure 6.38 and the corresponding eye diagram is shown in Figure 6.39. It reveals an increase in the noise for the 1-level compared to the eye diagram for a good channel (Figure 6.35), which could be caused by mode partition noise [2].

6.4 Conclusions

From theoretical calculations we derived that a tunable laser (or more in general a laser diode with an active section and one or more passive sections) exhibits a similar second order AM frequency response as e.g. a DFB laser. The square of the resonance frequency is however reduced by a factor Γ_z compared to a laser with only an active section, where Γ_z is a longitudinal confinement factor. This reduction can be counteracted to some extent by tuning the lasing frequency to a value below the peak frequency of the intra-cavity filter.

As in any laser diode, the resonance frequency and damping can be derived both from small-signal AM response measurements and from relative intensity noise measurements. From the variation of the resonance frequency and the damping with the drive current, the maximum intrinsic bandwidth can be estimated. RIN measurements were performed both on SSG-DBR and GCSR lasers. For the SSG-

DBR laser, the resonance frequency at 50 mA above the threshold current varied from 4 GHz to 6.9 GHz across the tuning range, with an average of about 5.5 GHz. The calculated maximum intrinsic bandwidth was above 10 GHz for most of the tuning range. For the GCSR laser, the resonance frequency at 50 mA above the threshold current was always close to 5 GHz. The extracted maximum intrinsic bandwidth was somewhat lower than for the SSG-DBR laser, though it was still above 8 GHz for the entire tuning range.

Large-signal modulation experiments were performed at a bit-rate of 1.244 Gbit/s, since the mounting and contacting techniques that were used limited the actual measured bandwidth to approximately 750 MHz for both the SSG-DBR laser and the GCSR laser. With a bias current chosen to obtain an extinction ratio of 10 dB, the SSG-DBR laser exhibited a time-averaged SMSR of at least 35 dB. In similar operating conditions, the GCSR laser however revealed a significantly reduced SMSR for some frequency channels (only 10 dB in the worst case). The inferior performance of the GCSR laser is attributed to the lower selectivity of the intra-cavity filters, which is in some cases further reduced by internal reflections at the interfaces between the different sections. The behaviour might be improved by redesigning the GCSR laser such that the cavity length is reduced.

Some results of transmission experiments using a directly modulated SSG-DBR laser were also presented. The maximum error-free transmission distance over standard single-mode fiber was about 80 km. This is less than what can be achieved using a directly modulated DFB laser (typically at least 100 km). The difference is probably due to the slow chirp in the SSG-DBR laser caused by the lower modulation bandwidth.

References

[1] A.E. Willner, "Mining the optical bandwidth for a terabit per second," *IEEE Spectrum*, vol. 34, no. 4, April 1997.

[2] K. Petermann, *Laser diode modulation and noise*, Kluwer Academic Publishers, Dordrecht, Holland, 1988.

[3] G. Morthier, and P. Vankwikelberge, *Handbook of distributed feedback laser diodes*, Artech House, Norwood, MA, 1997.

[4] F. Kano, M. Fukuda, K. Sato, and K. Oe, "High-speed intensity modulation of 1.5 µm DBR lasers with wavelength tuning," *IEEE J. Quantum Electron.*, vol. 26, no. 8, pp. 1340-1346, August 1990.

[5] F. Delorme, S. Slempkes, D. Mathoorasing, and J.-C. Bouley, "High speed and high density wavelength multichannel butt-jointed DBR lasers," *Electron. Lett.*, vol. 27, no. 21, pp. 1969-1971, October 1991.

[6] J.C. Cartledge, "Accessible tuning range of direct intensity modulated three-section DBR lasers in WDM applications," *J. Lightwave Technol.*, vol. 14, no. 3, pp. 480-4853, March 1996.

[7] C. Ougier, A. Talneau, F. Delorme, Y. Raffle, J. Landreau, and D. Mathoorasing, "Sampled-grating DBR lasers with 80 addressable wavelengths over 33 nm for 2.5 Gbit/s WDM applications," *Electron. Lett.*, vol. 32, no. 17, pp. 1592-1593, August 1996.

[8] S.-L. Lee, D.A. Tauber, V. Jayaraman, M.E. Heimbuch, L.A. Coldren, and J.E. Bowers, "Dynamic responses of widely tunable sampled grating DBR lasers," *IEEE Photon. Technol. Lett.*, vol. 8, no. 12, pp. 1597-1599, December 1996.

[9] B. Mason, S.-L. Lee, M.E. Heimbuch, and L.A. Coldren, "Directly modulated sampled grating DBR lasers for long-haul WDM communication systems," *IEEE Photon. Technol. Lett.*, vol. 9, no. 3, pp. 377-379, March 1997.

[10] F. Delorme, "Widely tunable 1.55-µm lasers for wavelength-division-multiplexed optical fiber communications," *IEEE J. Quantum Electron.*, vol. 34, no. 9, pp. 1706-1716, September 1998.

[11] A.A. Saavedra, P.-J. Rigole, E. Goobar, R. Schatz, and S. Nilsson, "Amplitude and frequency modulation characteristics of widely tunable GCSR lasers," *IEEE Photon. Technol. Lett.*, vol. 10, no. 10, pp. 1383-1385, October 1998.

[12] B. Tromborg, H. Olesen, X. Pan, and S. Saito, "Transmission line description of optical feedback and injection locking for Fabry-Perot and DFB lasers," *IEEE J. Quantum Electron.*, vol. 23, no. 11, pp. 1875-1889, November 1987.

[13] X. Pan, H. Olesen, and B. Tromborg, "Modulation characteristics of tunable DFB/DBR lasers with one or two passive tuning sections," *IEEE J. Quantum Electron.*, vol. 25, no. 6, pp. 1254-1260, June 1989.

[14] P. Vankwikelberge, G. Morthier, and R. Baets, "CLADISS - A longitudinal multimode model for the analysis of the static, dynamic, and stochastic behavior of diode lasers with distributed feedback," *IEEE J. Quantum Electron.*, vol. 26, no. 10, pp. 1728-1741, October 1990.

[15] *i-CLADISS – A longitudinal laser diode model*, Photon Design, 86 Courtland Road, Oxford OX4 4JB, UK. <http://www.photond.com/>

[16] C.H. Henry, "Phase noise in semiconductor lasers," *J. Lightwave Technol.*, vol. 4, no. 3, pp. 298-311, March 1986.

[17] R. Olshansky, P. Hill, V. Lanzisera, and W. Powazinik, "Frequency response of 1.3 µm InGaAsP high speed semiconductor lasers," *IEEE J. Quantum Electron.*, vol. 23, no. 9, pp. 1410-1418, September 1987.

[18] O. Kjebon, R. Schatz, S. Lourdudoss, S. Nilsson, and B. Stålnacke, "Modulation response measurements and evaluation of MQW InGaAsP lasers of various designs," *Proc. SPIE*, vol. 2684, pp. 138-152, San Jose, CA, USA, February 1996.

[19] R.F. Kazarinov, and C.H. Henry, "The relation of line narrowing and chirp reduction resulting from the coupling of a semiconductor laser to a passive resonator,", *IEEE J. Quantum Electron.*, vol. 23, no. 9, pp. 1401-1409, September 1987.

[20] G.P. Agrawal, and C.H. Henry, "Modulation performance of a semiconductor laser coupled to an external high-Q resonator," *IEEE J. Quantum Electron.*, vol. 24, no. 2, February 1988.

[21] K. Vahala, and A. Yariv, "Detuned loading in coupled cavity semiconductor lasers – effect on quantum noise and dynamics," *Appl. Phys. Lett.*, vol. 45, no. 5, pp. 501-503, March 1984.

[22] M. Öberg, O. Kjebon, S. Lourdudoss, S. Nilsson, L. Bäckbom, K. Streubel, and J. Wallin, "Increased modulation bandwidth up to 20 GHz of a detuned-loaded DBR laser," *IEEE Photon. Technol. Lett.*, vol. 6, no. 2, pp. 161-163, February 1994.

[23] R. Schatz, D. McDonald, and H. Hillmer, "Parameter extraction," *Chapter 9 in Photonic devices for telecommunications – How to model and measure*, ed. G. Guekos, Springer Verlag, Berlin Heidelberg, Germany, 1999.

[24] G.P. Agrawal, and N.K. Dutta, *Long-wavelength semiconductor lasers*, Van Nostrand Reinhold, New York, NY, USA, 1986.

[25] S. Hansmann, H. Walter, H. Hillmer, and H. Burkhard`, "Static and dynamic properties of InGaAsP/InP distributed feedback lasers - a detailed comparison between experiment and theory," *IEEE J. Quantum Electron.*, vol. 30, no. 11, pp. 2477-2483, November 1994.

[26] G.P. Agrawal, *Fiber-optic communication systems*, John Wiley & Sons, New York, NY, USA, 1997.

[27] Lucent D2511 1.55 µm digital isolated DFB laser module, Lucent Technologies - Microelectronics Group, 555 Union Boulevard, Room 30L-15P-BA, Allentown, PA 18103, USA. <http://www.lucent.com/micro/opto/>

[28] Infineon V23845-Lxy11-z116 1.55 µm DFB LD module for WDM, direct modulated 2.5 Gbit/s, Infineon Technologies - Fiber Optics, Wernerwerkdamm 16, Berlin D-13623, Germany. <http://www.infineon.com/fiberoptics/>

[29] Fujitsu FLD5F6CX-E 1550 nm MQW-DFB DWDM direct modulation laser, Fujitsu Compound Semiconductor, 2355 Zanker Road, San Jose, CA 95131-1138, U.S.A. <http://www.fcsi.fujitsu.com/>

Chapter 7

General conclusions – Topics for future research

Research on monolithically integrated tunable laser diodes already has a fairly long history (more than 20 years, cf. Chapter 2). However, until recently tunable laser diodes were by many people deemed unsuitable for applications in optical communication: they were too complex to control and they would never live up to the stringent requirements posed on components for telecom systems (e.g. 20 years of operational lifetime). Recent research results – among which the results reported in this thesis – have however proven them wrong. Nowadays, tunable lasers are considered to be essential components for the next generation of optical communication systems employing wavelength division multiplexing.

The key to this success is the fact that the tunable laser is not delivered as such, but is integrated into a module containing control electronics. These act as an interface between the external system and the laser, translating frequency and output power requirements to the appropriate values of the laser's control currents. To this end, a look-up table of operation points for all frequency channels used in the system is stored in a semi-permanent memory. To ensure long-term reliability and stability a feedback control system can be added.

As was discussed in Chapter 4, three parameters have to be stabilised: the emission frequency, the output power, and the side-mode suppression ratio. Stabilisation of the output power is the easiest, since the power can be measured directly and since it is easily adjusted by changing the active section current. An error signal that allows controlling the frequency is also obtained fairly straightforward, by using an optical filter to translate frequency variations into power variations (§4.1). Maintaining single mode operation is however not so simple. We discovered that local minima in the active section voltage (with respect to the tuning currents) mark operation points with high side-mode suppression ratio (§4.2). By adding a small dither to a tuning current, the derivative of the voltage with respect to this current can be measured. When a correction proportional to this derivative is subtracted from the tuning current, then the laser will be locked to the voltage minimum and a high SMSR will be maintained. The three types of feedback control were combined into a single control system, which could stabilise the laser with a frequency error of less than ±1.0 GHz, a constant output power and a side-mode suppression ratio well above 35 dB (§4.3). This system was demonstrated at the European Exhibition on Optical Communication in Nice, France in September 1999.

The fact that voltage minima mark single-mode operation points was also used to develop a characterisation procedure that can generate a look-up table for a tunable laser automatically (§5.4). The algorithm quickly maps out a set of optimised operation points covering the entire tuning range of the laser. When the frequency is measured for these operation points, a look-up table for any set of frequencies can be calculated by straightforward interpolation. Experimental verification of the generated look-up tables yielded extremely low frequency errors, less than ±0.5 GHz, and side-mode suppression ratios of at least 35 dB for all calculated set points. We even believe that if the laser is integrated into a control module with a few optical filters for frequency referencing, this procedure can be extended into a self-calibration procedure that no longer requires any external equipment.

To support the development of the above characterisation and control methods, we built a simulation model for longitudinally integrated tunable lasers. The model uses the classic rate equation approach to describe the laser's active section (§3.1), and calculates the complex amplitude reflectivities of the concatenated passive sections using transfer matrices (§3.2). Simulation results obtained with this model have been used throughout the thesis to explain or confirm experimental results. The transfer matrix description was also applied in design studies of novel types of Bragg reflectors with a comb-shaped reflectivity spectrum (§3.3).

Finally, in Chapter 6 we studied the direct modulation characteristics of the tunable laser diodes. Analytical expressions were derived for the small-signal modulation response and the relative intensity noise spectrum and these were compared to the well-known expressions for single-section DFB lasers (§6.1). In general, a tunable laser diode will have a somewhat lower modulation bandwidth, due to the longer laser cavity. Experimentally, the damping and the resonance frequency of the intrinsic laser diode were derived from measurements of the relative intensity noise spectrum, and from these the maximum modulation bandwidth was estimated. Both for the SSG-DBR and the GCSR laser, this yielded bandwidths of 8 GHz and more, depending on the operation point (§6.2 and §6.3).

When a large-signal digital modulation was applied, only the SSG-DBR laser maintained a high spectral purity. This is attributed to the higher selectivity of the intra-cavity filters in the SSG-DBR laser compared to the GCSR laser. NTT Optoelectronics recently demonstrated transmission at a bit-rate of 2.5 Gbit/s using a directly modulated SSG-DBR laser. Signals could be transmitted error-free up to distances of about 80 km, which is somewhat less than what is commonly achievable with a DFB laser (at least 100 km). Future development work could be aimed at increasing the transmission distance and/or the modulation bandwidth.

One problem that was not addressed in this thesis is how the look-up table should be kept up to date during the device operation. The feedback system from §4.3 can be used to maintain a laser at a particular channel, but when the current settings for this channel change, then the operation points for the other channel will also drift. In some applications, the laser could be switched out of the system to run an automatic re-calibration procedure at certain points in time (e.g. every few months, of whenever a current for an operation point has changed by more than X% relative to the value in the table). In other applications, the laser will have to be in operation all the time, which means that the look-up table would have to be updated based on the

changes in the drive currents for the frequency channel the laser is currently emitting in.

A final topic for future research is the development of lasers and control electronics that would allow rapid frequency switching, e.g. for optical packet switching applications (cf. Chapter 1). A typical requirement is that the laser module can switch between channels in 20 ns. This will not only require tuning sections with a very fast response, but will also have a significant impact on the control electronics.